ALFRED-WEGENER-INSTITUT
HELMHOLTZ-ZENTRUM FÜR POLAR-
UND MEERESFORSCHUNG

Universität Bremen

Processes affecting the oceanic iron cycle and their interaction with marine biology and climate

Author:
Anna PAGNONE

Supervisors:
Prof. Dr. Gerrit LOHMANN
Dr. Christoph VÖLKER
Dr. Ying YE

DISSERTATION

zur Erlangung des Grades

Dr. rer. Nat.

vorgelegt dem

Fachbereich Physik
der Universität Bremen

Examiners:
Prof. Dr. Gerrit LOHMANN
Dr. Thorsten WARNEKE

Bremen, November 2019

Abstract

The oceanic iron (Fe) cycle is an important component of the Earth system and its functioning has large implications for the climate. Due to the complexity of a number of processes that shape it, biogeochemical models still struggle to reproduce the global dissolved Fe distribution. The Fe model inter-comparison project FeMIP compared several global biogeochemical models and revealed large differences between the models' description of the Fe cycle. It thus highlighted the need of more constraints. This is becoming possible to some extent, thanks to the international GEOTRACES program which coordinats the measurement methods and measurements of a large number of trace components of ocean biogeochemistry. In recent years, GEOTRACES provided a large amount of dFe measurements. The aim of this thesis is to gain a better understanding of the marine Fe cycle by means of the biogeochemical model REcoM2, comparing the output with available data.

First, I investigated the state-of-the-art-performance of REcoM2 in reproducing dFe concentration in the world's oceans. Though some large scale patterns were reproduced, others were not. The surface dFe concentration in the subtropical North Atlantic Ocean was overestimated, while in the subtropical Pacific Ocean it was underestimated. Furthermore, the global deep ocean dFe concentrations were too homogeneous in comparison to the observations.

A sensitivity study on the loss rate of Fe through adsorption on particles, or scavenging, and on the strength of the sediment dFe source, which are both not well constrained from data, showed that a simple tuning exercise is inefficient in improving the model-observation agreement because of the strong non-linearity of the Fe cycle. A better agreement to the observations can thus only be achieved by introducing further new dFe sources and processes in the model. Furthermore, I observed that the sedimentary dFe source affected the dFe surface concentration in the Pacific Ocean differently than in the other basins. This highlighted the importance of basin-specific modelling studies on the Fe cycle, with particular attention to regional patterns and local processes. Thus, in this thesis, two regions were subsequently investigated with respect to new model descriptions of dFe sources and sinks: the subtropical North Atlantic and the Southern Ocean.

The subtropical North Atlantic is characterised by high rates of dust deposition, which bring in Fe, and intensive Fe cycling. In a sequence of changes to the model, the main dFe features along the GEOTRACES section GA03 such as a deep East-West gradient, a hydrothermal plume and a subsurface dFe minimum, could be better reproduced and explained. This was achieved by introducing scavenging on lithogenic particles and on phytoplankton, a new ligand parameterisation based on AOU, an increased sinking velocity of particles and a hydrothermal dFe source.

Differently, the Southern Ocean is the largest High-Nutrient Low-Chlorophyll region, where aeolian deposition is low and dFe is the main limiting micro-nutrient for phytoplankton. Here, the role of icebergs as a source of Fe was analysed, with respect to diatom and non-diatom net primary production, nutrient availability, as well as carbon, nitrogen and silica export. The results show a strong decoupling of the effects of Fe fertilisation by icebergs on the nitrogen and silica cycles. Different strengths of the Fe fertilisation allowed a speculation

on the effect of increased iceberg calving in future warmer climates to the antarctic marine biota.

Fe fertilisation of the Southern Ocean has also occurred during past glacial periods. The "Iron Hypothesis" suggests that the additional Fe supply to the ocean was an important factor causing lower atmospheric CO_2 concentrations in the glacial. In a laboratory experiment, I analysed the growth, carbon production and photophysiology of the Southern Ocean bloom-forming diatom *Pseudo-nitzschia subcurvata*, under simulated glacial and interglacial climatic conditions. Overall, the results indicated that the combination of higher Fe availability with lower pCO_2, like it has been in the glacial ocean, was beneficial for this diatom, with potential effects on the carbon export. These finding could be used to derive a better parametrisation of diatom growth in the biogeochemical model.

This thesis presents an investigation on different aspects of the quite complex marine Fe cycle. Particular attention is put on regional features and processes (subtropical North Atlantic Ocean vs. Southern Ocean), on the biological response to Fe deficiency and Fe enrichment, as well as on past and future climate scenarios.

Contributions to scientific journals

1) First author peer-reviewed publication

Chapter 5:

Processes affecting dissolved iron across the Subtropical North Atlantic: a model study

Anna Pagnone[1], Christoph Völker[1] and Ying Ye[1]

[1] Biogeosciences Section, Alfred Wegener Institute, Helmholtz Centre for Polar and Marine Research, Bremerhaven, Germany

Pagnone, Anna, Christoph Völker, and Ying Ye (2019). "Processes affecting dissolved iron across the Subtropical North Atlantic: a model study". In: Ocean Dynamics. doi: 10.1007/s10236- 019-01288-w.

Published in Ocean Dynamics

2) First author manuscripts

Chapter 6:

The role of icebergs in the Fe cycle

Anna Pagnone[1], Christoph Völker[1] and Ying Ye[1]

[1] Biogeosciences Section, Alfred Wegener Institute, Helmholtz Centre for Polar and Marine Research, Bremerhaven, Germany

Manuscript in preparation

Chapter 7:

Pseudo-nitzschia subcurvata flourished best under simulated glacial than interglacial ocean conditions

Anna Pagnone[1], Florian Koch[1,2], Franziska Pausch[1,3] and Scarlett Trimborn[1,3]

[1] Biogeosciences Section, Alfred Wegener Institute, Helmholtz Centre for Polar and Marine Research, Bremerhaven, Germany
[2] Hochschule Bremerhaven, Bremerhaven, Germany
[3] Marine Botany Department, Faculty 2 Biology/Chemistry, University of Bremen, Bremen, Germany

Manuscript in preparation

3) Further contributions

From the origin of feces - The impact of krill and salps on the iron biogeochemistry of iron-limited waters in the Southern Ocean

Sebastian Böckmann[1,2], Florian Koch[2,3], Franziska Pausch[1,2], Anna Pagnone[2], Dorothee Wilhelms-Dick[2], Luis M. Laglera[4], Camila Sukekava[5], Christel Hassler[6], Scarlett Trimborn[1,2]

[1] Marine Botany Department, Faculty 2 Biology/Chemistry, University of Bremen, Bremen, Germany
[2] Alfred Wegener Institute, Helmholtz Centre for Polar and Marine Research, Bremerhaven, Germany
[3] Hochschule Bremerhaven, Bremerhaven, Germany
[4] University of the Balearic Islands, Palma, Spain
[5] Federal University of Rio Grande, Rio grande do Sul, Brazil
[6] University of Geneva, Geneva, Switzerland

Manuscript in preparation

Contents

1 Introduction to the oceanic iron cycle

Oceanic biogeochemistry plays a decisive role in the Earth's climate, as it impacts the carbon cycle. Especially relevant in transforming and transporting carbon in the Earth's system is the role played by the iron (Fe) cycle, linking many different parts of the climate system. Fe is essential for almost all living beings, from plants to animals such as humans. In the ocean, Fe is a fundamental micronutrient for phytoplankton used to transfer electrons in key processes including photosynthesis, respiration, chlorophyll production, and carbon and nitrogen fixation (Raven, Evans, and Korb, 1999) (Section 1.1). Though Fe is the fourth most abundant element in the Earth crust, its concentration in seawater is extremely low. Other trace metals as manganese, cobalt, nickel, copper, zinc and cadmium share the same characteristic. A strong correlation between the concentration of Fe, ocean productivity, chlorophyll concentration, and carbon export was often observed (Johnson, Gordon, and Coale, 1997). Spatially, Fe regulates primary production in more than 25% (de Baar et al., 2005) and possibly in up to 50% (Moore et al., 2001; Boyd and Ellwood, 2010) of the world's oceans (Section 1.6). Henceforth, the global marine carbon drawn-down is significantly affected by Fe, making it one of the drivers of the oceanic carbon pump and thereby inducing feedback effects on climate (Section 1.2).

The cycling and distribution of dissolved Fe (dFe) in the ocean is regulated by chemical, physical and biological processes. The main external inputs of dFe to the ocean are atmospheric dust deposition (e.g. Mahowald et al., 2005; Jickells et al., 2005), fluxes from reducing sediments (e.g. Elrod et al., 2004) and hydrothermal vents (e.g. Resing et al., 2015) (Section 1.5). Furthermore, Fe is introduced by river and groundwater discharge (e.g. Hunter et al., 1997) and by volcanic ashes (e.g. Hamme et al., 2010). In polar regions, glacial, iceberg (e.g. Raiswell et al., 2008) and sea ice (e.g. Lannuzel et al., 2008) meltwater is a source of Fe. Fe then enters the biological cycle through phytoplankton uptake, is transferred within the food web and is remineralised by heterotrophic organisms at depth. Vertical export of biogenic material removes dFe from the water column (e.g. Balistrieri, Brewer, and Murray, 1981). Unlike other nutrients, dFe is additionally removed by scavenging, which is the term coined by Turekian (1977) for the loss of Fe from the dissolved phase through adsorption or precipitation on particle surfaces. This is influenced by dFe's extremely low inorganic solubility at seawater pH in the presence of oxygen (Liu and Millero, 2002) (Section 1.3 and Section 1.4). To some extent, this is mitigated by organic ligands which keep Fe in the dissolved phase (e.g. Gledhill and Buck, 2012). Physical transport of dFe (and Fe-binding ligands) by ocean currents, i.e. vertical mixing, upwelling of Fe-rich water masses or transport of specific ligand signatures, also influences the dFe distribution.

In the last decades, large improvements have been made in describing the global dFe distribution, as well as partially that of organic Fe-binding ligands. The efforts of GEOTRACES, which have led to the 2017 Intermediate Data Product (IDP) (Schlitzer et al., 2018), also revealed the importance of many previously disregarded processes, such as the strong influence of hydrothermal vents on deep-sea dFe distributions.

Many important processes affecting the Fe cycle are however not well constrained quantitatively. Important examples are the strength of Fe sources to the ocean or the rate at which

dFe is lost from the system through scavenging. Consequently, global biogeochemical models still differ much in their description of the marine Fe cycle, resulting in residence time estimates for dFe that vary over more than one order of magnitude (Tagliabue et al., 2016), as well as in an often too homogeneous distribution of dFe in the deep ocean. The details of the distribution of dFe concentration that are obtained with GEOTRACES, implicitly contain a wealth of information that can be used to constrain the quantitative representation of processes when combined with systematic parameter studies.

1.1 Iron in marine biology

The Archean ocean in which life first evolved was anoxic and rich in dFe in the form of the much more soluble redox state Fe(II). The first algae made substantial use of Fe in fundamental metabolic processes, as Fe is a good transition metal for redox reactions. Once oxygenic photosynthesis evolved and the O_2 concentrations in the ocean built up, dFe as Fe(II) was oxidised and large amounts of the now stable and insoluble Fe(III) precipitated, making dFe a rare good (Section 1.3). Living beings, however, had already established a stable role for Fe in many basic processes and that was carried on by genetic heritage over Earth's history (Saito, Sigman, and Morel, 2003; Williams and Rickaby, 2012). In phytoplankton, Fe is used in the electron transport system of photosynthesis and respiration, in enzymes involved in nitrate and nitrite reduction, in nitrogen fixation, in pigment production and degradation, and in DNA synthesis among others. As an example, I will refer to the role of Fe in the photosynthesis of phytoplankton described in Behrenfeld and Milligan (2013). Photosynthesis takes place in chloroplasts which contain thylakoids. Embedded in the thylakoid membrane are two photochemical reaction centres where photosynthesis actually occurs (upper part of Fig. 1.1). The photosystem I and II (PSI and PSII) are composed of proteins and pigments. The aqueous fluid in which the thylakoid is enclosed is called stroma, while the space within the membrane is called lumen. Light energy absorbed by pigments travels to the chlorophyll molecule within the photosynthetic reaction centres (gray in Fig. 1.1) and is transformed into chemical energy. The lower part of Fig. 1.1 shows the electron and proton pathways and the role of Fe-containing molecules in the light reaction of photosynthesis (see Behrenfeld and Milligan, 2013, for further description).

As mentioned above, the abundance of dFe is rather limited in the modern ocean and hence organisms evolved specific Fe acquisition strategies. Some prokaryotes such as bacteria release siderophores, Fe-binding organic molecules, to take up Fe from the surrounding (Vraspir and Butler, 2009), while eukaryotes such as diatoms do not. The presence of Fe-reducing enzymes on the membrane of the latter helps in the uptake process of Fe. Uptake can occur by reduction of Fe bound to ligands, which are sometimes the same siderophores produced by bacteria to facilitate their own Fe uptake, to Fe(II) by means of O_2 or reductase at the cell surface. Furthermore, specialised transport mechanisms allow direct transport of Fe(III) and Fe(II) ions across the cell membrane, as summarised in Morel, Kustka, and Shaked (2008). The efficient uptake of Fe is related to its availability but also to the size of the phytoplankton cell. Smaller phytoplankton with larger surface to volume ratio, absorb Fe more efficiently than larger phytoplankton. Indeed, they reduce Fe to a higher rate per unit biomass. For example, diatoms are less able to absorb Fe even though they have a higher demand (Morel and Price, 2003). The Fe demand by phytoplankton also depends on the species and the environment. For instance, it was shown that open ocean phytoplankton which evolved in an Fe-deplete surrounding, require less Fe than coastal ones (Sunda, Swift, and Huntsman, 1991). To adapt to the low dFe concentrations in seawater, organisms developed strategies to reduce their Fe requirement. For example, phytoplankton can reduce their cell size, minimise the number of Fe-containing enzymes and decrease the use of PSI in

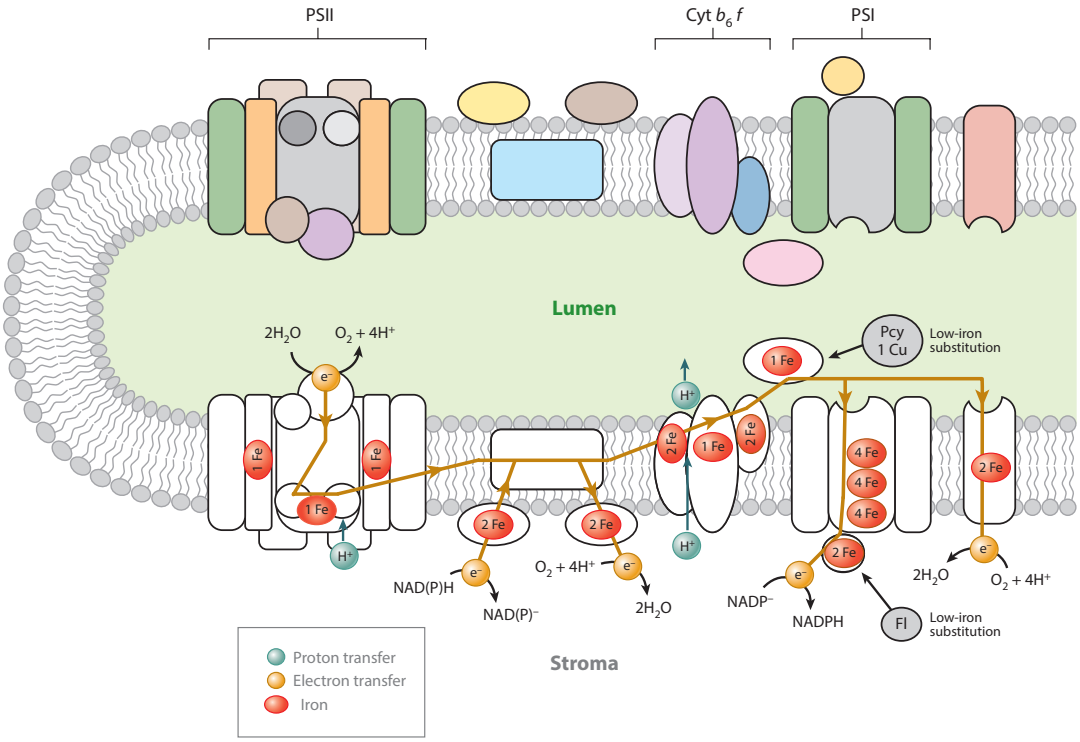

FIGURE 1.1: Fe requirements in photosynthesis and electron-proton transport in the thylakoid membrane (modified from Behrenfeld and Milligan, 2013)

comparison to PSII, considering that the latter needs less Fe (Strzepek and Harrison, 2004). Some diatoms have the ability to store Fe for Fe-poor times (Marchetti et al., 2009). Furthermore, Fe limitation alters the phytoplankton species composition and phytoplankton physiology. Blooms of Fe-stressed communities are usually dominated by small phytoplankton. In response to a relief from Fe limitation, the bloom shifts towards being dominated by larger cells, often diatoms (e.g. Landry et al., 2000). This was observed in several large-scale Fe fertilisation experiments in high-nutrient low-chlorophyll regions (HNLC) (Coale et al., 1996; Coale et al., 2004; Boyd et al., 2000) (Section 1.6). Furthermore, the experiments showed that Fe addition increased the phytoplankton growth rate, increased zooplankton grazing and changed the carbon (C) and silicon (Si) export (e.g. Behrenfeld et al., 1996; Assmy et al., 2013). Fe-containing particulate organic matter, which sinks through the water column is fed on by heterotrophic bacteria (Tortell, Maldonado, and Price, 1996; Strzepek et al., 2005), zooplankton grazers (Sarthou et al., 2008) and viruses (Mioni, Poorvin, and Wilhelm, 2005). The result of the feast is free and now bioavailable dFe ready for uptake by the biota (Boyd and Ellwood, 2010). Despite this efficient and rapid Fe recycling in the ocean interior, the dFe concentrations are low and the impact of dFe on primary production has repercussions on the C uptake and sequestration, thus on climate.

1.2 Iron and climate

The ocean plays a crucial role in the global C cycle both in terms of physical and chemical properties, as well as with regards to the biological pump. Since the deep ocean contains roughly 50 times more C than the atmosphere, most of the physical exchange of CO_2 at the ocean-atmosphere interface takes place in upwelling regions where deep water is brought

to the surface. Classical examples are the coast of California, Peru, Chile and Namibia. Strong fluxes of CO_2 are also observed in deep water formation regions as the North Atlantic Ocean and the Southern Ocean. In both these regions, relatively small changes in the ocean circulation can have large effects on the fluxes between ocean and atmosphere, and thus on the global C budget. On the other hand, phytoplankton in the ocean are responsible for about half of the photosynthetic fixation of C via primary production on Earth, converting about 45 Gt of atmospheric CO_2 to organic C through photosynthesis annually (Field et al., 1998; Falkowski, Barber, and Smetacek, 1998). Organic matter then sinks into the deep ocean, making this drawdown of C a substantial player in the C cycle. The efficiency of the biological pump depends on several factors as light, temperature and nutrient availability. The Southern Ocean is an important example for both physical and biological factors, driving CO_2 uptake from the atmosphere. It is both, an extensive deep-water formation area and the largest HNLC region. As such, it has the largest potential to influence atmospheric CO_2 concentration when the Fe supply changes compared to other oceans (Jickells et al., 2005). This example signals the relevance of Fe in the C cycle and climate.

The ocean is thought to be one major driver for the reduced atmospheric CO_2 concentrations during glacial (ca. 180 ppm) compared to interglacial (ca. 280 ppm) periods (Watson and Naveira Garabato, 2006). The exact mechanism responsible for this decrease of 80 - 100 ppm CO_2 is still not well understood and it is most likely a combination and complex interaction of physical and biogeochemical processes in the ocean. On the physical side, for example, changes in Antarctic sea ice extent during glacial periods induced surface water stratification. This limited the ocean ventilation, trapping more C in the deep ocean (e.g. Sigman and Boyle, 2000). Further, the northward displacement of the westerly winds during glacial times, prevented the upwelling of CO_2-rich deep waters (Toggweiler, Russell, and Carson, 2006). On the other hand, from a biological perspective, the Fe supply from the atmosphere to the ocean was higher in glacial times due to variations in land coverage (Werner et al., 2002). Additional Fe input reduced the Fe limitation in HNLC regions and consequently stimulated marine productivity, increasing both uptake of atmospheric CO_2 and C sequestration.

The influence of aeolian dust deposition on glacial-interglacial atmospheric CO_2 concentrations was first suggested by Martin (1990) and was henceforth called "Iron Hypothesis". For example, in the Southern Ocean, the atmospheric dust deposition during glacial periods was amplified because of a larger exposure of the Patagonia shelf, increased aridity in South America and increased strength and northward migration of the westerly winds (Martínez-Garcia et al., 2009, and references therein). It was suggested that the additional Fe input during the last glacial maxima accounted for up to 25% of the decrease in atmospheric CO_2 concentration (Sigman and Boyle, 2000). However, the extend of an enhanced productivity on the CO_2 variation between glacial and interglacial periods is still under discussion. Martínez-Garcia et al. (2009) suggested that sub-Antarctic regions alone could explain half of the ca. 100 ppm CO_2 variation, while other models advanced that the contribution is one third or less than a quarter (Lambert et al., 2015; Aumont and Bopp, 2006). The latter furthermore proposed other processes as changes in ocean ventilation and circulation, oceanic C storage and hydrothermal Fe supply, which may have contributed to the CO_2 variation.

In future climate scenarios, the ocean has been shown to become more acidic and less able to absorb further atmospheric CO_2. The upwelling of nutrient-rich deep water in the Southern Ocean is forecasted to become stronger (Hauck et al., 2013). Moreover, climate change also affects arid regions and consequently the amount of dust uplifted in the atmosphere and transported to the ocean (Prospero et al., 2002). Yet, it still remains uncertain whether dust deposition will increase or decrease with future warmer climate, as different patterns

of future dust have been predicted with different models (Kok et al., 2018). In case of a negative dust-climate feedback effect in which an increase of the dFe delivery to the surface water influence primary production, this has been shown to prosper with increased supply. Consequently, more sinking organic matter will increase the remineralisation, thus more Fe is again made available for biology. Furthermore, climate induced changes in pH, productivity, temperature and light intensity control the abundance and binding strength of ligands, again offering a feedback on dFe distribution. The resulting sequestration of C has implications for the atmospheric CO_2 concentration and therefore for the climate (Jickells et al., 2005). Accordingly, the oceanic Fe cycle presents many large-scale feedbacks effects which can impact both past and future climate scenarios.

1.3 Iron properties in the ocean

To understand the role of oceanic dFe in the Earth system, some properties have to be named. First of all, Fe in seawater is present in different chemical forms. The predominant redox state of dFe is Fe(III), ferric iron, which is thermodynamically stable in oxic seawater. Inorganic Fe(III) is composed of Fe^{3+}, $Fe(OH)_2{}^+$, $Fe(OH)_3$, $Fe(OH)_4{}^-$ and the relative concentration of each form depends on the pH of the water. For example, at the average seawater pH of 8, $Fe(OH)_3$ is dominant (Byrne, Kump, and Cantrell, 1988; Millero, Yao, and Aicher, 1995). However, $Fe(OH)_3$ is highly insoluble and usually gets scavenged and precititates as iron oxy-hydroxide minerals. On the other hand, Fe(II), ferrous iron, is stable in anoxic/reducing environments and is mostly present in the free ionic form Fe^{2+}. Since Fe(II) is oxidised to Fe(III) within minutes in the presence of oxygen, its concentration in seawater is rather low, with the exception of anoxic or low-oxygen environments as the oxygen minimum zones (Pakhomova, Rozanov, and Yakushev, 2009; Cutter et al., 2018). Due to the higher solubility of Fe(II) compared to Fe(III), the dFe concentration in these regions can be much higher. At the surface ocean, Fe(II) is produced by photochemical reduction of Fe(III) (Barbeau et al., 2001; Voelker and Sedlak, 1995). Furthermore, release via microbial remineralisation, lysis and grazing, as well as external inputs from atmospheric deposition, seafloor sediments, groundwater and hydrothermalism, influence the distribution of Fe(II) in the ocean, keeping its concentration detectable (Sedwick et al., 2015).

Liu and Millero (2002) observed that though Fe(II) is soluble, it is unstable and oxidises to Fe(III) which, on the contrary, is strongly insoluble in seawater. Considering the Fe inorganic solubility in waters of pH 8 and 25 °C temperature, a concentration of only 0.01 nM would be permitted (Liu and Millero, 2002). Nonetheless, a higher dFe concentration in the ocean is reached via the complexation of Fe by ligands (described below). About 99% of the total dFe is complexed by ligands and not present in the form of inorganic ferric or ferrous hydroxides (Gledhill and Buck, 2012). Organic complexation by Fe-binding ligands keeps Fe in solution, avoiding that it binds to OH^-, and preventing it from being scavenged.

Organic ligands are present everywhere in the ocean, typically with higher concentrations at the surface compared to depth, and near the coast compared to the open ocean. Laboratory analysis operationally distinguishes between a strong Fe-binding ligand class and several weak ones (Gledhill and Buck, 2012). Ligands of the strong class, L1, have conditional stability constants $K^{cond}_{FeL,Fe'}$ larger than 10^{12} kg mol^{-1}, which is defined as [FeL]/([L'] · [Fe']) with Fe' being inorganic Fe(III) and L' being the free ligand. The conditional stability constant of the ligands can also be expressed as $K^{cond}_{FeL,Fe^{3+}} = K^{cond}_{FeL,Fe'} \cdot \alpha_{Fe'}$, where $\alpha_{Fe'}$ is the inorganic side reaction coefficient for Fe and varies with pH (Gledhill and Buck, 2012). L1 ligands are suggested to be actively produced by organisms to bind Fe and make it available to specialised uptake systems (Granger and Price, 1999). These are mostly siderophores, already mentioned in Section 1.1, and are found mostly near to the surface (Rue and Bruland,

1995; Mawji et al., 2008; Boiteau et al., 2018). The weak ligands, L2, L3,..., Ln (number increasing with decreasing binding strength), are found more homogeneously distributed throughout the water column and are most likely a side product of bacterial degradation of organic matter and zooplankton grazing. Further sources appear to be viral lysis of cells and external input from dust and rain. Examples of weak ligands are humic substances, exopolysaccharides and pigments (Gledhill and Buck, 2012).

To sum up, the chemical mass balance equation of the total oceanic Fe pool can be written as: $Fe_{tot} = Fe' + FeL + Fe_{inert}$, where Fe' is the inorganic Fe, FeL is the organic ligand complexed Fe and Fe_{inert} is the Fe fraction that is bound up in matrices and is not labile in chemical reactions (Fig. 1.2) (Gledhill and Buck, 2012). Marine organisms effortlessly take up the bioavailable Fe' as mentioned in Section 1.1. However, the particle reactivity of Fe(III) and the fast oxidation of Fe(II) decrease the Fe' concentration in seawater. On the contrary, the organically complexed FeL pool is more abundant, however, less accessible for phytoplankton. Yet, several studies have shown this pool to be also bioavailable via specific uptake systems (Section 1.1). This highlights the need to better understand the impact of Fe speciation on the biological cycle of Fe in the ocean.

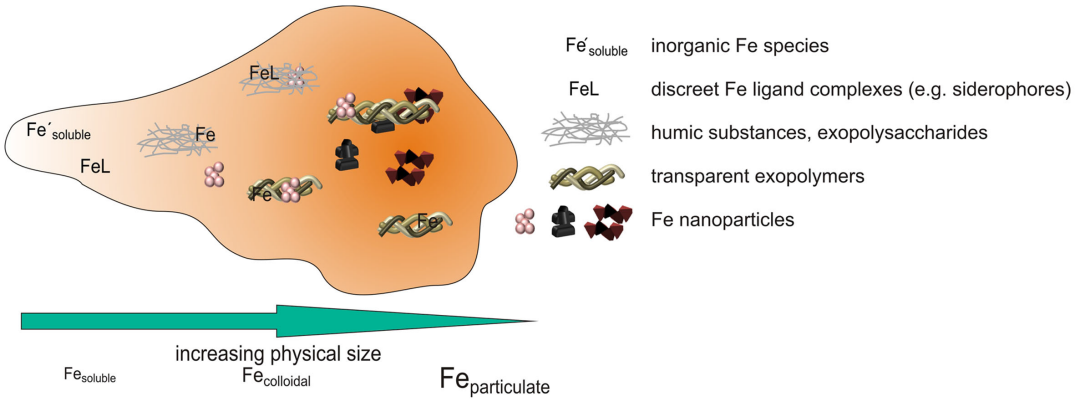

FIGURE 1.2: Components of the dFe pool from Gledhill and Buck (2012)

Another important property of Fe in seawater is its size distribution. Oceanic Fe is operationally differentiated into soluble Fe ($< 0.02\,\mu$m), colloidal Fe (0.02 - 0.2 or $0.4\,\mu$m), and particulate Fe ($> 0.4\,\mu$m). A physical mass balance equation can be written: $Fe_{tot} = Fe_{particulate} + Fe_{colloidal} + Fe_{soluble}$ (Fig. 1.2) (Gledhill and Buck, 2012). By definition, the dFe includes both the soluble and the colloidal fraction and is prescribed to be smaller than $0.2\,\mu$m (Cutter et al., 2017). The transition from colloidal to soluble Fe is indirectly favoured at the surface by photochemical reduction. Here, Fe(III), which due to its tendency to precipitate is often found in the colloidal form, is reduced to the mostly soluble Fe(II) (Öztürk et al., 2004). Colloidal Fe is quickly scavenged through the water column as dissolved organic matter creates gels and speeds up the aggregation of colloidal Fe to form particulates (Gledhill and Buck, 2012). This aggregation or coagulation of colloidal Fe is called "colloidal pumping" (Honeyman and Santschi, 1991). Nevertheless, the subdivision of dFe into soluble and colloidal Fe and into organically complexed and inorganic Fe represented in Fig. 1.2 are not totally exclusive, as they partially overlap. For example, Fe bound to humic substances is in the colloidal size range, while siderophore-bound Fe is classified as soluble (Gledhill and Buck, 2012).

The removal of dFe from the water column by scavenging is a two-stage process, similar to the one described for thorium isotopes (Balistrieri, Brewer, and Murray, 1981; Honeyman, Balistrieri, and Murray, 1988; Honeyman and Santschi, 1989; Savoye et al., 2006). First,

dFe reversibly absorbs on colloids and small particles, and secondly, it aggregates and subsequently gets removed by larger sinking particles. Truly soluble Fe bound to organic ligands is protected from scavenging, whereas dFe in colloidal size is still subject to scavenging. The scavenging removal rate of dFe is thus a function of both the particle size distribution and the chemical form of Fe in the water. When the concentration of dFe is larger than that of ligands a high scavenging regime occurs, while in the opposite conditions it is called a moderate scavenging regime (Moore and Braucher, 2007). In regions of high dust deposition such as the tropical North Atlantic Ocean, the scavenging process is pronounced. Indeed, dust deposition brings large amounts of particulate material to the ocean which offer potential surfaces for the particle reactive dFe to be scavenged on and which also intensify the aggregation on larger sinking particles. In this way, deposition of atmospheric dust onto the ocean surface has to be thought of as a sink of dFe aside from being a large source of dFe (Section 1.5). This double role of dust was first observed in a mesocosm experiment in which dust was added to Mediterranean seawater (Wagener, Guieu, and Leblond, 2010). It was detected that dust could lead to increased scavenging loss of dFe from the seawater. Whether dust behaves as source or sink of dFe depends on the concentration of dust particles, on the background concentration of ligands and dFe, as well as on the sinking velocity of particles out of the surface layer.

1.4 Role of biotic and abiotic processes for the distribution of iron

In Section 1.1 the role of dFe in marine biology as an essential micro-nutrient was summarised, followed in Section 1.3 by a description of the physical removal process scavenging. The combination of these aspects makes dFe a very peculiar element as it behaves both as a 'nutrient-type' and a 'scavenged-type' element. The vertical profile of dFe is similar to those of other nutrients, such as phosphate and nitrate, highlighting its biological role: near the surface the concentrations are low, they increase with depth, till they stabilise or slightly decrease at about 1000 m depth. However, the vertical profile is also influenced by the particle reactiveness of dFe. Many metals, as aluminium and lead, have concentrations that are highest at the surface and then decrease with depth. Boyd and Ellwood (2010) summarised a typical vertical profile of dFe in the ocean as in Fig. 1.3. This reflects that Fe is a nutrient for phytoplankton and its concentration is affected by remineralisation, but at the same time that it has a strong tendency to scavenge and precipitate. At the surface the scavenging loss of dFe and the remineralisation source of dFe counteract each other, while between 250 - 1000 m the contribution of remineralisation to the dFe concentration is larger than that of scavenging. Below 1000 m scavenging becomes the dominant process (Fig. 1.3).

The surface water dFe concentration is influenced by external and internal sources. Here, up to 50 - 60% of the dFe is in the form of the bioavailable Fe(II) (Gledhill and Buck, 2012), which is regulated by photoreduction and organic ligand concentration. The main removal process for dFe at the surface is biological uptake, resulting in low surface concentrations ranging between 0.03 - 1 nmol L^{-1} (de Baar and de Jong, 2001). These concentrations may show seasonal variations, as for example strong winter mixing can lead to lower production. Furthermore, in regions where primary production is limited by other factors than Fe, as nitrogen concentration or light, dFe can accumulate at the surface. The minimum dFe concentration is typically found in correspondence to the chlorophyll maximum (Johnson, Gordon, and Coale, 1997). Beneath the euphotic zone, the concentration of dFe increases with depth. Here, remineralisation of sinking organic matter is the main internal source of dFe. Average concentrations range between 0.4 - 2 nmol L^{-1} (de Baar and de Jong, 2001). At

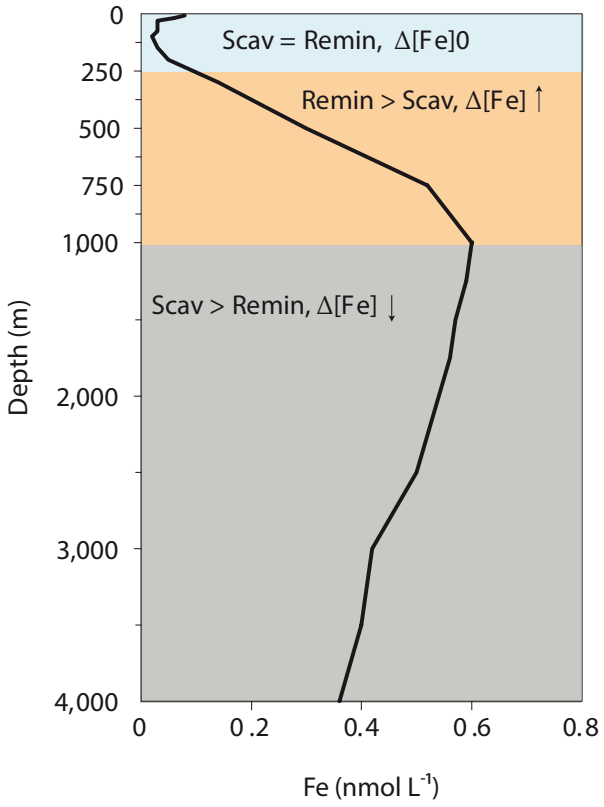

FIGURE 1.3: Influence of scavenging and remineralisation of a typical dFe vertical profile in the North Pacific Ocean (modified from Boyd and Ellwood, 2010)

depths greater than 1000 m scavenging removal outcompetes the supply of dFe by remineralisation, leading to a constant or slightly decreasing dFe concentration.

Another difference between the 'nutrient-type' and 'scavenged-type' elements is the residence time. While the residence time of the macro-nutrients nitrate, phosphate and silcic acid ranges between 10^3 - 10^5 yr, most metals are very particle reactive and their residence time is shorter than the oceanic circulation. Though the residence time of dFe is still subject to large uncertainties (6 - 410 yr - Hayes et al., 2018), it is considerably shorter than those of the macro-nutrients. This implies the importance of external sources to the dFe concentration and distribution. Furthermore, while 'nutrient-type' elements accumulate at depth with increasing age of the water mass, 'scavenged-type' elements precipitate on particles along the overturning circulation. Consequently, the first have higher concentrations in the Pacific Ocean than in the Atlantic Ocean, while the opposite is the case for the latter. dFe does show neither the inter-basin gradient between the Atlantic and the Pacific Ocean shown by 'nutrient-type' elements nor by 'scavenged-type' elements. However, its concentration at depth is far from being homogeneous. Nowadays observations, and particularly those of the GEOTRACES program, have revealed the dFe concentration in the deep ocean to show inter- and intra-basin variability, depending on the distance to deep sea sources, scavenging removal and ligand concentration.

1.5 Sources of iron to the ocean

The distribution of dFe in the ocean is strongly dependent on its external and local sources, much more than it is the case for other nutrients. We can distinguish between airborne Fe which was transported through the atmosphere to the ocean, and direct continental Fe input. The first includes desert dust, volcanic ashes, combustion particles from wildfires and biomass burning, industry and urban emissions, as well as extraterrestrial dust. The second category comprises of shelf sediments, rivers, icebergs, glaciers, hydrothermal vents, the interaction between bathymetry and currents, and island wakes. Sea ice serves as an Fe reservoir, which redistributes Fe over the polar regions through drifting. All these sources have different temporal and spatial signatures and can present seasonal variations or occur episodically. Consequently, their relative contribution to the global oceanic Fe cycle varies in space and time. For example, desert dust is the most dominant external source in the subtropical North Atlantic Ocean, while it has little impact in the Southern Ocean. Here, upwelling and hydrothermal activity determine the dFe concentration (Section 1.6). In the following a description of the main dFe sources is given.

Dust aerosols are produced in arid areas and the majority actually originates in the large deserts of the World. The production rate of dust that is uplifted and becomes aerosol depends on several factors, such as the erosion of rocks and the soil moisture, the topography and surface roughness, as well as the land use and vegetation. Furthermore, it can be affected by changes in the hydrological cycle as well as by changes in the vegetative coverage (Jickells et al., 2005). A lifetime of hours to weeks permits transport through the atmosphere for thousands of kilometres at several kilometres' height. The transport of the soil grains depends on atmospheric dynamics as uplift, wind speed and direction. Furthermore, it is influenced by the particle size distribution of dust with an average size of 2 μm (Jickells et al., 2005). The amount of dust reaching the ocean is also determined by the distance between the location of origin and the deposition region. Finally, dust aerosols are deposited at the ocean surface. The removal of dust from the atmosphere can occur by wet or dry deposition, depending on the possible interaction of the aerosol with meteorological water, and shows strong seasonal and inter-annual variability (Jickells et al., 2005). The particulate material deposited at the ocean's surface delivers important macro- and micro-nutrients to the oceanic ecosystem. For example, relevant for this thesis, desert dust aerosols contain on average 3.5 wt.% Fe (Wedepohl, 1995). Laboratory studies have analysed how much of the Fe included in dust actually dissolves in seawater and is then available for the marine biota. They published a wide range of solubilities, from 0.01% to 80% (Mahowald et al., 2005). However, considering the inventory of dFe in the ocean, its average solubility has to be low, from $<$1% up to 2%, meaning that only a small amount of the Fe present in aerosol is transformed into dFe (Jickells and Spokes, 2001). The solubility depends on the aerosol size and mineralogy and it moreover increases during cloud processes over long-range transports (Baker and Croot, 2010, and references therein). Furthermore, it can be impacted by anthropogenic combustion products (Li et al., 2017). The Fe flux estimated for mineral aerosols varies a lot between observations and models (Table 1.1). Duce and Tindale (1991) extrapolated the total dFe flux from a limited number of observations to global scale considering 3.5% of Fe and a solubility of 10%, and estimated it to be $3200 \cdot 10^9$ gFe yr^{-1}. On the other hand, models estimated a flux of $660 \cdot 10^9$ gFe yr^{-1} (Tegen and Fung, 1994) and $360 \cdot 10^9$ gFe yr^{-1} (Albani et al., 2014) for solubilities of 10% and 2%, respectively.

Different from lithogenic dust, volcanic ashes, combustion particles from wildfires and cosmic dust contribute rather little to the global aeolian Fe flux to the ocean (Table 1.1). Subaerial volcanic eruptions produce ash particles composed of silicate glass which are coated by Fe-rich salt. The external coat dissolves upon contact with seawater and the silicate glass

is then rapidly altered and releases Fe. As follows, volcanic ash contributes locally to the bioavailable Fe at the surface ocean (Duggen et al., 2010, and references therein). For the Pacific Ocean, Olgun et al. (2011) assessed an Fe flux from volcanism ranging between 0.17 - $4.2 \cdot 10^9$ gFe yr^{-1} (Table 1.1). Guieu et al. (2005) estimated a twice as high contribution of particles from wildfires, $8.3 \cdot 10^9$ gFe yr^{-1} (Table 1.1). This value was extrapolated globally from data of the Mediterranean Sea after large wildfires, which showed that 2% of the total Fe content in the aerosols dissolved in seawater. While pyrogenic fluxes are interesting for the dFe concentration at local scales, the cosmic dust Fe flux is globally homogeneously distributed. Interplanetary dust particles penetrate the atmosphere and evaporate to a large extend on their way down. However, some reach the ocean surface, contributing to the Fe flux with $7 \cdot 10^9$ gFe yr^{-1} (Johnson, 2001) (Table 1.1). Despite the rather small flux, they are thought to influence the Fe cycle in Fe limited regions as the Southern Ocean.

An airborne source of Fe which is becoming ever more important and interesting are Fe-containing particles of anthropogenic origin. In certain regions, as in south-east Asia, large amounts of soluble Fe have indeed been shown to have anthropogenic origin (Chuang et al., 2005). The estimated Fe flux from industrial combustion is $83 \cdot 10^9$ gFe yr^{-1} (Luo et al., 2008) (Table 1.1). Moreover, air pollution has been shown to acidify Fe-bearing aerosols (iron acid dissolution process) leading to an increased input of soluble Fe to the ocean (Li et al., 2017).

The second category of dFe sources comprehends those which deliver dFe from continental origin directly to the ocean. The largest of these dFe sources are sediments (Table 1.1). Usually, the sediment is characterised by an oxygenated surface layer at the sediment-water interface, a suboxic zone and an anoxic zone at depth. The Fe concentration in sediments close to the sediment-water boundary is low and increases with depth and O_2 depletion. Indeed, under anoxic conditions, bacteria oxidise organic matter by reducing Fe(III) to Fe(II) (Burdige, 1993). The Fe(II) in solution in the sediment's pore-water diffuses upwards and either repricipitates in the oxic sediment layer or is eventually released into the water. Additionally, Fe(II) is also delivered to the deep ocean by re-suspension of sediments at the seafloor. The reduced Fe from oxidation of organic matter in the sediments was shown to cause a significant Fe flux in coastal and estuarine regions (Berelson et al., 2003) as well as at higher depths (Elrod et al., 2004). Measurements of the exchange of dFe between the sediment and the water column were performed with benthic in-situ flux chambers along the California coast by Elrod et al. (2004). Extrapolating these findings to the global shelves, Elrod et al. (2004) calculated a contribution of shelf sediments to the global dFe budget of $4970 \cdot 10^9$ gFe yr^{-1} (Table 1.1). This very large flux is, however, based on data retrieved from few regions and considers a correlation of Fe flux to the remineralisation of C, which mostly occurs on shelves and not in open ocean regions. Furthermore, when the oxic ocean layer is reached, Fe(II) oxidises to Fe(III) and can be lost due to precipitation and scavenging. This is not considered in flux chamber measurements (Homoky et al., 2016). Also not considered in the estimate is the dependence of the release of dFe on the O_2 concentration above the sediments as well as the presence of ligands in the sediments themselves, which prevent Fe(III) from precipitating due to break-down of organic matter (Buck and Bruland, 2007; Jones, Beckler, and Taillefert, 2011; Beckler, Jones, and Taillefert, 2015). In conclusion, the estimate by Elrod et al. (2004) may be largely biased and other studies as Charette et al. (2016) report much smaller Fe fluxes, i.e. $130 \cdot 10^9$ gFe yr^{-1} (Table 1.1). Beyond the controversy of the strength of the sediment source in the global Fe flux, also the amount of released dFe reaching the euphotic layers and influencing primary production is still under discussion. This is particularly interesting in upwelling regions where Fe-rich deep waters reach the upper levels of the water column. Although upwelling can also occur to some extent in the western boundary shelves, surface replenishment with Fe-rich deep waters mostly

occurs along the eastern boundary continental shelves where the lateral transport of surface water leads to upwelling regions.

Rivers and groundwater transport material and nutrients, i.e. Fe, from the land to the coastal ocean. The dFe concentration in river waters is on average much higher than in the open ocean. Rivers discharge a large amount of particulate Fe in the estuaries and continental margin, as well as roughly two orders of magnitude fewer dFe which mainly consists of suspended inorganic colloidal Fe stabilised by humic substances (Oelkers et al., 2011). Upon mixing with seawater, dissolved and particulate Fe undergo disaggregation and aggregation dynamics producing precipitates. More than 90% of the dFe and particles are removed and deposited into the sediments. Consequently, only a very small fraction of the Fe discharged by rivers enters the dFe pool, with an estimated flux of $145 \cdot 10^9$ gFe yr^{-1} (de Baar and de Jong, 2001). Due to shelf sediments and river supply, dFe concentrations in the coastal shallow regions are generally elevated compared to those in the open ocean.

An important dFe source in the deep ocean are submarine hydrothermal vents which occur when water penetrates the ocean crust in a volcanic region. Hydrothermal vents are mostly located along the mid-ocean ridges and in island arcs (Beaulieu, Baker, and German, 2015). While it is circulating through the volcanic rock basement, the water is heated and chemically altered. Fluids emitted at the seafloor are buoyant and rise hundreds of meters up into the water column (German and Von Damm, 2003). While mixing with the cold and oxygenated seawater, non-buoyant plumes rich of sulphide and oxide particles evolve. These fluids are characterised by high concentrations of SO_4, P, Na and dissolved metals Fe, Mn, and Al (Elderfield and Schultz, 1996). It was observed that around hydrothermal vent systems the Fe concentration is extremely high, even a million times more concentrated than background deep-ocean Fe concentration (German et al., 2016). Large parts of the minerals contained in the fluids precipitate and form mineral chimneys which are colloquially named black and white smokers that mostly consist of iron-manganese oxides and sulphides. However, it was shown that a fraction of the emitted Fe can escape immediate precipitation. Several studies observed that hydrothermal Fe (dissolved and particulate) is transported thousands of kilometres away from the vent sites (Wu, Wells, and Rember, 2011; Resing et al., 2015; Nishioka, Obata, and Tsumune, 2013; Klunder et al., 2012; Hatta et al., 2015; Saito et al., 2013). Thus, hydrothermal vents impact the deep ocean Fe distribution and are expected to contribute with 5 to $500 \cdot 10^9$ gFe yr^{-1} to the dFe pool (Tagliabue et al., 2010) (Table 1.1).

TABLE 1.1: Estimates of Fe fluxes

Source	Fe flux (10^9 g yr^{-1})	Reference
Dust	3200	Duce and Tindale (1991)
	660	Tegen and Fung (1994)
	360	Albani et al. (2014)
Volcanic ash	0.17 - 4.2	Olgun et al. (2011)
Wildfires	8.3	Guieu et al. (2005)
Cosmic dust	7	Johnson (2001)
Anthropogenic origin	83	Luo et al. (2008)
Sediments	4970	Elrod et al. (2004)
	130	Charette et al. (2016)
Rivers	145	de Baar and de Jong (2001)
Hydrothermal vents	5 - 500	Tagliabue et al. (2010)
Icebergs	220 - 1700	Raiswell et al. (2016)

Hydrothermal Fe is partly observed in the form of pyrite which is oxidised less easily than dissolved Fe(II) (Yücel et al., 2011; Gartman, Findlay, and Luther, 2014). In order for dFe to be transported in non-buoyant plumes over long distance, it has to be preserved from scavenging and gravitational settling. It was suggested that complexation by organic ligands can protect dFe form precipitating in the near-field (Bennett et al., 2008; Sander and Koschinsky, 2011; Hawkes et al., 2013). Another approach hints towards a rapid reversible exchange between dissolved/colloidal and particulate Fe in the plume (Fitzsimmons et al., 2017). In upwelling regions as the Southern Ocean or in the case of shallow vents, dFe originated from hydrothermalism can reach the upper ocean. This contribution was modelled to be 10% of the dFe in the euphotic zone (Frants et al., 2016).

Additional dFe sources typical for polar regions are iceberg calving and melting, subglacial runoff and sea ice melting. Icebergs and glaciers contain visible terrigenous material, which originates from the erosion of continental bedrock (Gerringa et al., 2012). These iceberg-hosted sediments contain nutrients and trace elements, which are injected into the water column when icebergs melt. Of particular interest for this thesis are the reactive Fe-bearing minerals like ferrihydrite and goethite (Raiswell et al., 2008; Raiswell, 2011; Shaw et al., 2011). Analysis of meltwater of icebergs from the Southern Ocean showed concentrations of dFe much higher than those measured in seawater (Löscher et al., 1997; Lin et al., 2011; Raiswell et al., 2016). Furthermore, large amounts of particulate Fe from bedrock debris enter the ocean. These observations testify that melting icebergs and glaciers introduce 220 to $1700 \cdot 10^9$ gFe yr^{-1} (Raiswell et al., 2016) (Table 1.1) to the ocean and are consequently substantial sources of bioavailable Fe to the pelagic community (Raiswell et al., 2006; Raiswell et al., 2008; Smith et al., 2007). Indeed, several studies have reported hot spots of biological activity in proximity of free-drifting icebergs demonstrating Fe fertilisation from iceberg melting (Smith et al., 2007; Cefarelli, Vernet, and Ferrario, 2011; Duprat, Bigg, and Wilton, 2016). Duprat, Bigg, and Wilton (2016) even detected an increase in primary production within a few kilometres from an iceberg which can persist for more than a month.

In polar regions, sea ice also plays a crucial role in the oceanic dFe distribution. Rather than being a source of new dFe, sea ice acts as a reservoir. It redistributes during the melt season, the dFe which was previously trapped and collected during freezing periods. As described in Lannuzel et al. (2010), during autumn sea ice production, both dissolved and particulate material in seawater, like Fe bound to ligands or in nanoparticles, is incorporated by the newly forming frazil ice crystals. The material is trapped and accumulates in the sea ice. The high salinity brine in sea ice creates a density gradient, which induces vertical convection. This drives further Fe incorporation into sea ice. Additionally, over the years, sea ice accumulates Fe from aeolian deposition, as the coverage inhibits deposition onto the ocean. dFe in sea ice behaves partially as salt, thus is transported vertically by brine motion and is ejected to the seawater by gravity drainage, percolation and flushing (Vancoppenolle et al., 2013). In addition to the passive salt-like behaviour, dFe in sea ice is affected by a vigorous biological activity. Diverse communities of algae, bacteria, archea, heterotrophic protists, fungi and viruses live at the bottom, in the interior and at the surface of sea ice. As a result, the dFe concentration in sea ice is further influenced by algal uptake, remineralisation of organic matter by heterotrophs, as well as by the presence of ligands (Lannuzel et al., 2016). In spring, 70% of the Fe contained in sea ice is released within a few days triggering an algal bloom (Vancoppenolle et al., 2013). Advanced melting during summer flushes Fe out of the sea ice. It has been observed that Southern Ocean sea ice mainly contains Fe incorporated from the underlying seawater (Lannuzel et al., 2016), while in the subpolar North Pacific Ocean sea ice Fe appears to mainly originated from dust deposition (Kanna, Toyota, and Nishioka, 2014).

In this section, the major sources of dFe to the ocean were described and estimates of every Fe flux were named and reported in Table 1.1. These fluxes are however subject to large uncertainties which can be caused by scarcity of data collected only in few regions and then extrapolated to the global scale, or by experimental designs which do not consider all loss and gain processes.

1.6 Iron distribution

The concentration of dFe in the ocean ranges in the nanomolar order of magnitude. Consequently, measuring the dFe concentration is complicated as contamination is easy. Therefore, accurate trace metal clean techniques have to be used both in sampling and measurement (Cutter et al., 2017). Fig. 1.4 shows the distribution of dFe sampling in the world's oceans. Many of the cruise tracks are accredited to the GEOTRACES program (Schlitzer et al., 2018) which is producing an observational data set essential to gain a better understanding of the processes affecting the dFe distribution, both on global and regional scales.

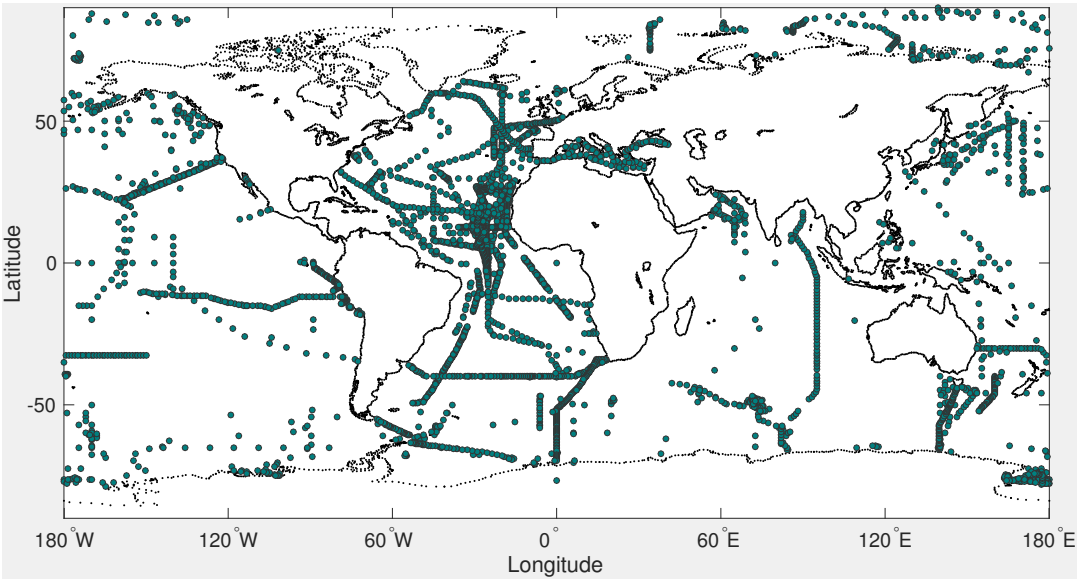

FIGURE 1.4: Location of dFe measurements from Tagliabue et al. (2012) and Schlitzer et al. (2018)

The horizontal distribution of dFe is characterised by high concentrations in coastal areas and low concentrations in the open ocean. This gradient is mainly induced by continental Fe sources as dust deposition, continental sediments and rivers. These lead to high biological productivity in coastal regions. It was observed that the coastal dFe input does not penetrate far off-shore at the surface (with elevated dFe concentrations decreasing with an e-folding scale of ca. 16 km with distance from the coast), while at depth the dFe coastal signature was observed to extend for 5000 km (Johnson, Gordon, and Coale, 1997). In the open ocean, the main dFe sources are either internal recycling of dFe brought to the surface by upwelling, vertical mixing and lateral transport, or hydrothermal sources at depth. Deep ocean dFe concentration is, unlike previously assumed, very heterogeneous. The North Atlantic and Pacific Ocean show rather similar concentrations ranging between 0.6 - 0.8 nM, whereas the concentration in the Southern Ocean is about half ranging between 0.3 - 0.4 nM (Moore and Braucher, 2007).

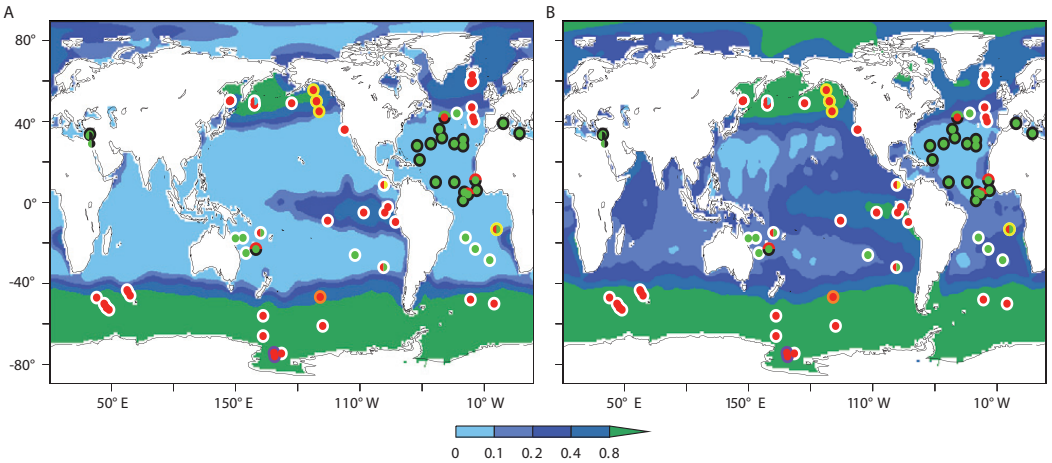

FIGURE 1.5: Surface concentrations of nitrate (A) and phosphate (B) in μmol kg^{-1}. The red cycles indicate Fe limitation (modified from Moore et al., 2013)

The dFe distribution also shows meridional differences. Low latitudes' waters have typically high dust deposition which act both as Fe source and sink. An illustrative example is the tropical Atlantic Ocean where dFe originated from sduring the melt season sub-Saharan dust was largely detected, as it carries a specific isotopic signature (Conway and John, 2014). Due to high productivity, these regions are often macro-nutrient limited. On the contrary, in the Pacific Ocean the dust input is small also at low latitudes. Here, the biological activity is limited by the availability of dFe. Similar low concentrations of the micro-nutrient dFe are observed in high latitude oceans. Fe limitation creates vast regions in which macro-nutrients, as nitrate and phosphate, are abundant but phytoplankton biomass is low (Fig. 1.5). These are called high-nutrient low-chlorophyll or HNLC regions and account for 25 - 50% of the world's ocean, and the major regions are the subpolar North Pacific Ocean, the Southern Ocean and the Equatorial Pacific Ocean just mentioned (Moore et al., 2001; de Baar et al., 2005). Here, Fe limitation occurs all year round, while in some upwelling regions HNLC can also manifest itself seasonally (Nielsdóttir et al., 2009). HNLC regions are often connected to low aerosol Fe input and dFe is mainly supplied by sediments, hydrothermalism, remineralisation and upwelling of Fe-rich deep water. For example, the dust input from South America, Africa and Australia does not reach far towards the high latitude Southern Ocean. However, since this is a region of strong upwelling where C and nutrients are brought to the surface, upwelling and vertical advection of Fe-rich deep water are the major dFe sources (Blain, Sarthou, and Laan, 2008). Furthermore, dFe input from continental margins and icebergs is observed, while sea ice melting in summer redistributes dFe at the surface. At depth large hydrothermal signals characterise the dFe distribution. The generally low surface concentration of dFe limits primary productivity in the Southern Ocean. However, there are areas where algal blooms as large as hundreds of kilometres can be observed. Here, additional Fe supply from resuspended sedimentary particles from islands or shelf regions favoured the biological activity, a process described as "natural iron fertilisation" (Morris and Charette, 2013). Typical examples of natural fertilisation within the Southern Ocean HNLC waters are the Kerguelen Plateau (Blain, Sarthou, and Laan, 2008; Bowie et al., 2015), the Antarctic Peninsula (Dulaiova et al., 2009), Crozet Island (Pollard et al., 2009) and South Georgia (Korb et al., 2008). The external sources and recycling of dFe may, however, still not be enough of a source for phytoplankton in high latitude regions, which may produce organic ligands if Fe-stressed. This leads to an excess of Fe-binding ligands which are submerged

and transported equatorward to lower latitudes, where they modulate the distribution of dFe in the ocean interior (Tagliabue et al., 2014).

In this chapter, the removal processes of dFe such as biological uptake (Section 1.1) and scavenging (Section 1.3), as well as the main sources (Section 1.5) were outlined. These are illustrated in Fig. 1.6 from Tagliabue et al. (2017) following the meridional distribution of dFe (Section 1.6).

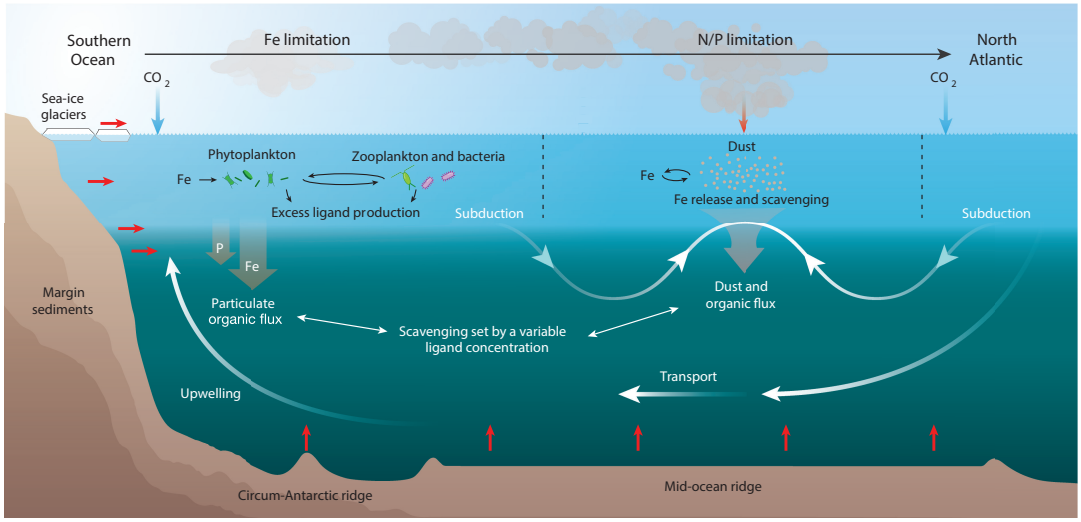

FIGURE 1.6: A schematic description of the oceanic Fe cycle (modified from Tagliabue et al., 2017) showing the meridional distribution in the Atlantic Ocean. Dust is dominant at low latitudes, while upwelling of Fe-rich water determines the distribution in the Southern Ocean. Further sources of dFe are hydrothermal vents, sediments and sea-ice and glaciers. The role of marine biota, ligands and particles is also illustrated

2 The oceanic iron cycle in biogeochemical models

Over the years, the oceanic Fe cycle has been modelled with many degrees of complexity. At first, only aeolian dust and rivers were considered to be important sources of dFe to the ocean. The first models (Lefèvre and Watson, 1999; Archer and Johnson, 2000) simply considered the dust input to be balanced by scavenging removal with a constant scavenging time-scale. Furthermore, they assumed a constant ratio of dFe uptake relative to that of carbon and nitrogen for all phytoplankton species and constant ligand concentration (Parekh, Follows, and Boyle, 2004). Here, for the first time, the importance of Fe-binding ligands and of their different strength in shaping the heterogenous deep ocean dFe concentration was recognised. Since then, a large range of observations revealed the significance of several other sources and processes. The release of dFe from sediments due to oxidation of organic matter was included in biogeochemical models. Lately, the influence of hydrothermal vents as well as icebergs and sea ice were modelled.

This chapter presents the evolution of our knowledge of forcing fields, e.g. aeolian and hydrothermal dFe input, from measurements and how the sources and sinks of dFe to the ocean are generally described in biogeochemical models including the one used in this thesis.

The role of aeolian deposition in the marine Fe cycle is long known and studied. The number of direct measurements of aeolian Fe deposition to the surface ocean is, however, limited, making it difficult to assemble a global data set of Fe flux from the atmosphere to the ocean. For this reason, climatologies of mineral aerosol deposition have been used. Considering the mineralogical composition of aerosols, the percentual content of Fe was detected. This was done for the first time by Duce and Tindale (1991), who presented a global data set of Fe flux to the ocean based on dust concentration measurements from the Pacific and North Atlantic Oceans over 10 years. Though these direct mineral aerosol measurements, both on land and at sea (Duce and Tindale, 1991; Mahowald et al., 1999; Ginoux et al., 2001), provide good constraints, they consist of just a few point measurements and hence do not present a realistic global view. Alternative studies provided data sets of mineral aerosol deposition in marine sediment cores and sediment traps, as well as estimates of fluxes based on thorium measurements (e.g. Kohfeld and Harrison, 2001; Kienast et al., 2016). These estimates offer the possibility to monitor the Fe flux to the ocean over longer time-scales. However, the influence of processes such as lateral transport within the ocean on sinking aerosols makes it difficult to interpret the data and thus infer the Fe flux accurately.

Deriving a global Fe flux from the atmosphere to the ocean based on observations is problematic. Atmospheric models, which interpolate the limited number of observations, thus are used for this purpose (Mahowald et al., 1999; Albani et al., 2014; Albani et al., 2016). In these models, the entrainment of dust into the atmosphere depends on vegetation cover, grain size, soil moisture and wind (Mahowald et al., 2009, and references therein). The mineral aerosols are then transported through the atmosphere by wind and vertical convection. Finally, their removal from the atmosphere is parameterised as dry and wet deposition. To convert dust into Fe, an average composition of continental crust containing 3.5 wt.% of Fe

is considered. Some recent studies distinguish different dust mineralogies and regions of origin in models (Zhang et al., 2015). Furthermore, only a small part of the Fe in dust is soluble in seawater. Most biogeochemical models consider a constant Fe solubility, usually between 1% and 2% of the total Fe in dust, although fields of dust Fe solubilities from atmospheric models are available (Myriokefalitakis et al., 2018). An example of the obtained global dust deposition field is shown in Fig. 1 in the next Chapter.

At first, dust deposition was considered to be the main source of dFe to the ocean (Duce and Tindale, 1991). In the following decades, however, several studies reported other dFe sources to be as important as the aeolian source to the oceanic Fe cycle. As described in Section 1.5, the release of dFe from the seafloor is associated with the degradation and remineralisation of organic matter. Some models incorporate the sediment source as a constant Fe flux from the bottom ocean grid to the ocean above a certain depth (Moore, Doney, and Lindsay, 2004). Other models make the leakage of dFe dependent on the oxygenation state of the sediment parameterised as a function of the sinking flux of organic matter. In this way, it is possible to account for the larger release of dFe by anoxic sediments. The sediment dFe source is also described in models as proportional to the degradation of organic matter by considering the sinking flux of particles. An example of the global dFe flux from sediments is shown in Fig. 1 in Chapter 4.

The discovery of hydrothermal vents discharging hot and mineral-rich water into the ocean mostly near mid-ocean ridges, has brought attention to a further Fe source. First, Fe emitted by hydrothermal vents, was thought to precipitate completely in the near-field. Recent studies have, however, reported long distance transport of hydrothermal dFe, highlighting its importance to the global Fe cycle. Consequently, the historically neglected contribution of hydrothermal vents is now considered an essential process, which has to be included in biogeochemical models. Tagliabue et al. (2010) first introduced the hydrothermal dFe source in a model. The simulation was based on the current knowledge of hydrothermal vent locations and ^{3}He measurements. Indeed, hydrothermal ^{3}He is emitted from vents and is inert in the water column. Thus, it is used as a proxy to follow the far-field hydrothermal plume over long distances. Tagliabue et al. (2010) assumed a constant Fe : ^{3}He ratio of $4.5 \cdot 10^8$ in the non-buoyant plume, i.e. after the initial mixing with surrounding seawater, considering that only 0.2% of the hydrothermally derived Fe enters the dissolved pool.

Conventionally, biogeochemical models considered a constant ligand concentration in the ocean, which stabilises dFe against scavenging (Parekh, Follows, and Boyle, 2004). More recent laboratory studies have provided a deeper understanding of the ligands' key role in the Fe cycle and described properties and classifications of ligands. Now, several models propose different ligand parameterisations. Tagliabue and Völker (2011) used the linear relationship between ligand concentration and dissolved organic carbon inferred by Wagener et al. (2008). On the other hand, Misumi et al. (2013) related the ligand concentration to the apparent oxygen utilisation. However, since it is questionable whether any of the two suggested parameterisations can be expanded to the global ocean, Völker and Tagliabue (2015) presented a prognostic model for ligands based on Hunter and Boyd (2007). Here, ligands are either produced passively via degradation of organic matter or are actively produced by organisms. Four loss processes are described in the model: bacterial degradation, photochemical degradation, uptake of organically complex Fe by phytoplankton and aggregation of colloidal ligands with sinking particles. Another approach was given by Frants et al. (2016), who considered the currently known ligand distribution instead of distinguishing between the different kinds of ligands. The different ways to consider ligands in biogeochemical Fe models, result in key differences in the set dFe loss by scavenging.

In biogeochemical models scavenging was first described as a uniform loss process with a fixed time-scale. Johnson, Gordon, and Coale (1997) assumed no particle scavenging below a certain concentration of dFe. Nowadays, most models express scavenging as a function of particle concentration and the concentration of uncomplexed dFe, Fe'. They assume that all the Fe scavenged from the water column is lost from the system (Archer and Johnson, 2000; Christian et al., 2001; Aumont et al., 2003; Parekh, Follows, and Boyle, 2004), even though recent studies have shown this not to be the case (Aumont et al., 2015). The way scavenging is represented in models is still a key uncertainty in the description of the Fe cycle in biogeochemical models.

As mentioned above, deposition of atmospheric dust onto the ocean surface is a large source of dFe. However, dust deposition also brings large amounts of particulate material to the ocean, which offer potential surfaces for dFe to scavenge on, and intensifies the aggregation with larger sinking particles. In this way, atmospheric dust has to be thought of as a sink of dFe as well. Ye, Völker, and Wolf-Gladrow (2009) showed that the particle concentration, aggregation and sinking speed as well as the concentration of organic ligands in the surface water may determine whether atmospheric dust behaves as a source or a sink of dFe. It was then clear that particle dynamics had to be included in models to be able to simulate the role of dust as scavenger. Models describing particle aggregation, sinking and disaggregation have many levels of complexity (Burd, 2013). The description in Ye and Völker (2017) included small non-sinking particles as well as biological and lithogenic aggregates.

Some models further incorporate rivers, icebergs, sea ice dFe input, describe the photochemically driven redox reactions in the surface layer, define several particle pools or include the colloidal pumping. The upper limit of complexity in describing the Fe cycle is not yet reached, making it a relevant and modern research field.

2.1 The REcoM2 model and its structure

In the model, the distribution of dFe is calculated from mass balance equations which take into account ocean circulation, the internal biogeochemical cycling of dFe and external dFe sources. The ocean circulation model that is used to calculate advective and diffusive tracer transport, is the General Circulation Model of the Massachusetts Institute of Technology (MITgcm) (Marshall et al., 1997). Our setup covers the globe from 80°S to 80°N, excluding the Arctic, and has a zonal resolution of 2° and a meridional resolution between 0.39° and 2°. The thickness of 30 vertical layers increases with depth, from 10 m at the surface to 500 m below 3700 m. The MITgcm is coupled with the marine ecosystem and biogeochemical model, REcoM2, described in detail in Hauck et al. (2013). REcoM2 describes two phytoplankton classes, diatoms and non-diatoms (small phytoplankton) with a variable elemental stoichiometry, following Geider, Macintyre, and Kana (2003) and Hohn (2009); a generic zooplankton class; and a class of organic particles sinking with vertically increasing velocity (Kriest and Oschlies, 2008). The model experiments were set up with the same initial conditions and forcing fields as in Ye and Völker (2017).

2.1.1 Process description

Here we describe the processes in our standard representation of the Fe cycle. Some of them will change in the following sections.

TABLE 2.1: Table of Parameters

Symbol	Parameter	Unit
U	Advection Velocity	$\mathrm{m\,d^{-1}}$
w	Sinking Velocity	$\mathrm{m\,d^{-1}}$
k	Diffusivity	$\mathrm{m^2\,d^{-1}}$
F	Dust Flux	$\mathrm{mg\,m^2\,d^{-1}}$
r_{Fe}	Iron in Dust	$\mu\,\mathrm{mol\,Fe\,mg^{-1}}$
sol	Solubility	-
d^N	Remineralisation Rate of Sediment Organic N	$\mathrm{d^{-1}}$
q_B^{Fe}	Benthic Fe : N Ratio	$\mu\mathrm{mol\,Fe\,mmol\,N^{-1}}$
q^{Fe}	Fe : N Ratio	$\mu\mathrm{mol\,Fe\,mmol\,N^{-1}}$
$r_{phy/dia/het}$	Phytoplankton/ Diatom/ Heterotroph Respiration	$\mathrm{d^{-1}}$
$p_{phy/dia}$	Phytoplankton/ Diatom N Uptake Rate	$\mathrm{d^{-1}}$
$N_{phy/dia/het/det/sed}$	Phytoplankton/ Diatom/ Heterotroph/ Detritus/ Sediment N	$\mathrm{mmol\,N\,m^{-3}}$
$C_{phy/dia/det}$	Phytoplankton/ Diatom/ Detritus C	$\mathrm{mmol\,C\,m^{-3}}$
ε_{het}^N	Heterotroph Excretion	$\mathrm{d^{-1}}$
$\rho_{N_{det}}$	Remineralisation Rate	$\mathrm{d^{-1}}$
f_T	Temperature dependent Arrhenius Function	-
k_{scav}^{Fe}	Scavenging Rate	$\mathrm{mmol\,C\,m^{-3}d^{-1}}$
$k_{scavdust}^{Fe}$	Lithogenic Scavenging Rate	$(\mathrm{mg\,m^{-3}})^{-1}\,\mathrm{d^{-1}}$
Fe'	Free Iron	$\mu\,\mathrm{mol\,Fe\,m^{-3}}$
$P_{small/large}$	Small/ Large Particles	$\mathrm{mg\,m^{-3}}$

The evolution of the dFe distribution over time is described by the following differential equation:

$$\frac{\partial dFe}{\partial T} = -(U+w)\cdot\nabla dFe + \nabla(k\nabla dFe) + S(dFe) \tag{2.1}$$

The first two terms on the right-hand side of Eq. 2.1 describe the physical transport and mixing in the system. *S(dFe)* is the sum of all internal dFe sources and sinks (see Table 2.1 for symbol description):

$$\begin{aligned} S(dFe) \quad = \quad & q^{Fe}((r_{phy}-p_{phy})\cdot N_{phy} + (r_{dia}-p_{dia})\cdot N_{dia} + (r_{het}-\varepsilon_{het}^N)\cdot N_{het} \\ & +\rho_{N_{det}}\cdot f_T\cdot N_{det}) - k_{scav}^{Fe}\cdot C_{det}\cdot Fe' \end{aligned} \tag{2.2}$$

dFe is released by phytoplankton during respiration and by heterotrophs during respiration and excretion. Another internal source is remineralisation of sinking organic particles. dFe is drawn down by uptake of phytoplankton and by scavenging on sinking particles. External inputs are aeolian dust Fe and sedimentary Fe. The model considers neither riverine Fe input nor dFe from sea ice melting. Parameters indicating the strength of individual processes are either taken from literature or are the result of sensitivity studies of the model.

Dust Deposition: The aeolian dFe source is a field of monthly averages of dust deposition (Mahowald et al., 2005). The flux to the ocean is:

$$k\frac{\partial dFe}{\partial z}\Big|_{z=0} = F_{dust}\cdot r_{Fe}\cdot sol \tag{2.3}$$

The model assumes that 3.5 wt.% of dust particles consists of Fe and that 2% of this Fe immediately dissolves when deposited in the surface ocean.

Sediment Source: The sedimentary Fe source at the sea floor is given by the release of dFe proportional to the degradation of organic material in a homogeneous sediment layer:

$$k\frac{\partial dFe}{\partial z}\Big|_{z=-H} = q_B^{Fe} \cdot d^N \cdot PON_{sed} \tag{2.4}$$

This goes back to Elrod et al. (2004), who found a significant correlation between the dFe flux from the sediment and the oxidation of organic matter. Sinking biogenic particles that reach the sediment are ultimately dissolved or remineralised and returned into the water column as a normal flux, whereas the dFe scavenged is permanently removed.

Phytoplankton Uptake: In the model, the total pool of dFe is assumed to be bioavailable and the dFe uptake is proportional to nitrogen assimilation. The phytoplankton growth rate is limited by dFe, in the form of a Michaelis-Menten function, and by an intracellular nitrogen and silica quota.

Remineralisation: In the first step of carbon or nitrogen remineralisation, the particulate organic matter (OM) is transformed into dissolved OM. Bacterial degradation then breaks it into dissolved inorganic carbon or nitrogen, which are bioavailable for phytoplankton. Since dFe is mostly organically bound anyway, the model returns Fe directly to the dissolved pool through remineralisation of particulate OM, with a rate of $\rho_{N_{det}} \cdot f_T \cdot N_{det}$.

Organic Complexation: The model considers two forms of Fe: the Fe bound to organic ligands, FeL, and the free inorganic Fe, $Fe^{'}$. The Fe tracer in the model is the sum of the two forms $dFe = FeL + Fe^{'}$. $Fe^{'}$ is calculated as in Parekh, Follows, and Boyle (2004) and represents only a small percentage of the total dFe pool. It is assumed that Fe and ligands are bound in a 1:1 ratio. In REcoM2 the ligand concentration is assumed constant at 1 μmol m^{-3} and the conditional stability constant is set to 10^{11}.

Scavenging: The scavenging is assumed to be proportional to the detritus carbon, thus to the mass of sinking particles, and to the $Fe^{'}$ concentration, $k_{scav}^{Fe} \cdot C_{det} \cdot Fe^{'}$.

To conclude, models allow to conduct exercises, which are impractical in the real world. For example, they allow to study the implications of Fe limitation on marine phytoplankton and higher tropic levels, the function of Fe in glacial-interglacial variations, or the role of Fe in the climate system and in the C cycle. However, one has to be alert not to place unquestionable confidence in the model results. Indeed, large uncertainties shadow the marine Fe cycle which is modelled in a variety of ways. Tagliabue et al. (2016) offered an overview of the different assumptions used in biogeochemical models. They include different sources of variable magnitude, different Fe chemistry, scavenging and particle dynamics, as well as different degrees of complexity in the ecosystem description. The struggle to simulate the complex Fe cycle is related to the limited number of observation available to constrain the models. In Chapter 4 this topic will be picked up.

3 Scientific questions and thesis outline

The oceanic Fe cycle is an interdisciplinary field of research which connects physical, biological and chemical processes. From previous studies, we know that the performance of biogeochemical models in reproducing the oceanic dFe distribution can be rather limited. Besides overestimation in the North Atlantic Ocean and underestimation of the surface Pacific Ocean, especially the too homogeneous deep ocean dFe concentration reveals an incomplete representation of the marine Fe cycle in biogeochemical cycles.

In Chapter 4 a sensitivity study on the scavenging rate of dFe and on the sediment dFe source aims to answer the following questions:

- How well does the standard state-of-the-art biogeochemical model REcoM2 reproduce dFe concentration in the world's oceans?
- Can the model-observation agreement be improved via a tuning exercise on a dFe source and a dFe sink?
- Do the sediment source of dFe and the scavenging rate differently affect the various ocean basins?

As research on the Fe cycle moves on, always new sources and processes appear to be of key importance. It is a challenging task for modellers to include these in biogeochemical models and to understand their global and regional role. This effort is supported by many scientific cruises measuring dFe concentrations in various ocean basins and disclosing regional differences in the Fe cycle.

The Fe cycle in the subtropical North Atlantic Ocean is intense and strongly influenced by a high dust deposition. Based on the dFe measurements of the GEOTRACES GA03 cruise, in Chapter 5 we focused on these points:

- What are the key processes affecting the dFe distribution in the subtropical North Atlantic Ocean?
- What is the effect of introducing dFe scavenging on lithogenic particles in the surface and deep ocean?
- Does scavenging on living phytoplankton cause the strong subsurface dFe minimum observed?
- Instead of a constant ligand concentration, does a new ligand parameterisation based on AOU better influence the dFe features observed?
- How deep is the remineralisation depth and which processes do impact it?
- How does dFe originated from hydrothermal vents shape the deep ocean dFe concentration?

- By including new processes and changing some parameterisations, does the new description of the Fe cycle improved the agreement between modelled and measured dFe distribution?

Differently to the subtropical North Atlantic, in polar regions, further dFe sources as sea ice and icebergs contribute to the dFe concentration. In Chapter 6, the role of icebergs in the Southern Ocean Fe cycle was analysed. This is particularly interesting since iceberg calving is predicted to increase in future warmer climate. The following points were investigated:

- To which amount and where do icebergs change the dFe concentrations in the surface Southern Ocean?
- How does this affect primary production, nutrient availability and export?
- Could the Fe fertilisation of the Southern Ocean by icebergs be a negative feedback effect for climate?

"Fe fertilisation of the Southern Ocean" is often mentioned to be one of several contributing factors which let to ca. 100 μatm lower atmospheric pCO2 in glacial compared to interglacial periods. This is called the "Iron Hypothesis" (Martin, 1990). In Chapter 7, I report of a laboratory experiment in which the ecologically important Southern Ocean diatom *Pseudo-nitzschia subcurvata* was grown under simulated glacial and interglacial conditions. These questions were addressed:

- How does *P. subcurvata* respond to different dFe concentrations (growth-limiting and non-limiting) and pCO_2 levels (180 and 280 μatm) with respect to growth, carbon production and photophysiology?
- What implications could it have on carbon export in glacial and interglacial times?

This thesis contributes to the process-understanding of the Fe cycle by introducing and testing the impact of some processes to the dFe distribution, with particular regional focus. A speculative view of the interconnection between the Fe cycle and the climate system is always provided. It further highlights the importance of a tighter collaboration between the model community and laboratory studies.

4 Sediment dFe source and scavenging rate

Abstract

Based on the current understanding of the marine Fe cycle, biogeochemical models struggle to reproduce the measured dFe distribution. The estimates of the contribution of sediments as a source of dFe are still questionable and the scavenging removal of dFe is yet largely unconstrained. Here, I present a sensitivity study on these two important components of the Fe cycle. I noticed that changes in the strength of scavenging similarly affect different ocean basins. Furthermore, while the sediment source mostly influenced the dFe concentration in the entire deep ocean in a similar way, the impact on the surface layer was mainly seen in the Pacific Ocean, which is know to be a region of shallow shelves and strong upwelling. This study highlights how different ocean basins react to changes in the dFe sediment source and scavenging rate and hints towards the inclusion of more processes in the description of the Fe cycle, with particular attention to ocean basin differences.

4.1 Introduction

Chapter 1 and Chapter 2 illustrated the complexity of the marine Fe cycle. In the "Fe Model Inter-comparison Project" (FeMIP), the dFe distribution simulated by 13 global ocean biogeochemical models has been compared (Tagliabue et al., 2016). The models included different sources of dFe: all had a dust source, most considered a sedimentary source and only a few included hydrothermal and riverine sources. Table 2 from Tagliabue et al. (2016) showed that even for the same source very different strengths are assumed in the various models. The dust dFe source ranges from 1.4 to 32.7 Gmol Fe yr^{-1}, and the sediment dFe source from 0.6 to 194 Gmol Fe yr^{-1}. Patterns of the dFe distribution in the ocean were analysed by comparing the output of biogeochemical models with observations. Tagliabue et al. (2016) noticed that, despite the large differences in total dFe input fluxes (66.9 ± 67.1 Gmol Fe yr^{-1}), the simulated mean dFe concentration was similar between the models (0.58 ± 0.14 nM). This is due to different representations of the removal processes between models. Indeed, including new dFe sources requires stronger loss processes to keep models close to observations. Furthermore, adding complexity in process descriptions also necessitates a revision of the strength of the loss processes.

The predominant physical sink of dFe is scavenging on sinking material (Section 1.3), which is, however, associated with some uncertainties on how models should treat it. These uncertainties are often sidestepped by tuning the scavenging rate for given dFe sources to ultimately match the global observations, which most analysed models reproduce modestly well. As a consequence, the dFe residence time in the models, defined as the oceanic dFe inventory over the total dFe flux, varies from 3.7 to 626.3 years. The dFe residence time retrieved through measurements also ranges over two orders of magnitude, from 3 to 410 years (Hayes et al., 2018, and references therein). This large uncertainty is mainly due to different methods, e.g. based on the scavenging rates of Fe in deep waters as in Bruland, Orians, and

Cowen (1994) and in Bergquist and Boyle (2006) versus the thorium supply based approach used in Hayes et al. (2015) and in Hayes et al. (2018). Furthermore, the residence time was observed to vary significantly between oceans which show different Fe speciation.

The above mentioned uncertainties in modelling the Fe cycle and the model comparison provided by Tagliabue et al. (2016), awoke the curiosity to discern the effect of varying the strength of dFe sources and sinks. Thereupon, a sensitivity study on the model parameters that determine the sediment dFe source and the scavenging rate was performed, in order to untangle the response of the Fe cycle and analyse whether the model-observation agreement can be improved in this way. Here, we show how a uniform scavenging rate affects different regions and basins in a model with a moderate complex Fe cycle, and discuss the impact of the strength of the sediment source to the global dFe distribution. The results presented in this study then lead to Chapter 5 and Chapter 6, where emphasis is put on differences in the Fe cycle between various ocean regions.

4.2 Model experiments

The REcoM2 model run presented in the model comparison in Tagliabue et al. (2016) is characterised by a relatively weak dust source and the smallest sediment source compared to other models' setup in the study, and consequently discloses a very long residence time. The aeolian dFe source (Section 1.5) used in the model is a field of monthly averages of dust deposition (Mahowald et al., 2005) with a solubility of 2%. The main dust plumes originate from the Saharan Desert, the Arabic Peninsula and Patagonia (Fig. 4.1A).

The parameterisation of the sediment source of dFe (Section 1.5) is based on the oxidation of organic matter (particulate organic nitrogen, or PON) which sank and reached the seafloor. The observed proportionality between sedimentary oxygen demand and the dFe flux from the sediment is represented in the model by a proportionality between the N and Fe fluxes out of the sediment. Thus, the strength of the sediment source depends on the benthic Fe:N ratio ($Fe{:}N_{benthos}$) set in the model. This parameterisation of the sediment source of dFe assumes a fast oxidation of sedimentary Fe(II) to Fe(III) which precipitates to a large amount close to the sediment-water boundary. Neglecting the Fe(II) fraction can, however, underestimate the source strength in oxygen minimum zones. A stabilising mechanism for dFe such as ligands in sediments or colloid/nanoparticle formation is not taken into account in the model, neither is re-suspension in shelf regions. Despite the high uncertainty in the parameterisation of sedimentary input, the parameterisation qualitatively ensures that dFe release is maximal at the coast and in shallow shelf areas, which agrees with the few available flux chamber measurements.This pattern can be seen in Fig. 4.1B which has been obtained from the standard model run with $Fe{:}N_{benthos} = 0.03 \mu mol\,Fe\,mmol\,N^{-1}$. This corresponds to a global dFe input from sediments of $0.6\,Gmol\,yr^{-1}$, which is less than 1% of the flux estimated by Elrod et al. (2004).

In REcoM2, the rate at which Fe is lost from seawater by scavenging is affected by the concentration of sinking particles as shown by Honeyman, Balistrieri, and Murray (1988). In the specific, model experiment analysed in Tagliabue et al. (2016) the rate constant k_{scav} is set to $0.0156\,(mmol\,C\,m^{-3})^{-1}\,d^{-1}$. In the model runs presented here, a constant ligand concentration across the oceans is assumed and neither a riverine nor a hydrothermal dFe source are included.

Starting from the model experiment provided to Tagliabue et al. (2016), we performed a sensitivity study on the strength of the sediment source and the scavenging rate with the goal

to reduce the bias between the model outcome and the observations compared to prior estimates. Practically, a matrix of 20 runs was performed with scavenging rates ranging from 0.0156 to 0.312 $(\text{mmol C m}^{-3})^{-1}$ d^{-1}, thus a 20-fold increase, and Fe:$N_{benthos}$ ratios ranging from 0.03 to 0.33 μmol Fe mmol N^{-1}, thus a 10-fold increase (Table 4.1).

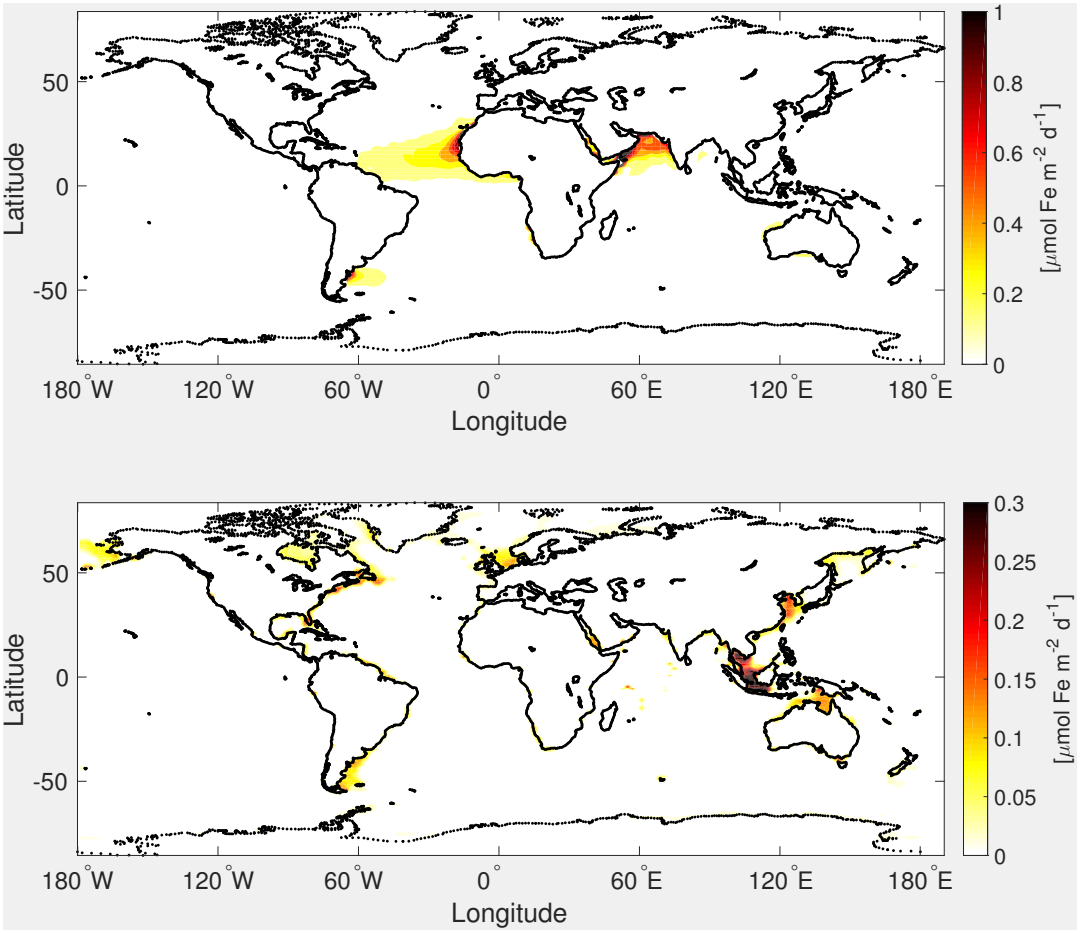

FIGURE 4.1: Modelled dFe input from (A) dust deposition and (B) sediments for the standard setup of our model, R1 (see Table 4.1)

TABLE 4.1: Model experiment matrix

Fe:$N_{benthos}$	k_{scav} $(\text{mmol C m}^{-3})^{-1}$ d^{-1}					
μmol Fe mmol N^{-1}	0.0156	0.02	0.03	0.07	0.15	0.312
0.03	R1	R2	R3	R4		
0.08	R5	R6	R7	R8		
0.15	R9	R10	R11	R12	R13	R14
0.33	R15	R16	R17	R18	R19	R20

The modelled annual mean dFe concentrations were compared with observations collected in Tagliabue et al. (2012) and Schlitzer et al. (2018). We excluded observations in the Arctic and Mediterranean Sea as the model does not cover these regions. Further, all values closer than 1 degree from the coast were neglected, as the model does not include riverine input

or subsurface groundwater discharge. Moreover, since the model runs presented here do not include hydrothermal dFe input, a bias in the deep ocean dFe concentrations will be seen in the following analysis. In the model-observations comparison, we first find the model grid box in the horizontal which is closest to the measurement, and subsequently interpolate in the vertical to the observation depth. The vertical depth interpolation in the comparison procedure is important because the strongest gradients are usually in the vertical. All measured dFe concentrations are compared with the model value obtained by interpolating over the corresponding grid. However, most observations are concentrated in the upper ocean. In a simple comparison of statistical quantities like means the few deep ocean measurements are overpowered from the many near-surface observations. We thus, split the water column into three layers: above 200 m, between 200 - 1000 m and below 1000 m. Furthermore, we distinguish between Atlantic, Indian, Pacific and Southern Ocean basins. This is necessary from an analytical point of view due to different degrees of observation coverage, but also to highlight that the world's oceans are differently influenced by dFe sources and sinks as well as by other factors as, for example, the movement of water masses.

4.3 Results

4.3.1 Global dFe distribution in the observations and in the model run R1

The dFe distribution in the oceans is strongly influenced by the biological role of dFe and on its tendency to scavenge on particles (Section 1.4), as well as on external sources which largely introduce local patterns (Section 1.5).

The data from Tagliabue et al. (2012) and Schlitzer et al. (2018) (Fig. 4.2A) show the meridional distribution of dFe in the surface North Atlantic Ocean which was described in Section 1.6: at high latitudes the dFe concentration is rather low, while at low latitudes the concentrations is high. Specifically, the measurements show low values in the North Atlantic Ocean starting from Greenland reaching ca. 30°N, with the exception of a broad region of higher concentrations off the European continent. The subtropical and tropical North Atlantic are characterised by generally higher dFe concentrations due to high dust deposition and coastal dFe input. These features are extensively observed in the subtropical North Atlantic Gyre stretching from Central America to the Golf Stream, as well as to a certain extent off the West Saharan and Sub-Saharan Africa, while lower dFe concentrations are observed further off-shore. On the contrary, the South Atlantic Ocean is characterised by very low dFe concentrations which reach their lowest range in the subtropical South Atlantic Gyre. The modelled dFe values (Fig. 4.2A) resemble to a certain degree the observed meridional differences. Indeed, in the model, the concentrations are rather low in the North Atlantic with average values of 0.5 nmol L^{-1}, increase in the subtropical gyre and decrease again in the southern hemisphere. The dFe concentrations in the subtropical North Atlantic downwind of the Sahara Desert are largely overestimated in the model. This results from a large dust input combined to a long residence time. This feature is, however, clearly improved when scavenging on lithogenic particles is included in the description of the Fe cycle (Ye and Völker (2017) and Chapter 5). In the subtropical South Atlantic Gyre, dFe concentrations lower than 0.1 nmol L^{-1} are simulated, matching the observations. Some very local high dFe concentrations were measured in the coastal region of Namibia and Argentina, the first as consequence of a strong upwelling, while the latter disclosed the dust input from Patagonia. Both these features are simulated by the model.

The Indian Ocean is characterised by high surface dFe concentrations in the Arabian Sea and low concentrations in the Bay of Bengal and further low concentrations in the open ocean from the Bay of Bengal to the Southern Ocean. While the first two observations are

reproduced in the model, the concentrations in the open ocean are underestimated with values smaller than 0.1 nmol L^{-1}. Moreover, high dFe values were found in proximity of the Kerguelen Islands, which are not seen in the model experiment.

The surface Pacific Ocean typifies a low dFe region. Indeed, the concentration of dFe is low with some sporadic local higher values due to coastal input of dFe as close to the Philippines, north of Papa-New Guinea, south of Tasmania, around Hawaii and in the far North Pacific Ocean. Furthermore, high concentrations are observed corresponding with upwelling regions such as along the coast of North America and Peru. The model simulates uniformly low dFe concentrations smaller then 0.1 nmol L^{-1}. This results in too Fe-limited surface waters in the subtropical Pacific Ocean. This may be caused by a too strong scavenging which is caused by the models' neglect of variable concentrations of organic ligands.

In the Southern Ocean, generally very low surface dFe concentrations were measured and these are roughly matched by modelled concentrations of 0.2 - 0.4 nmol L^{-1}. Exceptionally high concentrations were observed in the waters around the Antarctic Peninsula and in few data points in the Davis and west Ross Sea.

The dFe concentration between 50 and 200 m (Fig. 4.2B) in the subpolar North Atlantic and subtropical North Atlantic Gyre are lower than the ones measured in the surface layer. Interestingly, close to the Sub-Saharan countries the observations show an increase of the dFe concentration with depth, while the model simulates a decrease. Indeed, in the former, biology takes up more dFe than it is supplied by dust. In this case, at depth dFe is released by remineralisation. On the contrary, in the latter the too strong aeolian input overcomes the biological uptake, thus scavenging is predominant at depth. Everywhere else in the Atlantic Ocean, the modelled dFe concentration increases relative to the surface layer reaching average values of 0.6 - 0.7 nmol L^{-1} in the North, 0.8 -1 nmol L^{-1} off Africa and 0.3 nmol L^{-1} south of 40°. While the plume of higher dFe concentrations expanding from Argentina is reduced at depths between 50 and 200 m, along the whole African coast the concentrations of dFe are higher than at the surface.

Both in the Arabian Sea and the Bay of Bengal, the observations show higher dFe concentrations between 50 - 200 m depth compared to the surface. The extent of higher dFe concentrations till roughly 20°S is also simulated in the model.

The higher concentrations in the North Pacific Ocean are reproduced by the model, reaching values up to 0.5 nmol L^{-1}. On the contrary, the high dFe measurements close to the Philippines, Papa-New Guinea and Hawaii are not simulated. The high dFe concentrations off Peru and Mexico present a more expanded plume due to upwelling and continental input, while the open ocean measurements all show very low concentrations. These features are reflected to some extent in the model output. Furthermore, the modelled dFe concentrations in the South Pacific Ocean increase on average to 0.1 - 0.2 nmol L^{-1}.

At 50 to 200 m, the Southern Ocean still shows very low dFe concentrations except close to the Antarctic Peninsula. The modelled dFe concentration at these depths is much higher than at the surface, with average concentrations of 0.4 nmol L^{-1} at the coast, and ranging between 0.6 - 0.7 nmol L^{-1} off-shore.

Between 200 m and 1000 m depth the dFe concentration is globally higher than in the layers above (Fig. 4.2C), both in the observations and the model. The measured dFe concentrations are high in the subtropical North Atlantic Ocean and decrease in the southern hemisphere. In the model, the concentrations averagely range between 0.7 - 0.9 nmol L^{-1}, with exception of the subtropical South Atlantic Ocean where the concentrations are lower ranging between 0.5 - 0.6 nmol L^{-1}.

Especially high concentrations were measured in the Arabian Sea and Bengal Bay decreasing towards the Souther Ocean. This pattern is properly matched by the modelled dFe

distribution in the region. Here, higher values in the Indian Ocean reach 20°S, south of which concentrations as low as 0.3 nmol L^{-1} persist.

In the North Pacific Ocean high dFe concentrations were measured due hydrothermal activities in volcanic arcs, shallow shelves and upwelling. The modelled dFe values are as high as 0.8 nmol L^{-1} and reproduce to a certain extent the observations. Similarly high concentrations are also simulated in the Equatorial Pacific originating in Central America (e.g. Peru from the measurements) and expanding throughout the basin to the Philippines. On the contrary, measurements in both the North and the South Pacific Gyre display lower concentrations with modelled concentrations of 0.5 nmol L^{-1} and 0.3 - 0.4 nmol L^{-1}, respectively.

In the Southern Ocean, high concentrations were measured close to the Antarctic Peninsula and the Kerguelen Islands as well as in the west Ross Sea, while everywhere else the concentrations are low. On the contrary, the modelled dFe concentration south of 50°S ranges

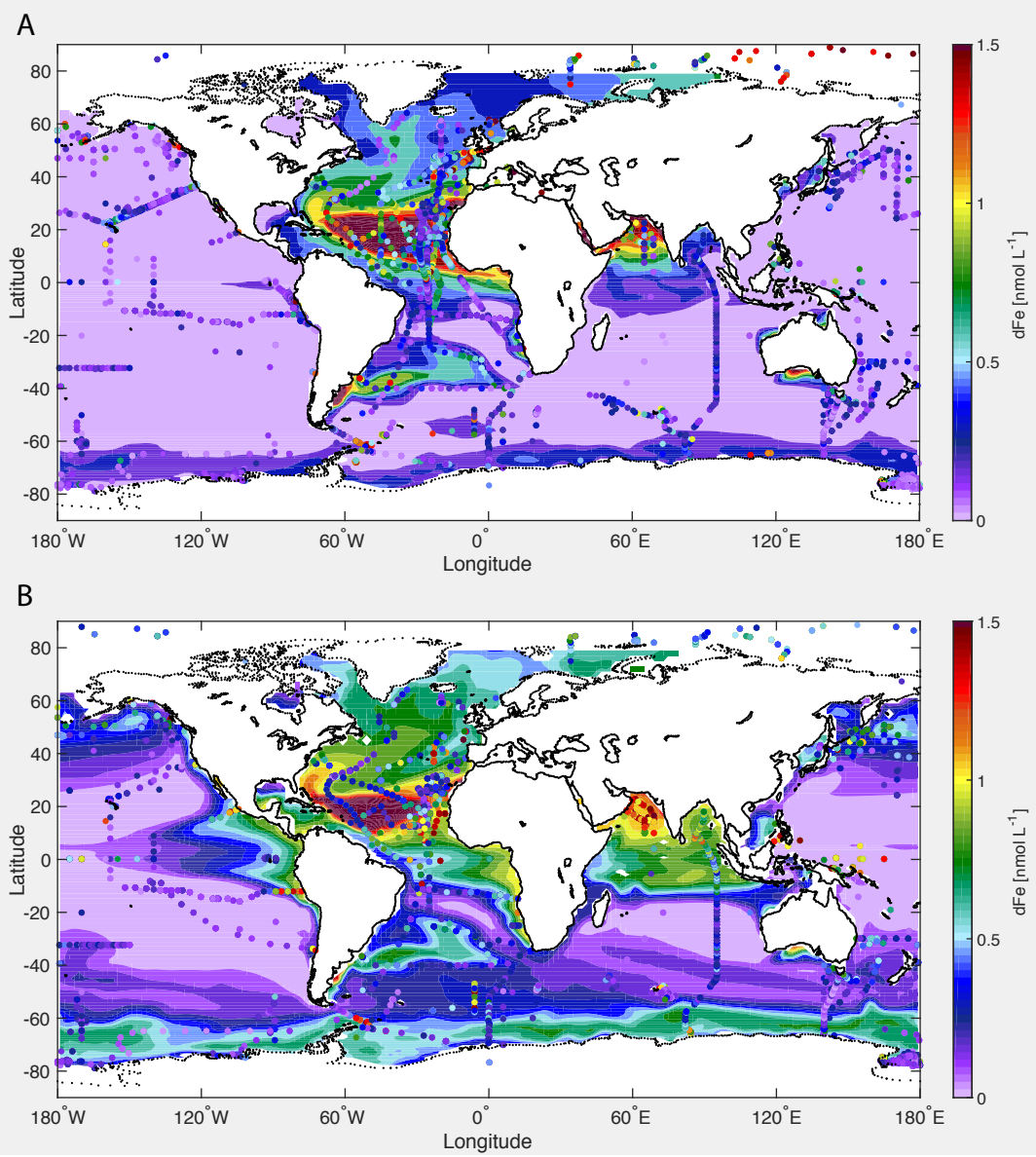

FIGURE 4.2: Modelled dFe distribution for model run R1 with measured dFe values as dots (A) in the upper 50 m, (B) between 50 -200 m, (C) between 200 - 1000 m and (D) below 1000 m (C and D in the next page)

between 0.7 and 0.8 nmol L^{-1}, overestimating most observations.

Extremely high concentrations, which the model is unable to reproduce, were measured in the tropical North Atlantic Ocean, off Namibia, off Chile and north of Japan.

The modelled deep ocean dFe concentration is almost homogeneously 0.7nmol L^{-1} (Fig. 4.2D). This is in contrast to the measurements, which show very different concentrations, and is most likely determined by a constant ligand distribution and the absence of a hydrothermal dFe source. Indeed, hydrothermal signals were observed along the Mid-Ocean-Ridge in the Atlantic Ocean, in the Indian Ocean, west of the East Pacific Rise, as well as in the Southern Ocean.

The Mediterranean Sea and the Arctic Ocean show very high surface dFe concentrations which decrease with depth in the Arctic (no data is available for the Mediterranean Sea at the depth). However, as mentioned before, these two regions are not included in the model, thus in the following sensitivity study the Arctic Ocean and the Mediterranean Sea, as well as data points closer than one degree to the coast, are excluded.

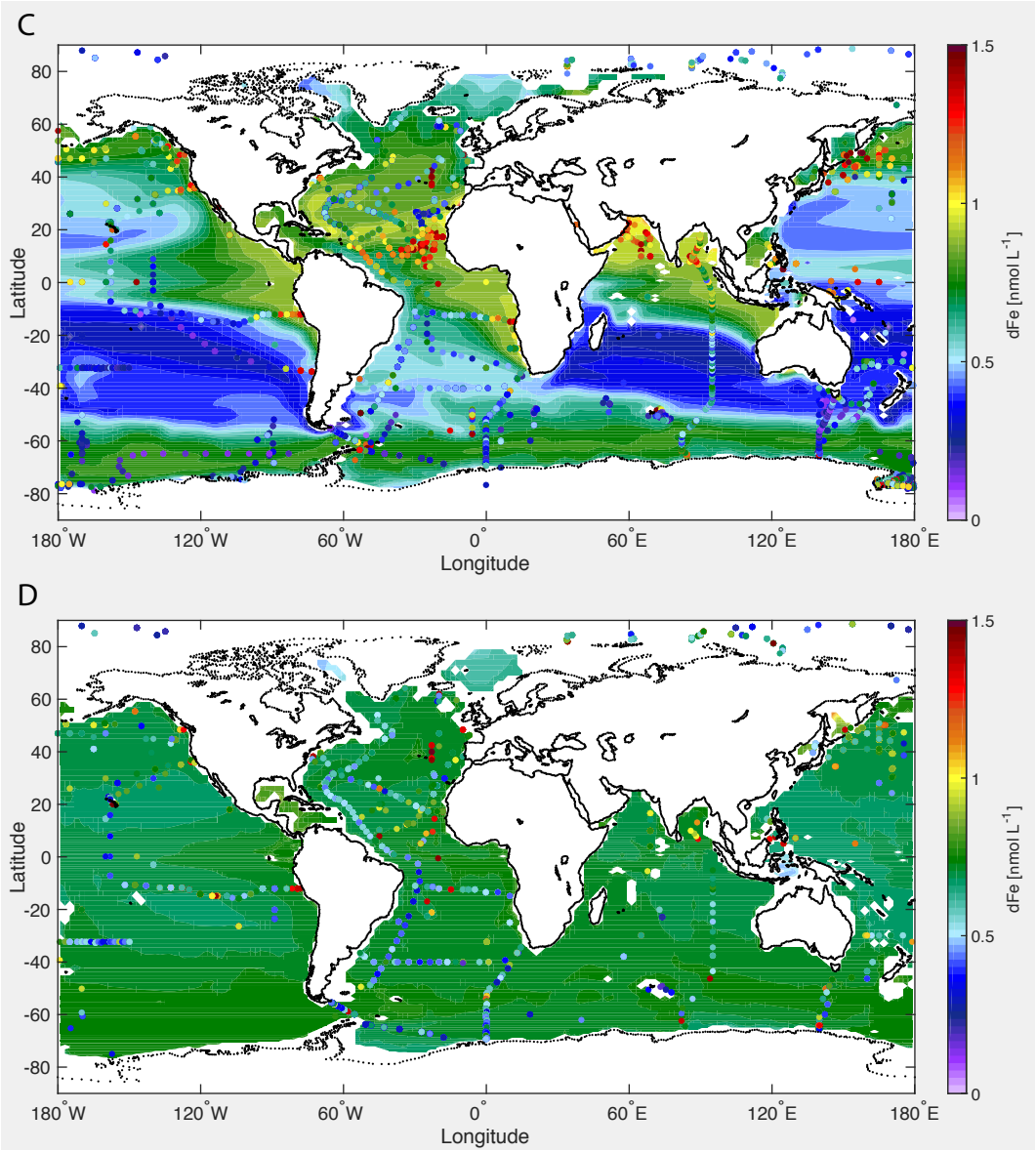

4.3.2 Sensitivity study

Fig. 4.3 shows the average dFe concentration within the subregions defined above, as a function of scavenging rate and sediment source strength. Also shown mean, median, and mean ± standard deviation for the observations, allowing to quantify the bias between modelled and measured dFe in the different model experiments. As expected, in all runs a higher scavenging rate led to lower dFe, while a larger sediment source led to higher dFe concentrations. Generally, at low scavenging rates, the modelled dFe concentration is too high and vice versa, regardless the strength of the sediment source assumed in this sensitivity study. Globally, for the modelled dFe mean to be close to the observed mean and median, the scavenging rate should range between 0.07 and 0.15 $(\text{mmol C m}^{-3})^{-1}\,\text{d}^{-1}$.

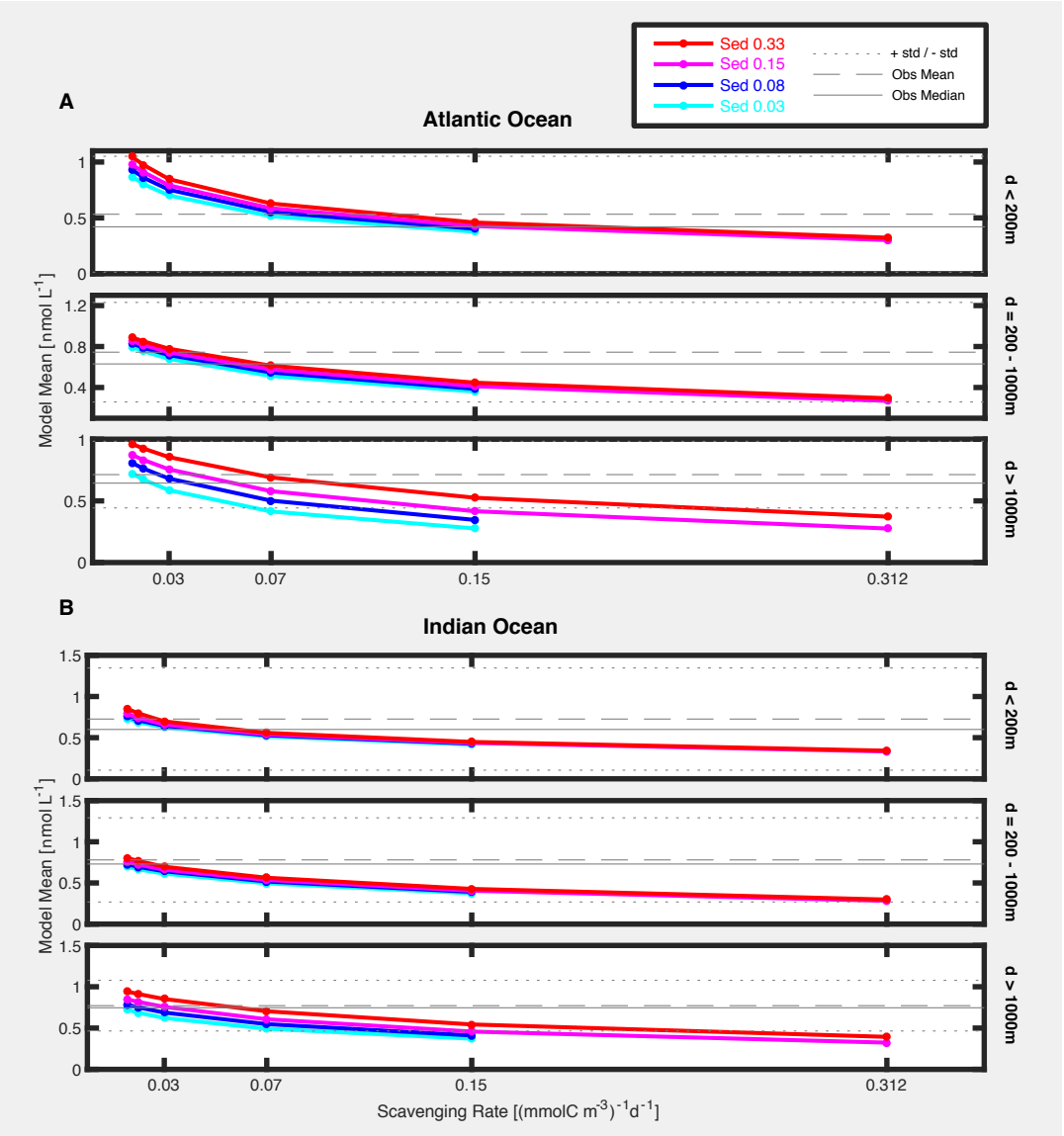

FIGURE 4.3: Mean modelled dFe concentration in the (A) Atlantic Ocean, (B) Indian Ocean, (C) Pacific Ocean and (D) Southern Ocean in the upper 200 m, between 200 -1000 m and below 1000 m as a function of scavenging rate constant (x-axis) and sediment source strength (colour). Also shown are mean, median, and mean ± standard deviation for the observations (C and D in the next page)

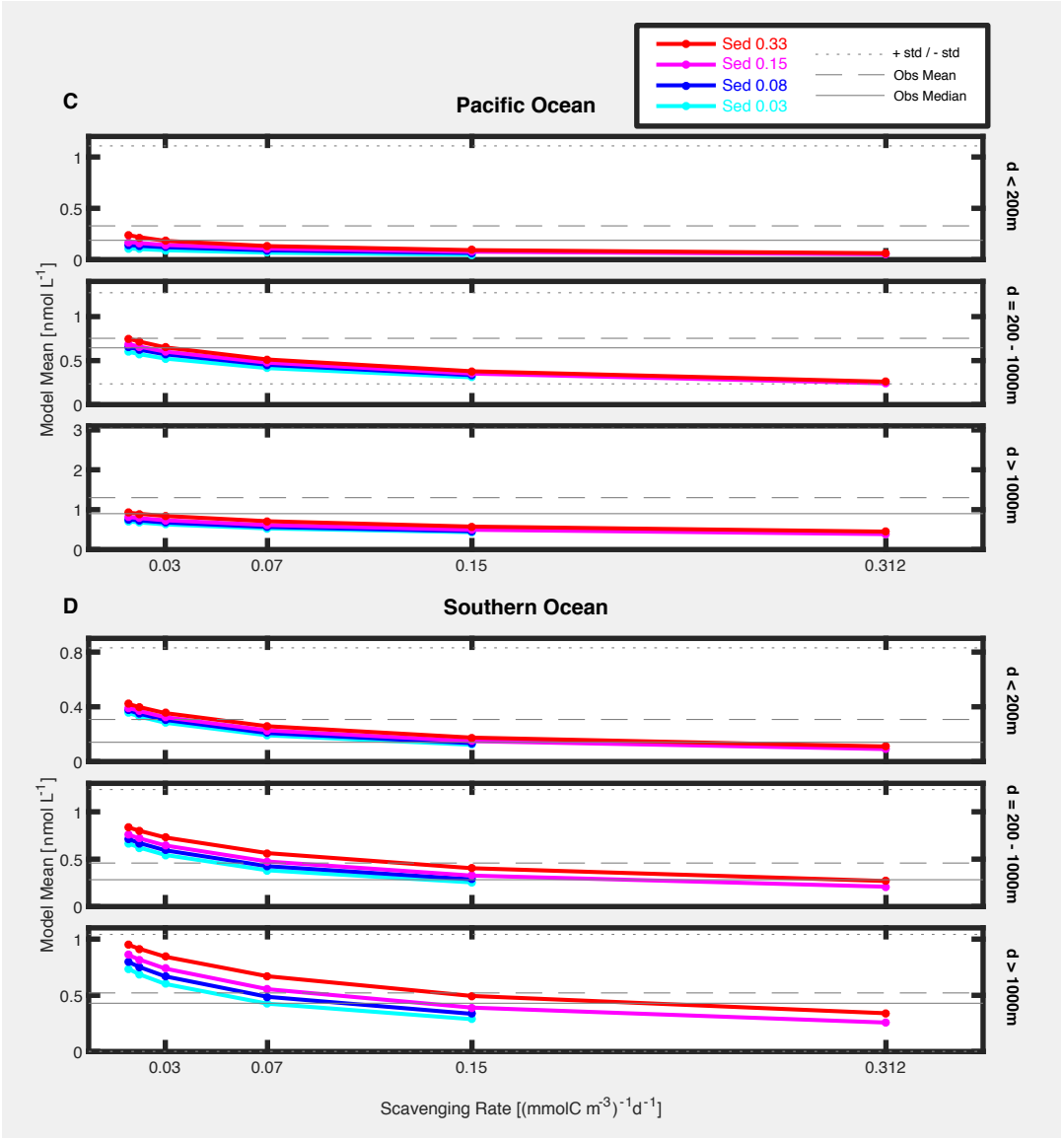

In the surface Atlantic Ocean (Fig. 4.3A), the mean of all runs lay within the observational standard deviation, with the closest match at scavenging rates of 0.07 and 0.15 $(\text{mmol C m}^{-3})^{-1}\,\text{d}^{-1}$. Between 200 - 1000 m, generally lower scavenging rates allow closer mean values. Differently, below 1000 m, both the combinations of low scavenging and low sediment dFe release ($0.0156\,(\text{mmol C m}^{-3})^{-1}\,\text{d}^{-1}$ - $0.03\,\mu\text{mol Fe mmol N}^{-1}$), and higher scavenging and high sediment dFe release ($0.07\,(\text{mmol C m}^{-3})^{-1}\,\text{d}^{-1}$ - $0.33\,\mu\text{mol Fe mmol N}^{-1}$), show the best affinity. For even higher scavenging rates, the dFe concentrations is underestimated in all model experiments. This happens similarly at all depths in the Indian Ocean (Fig. 4.3B) for scavenging rates larger than $0.03\,(\text{mmol C m}^{-3})^{-1}\,\text{d}^{-1}$, while for values smaller than $0.03\,(\text{mmol C m}^{-3})^{-1}\,\text{d}^{-1}$ the model mean and the observation mean fit well. In the Pacific Ocean (Fig. 4.3C), the surface observations show extremely low concentrations and the huge standard deviation results from outliers with high concentrations found close to Chile, Peru, north Japan and Indonesia. At this depth, all model experiments underestimate the dFe concentrations compared to the mean observed concentration. Between 200 - 1000 m only the combinations of low scavenging and high sediment dFe source reproduce the observed mean. All other runs display too low dFe concentrations both between 200 - 1000 m

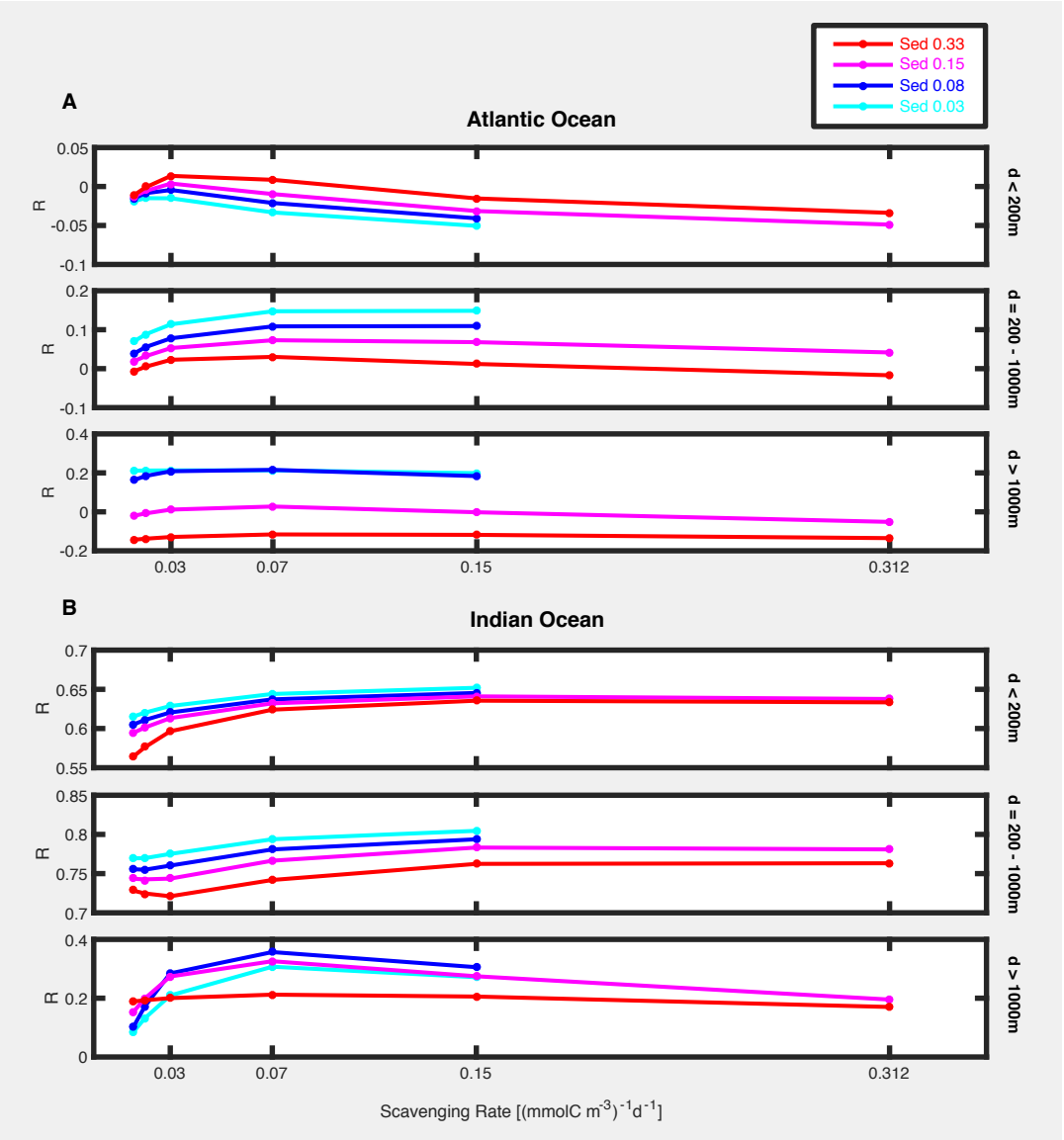

FIGURE 4.4: Correlation coefficient between modelled and observed dFe concentration in the (A) Atlantic Ocean, (B) Indian Ocean, (C) Pacific Ocean and (D) Southern Ocean in the upper 200 m, between 200 - 1000 m and below 1000 m as a function of scavenging rate constant (x-axis) and sediment source strength (colour) (C and D in the next page)

and at depth. Finally, in the surface Southern Ocean (Fig. 4.3D), the most fitting scavenging rates are those at the lower range. Between 200 - 1000 m, a higher scavenging rate of 0.07 $(\text{mmol C m}^{-3})^{-1}\,\text{d}^{-1}$ is needed to match the observed mean, and at depths greater than 1000 m, the scavenging rate should lay between 0.07 - 0.15 $(\text{mmol C m}^{-3})^{-1}\,\text{d}^{-1}$.

Fig. 4.4 displays the correlation coefficient between modelled and measured dFe concentrations in the three layers of the four ocean basins. While Fig. 4.3 offers an insight on the large scale oceanic dFe mean, Fig. 4.4 underlines the quality of the representation within each basin. It indicates how well or not the model reproduces the large variety of patterns observed in the different ocean basins.

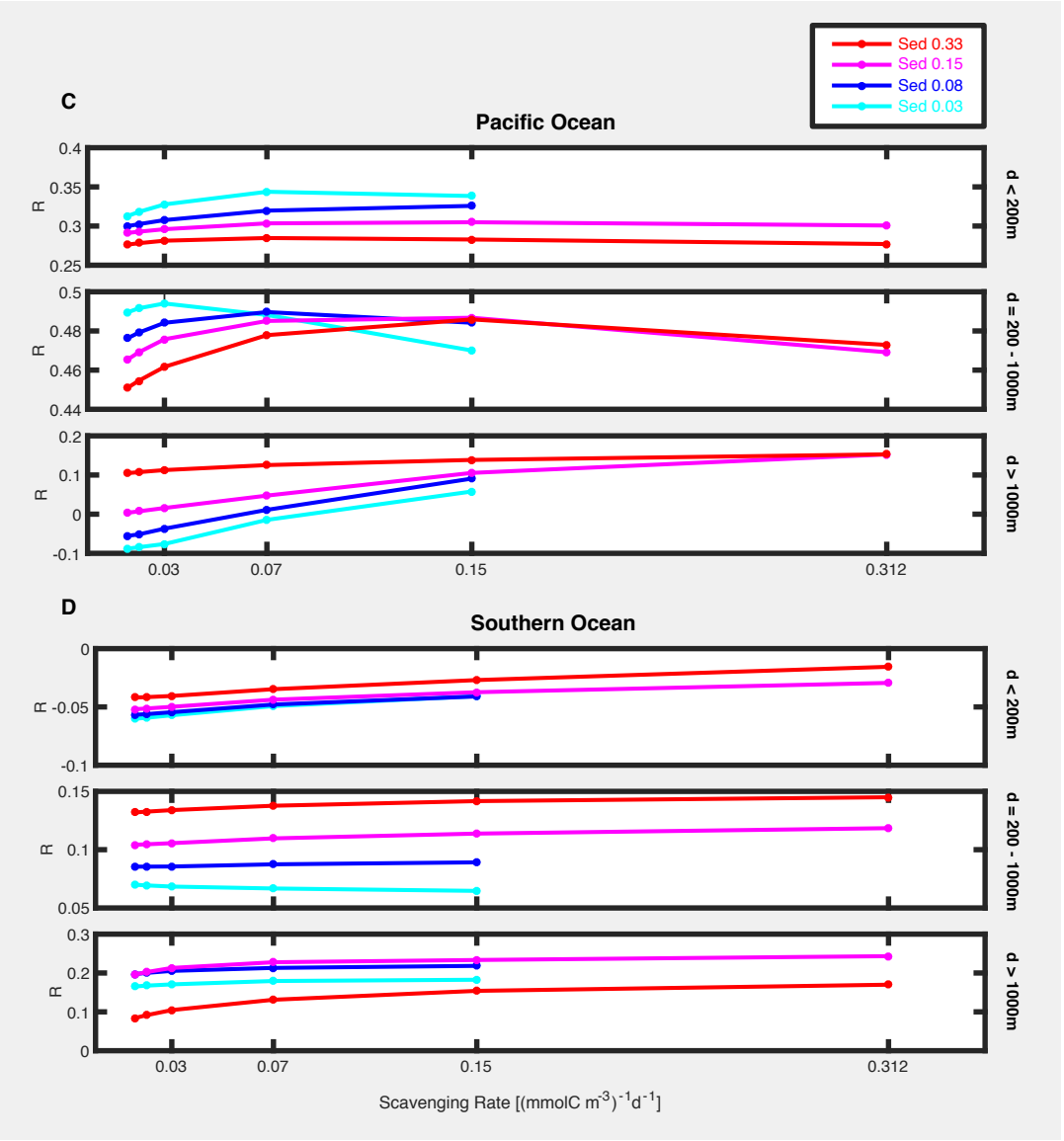

We notice that in some correlation plots in Fig. 4.4, an "optimal" sediment source-scavenging rate combination is found. The correlation coefficient in the Atlantic Ocean (Fig. 4.4A) ranges between -0.05 and 0.2, indicating that the model has almost no predictive power with respect to spatial variations within these subregions. At the surface, the best fit is given by high sediment sources, while below 200 m the smallest sediment source seems to be the best choice. The absence of correlation results from a very broad fan of high and low measured dFe concentrations over the basin. The Atlantic Ocean is characterised by manifold patterns from high to low latitudes as described in Section 1.6, which are not well reproduced by a rather simple global model. The best correlation coefficient between modelled and measured dFe concentrations was calculated for the Indian Ocean (Fig. 4.4B). The maximal correlation coefficient at the surface, between 200 - 1000 m and at depth are R = 0.65, R = 0.82 and R = 0.36, respectively. Above and below 1000 m, the optimal combinations are given by $k_{scav} = 0.15\ (\text{mmol C m}^{-3})^{-1}\ \text{d}^{-1}$ and $\text{Fe:N}_{benthos} = 0.03\ \mu\text{mol Fe mmol N}^{-1}$, and by $k_{scav} = 0.07\ (\text{mmol C m}^{-3})^{-1}\ \text{d}^{-1}$ and $\text{Fe:N}_{benthos} = 0.08\ \mu\text{mol Fe mmol N}^{-1}$, respectively. In the surface Pacific Ocean (Fig. 4.4C), the lowest sediment source fits the observations best, irrespectively which scavenging rate is used. Here, the correlation coefficient is affected by

high dFe outliers like those in the oxygen minimum zone off Peru. Between 200 - 1000 m, low scavenging rates are best associated with a low sediment source of dFe. However, from a scavenging rate of 0.07 $(\text{mmol C m}^{-3})^{-1}\,\text{d}^{-1}$ upwards, also a higher sediment source is needed to maintain the correlation coefficient around 0.5. At depth, no correlation between the model experiments and the observations was found, just like in the Southern Ocean where the correlation between model and observations is absent over the whole water column (-0.05 ¡ R ¡ 0.25).

4.4 Discussion

4.4.1 The effect of increasing the dFe sediment source

Estimates of the dFe flux from sediments to the water column are still subject to large uncertainties due to scarcity of measurements which are often restricted to few regions. Here, we analyse the effect of different strengths of the sediment source to the dFe mean in four ocean basins. Fig. 4.5 compares the observed mean dFe values with two model experiments having the same scavenging rate $k_{scav} = 0.0156\,(\text{mmol C m}^{-3})^{-1}\,\text{d}^{-1}$, but different $\text{Fe:N}_{benthos}$. We notice that a small sediment source and small scavenging rate represent the measurements well in the Indian Ocean at all depths (Fig. 4.5A). Here, also the intermediate and deep Atlantic Ocean match the observations. On the contrary, the modelled surface Atlantic Ocean mean dFe concentration is 64% higher than the observations. Indeed, the dFe concentrations off the African continent are too high in the model since the scavenging on lithogenic particles is not included in these simulations (see Chapter 5). Increasing the sedimentary dFe source aggravates this overestimation (Fig. 4.5B). Fig. 4.5A shows that the modelled dFe in the Southern Ocean is higher than the observations by 40-46% in the intermediate and deep ocean, but at the surface the overestimation is restricted to 13%. With a small sediment source, the dFe concentrations in the Pacific Ocean are largely underestimated at all depths (Fig. 4.5A). A ten times larger sediment source results in an increase of the mean modelled dFe concentration in the surface Pacific Ocean by 118%, thus improving from 67% to 27%

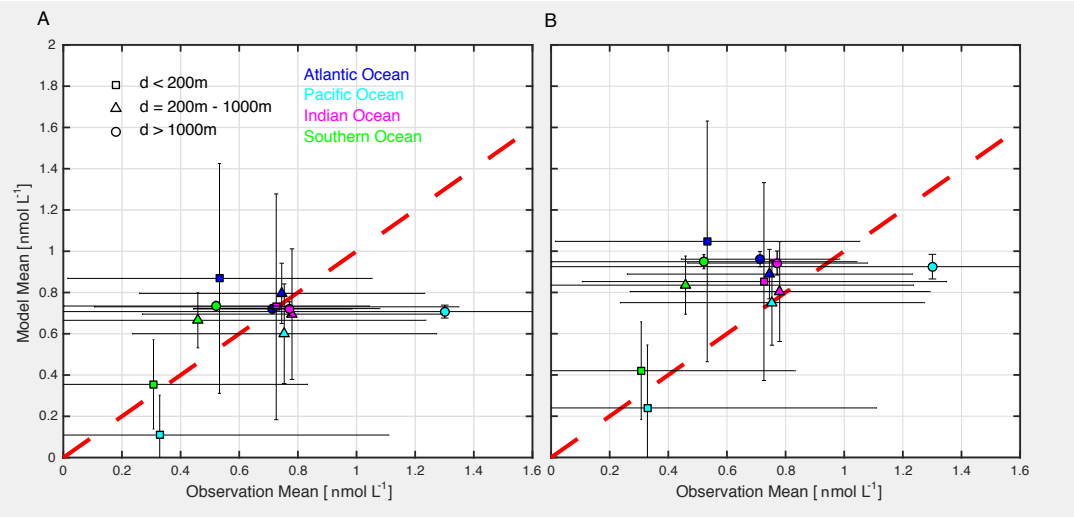

FIGURE 4.5: Observed mean from the Atlantic, Pacific, Indian and Southern Oceans compared to the model experiment with (A) low dFe sediment source ($\text{Fe:N}_{benthos} = 0.03\ \mu\text{mol Fe mmol N}^{-1}$) and (B) high dFe sediment source ($\text{Fe:N}_{benthos} = 0.33\ \mu\text{mol Fe mmol N}^{-1}$)

lower dFe mean compared to the observations. This large increase in dFe concentration reflects the sensitivity of shallow shelves in the west Pacific Ocean and strong upwelling regions in the east Pacific Ocean to changes in the dFe sediment source. This explains the dFe increase in the sub-Arctic Pacific as well as in east-south-east of Australia and New Zealand with a higher sediment source (not shown). Another reason for the significant increase is the strong upwelling region close to the coast of Peru. Here, Fe-rich deep waters are brought up to the surface and expand into the subtropical gyre (not shown).

Across all basins, a ten-fold increase of the sediment source led to roughly 30% higher dFe concentrations at depth. The extent of the increase in the upper ocean layers, and specifically in the surface water, is, among others, due to the relative contribution of dust and sediments to the dFe pool. Oceans with a dominant aeolian source, as the Indian and the Atlantic Ocean, show a relatively small increase in the surface and intermediate waters. On the contrary, in the Pacific and the Southern Ocean the main source of dFe comes from down beneath and not from the atmosphere and the effect of higher sediment source to the dFe concentration in surface and intermediate waters is large.

The parameterisation of the sediment source of dFe in the model is described in a rather simple way. In fact, the relationship between dFe release from sediment and oxidation of PON used in this model, neither takes into account the bottom water O_2 concentration and redox reactions explicitly, nor the release of organic ligands from sediment.

4.4.2 The effect of increasing the scavenging rate

To analyse the effect of scavenging on the mean dFe concentration we consider two model experiments featuring a sediment source of intermediate strength characterised by $\mathrm{Fe{:}N}_{benthos}$ = 0.15 μmol Fe mmol N^{-1}, and scavenging rate of 0.02 and 0.07 (mmol C $m^{-3})^{-1}$ d^{-1}. We notice that a 3.5-fold increase in the scavenging rate led to a general reduction of the dFe concentrations around the globe and at all depth by averagely 30%. The Indian Ocean moved from having comparable concentrations to the observations to being underestimated. Also, dFe concentration in the Pacific Ocean was reduced everywhere (Fig. 4.6B). As mentioned

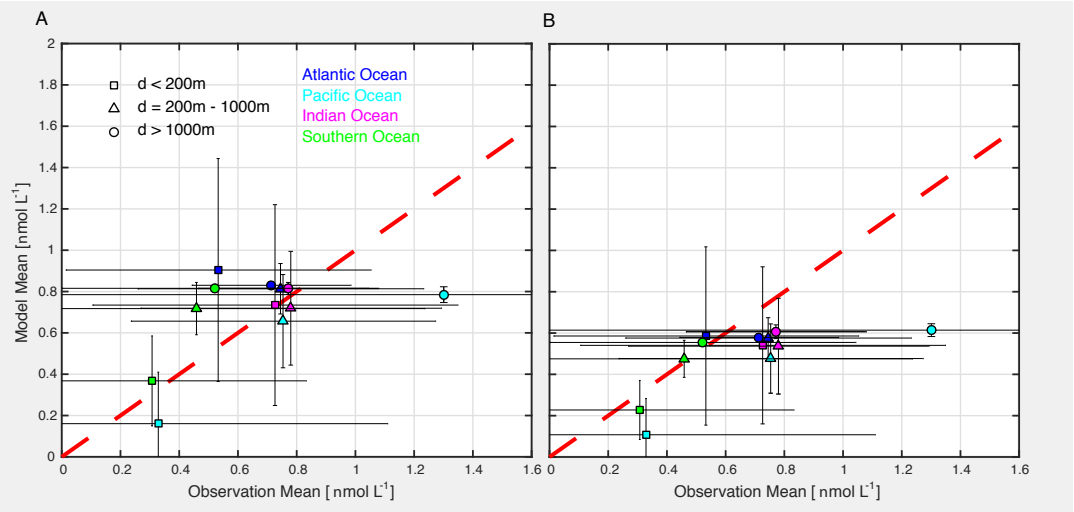

FIGURE 4.6: Observed mean from the Atlantic, Pacific, Indian and Southern Oceans compared to the model experiment with (A) low dFe sediment source (k_{scav} = 0.02 (mmol C $m^{-3})^{-1}$ d^{-1}) and (B) higher scavenging rate (k_{scav} = 0.07 (mmol C $m^{-3})^{-1}$ d^{-1})

before, dFe in the surface Atlantic Ocean is overestimated in the model (Fig. 4.6A). Nevertheless, by increasing the amount of dFe scavenged, the surface dFe concentration is reduced by 34%, bringing the model output in good agreement with the observations (Fig. 4.6B). At the same time, increasing the scavenged dFe at the surface, consequently reduces the dFe concentration in the water below (Fig. 4.6B). Finally, in the Southern Ocean, a larger scavenging rate reduced the modelled dFe below 200 m, featuring dFe concentrations which fit much better the observations (Fig. 4.6B).

The rate at which Fe is lost from the water through scavenging in reality depends on the ligand concentration in the water column. Consequently, the spatial variability of dFe concentration is not only affected by the source strength and scavenging rate, but also the spatial variability of organic ligands. This version of our model, however, does not take into account variable ligands which could partly explain the mismatch between the modelled and the observed dFe concentrations in different ocean basins.

4.5 Conclusion

The sensitivity study showed that varying the strength of the sedimentary dFe source and the rate at which dFe is scavenged impacts the dFe concentration and the degree of agreement with observational data to some extent. While scavenging affects all oceans and all depths similarly, the sediment source mainly influences the deep dFe concentration, with exception for the surface Pacific Ocean.

The variability of the dFe concentration at depth in the Atlantic, Indian, Pacific and Southern Ocean can not be represented in the model by just varying the sedimentary source and scavenging rate, although strengthening the sediment source resulted in larger spatial variations in the deep model layers (Fig. 4.5).

From our sensitivity study on scavenging and the dFe sediment source we notice that only small improvements in the model-observations agreement can be achieved by tuning the model with these two parameters. This highlights the importance of including more processes involved in the Fe cycle in global biogeochemical models such as additional dFe sources, e.g. the hydrothermal source and icebergs, a more complex representation of organic ligands, coupling with a comprehensive sediment model, and a variable dFe solubility. Some of these processes are particularly important in the representation of the Fe cycle in specific ocean basins. Indeed, missing these processes, the current state of the global model is not capable of describing the spatial variability in wide regions of the oceans, as noticed in this study. While the Indian Ocean has already a good correlation and the Pacific Ocean a modest one, the Atlantic and the Southern Ocean do not correlate with the observations. A global model should be robust and reproduce the observations as uniformly well as possible in different regions to support ecosystem and climate studies. Thus a more comprehensive investigation on the importance of different processes in the various regions of the world's oceans is required (Chapter 5 and Chapter 6).

5 Processes affecting dissolved iron across the Subtropical North Atlantic – a model study

Abstract

Trace metal measurements in recent years have revealed a complex distribution of dissolved iron (dFe) in the ocean that models still struggle to reproduce. The GEOTRACES section GA03 across the subtropical North Atlantic was chosen to study the driving processes involved in the Fe cycle in the region. Here, field observations found elevated dFe near the surface under the Saharan dust plume, a strong dFe minimum below the mixed layer depth, a maximum at the oxygen minimum zone near the African shelf, a hydrothermal maximum near the Mid Atlantic Ridge, and lower dFe values in the deep eastern basin than in the west. We show that several of these features can be understood and be reproduced in models when they take into account scavenging on dust particles and phytoplankton, a variable ligand concentration and a hydrothermal dFe source. By doing so in a sequence of parameterisation changes, we are able to relate physical and biological processes, as well as internal and external dFe sources to observed features of the dFe distribution. In agreement with the observations, the additional scavenging on dust generates lower dFe concentrations in the deep eastern basin while the new ligand distribution results in a dFe maximum in the intermediate waters in the east basin and moderates the deep dFe gradient between the eastern and western basins.

5.1 Introduction

In this chapter, we try to understand which processes determine the dFe distribution in the Subtropical North Atlantic Ocean. The relevant local processes are scavenging on biogenic and lithogenic particles, biological uptake, export and remineralisation. We have picked the GEOTRACES GA03 (Boyle et al., 2015) cruise leg from Bermuda to Cape Verde as our study area. This region was chosen because it is a place of very intensive Fe cycling due to strong dust input and the flourishing biological activity in the Mauritanian upwelling region. Here, the processes of interest are more pronounced compared to other regions. In this process-oriented study on the GA03 cruise leg, we show how several details of the dFe distribution can be reproduced by introducing new processes and by changing existing parameterizations of processes affecting the Fe cycle. The final model includes the effects of scavenging on dust and non-sinking biogenic particles, a non-constant ligand concentration, and, for completeness, a hydrothermal dFe source. For better understanding we present this output of a fairly extensive parameter study by selecting only a simple sequence of steps in changing the models parameters that lead from our initial model set-up to a final one. This presentation allows to discuss the contribution of the individual processes and parameterization changes to the final outcome. As the Fe system reacts nonlinearly to the parameterization changes, however, the magnitude of the changes in dFe distribution in the intermediate steps – but not

in the final outcome – is somewhat dependent on the sequence of changes. The succession of refinements intends to disclose the role of different processes in controlling the distribution of dFe and their importance in biogeochemical models.

5.1.1 The GA03 Section

The GEOTRACES GA03 cruise leg (Boyle et al., 2015) from Bermuda to Cape Verde took place in November 2011. The aim of the cruise was to document the distribution of trace elements and isotopes in the region and to diagnose the nature of the controlling biogeochemical and physical processes. We focus on the dFe distribution (Sedwick et al., 2015) (Fig. 5.1) in the open ocean from station USGT11-10 to station USGT11-24 (Fig. 5.11 in the supplement in Section 5.5.1).

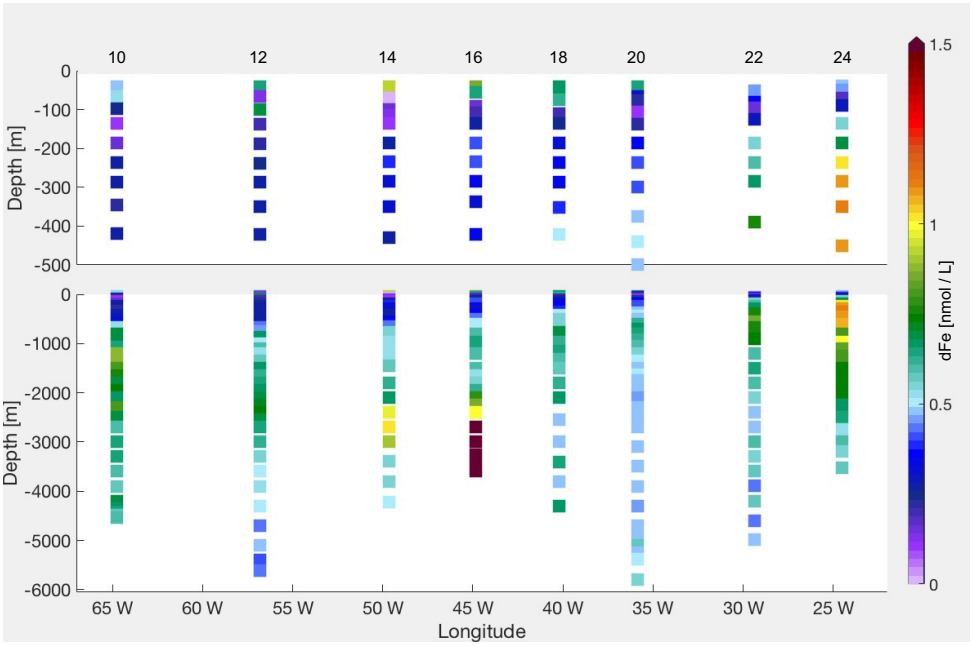

FIGURE 5.1: Measured dFe along GA03 (Sedwick et al., 2015)

The dFe concentrations (Fig. 5.1) within the surface mixed layer are high, ranging between 0.37 and 0.98 nmol L^{-1} (or equivalently μmol m^{-3}), caused by the North African dust flux (Hatta et al., 2015). The aerosol Fe from Saharan dust is predominantly released in the colloidal phase, having important implications for dFe availability to phytoplankton (Fitzsimmons et al., 2015a). This appears to be representative of dFe in the tropical and subtropical surface Atlantic underlying the North African dust plume (Bergquist, Wu, and Boyle, 2007; Fitzsimmons et al., 2015b).

Across the gyre (Fig. 5.1), dFe displays a pronounced concentration minimum in the lower euphotic zone at the depth of the deep chlorophyll maximum (DCM). Such features have been previously reported in the subtropical and tropical North Atlantic (Sedwick et al., 2005; Bergquist and Boyle, 2006), and are supposedly caused by removal via biological uptake and particle scavenging (Fitzsimmons et al., 2015a; Sedwick et al., 2015).

In the intermediate waters at station USGT11-24 (Fig. 5.1), no correlation between dFe and dissolved manganese was found, excluding sedimentary Fe from being the main source (Hatta et al., 2015). This finding was also supported by δ^{56}Fe measurements in Conway and John (2014). The correlation with the apparent oxygen utilisation (AOU) implies that the dFe maximum is here strongly associated with an addition of Fe via remineralisation alone

TABLE 5.1: Steps in model development

Model Run	Process added	Remarks
Standard	Generic dFe modelling	
Dust	+ Scavenging on dust particles	$k^{Fe}_{scavdust} = 7.5 \cdot 10^{-4}/(\mathrm{mg/m^3})/\mathrm{d}$
AOU-Lig	+ Ligands from AOU	$\mathrm{L} = (1{+}0.005 \cdot \mathrm{AOU})\mathrm{nmol\,L^{-1}}$
Scav Phyto	+ Scavenging on phytoplankton	
Scav Phyto 2	+ Reduced $k^{Fe}_{scavdust}$	$k^{Fe}_{scavdust} = 2 \cdot 10^{-4}/(\mathrm{mg/m^3})/\mathrm{d}$
VS	+ Increased Det sink velocity	velocity slope $0.0288\,\mathrm{d^{-1}} \rightarrow 0.0432\,\mathrm{d^{-1}}$
Hydro	+ Hydrothermal Fe source	

(Hatta et al., 2015) (distributions of AOU and dissolved oxygen were reported in Jenkins et al. (2015)). Model experiments by Pham and Ito (2018) argue that the intermediate water dFe maxima are formed by the simultaneous release of scavenged Fe and ligands from organic particles.

Along the western edge of the transect (Fig. 5.1), waters are enriched in dFe due to Fe advected from the North American continental shelf as part of the Upper Labrador Sea Water (Hatta et al., 2015) and are probably due to sedimentary resuspension. Below the thermocline, these elevated concentrations extend eastward beyond Bermuda.

In the intermediate and deep waters, the observations show a gradient between the east and the west basin, the latter having higher dFe concentrations (Fig. 5.1).

A large dFe anomaly with a concentration of up to 68 $\mathrm{nmol\,L^{-1}}$ is observed at station USGT11-16 directly over a hydrothermal site. The hydrothermal signal extends at 2000 - 4000 m depth at least 500 km west of the Mid Atlantic Ridge (MAR) between 40°W and 50°W, with concentrations up to 1.13 $\mathrm{nmol\,L^{-1}}$, demonstrating that hydrothermalism contributes to the Fe pool in the deep ocean (Hatta et al., 2015).

5.1.2 Model experiments

Results of the FeMIP Project show many differences between Fe cycle models (Tagliabue et al., 2016). However, some of the assumptions are similar and the REcoM2 model shares many of them. Looking at the GA03 section, these result in an incomplete representation of the observations, where some important features of the dFe distribution are either not captured or their magnitude is misestimated. This may imply an inadequacy of the current Fe cycle modelling for the region in focus.

Different processes that affect the Fe cycle are often non-linearly dependent, meaning that a simple parameter-tuning exercise is difficult. For this reason, in the following we show the changes in dFe concentration by introducing subsequently new processes in the model. Each model run was integrated for 1000 years from a state of rest. The five steps taken are from the ***Standard*** run, to the ***Dust*** run which includes scavenging on lithogenic particles, to the ***AOU-Lig*** run where a parametrisation of ligands was introduced, to the ***Scav Phyto*** run in which an additional scavenging on phytoplankton was added, to the ***VS*** run where the velocity of sinking particles is changed, to the final ***Hydro*** run which includes a hydrothermal dFe source (Table 5.1). The details of these changes are explained in Results (Section 5.2).

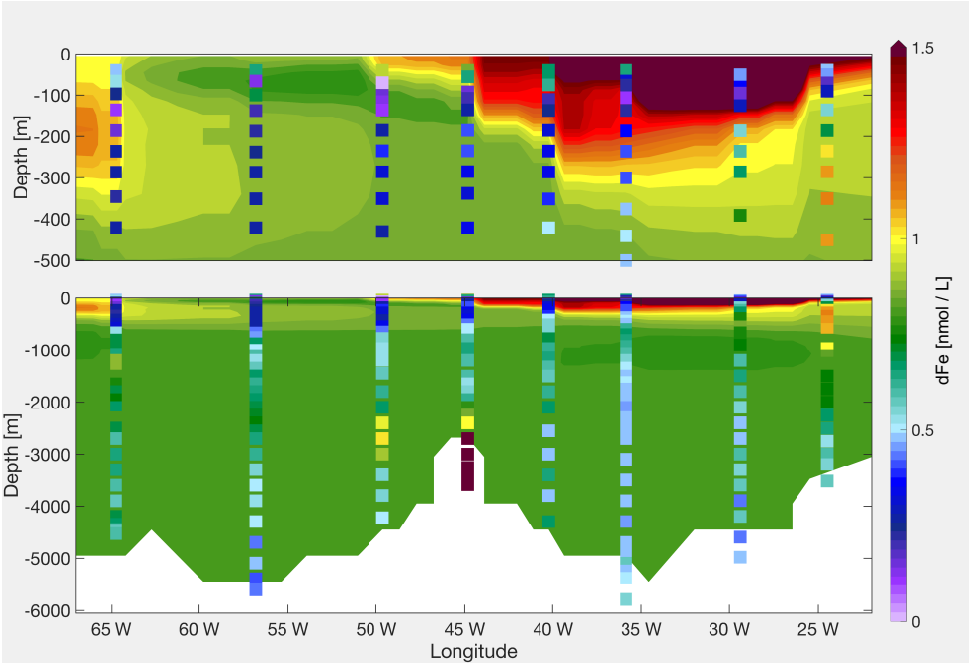

FIGURE 5.2: Modelled dFe along GA03 in the *Standard* run, with measured dFe values as dots

5.2 Results

5.2.1 Standard

In the *Standard* run the scavenging rate is $k^{Fe}_{scav} = 0.02\,\mathrm{mmol\,C\,m^{-3}\,d^{-1}}$. The model shows (Fig. 5.2) high dFe concentrations at the surface of the east basin (east of the MAR - east of 45°W) due to strong aeolian input from the African continent. This influences the layers below until ca. 300 m depth. In the west basin (west of the MAR - west of 45°W) we see a minimum at ca. 50 m, which corresponds to the DCM and is an expression of biological dFe uptake. Both these features are also seen in the GEOTRACES data (Fig. 5.1). However, compared to the observations, the model generally overestimates dFe. Near the American coast at 200 - 300 m a dFe maximum is observed in the model which is not seen in the data (Fig. 5.2). This dFe is transported north from the region off Puerto Rico. Below 500 m the dFe concentration is fairly homogenous in the model, slightly lower on the west side of the MAR. The model does not reproduce the dFe variability in the intermediate and deep ocean, one reason being that the hydrothermal dFe input is neglected here.

5.2.2 Standard + Dust Scavenging

In the Subtropical North Atlantic, scavenging on lithogenic particles is a major process in the Fe cycle. Ye and Völker (2017) argue that neglecting dust particles as scavengers is one main reason for overestimation of dFe under the Saharan dust plume. The particle dynamics in the model considers aggregation and disaggregation of fine dust particles and large organic and lithogenic particles. Scavenging now occurs on lithogenic particles as well as organic particles (Eq. 2.2):

$$(k^{Fe}_{scav} \cdot C_{det} + k^{Fe}_{scavdust} \cdot (P_{small} + P_{large})) \cdot Fe' \tag{5.1}$$

where $k^{Fe}_{scavdust} = 7.5 \cdot 10^{-4} (\mathrm{mg\,m^{-3}})^{-1}\,\mathrm{d^{-1}}$ (Table 2.1). For further details, see Ye and Völker (2017).

Including removal by lithogenic particles reduces the dFe concentration everywhere in the transect (Fig. 5.3). The largest effect occurs in the water column under the dust plume where the water in the upper 100 m loses 30% of dFe, whereas the intermediate and deep waters lose 70% of dFe.

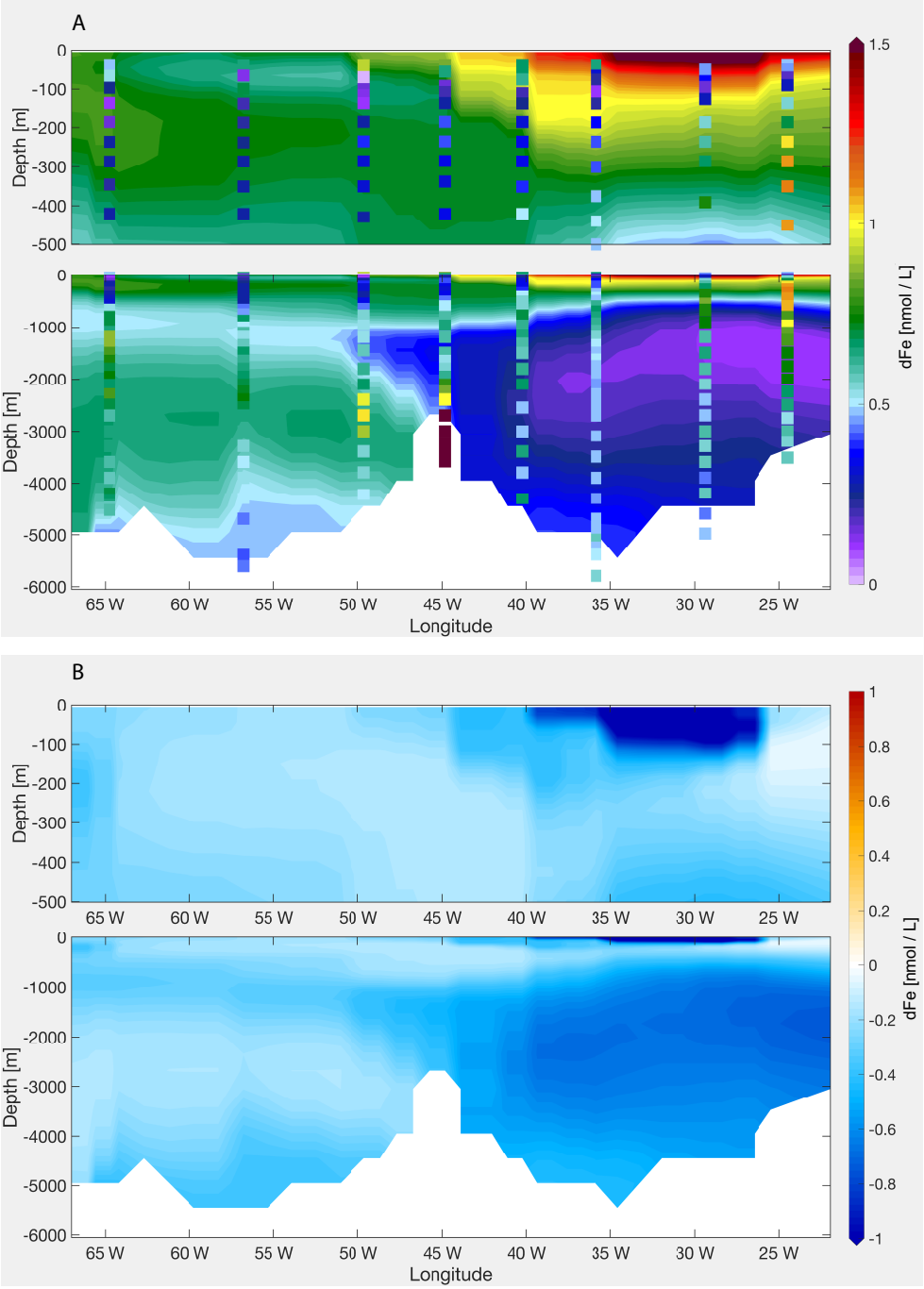

FIGURE 5.3: (A) Modelled dFe concentration in the *Dust* run along GA03, with measured dFe values as dots; (B) dFe difference between the *Standard* run and the *Dust* run

While in the *Standard* run the scavenging loss of surface dFe is limited to the upper 50 m and east of 26°W, reaching a maximum of 4.5 nmol L^{-1} yr^{-1}, the effect now is more widespread, reaching as far as 40°W, and into the oligotrophic waters of the subtropical gyre at 100 m depth. The scavenging strength reaches here a maximum of 12 nmol L^{-1} yr^{-1}. Consequently, the dFe concentration is reduced by more than 1 nmol L^{-1} between 25°W and 40°W (Fig. 5.3B), but it is still too high compared to the observations. Here, the biogenic and lithogenic scavenging is the most dominant process affecting dFe distribution compared to biological uptake and remineralisation as can be seen in the upper layers in the east basin (ED1) in Fig. 5.12 in the supplement in Section 5.5.1 where the integrated contribution of scavenging, biological uptake and remineralisation to the dFe pool are shown.

Alterations in the surface dFe distribution caused by the additional scavenging onto dust particles were already observed by Ye and Völker (2017). However, the changes are not limited to the surface ocean: while the *Standard* run gives homogenous dFe concentrations below 500 m, the scavenging on dust introduces longitudinal structure, showing a strong gradient between the east and the west basin (Fig. 5.3). A similar but weaker gradient was also seen in the observations (Fig. 5.1). dFe in the model decreases in the east basin by roughly 0.6 nmol L^{-1}, and by only 0.15 nmol L^{-1} in the west basin, with the result that the dFe concentrations in the east basin are too low. It should be noted that here we used the same dust scavenging rate and aggregation and disaggregation coefficients as in Ye and Völker (2017). With more data for particles in different size-fractions, a full sensitivity study on the aggregation and disaggregation rate could be performed.

5.2.3 Standard + Dust Scavenging + AOU Ligands

The eastern part of the GA03 shows a dFe maximum between 300 m and 600 m where an oxygen minimum zone (OMZ) spreads from the Mauritanian coast (Fig. 5.1). This pronounced OMZ has shown a correlation to the elevated dFe concentrations in this particular region (Rijkenberg et al., 2012). Here, remineralisation of sinking organic material releases both dFe and organic ligands which prevent dFe from scavenging removal. Previous studies also ascribed the dFe maximum along GA03 to remineralisation processes (Hatta et al., 2015), dissociation of adsorbed Fe from sinking particles and ligands from organic particles (Pham and Ito, 2018).

Our model runs, however, do not reproduce this feature, despite having a strong remineralisation of dFe. Based on the strong correlation between AOU and dFe in GA03 (Hatta et al., 2015), we decided to introduce a ligand parametrisation based on AOU in a similar way to Misumi et al. (2013), who applied a linear relationship between AOU and the weak binding ligands L_2. Comparing the AOU values from the World Ocean Atlas (Garcia et al., 2010a) with the ligand data along GA03 (Buck, Sohst, and Sedwick, 2015), we notice a correlation between AOU and the strong binding ligands L_1, rather than L_2. The Pearsson correlation coefficient is 0.45 when using ligand data between 200 m and 3000m depth. This emphasises that oxidation of OM is an important source of ligands. Instead of using a constant ligand concentration of 1 nmol L^{-1}, we adapted the parameterisation of Misumi et al. (2013) to represent the abundance of total ligands in the *AOU-Lig* run:

$$L = 1\,nmol\,L^{-1} + 0.005\,\frac{nmol\,L^{-1}}{\mu mol\,L^{-1}} \cdot AOU \tag{5.2}$$

where 0.005 is the slope of the fit between AOU and L_1.

The new ligand distribution changes in a similar way to dFe in Fig. 5.4. It is reduced to ca. 0.95 nmol L^{-1} at the surface; east of 30°W between 200 m and 1000 m the concentration is now higher than 2 nmol L^{-1}; a tongue of ca. 1.5 nmol L^{-1} ligand's concentration extends

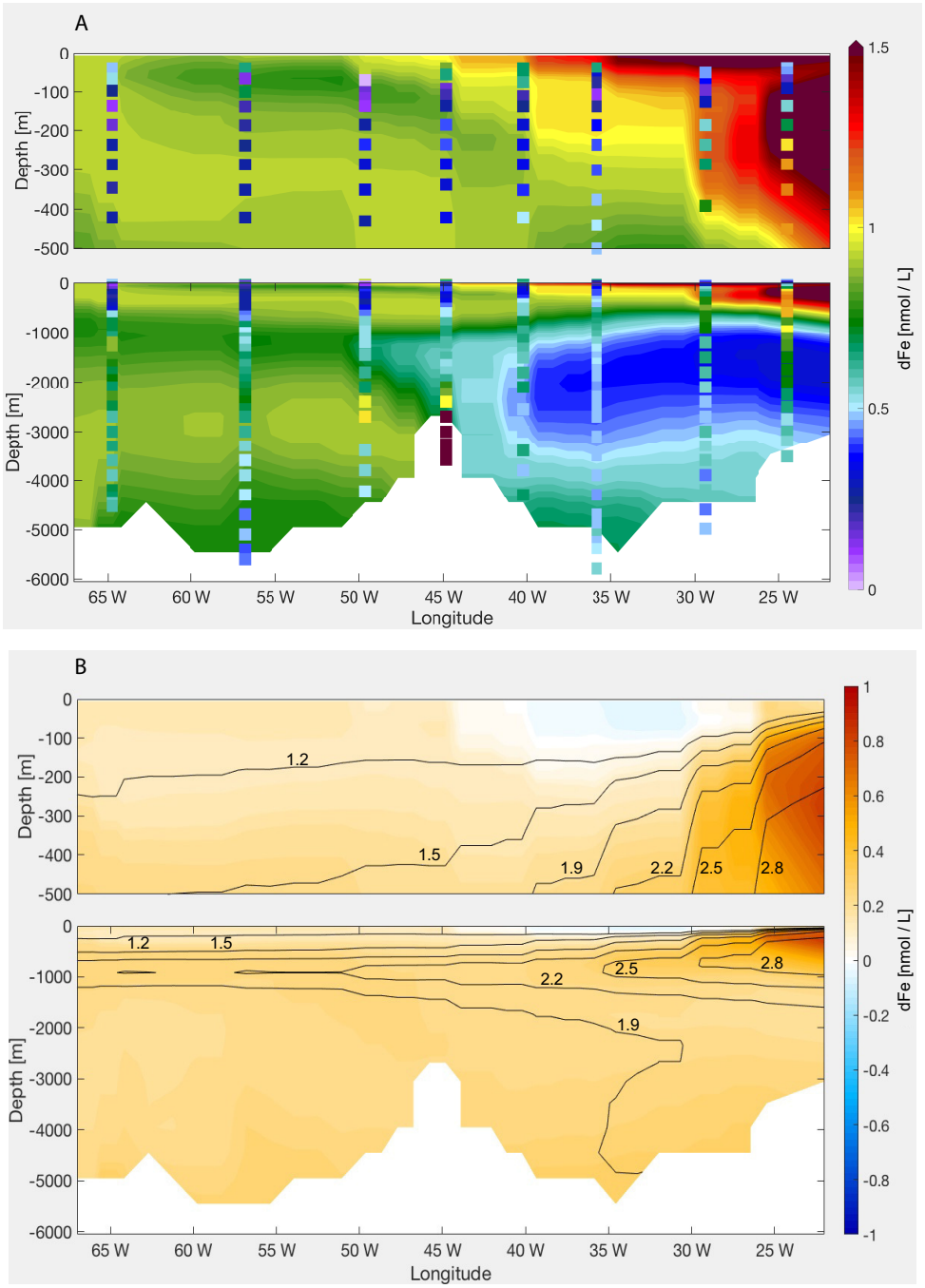

FIGURE 5.4: (A) Modelled dFe along GA03 in the *AOU-Lig* run, with measured dFe values as dots; (B) dFe difference between the *Dust* run and the *AOU-Lig* run. The contour lines show the new ligand concentration (nmol L^{-1})

at 1000 m from the east to the west; the average concentration below 2000 m in the east basin is 1.5 nmol L^{-1}, while in the west basin it is 1.3 nmol L^{-1}. Since the ligand concentration becomes higher than 1 nmol L^{-1} everywhere but at the surface, we see lower scavenging loss and an average increase of dFe concentrations of 0.3 nmol L^{-1} along the transect (Fig. 5.4). East of 26°W, at the depth of the AOU maximum, the dFe concentrations are on average 0.8 nmol L^{-1} higher than the *Dust* run, stretching vertically from the surface to 500 m. Below 1000 m, the increase of dFe is 150% in the east basin, which had before a too low iron concentration, and only of 50% in the west basin.

A limitation of this ligand parameterisation is that it can not be applied globally. This parameterisation is an approximation for younger water masses like the deep Atlantic Ocean, but leads to too high ligand concentrations in older water masses such as in the deep Pacific Ocean (not shown) (Section 5.3.4).

5.2.4 Standard + Dust Scavenging + AOU Ligands + Phytoplankton Scavenging

A strong subsurface dFe minimum occurs within the centre of the North Atlantic subtropical gyre and stretches across the Atlantic basin. The minimum at the DCM between 100 m and 200 m is argued in the literature to be caused by combined dFe scavenging and biological uptake (Hatta et al., 2015). As described in Section 5.2.1, the *Standard* run does reproduce a subsurface minimum, it is however not pronounced enough. Since the modelled primary production in this region is comparable with observations, we take a closer look at the scavenging process. Phytoplankton can be considered as small particles which offer a surface to scavenge dFe (Hudson and Morel, 1989). In Eq. 2.2 the scavenging term is (Table 2.1):

$$(k^{Fe}_{scav} \cdot (C_{det} + C_{phy} + C_{dia}) + k^{Fe}_{scavdust} \cdot (P_{small} + P_{large})) \cdot Fe^{'} \tag{5.3}$$

The dFe concentration is reduced everywhere along GA03 (Fig. 5.5), with the major effect in the upper 100 m, with the maximal dFe loss of 0.5 nmol L^{-1}. Here, introducing scavenging on phytoplankton leads to a scavenging increase between 50% and 300% between 45°W and 65°W. Though scavenging on phytoplankton is limited to the euphotic zone, we also observe a decrease of dFe in the deeper layers. This is caused by a decrease in the pre-formed dFe concentration in the water mass formation regions.

To prevent an overly low dFe at depth, we reduce the scavenging rate of dust particles, $k^{Fe}_{scavdust}$, to $2 \cdot 10^{-4}$ $(mg\,m^{-3})^{-1}\,d^{-1}$ (*Scav Phyto 2* run) (Fig. 5.5C). This mainly affects the deep east basin, where the average concentration of 0.3 nmol L^{-1} is increased to ca. 0.5 nmol L^{-1}, since more dFe sinks to the deep ocean by reducing the scavenging under the dust plume. The west basin is almost unchanged due to the limited influence of dust in this region.

The observed dFe shows very low concentrations also below the DCM, where the dFe concentration is expected to increase again due to remineralisation. The low dFe concentrations extend down to 700 m (Fig. 5.1). Neither the *Standard* run nor the *Scav Phyto 2* run reproduce this feature, the reason is discussed in Section 5.3.3.

5.2.5 Standard + Dust Scavenging + AOU Ligands + Phytoplankton Scavenging + Increased Velocity Slope

The observed intermediate water dFe maximum, which is mainly driven by remineralisation, is deeper compared to the modelled one. In addition, the vertical maximum of dissolved inorganic nitrogen (DIN) in the model is shallower than the observations in WOA (Garcia et al., 2010b), indicating that also the remineralisation process in the model is too shallow. The depth of remineralisation depends on how fast organic particles sink. In the model, the sinking speed of detritus is 20 m d^{-1} at the surface and increases linearly with depth after Kriest and Oschlies (2008) with a slope of 0.0288 d^{-1}. To deepen the remineralisation flux, we increased the slope of the sinking velocity by 50%, to 0.0432 d^{-1}, so that biogenic particles sink out of the surface, and the water column, faster.

In the upper 100 m this results in a slight increase of 5% in dFe concentration along the transect (Fig. 5.6), despite an increase of scavenging and a decrease in remineralisation. The biological production in the Subtropical North Atlantic Ocean is macro-nutrient limited. Increasing the sinking velocity of particles, the residence time of organic particles in the

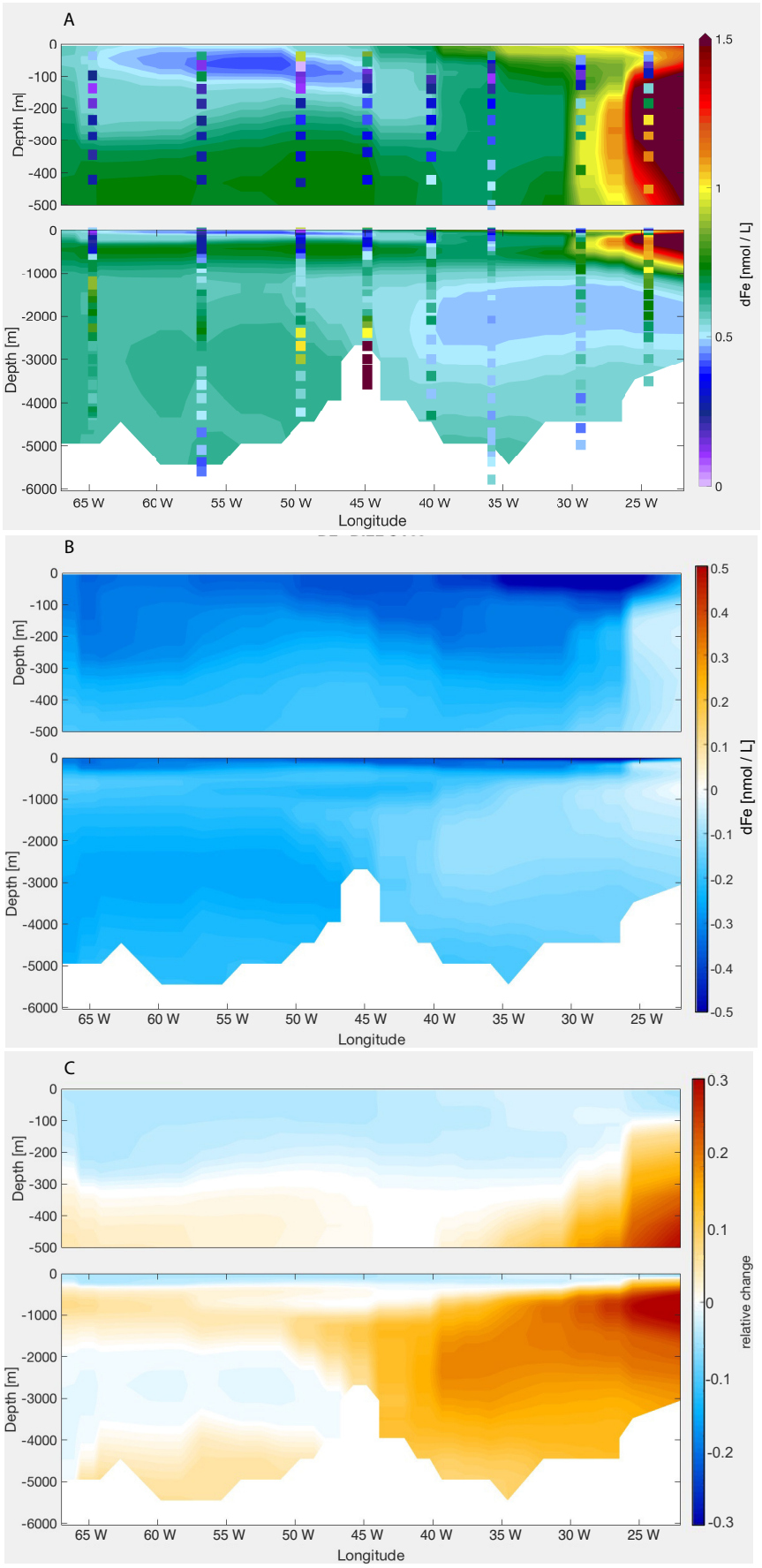

FIGURE 5.5: (A) Modelled dFe the GA03 in the *Scav Phyto* run, with measured dFe values as dots; (B) dFe difference between the *AOU-Lig* run and the *Scav Phyto* run; (C) dFe difference between the *Scav Phyto* run and the *Scav Phyto 2* run

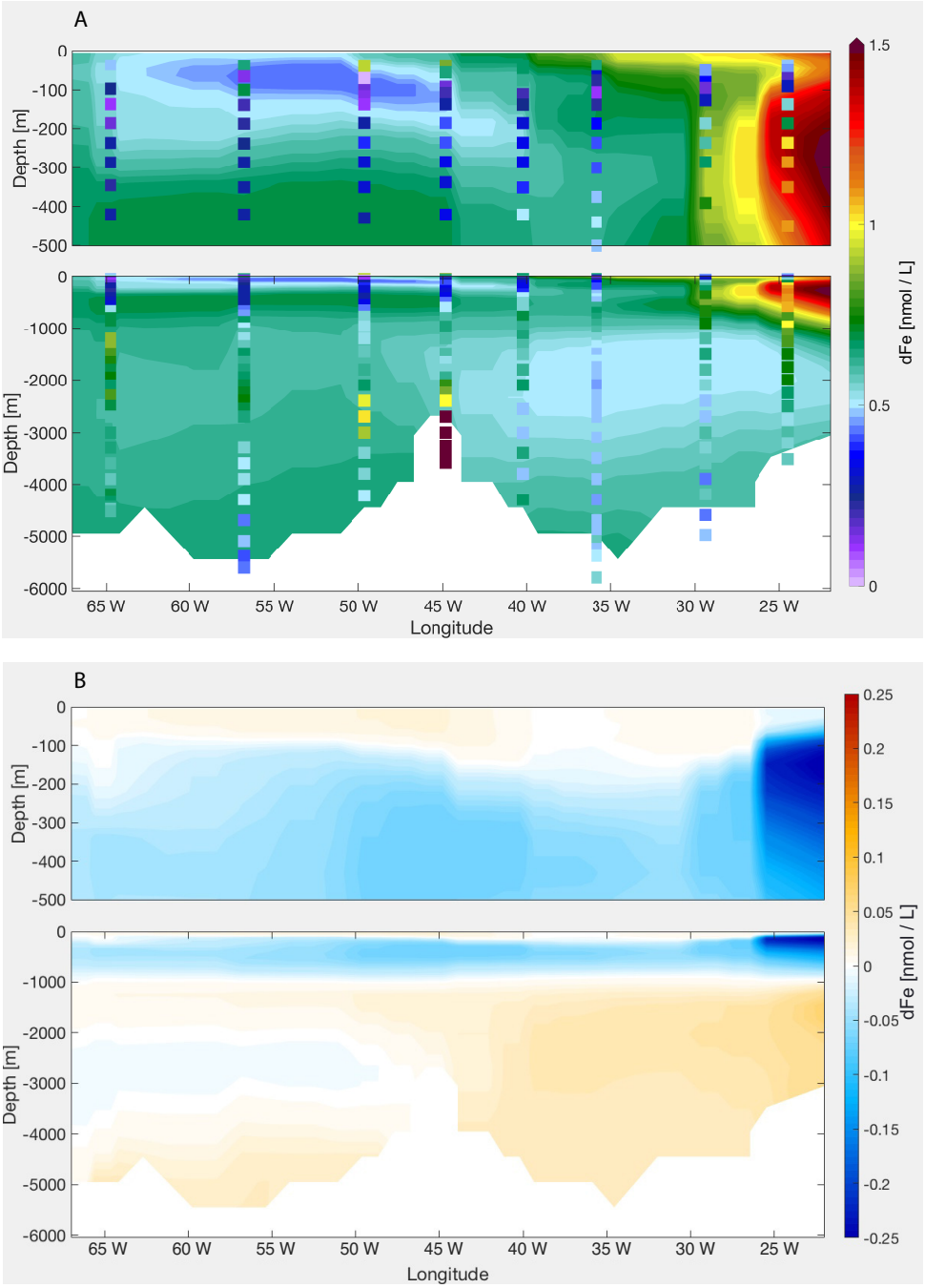

FIGURE 5.6: (A) Modelled dFe along GA03 in the *VS* run, with measured dFe values as dots; (B) dFe difference between the *Scav Phyto 2* run and the *VS* run

water column is reduced and so the remineralisation of nutrients, leading to an intensified nutrient limitation of phytoplankton growth. This induces a weaker biological production, thus weaker uptake of dFe, leaving more dFe in the water. At the same time, increasing the sinking velocity means that large particles remain a shorter time in the upper water column, while small particles increase due to less aggregation. The dFe removal by scavenging is reinforced by this higher concentration of small particles. The competition of these two processes leads to different features west and east of 26°W. West of 26°W, the dFe loss term at the surface is dominated by biological uptake compared to scavenging, explaining the

dFe increase in the upper 100 m. On the other hand, east of 26°W, under the dust plume, scavenging is mainly controlling dFe concentration. Here, the dFe concentration is reduced.

Between 100 m and 1000 m dFe decreases while below it increases, both ranging from 5% to 15%, with a maximal effect in the east. The mean scavenging is reduced by approximately 5% below 200 m, except east of 26°W where it is reduced by 40%. In general, the mean remineralisation in this run is reduced by 20% to 40% in the upper 1000 m (Fig. 5.13 and Fig. 5.12, e.g. ED1 and ED2, in the supplement in Section 5.5.1), while it increases by the same amount below 1000 m. West of 65°W the remineralisation increase reaches 80% (Fig. 5.13 and partially seen in Fig. 5.12, WD3 in the supplement in Section 5.5.1). This does not only affect local dFe profiles but also the entire Fe cycle because of the longer residence time of dFe.

5.2.6 Standard + Dust Scavenging + AOU Ligands + Phytoplankton Scavenging + Increased Velocity Slope + Hydrothermal Vent

The measurements of GA03 show a strong hydrothermal dFe input from the MAR at 45°W (Fig. 5.1). Though the representation of hydrothermal vents as a source of dFe to the deep ocean is not new (Tagliabue et al., 2010), we present the result of the *Hydro* run here as an additional and final step since the effect of each process investigated in this study on the dFe distribution does not add on linearly. As Tagliabue et al. (2010) we assumed proportionality of the release of dFe to that of ^{3}He at known position of hydrothermal vents. The distribution of hydrothermal vents used in the model includes a vent site located about 1° to the west of station USGT11-16. The uncertainty of the location of hydrothermal vents and in the proportionality of dFe to ^{3}He has to be mentioned.

The *Hydro* run was started from the output of the *VS* run after 900 years and was then integrated for a further 100 years to include the local hydrothermal effect. The effect of the hydrothermal source of dFe is strongly influenced by the AOU based ligand parameterisation, thus switching on the hydrothermal source in combination to the new ligand distribution for longer integrations leads to a non-local signal in our set up - in Section 5.3.4 this topic will be discussed.

As expected, in the model a far field plume of high concentrations up to 0.9 nmol L^{-1} is expanding at a depth of 2000 m to 3000 m, up to 5° east and 5° west of the source (Fig. 5.7). The lateral spreading of dFe over large distances, which has been observed in the GEOTRACES program, has been ascribed to the concomitant release of organic ligands (e.g. Bennett et al., 2008) or the formation of microparticles which hardly sink (e.g. Yücel et al., 2011) and which possibly exchange Fe reversibly with the dissolved phase (Fitzsimmons et al., 2017). Neither of these processes is present in the model. The extremely high values observed at station USGT11-16 in the buoyant plume, up to 68 nmol L^{-1}, can not be represented by models with coarse resolution, where dFe is homogeneously mixed in the bottom box. Such high point values are important for the first scavenging loss in the near field of vents but not for biogeochemistry at the scale of model resolution.

5.3 Discussion

The dFe concentrations along GA03 give indications on which processes are important in shaping its distribution in the Subtropical North Atlantic. The main features and their controlling processes can be summarised (Fig. 5.8A): 1) A strong aeolian deposition leads to surface dFe maximum; 2) In the lower euphotic zone, the dFe concentration is very low due to biological uptake and scavenging onto biogenic and lithogenic particles; 3) Between 200 m and 1000 m east of 30°W the elevated dFe concentration is determined by remineralisation and high ligand concentration; 4) At the west edge, between 200 m and 700 m, dFe-poor

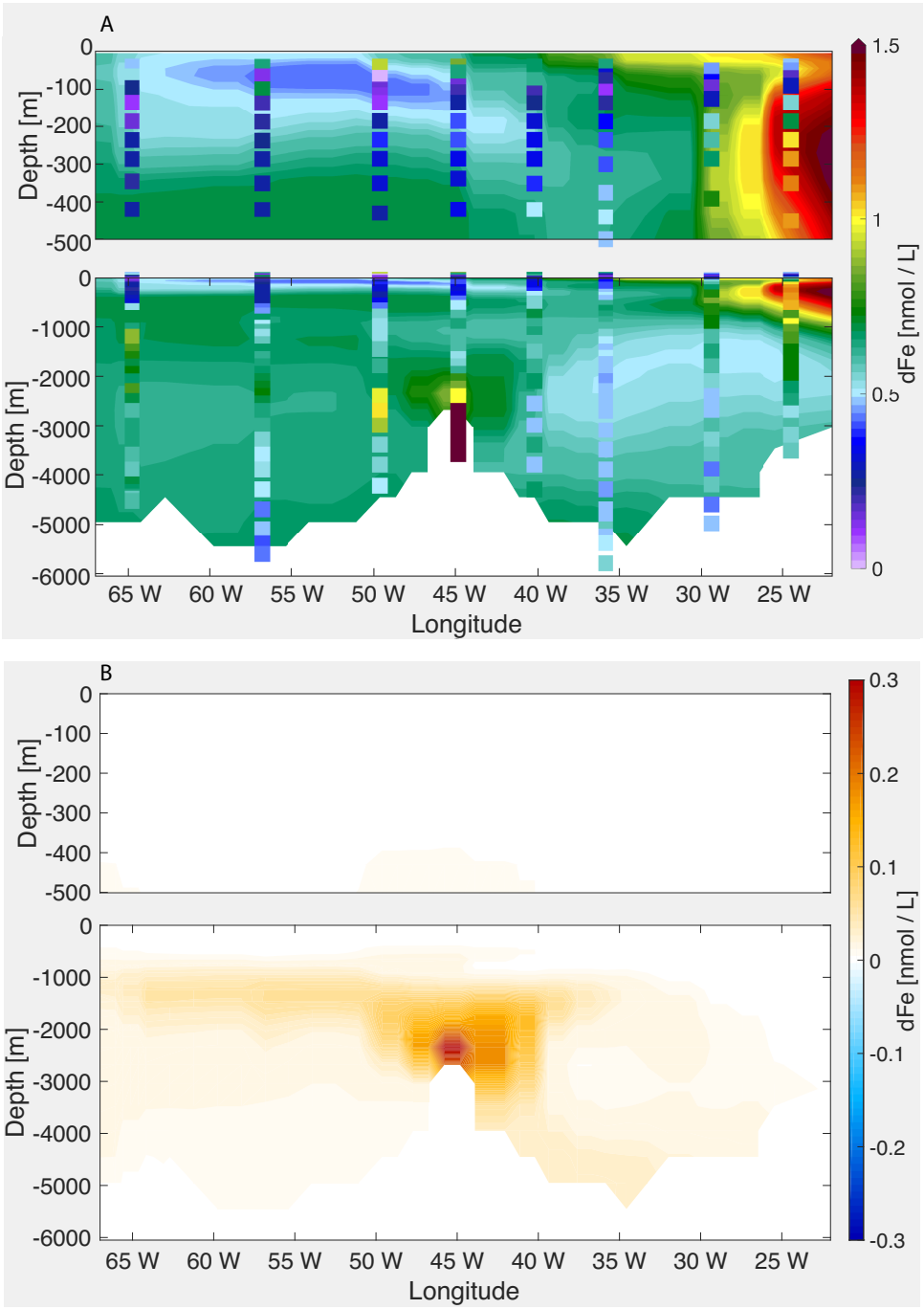

FIGURE 5.7: (A) Modelled dFe along GA03 in the *Hydro* run (100 years), with measured dFe values as dots; (B) dFe difference between the *VS* run and the *Hydro* run (100 years)

water is advected from the north; 5) Close to Bermuda a dFe increase between 1000 m and 2000 m is observed in correspondence of sedimentary dFe-rich water transported from the Upper Labrador Sea; 6) Extremely high dFe concentrations are found over and around the hydrothermal vents on the Mid Atlantic Ridge.

These features and processes are not well represented in our *Standard* run (Fig. 5.8B): 1) The dFe concentrations at the surface are overestimated; 2) Only a much weaker dFe subsurface minimum is found; 3) No dFe maximum is reproduced close to Cap Verde between

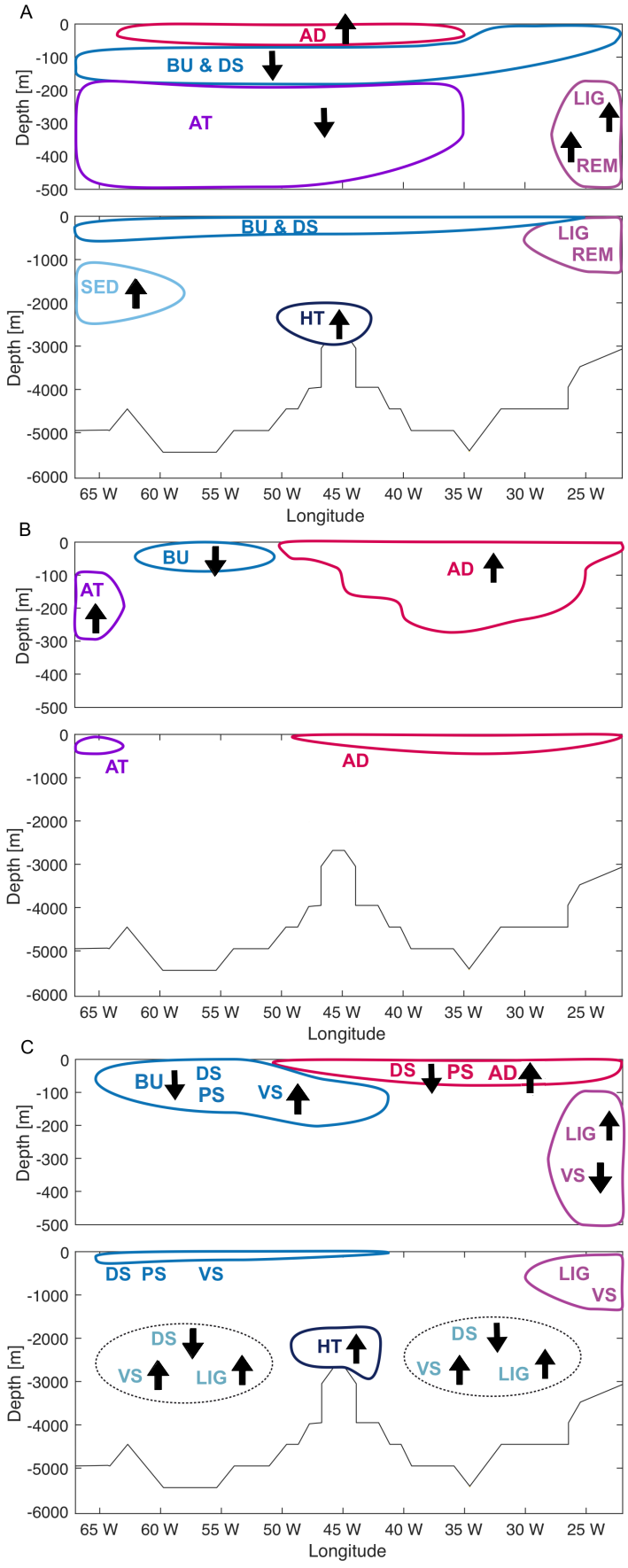

FIGURE 5.8: Pattern of dFe in the observations (A), in the *Standard* run (B) and in the *Hydro* run (C). The most important processes influencing the dFe distribution are: AD = Aeolian Deposition; HT = Hydrothermal input; BU = Biological Uptake; DS = Dust Scavenging; LIG = Ligand binding; REM = Remineralisation; SED = Sedimentary input; AT = Advective Transport; PS = Phytoplankton Scavenging; VS = Sinking Velocity. The arrows indicate whether the process is a source or a sink of dFe.

200 m and 1000 m; 4) Close to Bermuda, between 100 m and 300 m, the model features dFe-rich water advected from the south; 5) The model does not reproduce the dFe variability in the intermediate and deep ocean, as below 500 m the dFe concentration is almost constant.

The steps undertaken in this study to improve the understanding of key processes as well as the model-data agreement are: including scavenging by both lithogenic particles and phytoplankton (5.2.2, 5.2.4); keeping remineralised dFe in solution by moving from a constant ligand distribution to one which has higher ligand concentration in the OMZ (5.2.3); deepening the Fe remineralisation by accelerated sinking of biogenic particles (5.2.5); considering the hydrothermal dFe source (5.2.6).

The final model set up describes the dFe distribution in the Subtropical North Atlantic more realistically (Fig. 5.8C). The dFe surface concentration is mainly regulated by dust and phytoplankton scavenging, with the major effect under the dust plume. The effect of phytoplankton scavenging is widespread and generates a subsurface dFe minimum. Relating ligand concentration to AOU increases the dFe concentration mostly east of 26°W. Even though the dFe values shown here are too high compared to the observations (Fig. 5.4), with this parametrisation of ligands, we are able to reproduce the local vertical maximum. Increasing the sinking velocity of the biogenic particles, the remineralisation source of dFe is shifted towards depth with a decrease of dFe concentration between 100 m and 1000 m and an increase below. At depth, the scavenging on dust introduces longitudinal structure which is somewhat mitigated by a gradient in ligand concentrations. The local hydrothermal input leads to high concentrations above the vent, even though not as high as in the measurements.

While Fig. 5.8A, B and C show the qualitative effects of each new process on the dFe distribution, a more quantitative approach is given in the supplement in Section 5.5.1 and Fig. 5.12.

5.3.1 Statistical assessment

We examined the Pearson correlation between the observed and modelled dFe at the same locations in the initial *Standard* run and the final *Hydro* run (Table 5.2). Taking into account the entire water column along GA03, the correlation coefficient between modelled and observed dFe is R = -0.26 in the *Standard* run and it improved to R = 0.25 in the *Hydro* run. The mean bias against observations is reduced from 0.39 nmol L^{-1} to 0.11 nmol L^{-1}.

To better analyse the local effects of the processes, we split the section into six sectors by considering an east and a west basin (east and west of 45°W), and by defining three depth layers, being D1 from the surface to 200 m, D2 from 200 m to 1000 m and D3 from 1000 m to the sea floor. In each sector, the biases are notably reduced by 46% to 99%, indicating that the model output of the *Hydro* run is much closer to the observations than the initial *Standard* run. The smallest biases are found in both basins below 1000 m, indicating that the model now produces a realistic deep east-west gradient. Almost all correlation coefficients increase, in some cases however just moving from an anticorrelation to no correlation. The D2 depth stratum in the east basin shows the highest correlation (R = 0.76) due the new ligand parameterisation, followed by D1 in the east basin with R = 0.45. The improvement in the deep layer was obtained by examining the effect of scavenging on dust at depth, which first introduced an inter-basin gradient. Additionally, considering the hydrothermal dFe input enabled a better agreement around 45°W. Here, the relative standard deviation ($\sigma(obs)/\sigma(mod)$) in the east and west basin is reduced in the *Hydro* run by 82% and 68%, respectively, pointing out that the solution for the too homogenous dFe distribution in the model has come closer.

Sector	Bias *Standard*	Bias *Hydro*	R *Standard*	R *Hydro*
ALL	0.39	0.11	-0.26	0.25
W D1	0.52	0.09	0.54	0.45
E D1	1.17	0.40	-0.16	0.17
W D2	0.46	0.25	-0.75	0.15
E D2	0.21	0.06	-0.14	0.76
W D3	0.17	0.002	- 0.26	0.30
E D3	0.27	0.03	-0.46	-0.20

TABLE 5.2: Model Statistics: Bias (nmol L^{-1}) and correlation coefficient (R) between the observed and modelled dFe in the *Standard* run and the *Hydro* run. W = West of 45°W, E = East of 45°W, D1 = 0 - 200 m, D2 = 200 - 1000 m, D3 = 1000 - 6000 m

5.3.2 Surface dFe

Saharan dust outbreaks occur episodically and their trajectories change with the seasonal and latitudinal fluctuation of the Intertropical Convergence Zone (Chiapello et al., 1995), affecting surface dFe concentration. Available measurements (Tagliabue et al., 2012; Schlitzer et al., 2018) between 10°N and 40°N (Fig. 5.14 in the supplement in Section 5.5.1) show strong variability, both with longitudinal location and the month of sampling (Fig. 5.9). The data were compared to dFe output from the *Standard* run, the *Dust* run and the *Scav Phyto 2* run, those runs which have shown to mostly affect the surface concentration. In each run, we considered the monthly dFe minimum and maximum within the latitude band from 10 to 40°N. The observations should lay in the range of latitudinal-temporal variability defined by the minimum and maximum modelled dFe.

The *Standard* run maximum (Fig. 5.9) has low dFe values at the American coast, an increase in the open ocean, a decrease around ca. 23°W and very high dFe value between 20°W and the African continent.

The effect of dust scavenging (*Dust* run) depends on the relative amount of biogenic and lithogenic particles. Close to the American coast the biological productivity is comparatively high and dust deposition is small, thus the *Dust* run reduces dFe by only 15% (Fig. 5.9). The dFe concentration in the subtropical gyre between 25°W and 65°W, where biology is weak, is reduced by 45% and the maximum east of 20°W, where productivity and dust deposition are both high, is reduced by 25% .

Adding variable ligands and scavenging on phytoplankton (*Scav Phyto 2* run) (Fig. 5.9), further scales down the maximum dFe concentration in the region by 14% in the west, 32% in the centre and 13% in the east, where scavenging is 10% less than in the centre.

The monthly minima do not differ much in the three model runs.

Both changes bring the model much closer to the measured surface values, even though the model still overestimates the dFe concentration directly under the Saharan dust plume. A reason could be that our model does not include a direct removal of dFe via 'colloidal pumping' (Honeyman and Santschi, 1989), i.e. the fast aggregation of colloidal particles with larger particles. Aerosol Fe is predominantly released into the colloidal size fraction (Section 5.1.1) (Fitzsimmons et al., 2015a). Therefore, we could be missing an important loss process of dFe. Furthermore, in our model, the input from dust deposition is calculated with an uniform solubility of 2%, while it has been shown that Saharan's dust solubility is smaller because of its mineralogy and small anthropogenic contribution (Bonnet and Guieu, 2004). Considering a variable solubility in the model might further improve the model-data agreement.

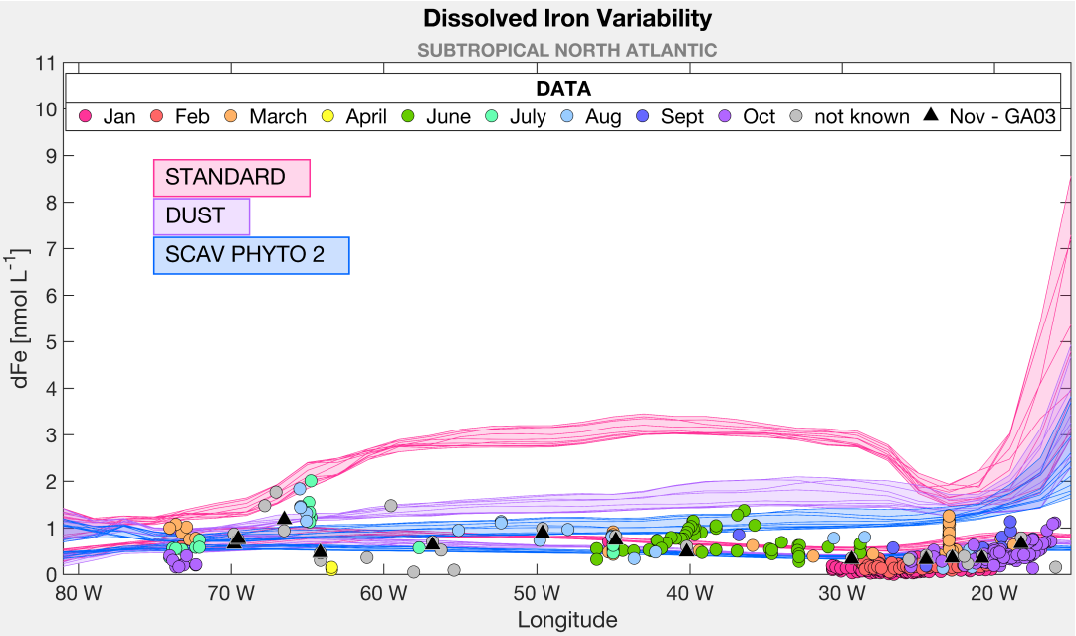

FIGURE 5.9: Latitudinal-temporal variability of observed and modelled surface dFe. For each model run (*Standard*, *Dust* and *Scav Phyto 2*) 12 lines represent the monthly maximum and further 12 lines represent the monthly minimum.

5.3.3 Subsurface dFe

The GA03 exhibits very low subsurface dFe concentrations at depths between 100 m and 200 m and extending to 700 m in the western basin, implying a remarkably strong dFe sink which draws down almost all dFe deposited at the surface. The decrease of dFe to low concentrations between 30 m and 70 m is associated with the DCM and is explained by removal mechanism as a strong biological uptake and scavenging on phytoplankton (and maybe colloidal aggregation which however is not included in our model). Below the DCM we would expect an increase in dFe, however, west of 35°W the dFe concentrations remain low until ca. 700 m. Bergquist and Boyle (2006) point out this broad dFe minimum to be characteristic for dFe profiles in the North Atlantic subtropical gyre and to be enclosed in a pycnocline as deep as 700 m. Jenkins et al. (2015) show that the thermocline waters in the GA03 section lie between the winter mixed layer and the density boundary $\sigma_0 = 27\,\mathrm{kg\,m^{-3}}$, which separates them from the intermediate water masses. The σ_0 density boundary lies roughly between 600 - 800 m. Along the section, 90% of the thermocline waters' end member water types consists of the North Atlantic Central Waters. At the outcrop of this water (ca. 40°N) (Tchernia, 1980) dust deposition is lower, and therefore water masses have potentially lower surface dFe values. This water then spreads along isopycnals towards the subtropics.

In the *Hydro* run (Fig. 5.7) the subsurface dFe minimum is present, however only extends to a depth of ca. 200 m. Below, dFe increases, instead of maintaining very low observed values. In the model, the isopycnal $\sigma_0 = 27\,\mathrm{kg\,m^{-3}}$ along GA03 is found at similar depths as in Jenkins et al. (2015), thus the modelled water mass is formed approximately at the same latitude as the observed. Despite the dust deposition in the North Atlantic is relatively low in the model, the modelled dFe concentrations north of GA03 section along the isopycnal (Fig. 5.10) are too high compared to the observed values along GA02 (Rijkenberg et al., 2014). Most likely this is due to a surface northward advective transport from the subtropical gyre characterised by too high dFe under the dust plume. Other explanation could be a

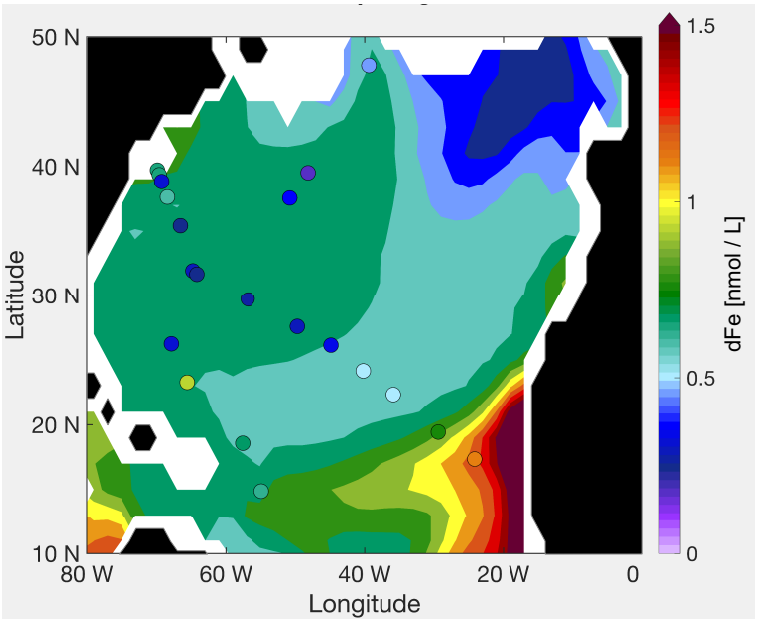

FIGURE 5.10: Modelled and observed dFe concentration along the isopycnal $\sigma_0 = 27\,\mathrm{kg\,m^{-3}}$

still too shallow remineralisation, a too low consumption by phytoplankton and higher Fe:C. The first was tested in the *VS* run and the latter is discussed in Section 5.5.2. Fitzsimmons, Zhang, and Boyle (2013) derived Fe:C rations ranging between 9.6 - 12.4 μmol/mol, which agrees with previous findings by Bergquist and Boyle (2006) (11 μmol/mol). The enriched Fe:C ratio in the tropical North Atlantic could reflect "luxury uptake" by phytoplankton, thus the storage of dFe for future dFe-poor times (Fitzsimmons, Zhang, and Boyle, 2013). By any means, the southward transport of these water masses along the isopycnal leads to an overestimation of the subsurface dFe concentration in our model.

5.3.4 Intermediate and deep dFe

In the intermediate and deep waters, the dFe concentration is determined by remineralisation, ligand concentration, transported water enriched with sedimentary dFe and hydrothermal dFe input. Additionally, we observed that scavenging on lithogenic particles, which has mostly be analysed in relation to surface dFe distribution (Ye and Völker, 2017), also has a great effect at depth. Indeed, in the *Dust* run, the very homogenous dFe concentrations below 1000 m in the *Standard* run are replaced by an inter-basin gradient. Scavenging at depth is smaller than at the surface right under the dust plume, however the relative change is maximal in the deep waters in the east basin. Here, the dFe decreases by three orders of magnitude because considering both organic and lithogenic particles, we have now 8000 times more mass available in the deep ocean for the dFe to scavenge on. As a consequence, the produced dFe concentrations in the deep east basin are too low compared to the observations (Fig. 5.3). In the *AOU-Lig* run and the *VS* run we observe how additional ligands and fewer particles at depth, respectively counteracted this trend. 1) While being able to reproduce the dFe vertical maximum close to Cape Verde is not new, the combined effect of a AOU based ligand distribution and the scavenging on lithogenic particles on the dFe distribution at depth was not yet addressed. As a matter of fact, in the *AOU-Lig* run the higher ligand concentration in the deep east basin compared to the deep west basis, partially compensate the too strong east-west gradient produced by dust scavenging. 2) An interesting side effect in the *VS* run is

that fewer dust particles are found in the deep ocean. In fact, dust particles either sink slowly on their own or they aggregate with biological particles and sink with them, faster. When we increase the sinking velocity of detritus, its concentration near the surface decreases. Consequently, there is less aggregation. The existing large lithogenic aggregates sink faster out of the water column, reducing the amount of small particles released by disaggregation at depth. This has repercussions on scavenging and remineralisation.

In conclusion, we observe that in this study the dFe cycle in the deep Atlantic shifted from being similarly influenced by remineralisation and scavenging in the initial *Standard* run to a dominance of scavenging in the final *Hydro* run. In Fig. 5.12 (supplement in Section 5.5.1) WD3 and ED3 we observe that in the *Standard* run the integrated release of dFe from remineralisation and the integrated loss of dFe by scavenging are of the same order of magnitude in both basins. On the other hand, in the *Hydro* run, while remineralisation remained of similar strength, the scavenging loss increased drastically. This relative increase was more pronounced in the east basin (ED3) compared to the west basin (WD3), leading to lower dFe concentrations in the east, thus to an inter-basin dFe gradient.

In Section 5.2.6 we mentioned that switching on the hydrothermal dFe source for 1000 years results in a distortion of the dFe distribution at depth. An additional preformed dFe signal transported from the Southern Ocean and the Indian Ocean induces a general increase of dFe concentration below 500 m. This increase of dFe is the result of the interaction of ligands and hydrothermalism in other regions of the global ocean. In our model, hydrothermal dFe is stabilised through the ligands parameterised from AOU. As the iron-binding ligands released by remineralisation are themselves prone to bacterial drawdown, the relationship between ligands and AOU is expected to be different in younger and older waters (like in the deep Atlantic and Pacific, respectively) since in younger waters the ligands have not yet been degraded. Thus, as mentioned before, the ligand parametrisation used here is only applicable to the Atlantic Ocean as it gives too high concentrations in the deep Pacific Ocean. This leads to a too strong stabilization of hydrothermal dFe in the Pacific, which affects the dFe distribution globally after too long model integration. Since the dFe distribution in other ocean basins is beyond the scope of this regional study, we just acknowledge this bias.

5.4 Conclusion

In this paper, we explain step by step which main processes are influencing the dFe distribution in the Subtropical North Atlantic, a region characterised by high dust deposition. The model outputs were compared to the dFe values obtained along GEOTRACES GA03 cruise (Sedwick et al., 2015). Starting from a fairly standard set of parameters, including new processes and parameterisations, we found out that several processes can explain the main features, thus supporting their importance in the regional dFe distribution. This helps to better reproduce the observations along the GA03 cruise. Scavenging on dust reduces the excess dFe at the surface and produces a deep east-west gradient, replacing the homogeneous deep dFe concentration. Together with scavenging on biomass, it also strengthens the shallow dFe minimum below the mixed layer. A non-constant ligand distribution generates the high dFe values in the upper 1000 m west of Cap Verde. Faster sinking particles deepen the remineralisation maximum affecting dFe concentration throughout the water column. A hydrothermal signal was included for completeness. Though the model refinements clearly improve the agreement between modelled and observed dFe distribution, further work is required in the development of the model.

As a consequence of the complexity of the Fe cycle, models designed for capturing the main features of the global dFe distribution, may fail to reproduce regional features. The

processes at play in the Fe cycle influence each other in a way that the system is highly non-linear, i.e. the changes in dFe caused by changes in different process parameterisations do not add linearly. This makes a full parameter-tuning exercise very difficult, explaining why our initial attempt to use the linear approach of the Green's function like in Menemenlis and Wunsch (1997), had no success. One possibility might be to use data assimilation methods, such as the adjoint method. This method has been applied to the oceanic iron cycle in steady state by Frants et al. (2016), but requires a construction of the adjoint of the model equation. Another possible solution is to work on regional scales.

This process-oriented regional study is possible thanks to field work performed in the area. With data from other regions becoming available, the global validity of processes and parameterisations considered here can be assessed for future development of dFe biogeochemical models.

Acknowledgements

We thank the editor and three anonymous reviewers for their helpful and constructive suggestions for improvement of the manuscript. We thank Peter Sedwick for publishing dFe data from the GEOTRACES cruise GA03. Work presented here was made possible through the PalMod project, funded by the German Federal Ministry for Education and Research under the grant number 01LP1505C.

5.5 Supplementary material

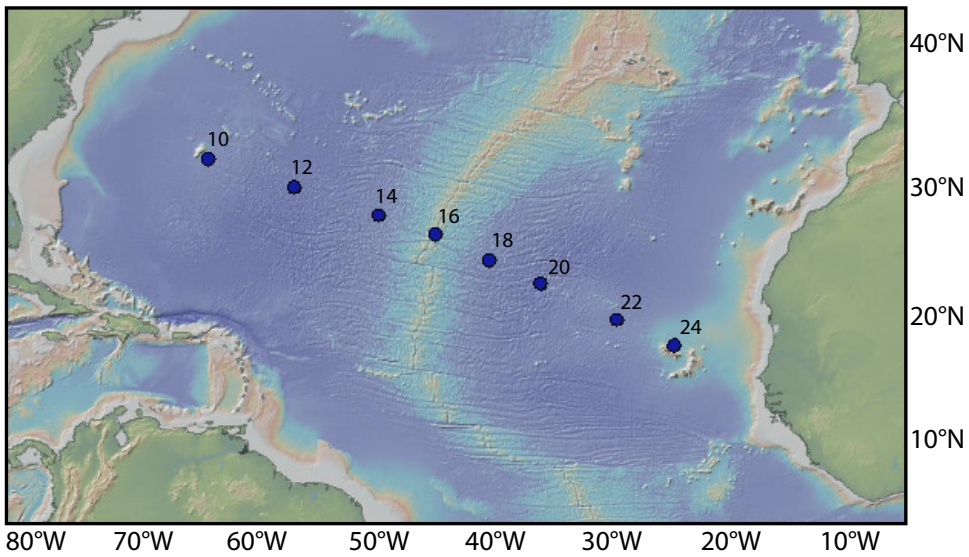

FIGURE 5.11: GA03 stations considered in this study

5.5.1 Remineralisation, scavenging and biological uptake

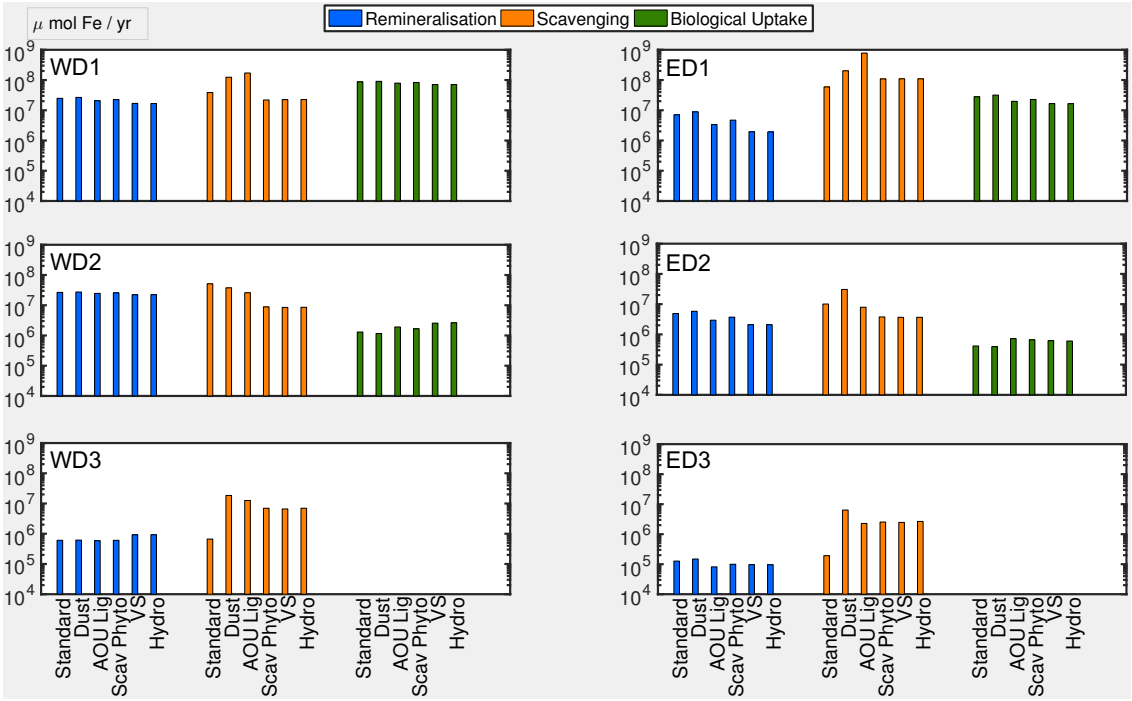

FIGURE 5.12: The integral amount of dFe lost by scavenging and biological uptake and gained by remineralisation in each model run in the six boxes along GA03. W = West of 45°W, E = East of 45°W, D1 = 0 - 200 m, D2 = 200 - 1000 m, D3 = 1000 - 6000 m

The transect of the GA03 was split up with the same criterion as in Section 5.1, thus in three depth layers, D1 from the surface to 200 m, D2 from 200 m to 1000 m and D3 from 1000 m to the sea floor, and in east and west basin (east and west of 45°W). The bars in Fig. 5.12 in the supplement in Section 5.5.1 represent the integrated amount of dFe in μmol Fe yr^{-1} in each box and for each model run. Shown is the amount of dFe gained and lost through remineralisation and scavenging and biological uptake, respectively.

Looking at the west basin, the surface dFe concentration in both the initial *Standard* run and the final *Hydro* run is dominated by biological uptake. Between 200 - 1000 m, scavenging decreases and biological uptake increases from the *Standard* to the *Hydro* run.

In the east basin, the scavenging loss of dFe is most dominantly affecting the dFe cycle. At the surface, biological uptake decreases from the *Standard* to the *Hydro* run. Remineralisation decreases in the surface and intermediate layers from the initial to the final run due to increased particle flux. Below 2000 m, scavenging increases in both basins. The system shifts from being similarly influenced by remineralisation and scavenging (*Standard* run), to being predominantly driven by scavenging (*Hydro* run).

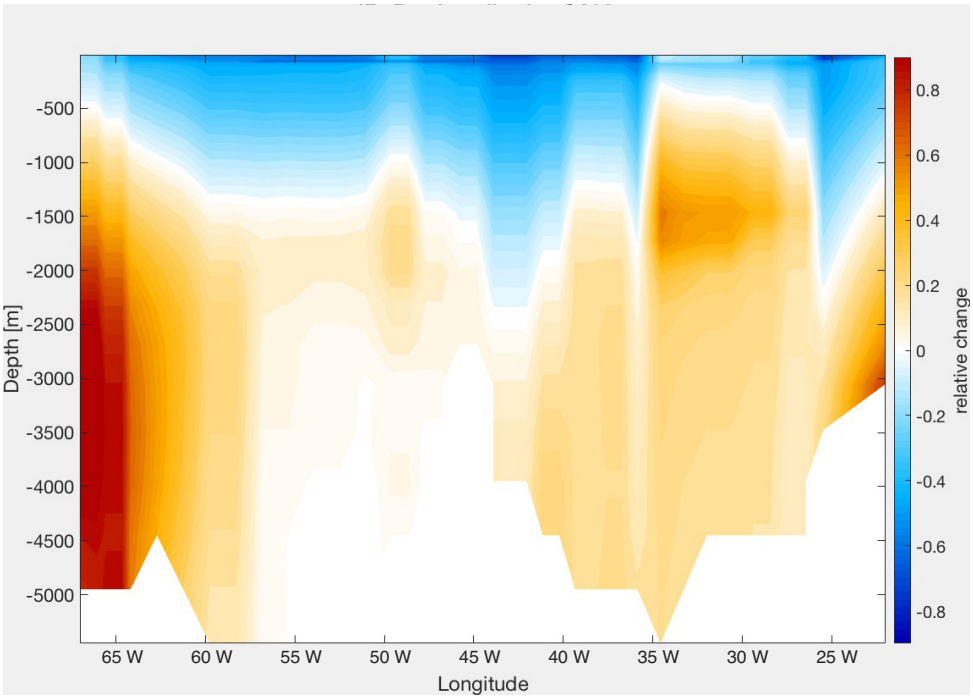

FIGURE 5.13: The relative difference of dFe remineralisation between the *Scav Phyto 2* run and the *VS* run

5.5.2 Fe:C

In the REcoM2 model the Fe:N is set to a constant value of 33 μmol/mol (equivalent to Fe:C 5 μmol/mol after Redfield C:N). Here, we tested the effect of a Fe:N of 66 μmol/mol (equivalent to Fe:C 10 μmol/mol after Redfield C:N).

At the surface the dFe concentration is reduced over a broad area (Fig. 5.15), resulted from an enhanced biological uptake of dFe. Thus this process could be a candidate for explaining the low dFe concentration at the surface. However, we notice a drastic worsening below the thermocline, at depth between 300 m and 800 m, since the remineralisation releases dFe proportionally to DIN with a higher Fe:N ratio. This depicts that what has been additionally removed from the surface is released below by remineralisation and respiration.

Consequently, even though the agreement between model and observations is improving at the surface and shallow subsurface, a maximum of dFe is modelled in the intermediate waters which disagrees with observations. A thorough study of the effects of changing Fe:C or Fe:N ratios would require the implementation of a physiological dependency of Fe:C, like in Buitenhuis and Geider (2010)

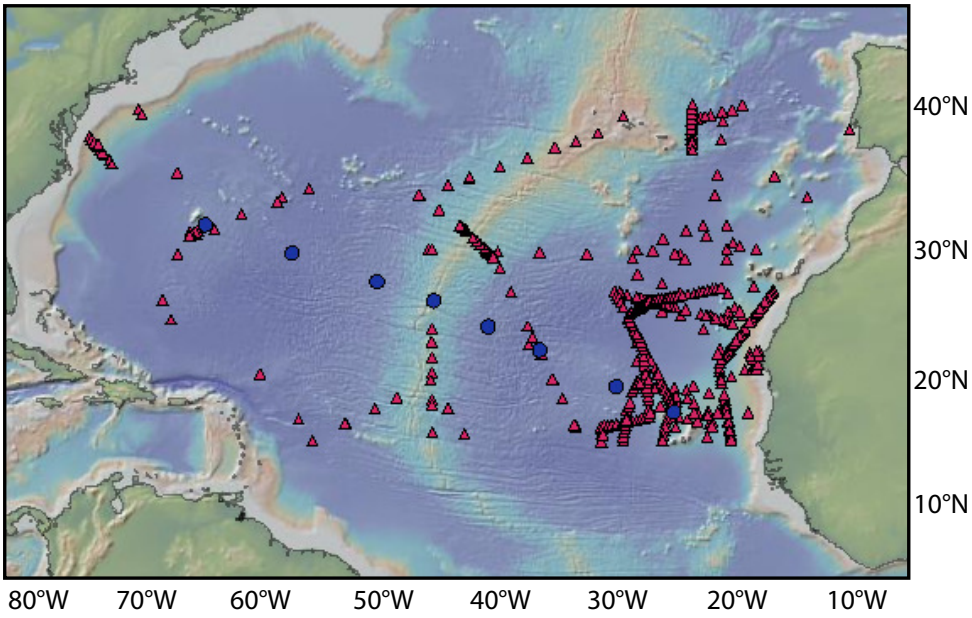

FIGURE 5.14: dFe surface observations in the Subtropical North Atlantic discussed in Section 5.3.2

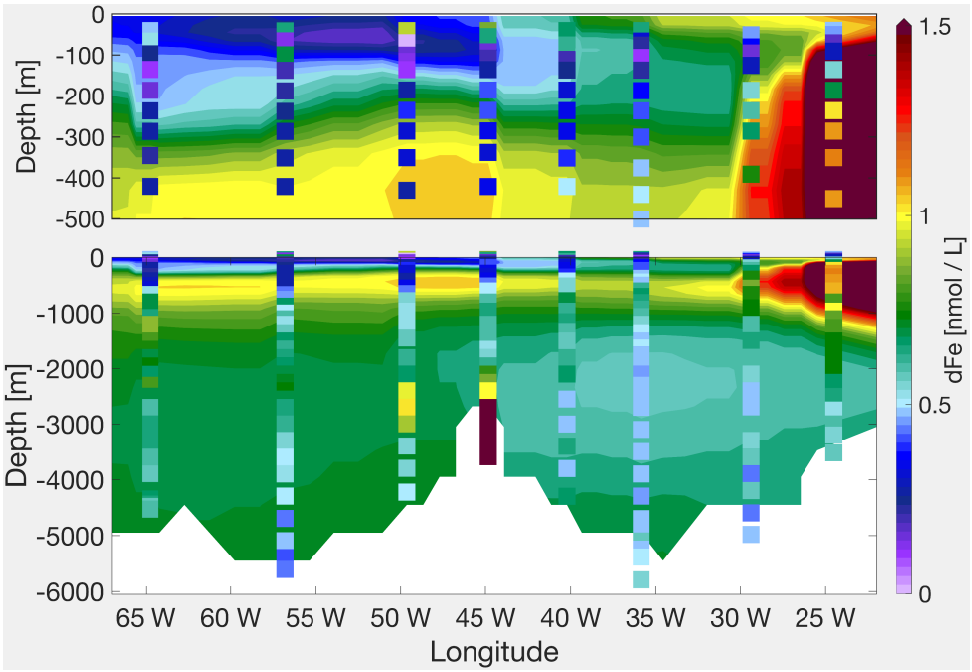

FIGURE 5.15: Modelled dFe along GA03 when doubling the Fe:N ratio, with measured dFe values as dots

6 The role of icebergs in the Fe cycle

Abstract

Several studies have found icebergs to be sources of bioavailable iron to the Southern Ocean which are at least regionally important. Thus it is essential to include them in the modelling of the marine Fe cycle. We present a sensitivity study on the strength of the iceberg dFe source, using a new model-generated data set on iceberg meltwater flux, and discuss its impact on the biology of the Southern Ocean. The Fe fertilisation results in a reduction in the Si:N ratio in diatoms, as has already been observed in laboratory and field experiments. Faster growth of diatoms stimulates N uptake and photosynthesis but hardly changes, and even reduces Si uptake in some regions. Consequently, the Si:N export from the water column is reduced. A thought experiment can be done speculating on the effects of a warmer future climate, in which an increase in iceberg calving is predicted, on the productivity and export in the Southern Ocean.

6.1 Introduction

6.1.1 Iron in the Southern Ocean

The Southern Ocean (SO) is one of the largest HNLC (high-nutrient low-chlorophyll) regions in the world ocean, characterised by low concentration of dissolved iron (dFe), an essential micro-nutrient for phytoplankton. That phytoplankton growth in the SO is restricted due to Fe limitation was shown by the comparatively stronger growth in naturally Fe fertilised regions (e.g. Blain, Sarthou, and Laan, 2008), in shipboard bottle enrichment experiments (e.g. Martin et al., 1994; de Baar et al., 1999) and in situ mesoscale Fe enrichment experiments (e.g. Boyd et al., 2000; Smetacek et al., 2012), as well as in many laboratory incubation experiments (e.g. Marchetti et al., 2006; Schuback et al., 2015; Koch et al., 2018).

Several sources of dFe contribute to the Fe budget of the SO like dust deposition, sedimentary dFe, sea ice, icebergs and dFe in deep water upwelling (Section 1.5). The aeolian Fe source is dominant north of the ACC (Antarctic Circumpolar Current), downwind of the arid continental region (Cassar et al., 2007; Tagliabue, Bopp, and Aumont, 2009), whereas, south of the ACC, where dFe is a limiting factor, this source is small compared to other sources as shelf sediments or icebergs (Lancelot et al., 2009). Indeed, continental-shelf sediments and sediment re-suspension are main sources of dFe in coastal regions of the SO (Johnson, Chavez, and Friederich, 1999; de Baar and de Jong, 2001; Borrione et al., 2014). This effect is propagated into the open ocean by lateral transport (Moore and Braucher, 2008). The Antarctic Peninsula (Dulaiova et al., 2009; Wadley, Jickells, and Heywood, 2014) and the Kerguelen Plateau in the Indian sector of the SO (Blain, Sarthou, and Laan, 2008; Bowie et al., 2015) are two well documented examples of large continental dFe input. Discharge of glacial meltwaters draining the Antarctic bedrock also contributes to the supply of terrigenous Fe-bearing material to the near-shore seawater (e.g. Statham, Skidmore, and Tranter, 2008). Furthermore, due to Ekman pumping caused by the strong westerly wind belt around Antarctica, the SO is an upwelling region where carbon and nutrients are brought up to the surface layer, thus upwelling of Fe-rich deep waters is one of the main dFe sources in the

open SO (de Baar et al., 1995). The higher dFe concentrations that reach the surface in upwelling regions, are partly fuelled by hydrothermal activity (Tagliabue et al., 2010). During winter ice formation, sea ice collects aeolian dust and incorporates dFe from sea water. During summer melt, bioavailable dFe is set free in the marginal ice zone (Sedwick and DiTullio, 1997; Lannuzel et al., 2008; Lannuzel et al., 2016), thus sea ice redistributes Fe geographically due to seasonality and ice motion. Also, icebergs are a mobile and episodic dFe source in the SO which transport Fe and other nutrients from the continent to HNLC regions (Smith et al., 2007; Lin et al., 2011; Duprat, Bigg, and Wilton, 2016; Raiswell et al., 2016). Further dFe sources are island-wake effects like those documented near Crozet Island (Pollard et al., 2009), South Georgia (Korb et al., 2008) and Kerguelen (Blain, Sarthou, and Laan, 2008), as well as extra-terrestrial dust (Johnson, 2001). The different sources of dFe in the SO show prominent geographical patterns. However, their strength and the extent of their contribution to the total pool of dFe in the region are still under discussion. Modelling studies have explored the relative weight of different dFe sources (Borrione et al., 2014; Death et al., 2014; Lancelot et al., 2009; Tagliabue, Bopp, and Aumont, 2009; Wadley, Jickells, and Heywood, 2014). Wadley, Jickells, and Heywood (2014) state that sediment-derived dFe mainly influences production in the SO, rather than icebergs or atmospheric dust with contributions of 89%, 11% and 0.3%, respectively. Also, model simulations by Lancelot et al. (2009) showed that 50 - 90% of chlorophyll *a* stimulation in austral summer could be traced back to dFe input from continental shelves. Second in order is the contribution of icebergs with 25%, while atmospheric deposition has little effect on the chlorophyll *a* at high latitudes. Though aeolian dFe accounts for the smallest part, it is much more effective at driving primary production compared to sedimentary and iceberg dFe (Wadley, Jickells, and Heywood, 2014). Raiswell et al. (2016) argued that the input of Fe to the SO from icebergs is 3.2 - 25 Gmol yr^{-1} compared to the 0.01 - 0.02 Gmol yr^{-1} from aeolian deposition.

6.1.2 The role of icebergs

Iceberg calving is estimated to currently cause a mass loss from the Antarctic ice sheet of ca. 1300 Gt yr^{-1} (Depoorter et al., 2013), contributing largely to the SO freshwater cycle. Large to giant icebergs first tend to drift in the counter-clockwise flow of the Antarctic Coastal Current westward along the Antarctic coast until they reach separation points in the Weddell Sea, in the Kerguelen Plateau and in the Ross Sea (Rackow et al., 2017). From here on their velocities have a north-eastward component and they can reach beyond 50°S. In the Weddell Sea this iceberg dense area is called Iceberg Alley (e.g. Schodlok et al., 2006). Smaller icebergs have a northward motion towards the open ocean everywhere around Antarctica until entering the ACC when they move eastwards. Icebergs undergo basal melting, lateral buoyant convection below the wave level due to temperature difference between ice and ocean, and lateral wave erosion (Gladstone, Bigg, and Nicholls, 2001; Rackow et al., 2017). A modelling challenge is to simulate the different iceberg size classes and the calving sites. The presence of smaller icebergs in one specific year is representative also for other years, while calving of giant icebergs is a rare and unpredictable event, and should thus be treated in models as a random process (Stern, Adcroft, and Sergienko, 2016).

It was shown that icebergs also play an important role in the supply of nutrients to the SO. Indeed, icebergs are substantial sources of terrigenous Fe to the SO (Raiswell et al., 2006; Raiswell et al., 2008; Smith et al., 2007), as revealed by elevated radium isotopes, a tracer of terrigenous material, in proximity of icebergs (Smith et al., 2007; Shaw et al., 2011). In his mineralogical analysis of iceberg-hosted sediments, Raiswell identified reactive Fe-bearing minerals like ferrihydrite and goethite and determined the bioavailability of the Fe present

(Raiswell et al., 2008; Raiswell, 2011; Shaw et al., 2011). These Fe-rich minerals are concerted as nanoparticulate clusters in the ice transported by icebergs from the coastal region towards the open ocean. They present a bioavailable Fe source to the pelagic community when icebergs melt (Raiswell et al., 2008). Iceberg calving, however, occurs in different geographical and geological regions of Antarctica, resulting in different Fe and nutrient characteristics and making it difficult to quantify a mean supply of bioavailable Fe (Duprat, Bigg, and Wilton, 2016; Hopwood et al., 2017). Löscher et al. (1997) found the Fe content in the glacial ice from an icebergs to be 20.4 nM and Lin et al. (2011) measured Fe concentrations in ice following large icebergs ranging between 4 and 600 nM. However, the highest concentrations were reported by Raiswell et al. (2016). They detected that 0.076 wt.% of the sediment load in icebergs is extractable Fe and thus, based on a poorly constrained concentration of sediments in icebergs (ca. 0.5 g L^{-1}), the Fe content in icebergs is of averagely 6700 nM. The highly variable Fe content in the ice of icebergs leads to a spatially heterogeneous environment around different icebergs. However, the number of studies focusing on which sediments are enclosed in icebergs and their fraction of bioavailable Fe, is limited. Additionally, an important open question concerns the relative amount of released Fe which is immediately lost e.g. by reprecipitation or scavenging and the fraction which actually becomes bioavailable.

Still, the bioavailable dFe in icebergs has been shown to be sufficient to influence the Fe cycle in the SO. Several studies have reported high chlorophyll concentrations and primary production in proximity of free-drifting icebergs. Smith et al. (2007) observed a correlation between icebergs and hot spots of biological activity in the Weddell Sea and suggested this enhanced productivity to be a consequence of dFe enrichment from terrigenous debris. Duprat, Bigg, and Wilton (2016) showed from satellite data that the primary production increased within a few kilometres from an iceberg. Higher dFe in the water leads to enriched diatom concentration near the iceberg (Cefarelli, Vernet, and Ferrario, 2011). Furthermore, a phytoplankton bloom following an iceberg brings changes in the food web at many tropic levels. For example, while the zooplankton species composition does not change, the biomass increases near the ice face (Sherlock et al., 2011), increasing the grazing pressure on phytoplankton (Vernet et al., 2011). Expansive krill swarms and consequent effects on top marine predators, as well as seabirds have also been observed in the proximity of icebergs (Smith et al., 2007).

Future climate simulations predict that higher temperatures in West Antarctica and the Antarctic Peninsula will lead to retreating glaciers and increasing iceberg calving especially in the Weddell and in the Ross Seas (Rignot et al., 2008; Smith, 2011, and references therein). The additional dFe supplied by icebergs to the seawater could stimulate productivity in the SO in the coming years and consequently enhance the carbon export. More frequent iceberg calving could thus provide a negative feedback effect on rising atmospheric CO_2 concentrations (Jickells et al., 2005; Raiswell et al., 2008). The dFe input from icebergs has been long neglected in global biogeochemical models, as it is the case in all models participating in the FeMIP exercise (Tagliabue et al., 2016). However, even though the uncertainties of the dFe flux from icebergs to the seawater and the impact on the SO productivity are still very large, for past and future climate simulations, the dFe input from icebergs should not be overlooked any longer.

In this chapter, we use the climatology by Rackow et al. (2017) which includes the contribution of large icebergs, which have previously been ignored to model the supply of dFe by icebergs in the SO. dFe fluxes of different strength were simulated with the aim to detect the effect on small phytoplankton and diatoms. Particular interest was put in the export of C, N and Si. The goal is not to reproduce the supply of dFe since this is also quite difficult due to scarcity of available data, but to perform experiments on the biological response in a range of scenarios ranging from small to extreme dFe input from iceberg meltwater.

6.2 Model experiments

For the study presented in this chapter, we implemented a simple representation of the dFe source from icebergs in the biogeochemical model REcoM2. We used the seasonal climatology of freshwater flux from icebergs in the SO by Rackow et al. (2017), who implemented a global ocean-sea ice model with an iceberg drift and decay model around Antarctica into the Finite-Element Sea-Ice Ocean Model (FESOM). The iceberg model was initialised with almost 7000 observed icebergs during September/October 1997 compiled by Wesche and Dierking (2015). This data set provided both near-shore iceberg positions and sizes ranging from small to giant icebergs.

The dFe supply from melting icebergs to the SO was simulated in the model by combining the estimated icebergs' meltwater flux climatology by Rackow et al. (2017) with the dFe load in icebergs' sediments. However, since the concentration of bioavailable Fe in the icebergs' melt water is still under research and is subject to large uncertainties, we performed a sensitivity study in which this value was varied from 20 to 4000 nM. The sensitivity study starts from a ***Control*** model run, which includes dust and sediments as external dFe sources and has a constant ligand concentration in seawater of 1 μmol m^{-3}. This *Control* experiment neglects the dFe input from icebergs and will be used as reference in the following sensitivity study. Following that, we designed 8 model experiments with increasing concentrations of dFe in the meltwater of icebergs (20, 50, 100, 200, 500, 1000, 2000 and 4000 nM), called respectively ***20***, ***50***, ***100***, ***200***, ***500***, ***1000***, ***2000*** and ***4000*** runs. The *Control* model run was integrated for 900 years from a state of rest. Further 100 years were then simulated with no icebergs and with icebergs containing different amounts of soluble Fe. The modelled dFe concentrations are compared to available dFe observation in the upper 50 m of the ocean south of 50°S collected in Tagliabue et al. (2012) and Schlitzer et al. (2018).

From the Rackow et al. (2017) climatology, three major windmill-like iceberg alleys were simulated, one in the Weddell Sea, one near the Kerguelen Plateau (60 - 90°E) and one in the Ross Sea (180°E) (Fig. 6.1). In the Weddell Sea, the branch splits into two, the outer part corresponding to the iceberg alley drifting along the ACC and the inner part reaching 60°S. Including large icebergs leads to longer trajectories and more freshwater input at lower latitudes. The total integrated annual meltwater flux in the model is 1074 Gt yr^{-1}. The corresponding annual dFe input for concentrations of 20, 50, 100, 200, 500, 1000, 2000 and 4000 nM, amounts to 0.02, 0.05, 0.11, 0.21, 0.54, 1.07, 2.15 and 4.30 Gmol Fe yr^{-1}, respectively.

6.3 Results

Simulations including exclusively small icebergs show a strong seasonality in melting rates linked to seasonal sea ice extent which reduces the lateral wave erosion during winter (Merino et al., 2016; Rackow et al., 2017). The seasonality is successively reduced when larger icebergs are included in the model since basal melting is more important (Rackow et al., 2017). We therefore limit our analysis here to annual means of the different parameters.

6.3.1 Dissolved iron

Fig. 6.2A shows the annual mean dFe distribution averaged over the surface 50 m of the SO in the *Control* experiment. The dFe concentration close to the coast has concentrations of ca. 0.3 nmol L^{-1} decreasing towards lower latitudes. North of 60°S the dFe concentration approaches values below 0.05 nmol L^{-1}. At the tips of the Antarctic Peninsula and east of the south tip of Chile the dFe concentrations are elevated due to sedimentary input. Generally, the simulated dFe concentrations in the open ocean south of 50°S do qualitatively match

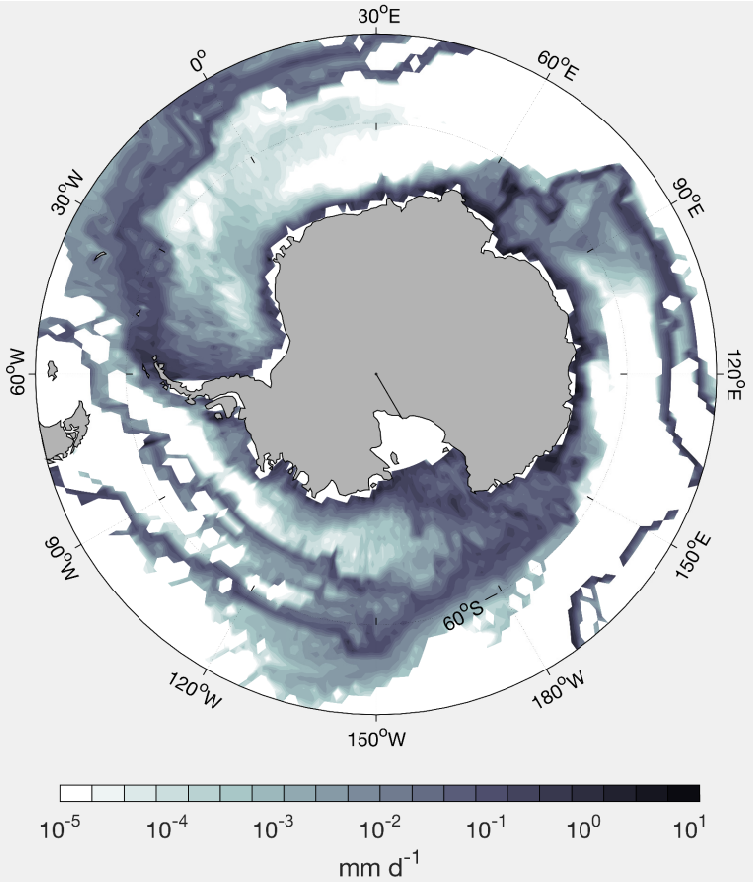

FIGURE 6.1: Annual mean freshwater input from icebergs (from Rackow et al. (2017))

the observations. However, higher measured values close to the Antarctic continent and in proximity of island are not reproduced by the model, as well as the higher concentrations over the Kerguelen Plateau in the Indian sector of the SO, resulting in no significant correlation between the model and the observations.

By adding dFe from icebergs, higher surface dFe concentrations are simulated all around the Antarctic coast (Fig. 6.2 - 6.3). Most noticeable are the dFe enhancements between 60°E and 150°E in the Cooperation, Davis, Mawson and D'Urville Seas, at 150°W in the east Ross Sea and at the tip of the Antarctic Peninsula. These anomalies are already seen in runs with relatively little additional dFe (Fig. 6.2B and Fig. 6.3A - run *20 - Control*; note that Fig. 6.3 presents the difference in dFe between one run and the previous in terms of strength of the dFe input). In the Cooperation Sea and the Somov Sea, a marked plume of high dFe concentrations expands until 60°S (Fig. 6.2C - D and Fig. 6.3C - run *500 - 100*). Very high dFe input from icebergs (run *1000* and *2000*) does further increase the dFe concentration in the coastal region but also stretches to off-shore areas at lower latitudes (Fig. 6.2E - F and Fig. 6.3D - E). The dFe increase patterns resembles the windmill-like icebergs trajectories set going in the Cooperation Sea, in the Somov and Ross Sea and in the west Weddell Sea along the Antarctic Peninsula (Fig. 6.3D - E - run *1000 - 500* and run *2000 - 1000*).

Accordingly, the spatial extent of the dFe anomalies becomes larger with increasing iceberg dFe source, reaching low latitudes in all Atlantic, Indian and Pacific sectors. Close to the continent (south of 63°S) the longitudinal variations of dFe are larger than in the outer open ocean region (north of 63°S) (Fig. 6.4). The largest variation between the experiments

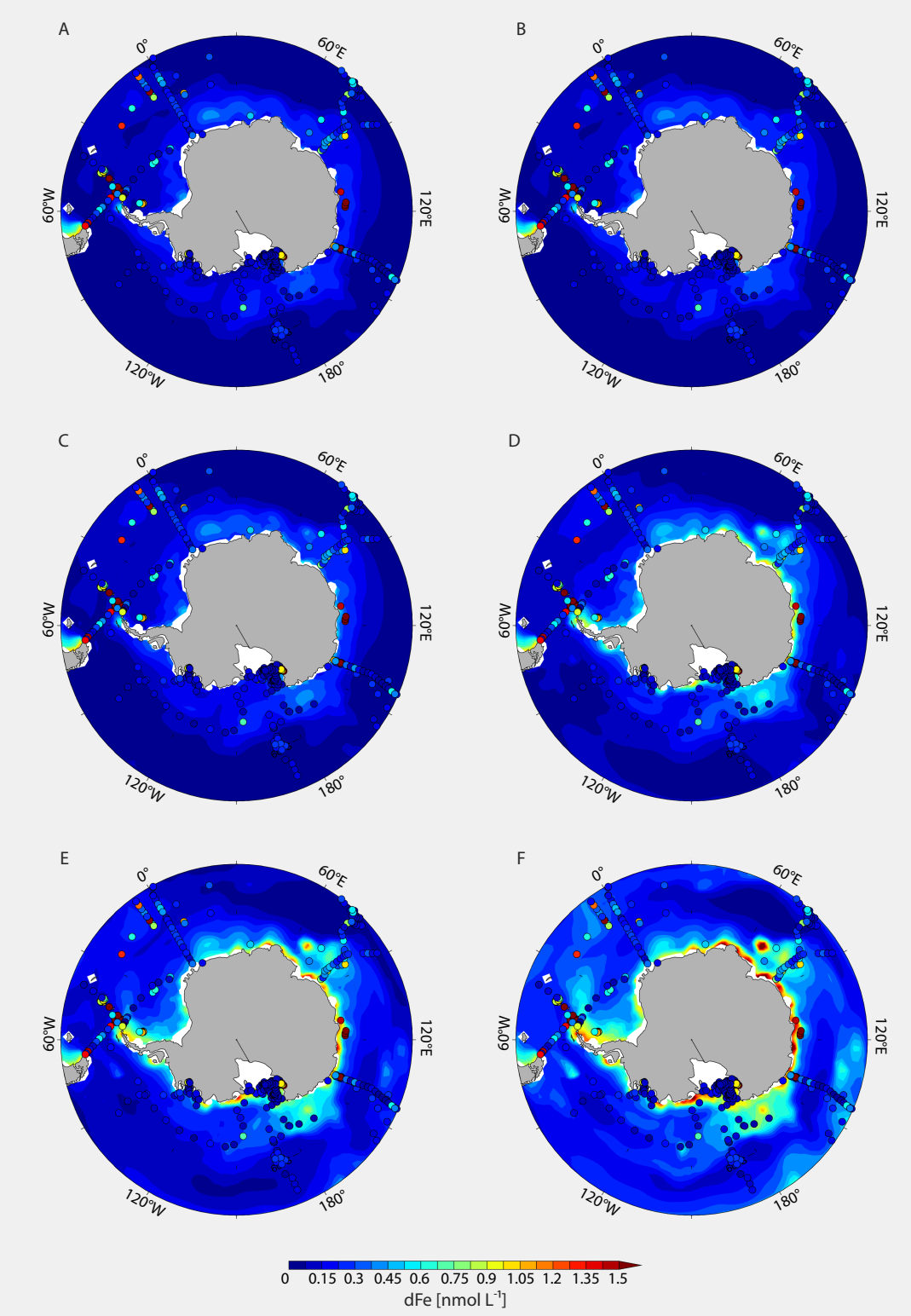

FIGURE 6.2: Modelled dFe in the surface 50 m south of 50°S with measured dFe values as dots: (A) *Control* run; (B) run *20*; (C) run *100*; (D) run *500*; (E) run *1000*; (F) run *2000*

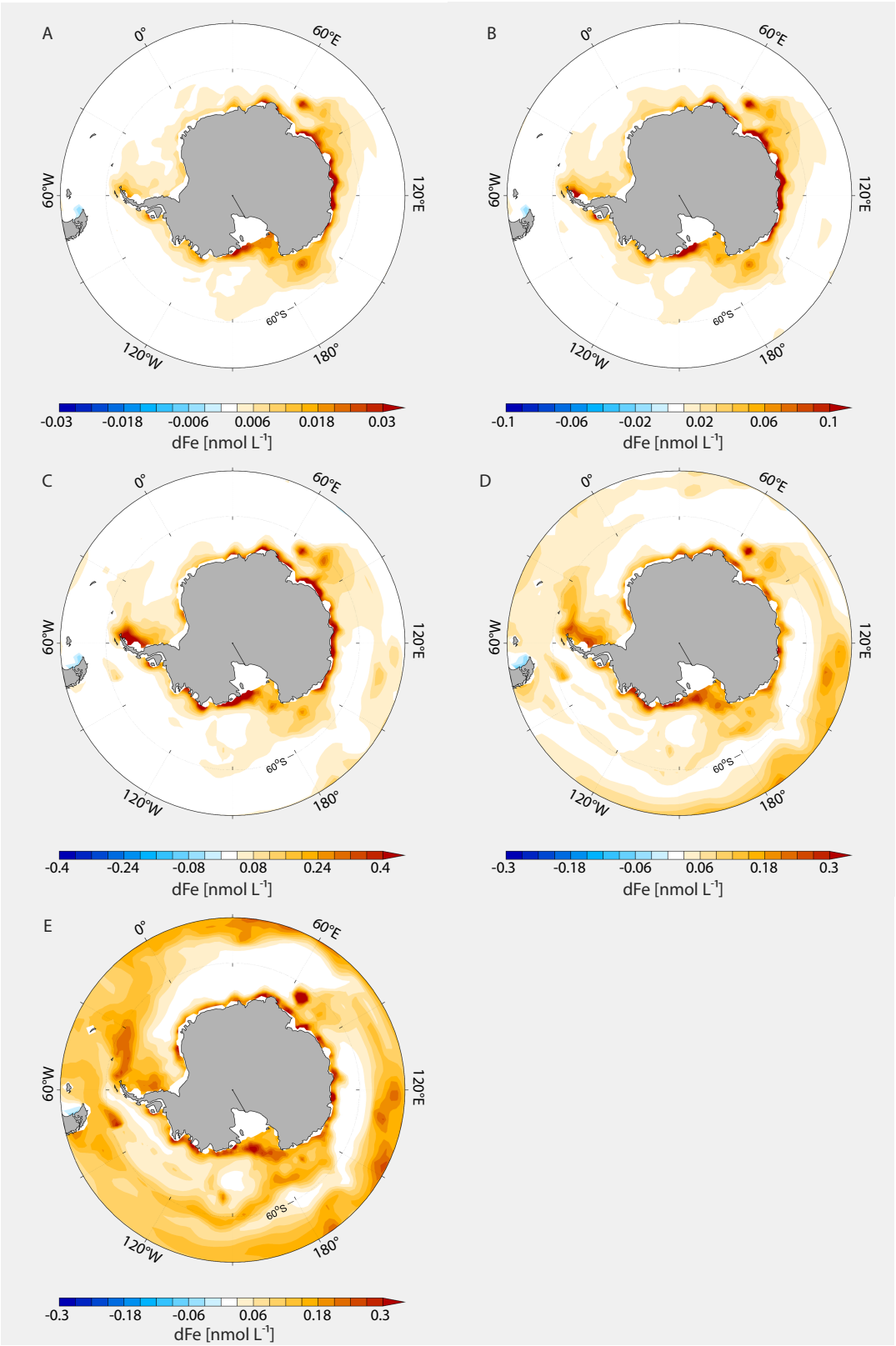

FIGURE 6.3: dFe differences between (A) run *20* - *Control* run; (B) run *100* - run *20*; (C) run *500* - run *100*; (D) run *1000* - run *500*; (E) run *2000* - run *1000*

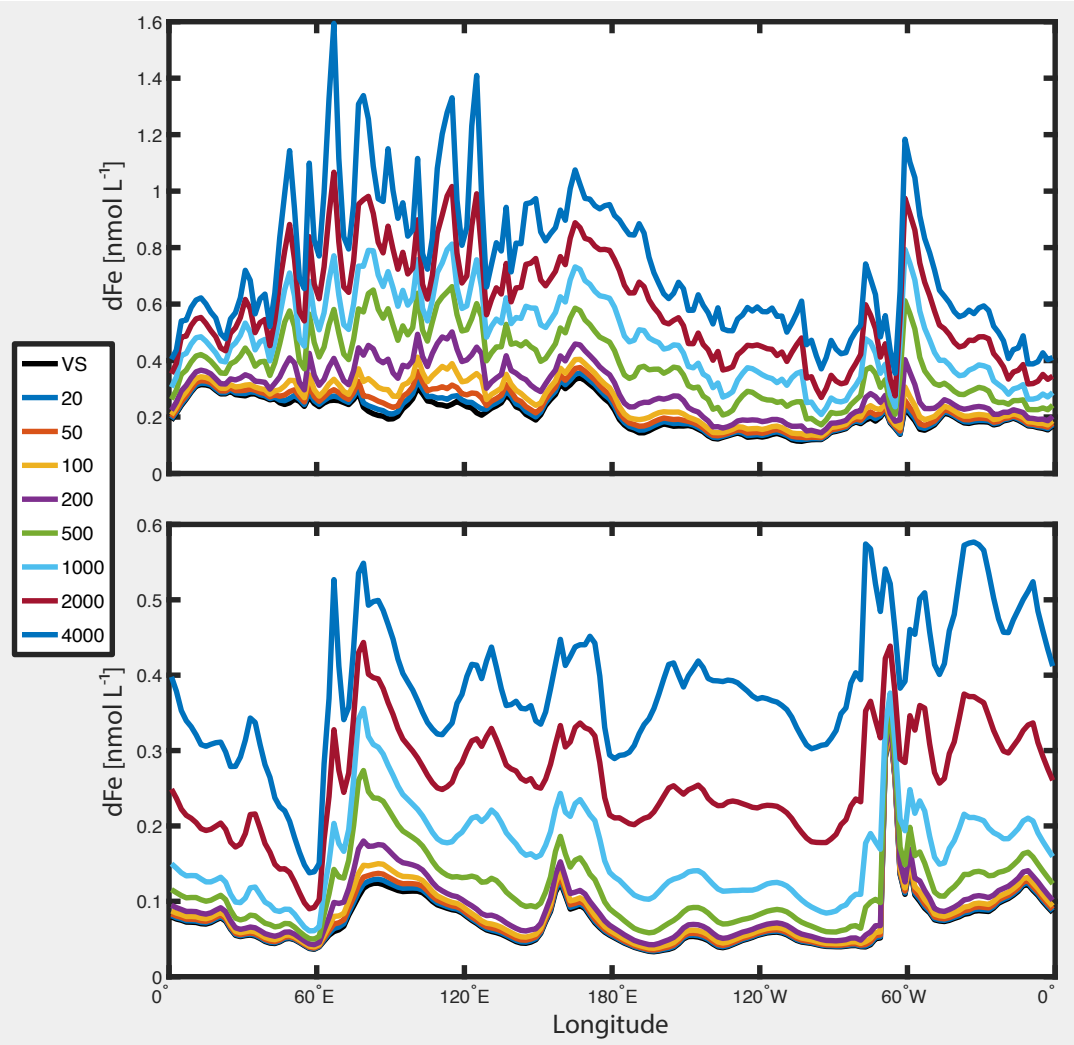

FIGURE 6.4: Integrated dFe (A) south of 63°S; (B) north of 63°S and south of 50°S

south of 63°S is observed between 60 - 180°E, thus in the Indian sector (Fig. 6.4A). Here, dFe concentration is highest. Differently, in the Pacific and Atlantic sectors between 180°E - 30°E, dFe is lower (almost half), with exception of 60°W where high dFe values are observed close to the Antarctic Peninsula (Fig. 6.4A). On the other hand, north of 63°S the Atlantic sector shows dFe concentrations as high as in the Indian, while the Pacific sector has less dFe (Fig. 6.4B). Also, at 60°W we observe high dFe concentrations, this time due to influence from the tip of Chile (Fig. 6.4B).

We notice that close to the Antarctic continent a relatively small contribution of icebergs to the dFe input is already sufficient to largely impact the dFe contribution. Indeed, south of 63°S (Fig. 6.4A), an input of 200 nmol L^{-1} significantly increases the dFe concentration. Most pronounced is the increase by ca. 100% in the Indian sector, while in the Pacific sector the dFe concentration increases by ca. 50% and in the Atlantic sector by ca. 25%. On the contrary, for the dFe concentration to change significantly in the northern part of the SO, a larger dFe input from icebergs is needed. North of 63°S (Fig. 6.4B), the same dFe input (i.e. 200 nmol L^{-1}) produces a more restrained enhancement of the dFe concentration (ca. 35% in the Indian sector and ca. 20% everywhere else). This matches the general pattern in which

small dFe input from icebergs mainly influences the coastal regions, while a larger contribution is needed to affect the open ocean.

While the correlation between modelled and measured dFe is close to zero for all runs, increasing the dFe release from icebergs has an impact on the bias. The bias in the *Control* and *50* runs is ca. -0.21 nmol L^{-1}, thus the model underestimates the observations. The smallest biases are found in the *500* and *1000* runs, -0.06 and 0.06 nmol L^{-1} respectively. Higher dFe inputs in the *2000* and *4000* runs lead to an overestimation of the observations with biases of 0.19 and 0.32 nmol L^{-1}, respectively.

6.3.2 Dissolved inorganic nitrogen

The *Control* run presents average concentrations of DIN of about 25 μmol N L^{-1} all around Antarctica (Fig. 6.5A). The concentration gradually decreases with reduced latitude. At 50°S the average concentration is 10 μmol N L^{-1}, with slightly higher values of 13 μmol N L^{-1} between 0 - 60°E. Adding a little dFe from icebergs first reduces the concentration of DIN at the coast between 60 - 150°E, 120 - 150°W and east of the Antarctic Peninsula by on average 4 μmol N L^{-1}. While a further increase in iceberg dFe does not lead to considerable additional changes in the coastal DIN concentrations, it varies the concentration north of 60°S. Indeed, with respect to the *Control* run, the concentration north of 60°S is reduced by 20 - 70%, 40 - 90% and 60 - 95% in the runs *500*, *1000* and *2000*, respectively (Fig. 6.5E). The consequence is a similar pattern of DIN around the Antarctic continent between the model runs, but with a much sharper gradient from high coastal to low off-shore concentrations. The addition of dFe from icebergs leads to an expansion of the region of N-limitation till south of 60°S in run *2000* (Fig. 6.5C).

6.3.3 Dissolved silicate

In the *Control* run, the Si concentration in seawater is generally high all around the Antarctic continent and low north of 60°S (Fig. 6.5B). The near-shore concentrations are heterogenous ranging between 13 and 63 μmol Si L^{-1}. The lowest values are found in the Cooperation and Davis Seas between 70 - 90°E and in the Amundsen Sea at 120°W - on average 20 μmol Si L^{-1}. In the Lazarev and Riiser-Larsen Seas between 0 and 30°E the concentrations are maximal with values up to 63 μmol Si L^{-1}. The west Ross Sea and the Somov Sea also show relatively high concentrations between 30 - 45 μmol Si L^{-1}. On the contrary, the east side of the Antarctic Peninsula has exceptionally low coastal Si concentrations between 4 - 7 μmol Si L^{-1}. North of 60°S, the Si concentration is generally lower than 8 μmol Si L^{-1}, with exception for a plume with average concentration of 10 μmol Si L^{-1} expanding from the Antarctic Peninsula towards the Antarctic Polar Front.

Fig. 6.5D - F represents the Si concentration in the run with high dFe input (*2000* run) and the difference of the latter with the *Control* run. In the subsequent steps taken by increasing the dFe input by icebergs, the Si concentration south of 60°S is only slightly affected by higher dFe input, with exception of the Weddell Sea. Here, Si increases by 25% and along the Antarctic Peninsula by 60%. North of 60°S, adding dFe from icebergs reduces the Si concentration everywhere. The Indian sector is affected the most and the already low Si concentrations are further reduced by 95%. Differently, the Si concentration in the Atlantic sector is reduced by averagely 40%.

6.3.4 Net primary production

In the *Control* run, the only regions with high total net primary production (NPP) - average 35 mmol m^{-2} d^{-1} - south of 50°S are the coastal regions east of Chile and the tip of the

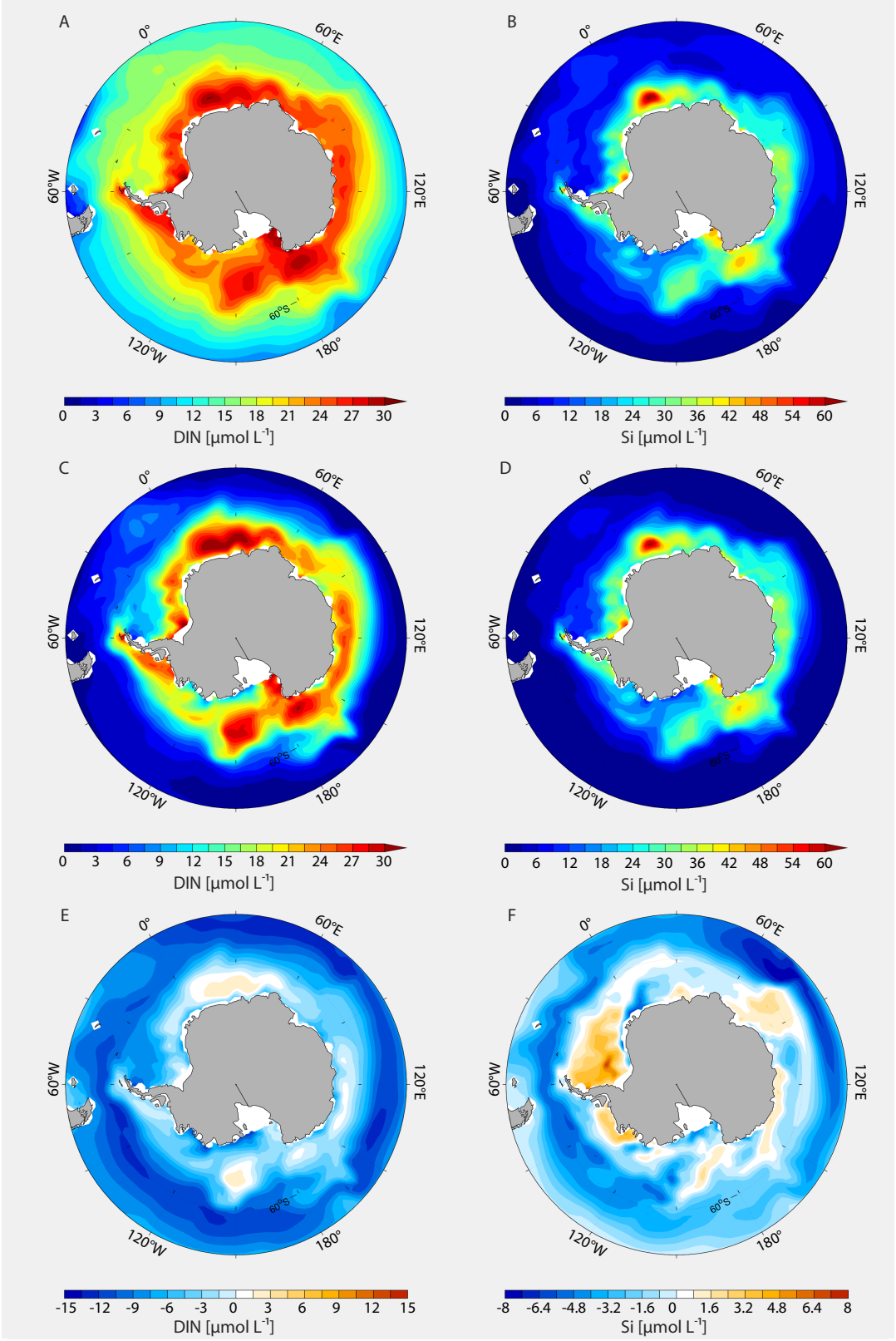

FIGURE 6.5: (A) DIN in the *Control* run; (B) Si in the *Control* run; (C) DIN in the run *2000*; (D) Si in the run *2000*; (E) DIN difference between run *2000* - run *Control*; (F) Si difference between run *2000* - run *Control* in the surface 50 m south of 50°S

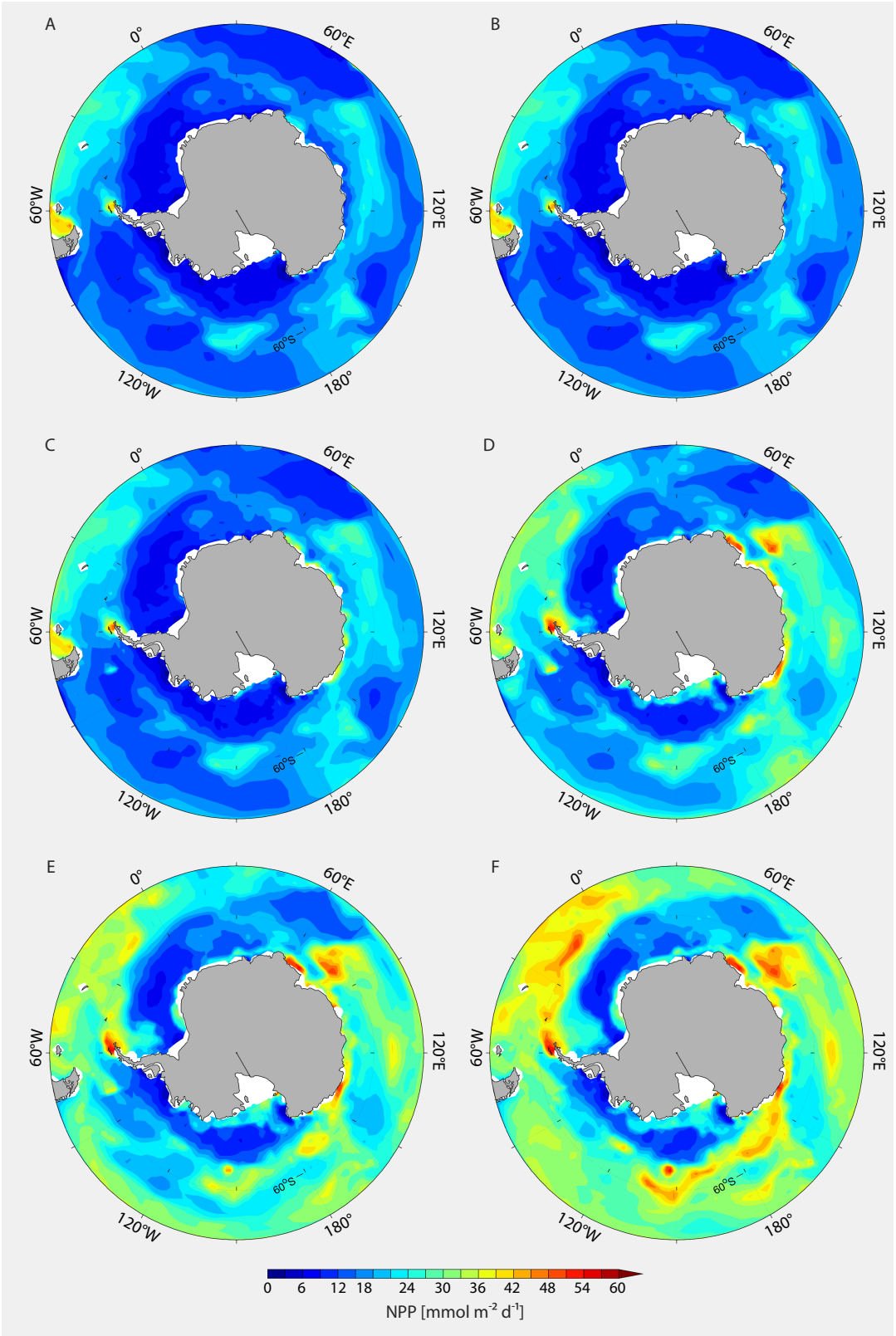

FIGURE 6.6: Total net primary production (NPP) south of 50°S: (A) *Control* run; (B) run *20*; (C) run *100*; (D) run *500*; (E) run *1000*; (F) run *2000*

Antarctic Peninsula (Fig. 6.6A). From 0 - 180°W the production south of 65°S is on average as low as 6 mmol m^{-2} d^{-1}, while from 0 - 180°E the average value is 25 mmol m^{-2} d^{-1}. When 100 nmol Fe L^{-1} are added from icebergs, we notice that the total NPP increases at the coast of Antarctica in the Davis, Mawson and D'Urville Seas from 60 - 150°E (Fig. 6.6C). In the run *500* the coastal NPP further increases, also in the coastal regions along West Antarctica, though the production is still low (Fig. 6.6D). Patches of high total NPP establish in the Atlantic and west Indian sectors (Fig. 6.6D). These further grow with increasing dFe concentration following windmill-like patterns (Fig. 6.6E - F). In some specific locations the total NPP reaches values of ca. 60 mmol m^{-2} d^{-1}. The total NPP south of 50°S in the *Control* run was 3.07 Pg C yr^{-1}, and increases in the study (Table 6.1). Roughly, a 100-fold increase in dFe from icebergs leads to almost a doubling of the total NPP in the region.

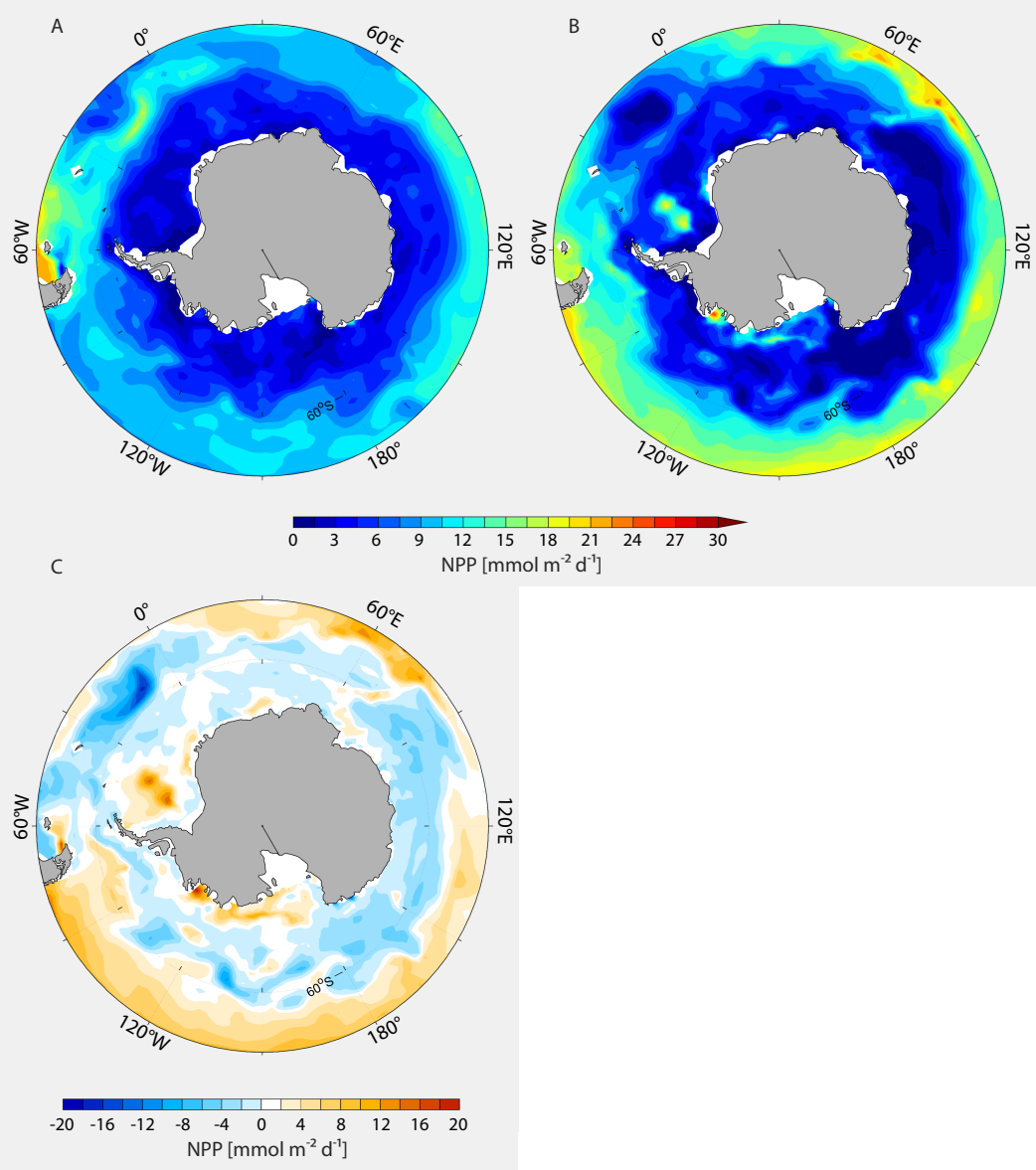

FIGURE 6.7: Net primary production of small phytoplankton south of 50°S: (A) *Control* run; (B) run *2000*; (C) run *2000* - *Control* run

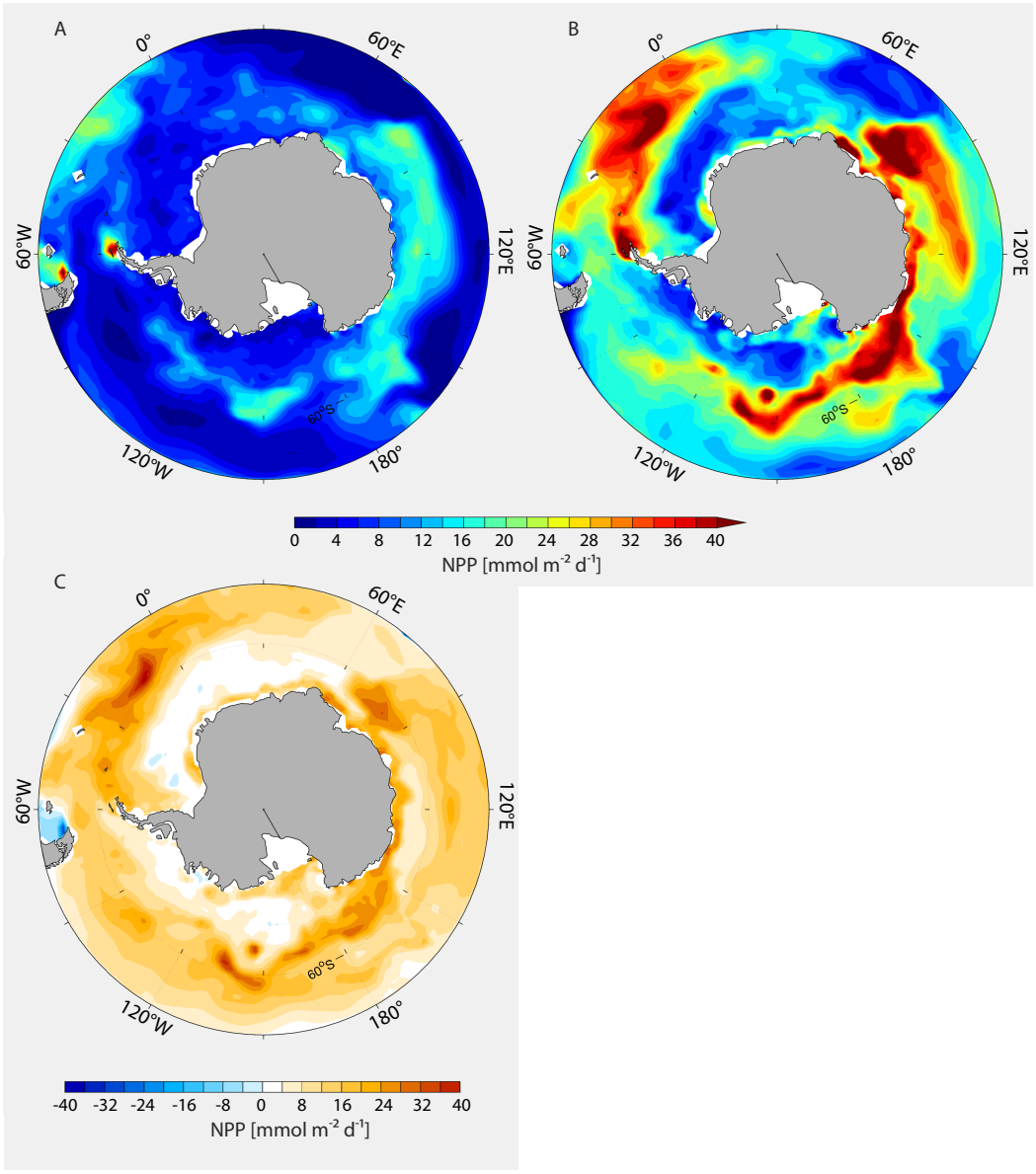

FIGURE 6.8: Net primary production of diatoms south of 50°S: (A) *Control* run; (B) run *2000*; (C) run *2000* - *Control* run

The behaviour of the total NPP is split into net primary production from small phytoplankton and from diatoms. By adding and increasing dFe from icebergs small phytoplankton flourish north of 60°S increasing the net primary production to values higher than 20 mmol m^{-2} d^{-1}. An exception is the Atlantic sector where the production is reduced (Fig. 6.7), just like south of 60°S between 60°E - 170°W. The resulting integrated net primary production of small phytoplankton increases by 8% (Table 6.1). On the contrary, diatoms net primary production south of 50°S increases by 190% (Table 6.1). Diatoms net primary production in the *Control* run is highest at the tip of Chile and at the tip of the Antarctic Peninsula. High productivity is also observed south of 60°S from 60°E - 150°W with average value 15 mmol m^{-2} d^{-1} (Fig. 6.8A). By introducing and increasing the dFe input from icebergs diatoms NPP roughly increases in the regions where diatoms were already present before, thus close to the Antarctic Peninsula, in the Scotia, Cosmonauts, Cooperation, Davis, Mawson, D'Urville, Somov Seas (80 - 170°E) and north of Ross Sea. In the extreme case of

a dFe input of 2000 μmol Fe m^{-3}, diatoms productivity perfectly reproduces the windmill-like iceberg trajectories, thus the pattern of dFe (Fig. 6.8B). From the Antarctic Peninsula the whole Atlantic sector north of 60°S shows primary productions by diatoms as high as 41 mmol m^{-2} d^{-1}. In the coastal waters of East Antarctica, diatoms bloom and from the Cooperation Sea and the Somov Sea plumes of high productivity expand eastward to lower latitudes (Fig. 6.8B).

Between the *2000* and *4000* model runs the NPP of small phytoplankton decreases by 3%. Since no further experiments with higher dFe input have been carried out, we do not know if this is the start of a decreasing trend and whether 2000 nmol Fe L^{-1} could be a tipping point for small phytoplankton which could be related to changes in nutrient and light limitations, or to increased competition with diatoms or greater grazing pressure.

TABLE 6.1: Total NPP and NPP of small phytoplankton and diatoms in Pg yr^{-1} south of 50° S in the different runs

	Control	20	50	100	200	500	1000	2000	4000
Total	3.07	3.13	3.22	3.36	3.60	4.19	4.95	5.71	6.13
Phytoplankton	1.54	1.55	1.56	1.57	1.55	1.57	1.70	1.72	1.67
Diatom	1.54	1.58	1.66	1.79	2.05	2.62	3.25	3.99	4.46

6.3.5 Export

The C export in the *Control* run is maximal in the Atlantic sector north of 60°S and in some patches along 60°S in the Indian and Pacific sectors. In Fig. 6.9A - B we observe that the C export south of 50°S increases significantly when dFe is released by melting icebergs. In the run *100* (not shown) we observe already a strong impact from additional dFe to the C export. Generally, the open ocean shows an increase smaller than 20% with exception for a plume at 120°E and north of 60°S where the C export rises by 50%. However, as for other parameters, the largest effect is seen in the coastal region. Between 60 - 150°E C export rises by averagely 95-150%, whereas in the east Ross Sea the increase reaches 250% in the *100* run. This results in 11% increase of the integrated C export from the *Control* to the *100* run (Table 6.2). By further intensifying the input of dFe from icebergs, C export is promoted in broad regions of the SO following the windmill-like patterns of dFe (Fig. 6.9B). At the centre of the windmill sails the C export increased by average 100%, while in the west Weddell Sea and Ross Sea, regions which showed little C export in the *Control* run, it increased by 200% and more. This results in 80% enhancement of the total integrated C export from the *Control* run to the high-dFe *2000* run, from 1.3 to 2.3 Pg C yr^{-1}, respectively (Table 6.2).

Equivalent to C export, the N export successively developed windmill-like patterns in the *2000* run (Fig. 6.9D). N export in the coastal regions increased by ca. 150% from the *Control* to the *2000* run. In a circle around the continent along and north of 60°S, N export increases in average by 100%. The outcome is an integrated increase of N export in the SO by 60%.

The smallest change in export is observed for Si, which increases by only 6% from the *Control* to the *2000* run (Table 6.2).

Though, the degree to how much the total export of the three elements increases in the different experiments is specific for each element, the increase resembles a saturation curve in all cases (Fig. 6.10). Si and N show an initial steep increase up to an dFe input of 1000 nmol L^{-3} and then slowly flatten. Likewise, C export increases sharply at first yet keeps the positive slope also at dFe input of 4000 nmol L^{-3}.

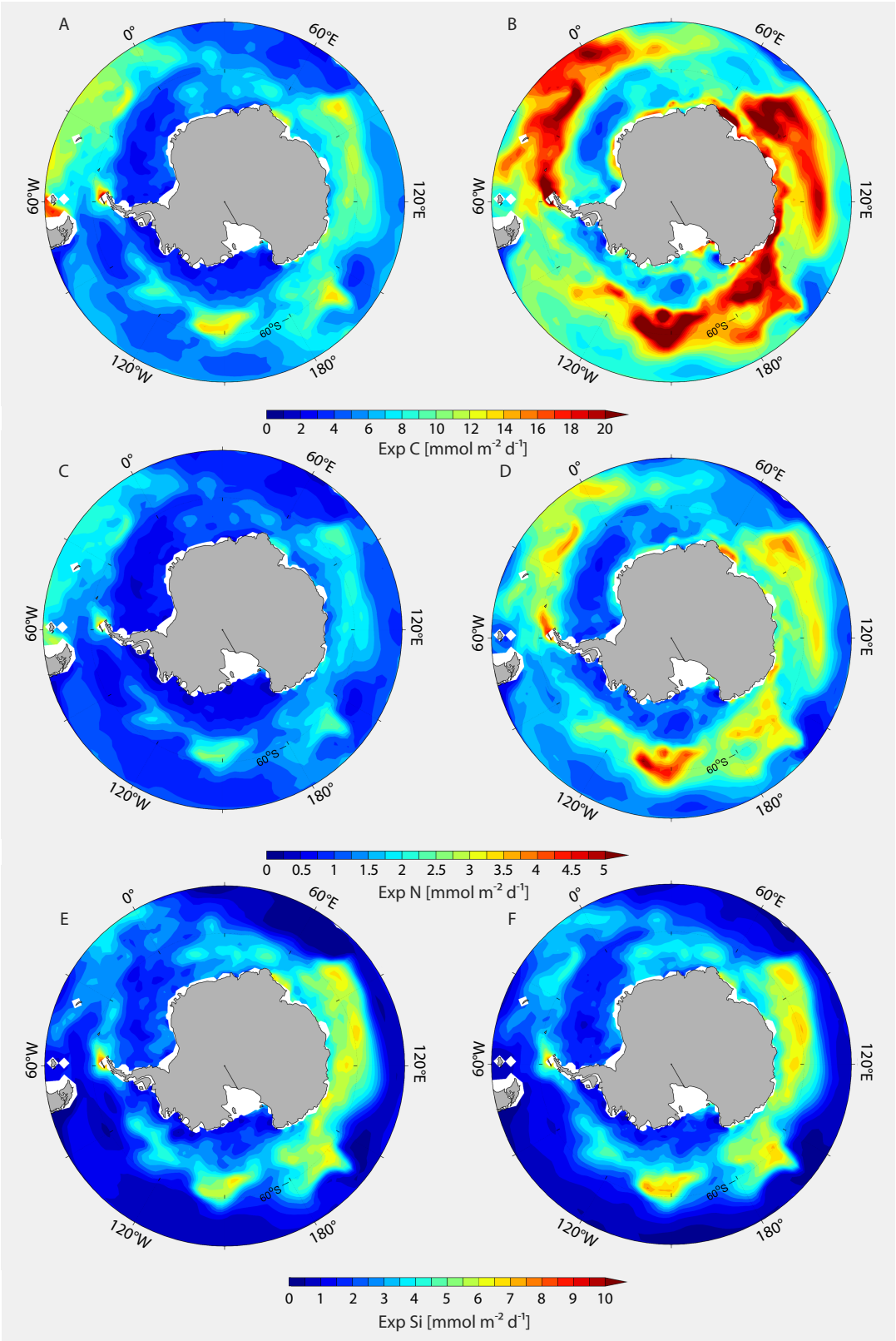

FIGURE 6.9: Export of C in the (A) *Control* run and (B) run *2000*; export of N in the (C) *Control* run and (D) run *2000*; export of Si in the (E) *Control* run and (F) run *2000*

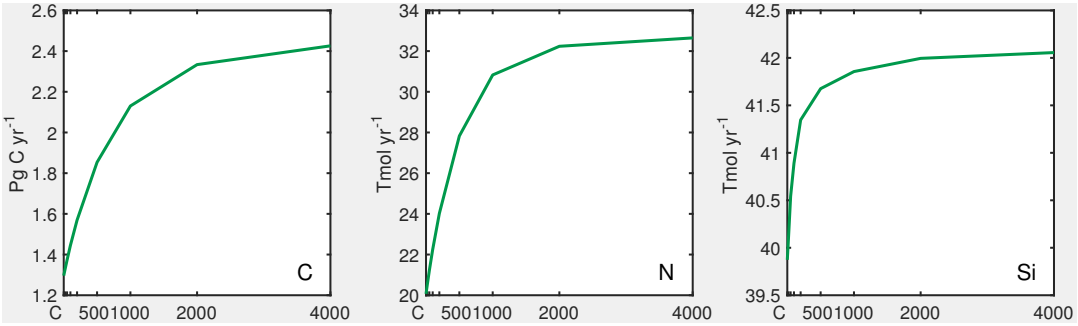

FIGURE 6.10: Total export south of 50°S of (A) C, (B) N and (C) Si

6.4 Discussion and conclusion

In the presented sensitivity study the intensity of the iceberg dFe source and its fertilisation capacity in the SO were explored. We analysed the effect on biology (small phytoplankton and diatoms), on nutrient distribution and uptake, and on elements' export from the water column. We noticed that, in case of a relatively small increase in dFe input, the dFe concentration will mainly increase along the coast of the Antarctic continent. The aforementioned maximal dFe release by icebergs predicted close to the Antarctic coast, has already been observed by Lancelot et al. (2009). However, they suggested that the near-shore contribution of dFe from icebergs is limited compared to other more dominant sources. Be that as it may, comparing the contribution of icebergs to the dFe budget is beyond the scope of this study, thus we cannot comment on this finding. We further observed that the higher the dFe input, the further north the dFe anomaly reaches. With high dFe input, the windmill-like iceberg patterns are observed also in the dFe distribution. From our scenarios, a total input of dFe from icebergs which lays halfway in the tested range, resulted in the lowest bias between model and observations.

The fertilisation by icebergs has been argued to have only minor effects on dFe concentrations and NPP in the Weddell and Scotia Seas, whereas it is a more critical dFe source in the Ross Sea, in the northern limbs of the Weddell Gyre and in the Pacific and Indian sectors of the SO (Lancelot et al., 2009; Lin et al., 2011). In our model experiments, we notice a general increase in the NPP of diatoms and a more complex response by small phytoplankton (Fig. 6.7 and Fig. 6.8) (in the following we compare the *Control* run with the run *2000*). Small phytoplankton biomass increases by ca. 10% north of 55°S, while diatom biomass increases by more than 190% along the west Antarctic coast and in a windmill-like pattern similar to the iceberg dense area modelled by (Rackow et al., 2017). In particular, the NPP of both phytoplankton and diatoms increases a) in the Weddell Sea, the latter mainly in the west part (more below); b) at the tip of Chile, where the dFe concentration decreases, as does the primary production of diatoms, while small phytoplankton slightly increase, suggesting that

TABLE 6.2: Export of C (Pg yr^{-1}), N (Tmol yr^{-1}) and Si (Tmol yr^{-1}) south of 50° S in the different runs

	Control	20	50	100	200	500	1000	2000	4000
C	1.30	1.33	1.37	1.44	1.57	1.85	2.13	2.33	2.43
N	20.1	20.5	21.2	22.2	24.0	27.8	30.8	32.2	32.6
Si	39.9	40.1	40.5	40.9	41.3	41.7	41.9	42.0	42.1

small phytoplankton outcompete diatoms which could be attributed to Si-limitation; c) along the coast where the diatom NPP is particularly enhanced between 60 - 180°W; d) in the northern limb of the Weddell Gyre and in the Atlantic sector, where diatom growth is favoured, while phytoplankton productivity is reduced; e) in the Ross Sea and in both the Indian and Pacific sectors, where both phytoplankton and diatoms increase. The general enhancement in NPP through the input of dFe from icebergs of course has effects on the nutrient concentration in the SO. In the following we give a more detailed description of these, splitting the study area into two: one south and one north of 60°S.

- South of 60°S the NPP of diatoms mainly increases at the coast around the Antarctic continent, while phytoplankton production decreases everywhere but in the Amundsen and central Weddell Sea. DIN in seawater is reduced at the coast, mostly due to uptake by diatoms. Indeed, almost everywhere at the coast the N content in diatoms increases (Fig. 6.11A). The Si concentration in seawater decreases, with exception of the Weddell, Bellinghausen and Cooperation Seas. In these areas, the production of diatoms stays the same, while phytoplankton are favoured, meaning that diatoms take up less Si (Fig. 6.11B). As a consequence of the increased N uptake by diatoms, the N export by dead organic material increases everywhere south of 60°S, and mostly at the coast (Fig. 6.12). The changes in Si export show more patterns than those in N export (Fig. 6.12). After all, these match the patterns observed in the Si content in diatoms. The resulting Si:N export is reduced all around Antarctica, conformant with the Si:N ratio in diatoms (Fig. 6.13). This is driven by a strong Si decrease and a minor N increase in diatoms.

- North of 60°S the NPP of diatoms and phytoplankton generally increases. An exception is however seen in the Atlantic sector, where the primary production of small phytoplankton is reduced. We observe a decrease of DIN and Si in seawater, the latter being particularly decreased in the Indian sector. N is taken up more in the *2000* run than in the *Control* run (Fig. 6.11A). On the contrary, the uptake of Si is slightly reduced, with exception of the Indian sector (Fig. 6.11B). The N export increases generally quite homogeneously with exception of the Atlantic sector where it deceases because of the decrease in diatoms NPP (Fig. 6.12). The export of Si shows also north of 60°S a rather mixed distribution, in some region increasing and in other decreasing (Fig. 6.12). Si:N export generally decreases since the increase in N export is larger than the average variation in Si export, reflecting the internal diatom Si:N ratio (Fig. 6.13).

To sum up, we noticed a decrease in Si:N ratio in diatoms in the SO with addition of dFe from icebergs. South of 60°S, thus closer to the continent, the decrease is driven by a reduced uptake of Si by diatoms compared to northern regions. On the other hand, north of 60°S, thus in the open ocean, the decrease in Si:N in diatoms is caused by by a larger increase in N uptake relative to that of Si by diatoms.

We now consider a region which steps out of line, the Weddell Sea, in which the primary production is small. Along the eastern coast of the Weddell Sea towards the Lazarev Sea, NPP of diatoms increased, while the NPP of small phytoplankton did not change much. Here, the higher productivity of diatoms increases both the Si and N export from the water column (Fig. 6.12). In the east part of the Weddell Sea, the NPP of diatoms decreases. Consequently, the Si uptake and export are reduced (Fig. 6.11B and Fig. 6.12B). At the same time, less N is taken up by diatoms (Fig. 6.11A). However, more small phytoplankton grow in the central Weddell Sea, assimilating more N. The result is a somewhat balanced N export. In the western part of the Weddell Sea, the productivity of diatoms again increases. However, they seem to need less Si, since its concentration increased in seawater and decreased in diatoms.

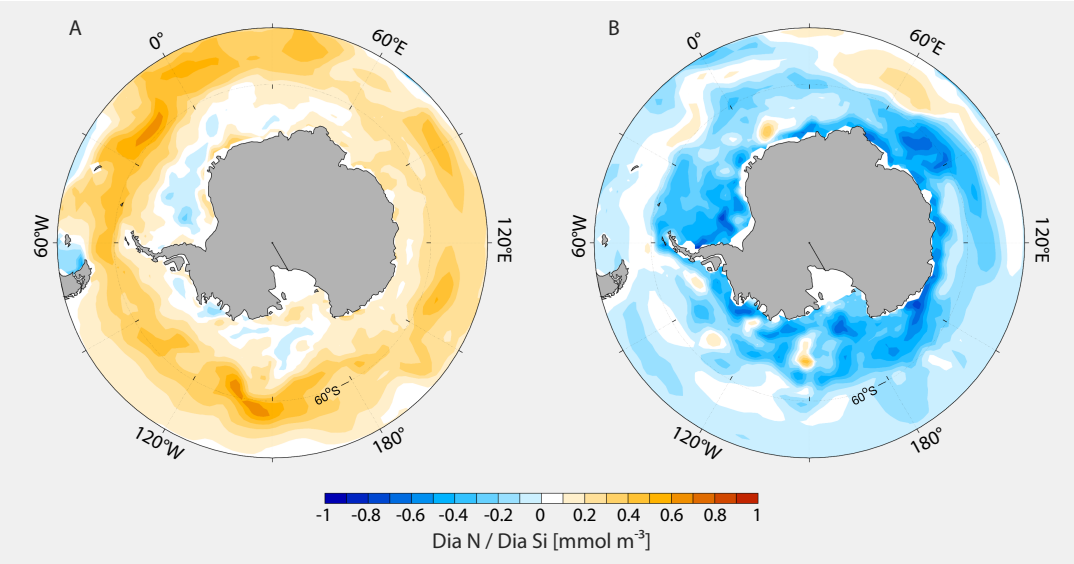

FIGURE 6.11: Changes in the concentration of (A) N and (B) Si in diatoms between run *2000* - *Control* run

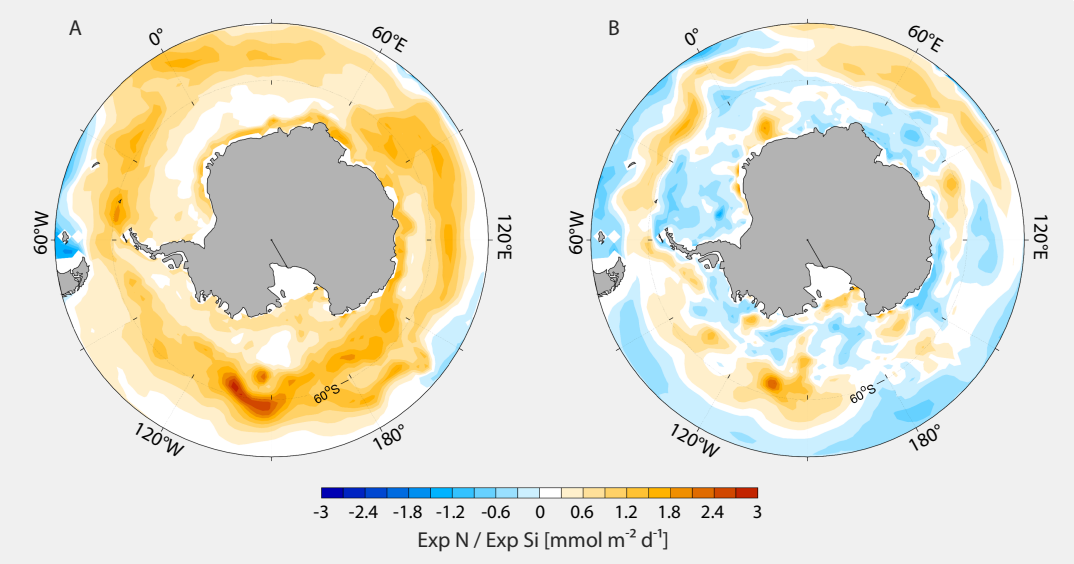

FIGURE 6.12: Changes in the export of (A) N and (B) Si between run *2000* - *Control* run

On the contrary, they still assimilate a lot of N and, in combination to the consumption by small phytoplankton, the DIN in seawater is reduced much more. To conclude, it seems as if the Si:N export in the east Weddell Sea would decrease mainly because of a decrease in Si export due to less diatom primary production, while in the west Weddell Sea, it decreases because of an increased N export related to a combined increase in diatom and phytoplankton production.

It is known, that under Fe-limitation, and partly also under other nutrient limitations, diatoms continue to take up Si relatively unhindered, leading to an increase in the Si:N and Si:C ratio of diatom cells (Takeda, 1998; Hutchins and Bruland, 1998). This effect is present in our

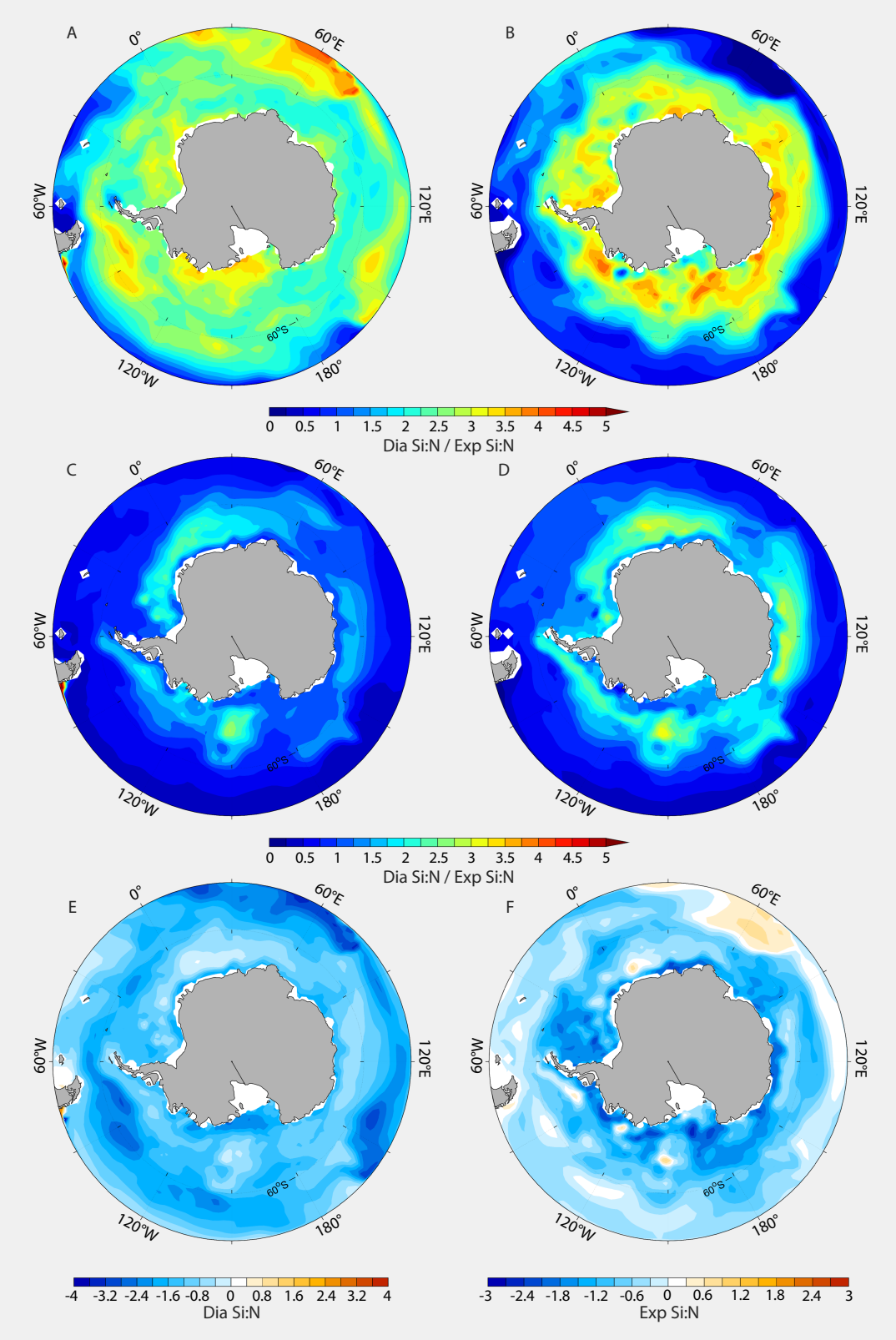

FIGURE 6.13: (A) Si:N ratio in diatoms in the *Control* run; (B) export Si:N in the *Control* run; (C) Si:N ratio in diatoms in the *2000* run; (D) export Si:N in the *2000* run; (E) difference of Si:N ratio in diatoms between the *2000* run - *Control* run; (F) difference in export Si:N between the *2000* run - *Control* run

model, and leads to elevated Si:N drawdown and export ratios in the more Fe-limited *Control* model run. In the runs with additional dFe input from icebergs, Si:N of diatoms decreases. Therefore, the additional N drawdown through increased growth is accompanied by a smaller increase in Si drawdown. It is important to realise that a similar effect could be produced also by a shift in species composition away from diatoms to non-siliceous phytoplankton. However, in our model results, it is predominantly the diatoms that increase in growth. Within diatoms, it was shown that Fe fertilisation in the SO shifts the community from heavily silicified phytoplankton species, like *Fragilariopsis kerguelensis*, to less strongly silicified ones, like *Chaetoceros* species (Assmy et al., 2013; Hoppe et al., 2013). However, since our model only incorporates one group of diatoms, such an effect cannot be modelled.

Another limitation of the present study deals with the depth of the injected dFe. In our model, as in almost all others, the dFe supply from icebergs in introduced in the upper model box. However, it is actually not known where the dFe supply occurs in the water column, considering that melting occurs to some extent at the base of the iceberg. Since the meltwater is lighter than the surrounding water, it will rise to the surface at the iceberg's side. Thus, a purely surface description may still hold true, but the effect may be biased. Indeed, in this representation the mixing of the meltwater and the surrounding seawater which could occur during the upward flow is not considered. A Recent study by Person et al. (2019) compared the dFe distribution distinguishing between the case that the meltwater is injected at the surface or throughout the mixed layer. They showed that the dFe concentration at the surface in summer is smaller when the input of dFe from icebergs is distributed over the top 120 m.

In conclusion, the results of this study can be put into a climatic context. In a warmer future climate, an increased mass loss of Antarctic glaciers, and hence an increased iceberg calving is predicted. Already now, there are observations pointing to an acceleration of several glacier flows towards the coast, especially in the West Antarctic (Rignot et al., 2002; Cook et al., 2016; Milillo et al., 2018). Several studies suggest that this would imply an increased dFe input to the SO. We observed that a suspension of Fe-limitation in many regions of the SO, results in a reduction in the Si:N export, which reflects the reduced Si:N ratio in diatoms. In Fe-limited conditions, i.e. the *Control* run, the uptake of Si was probably not down regulated, thus an increase in dFe availability did not change the Si uptake considerably, despite a drastic increase in productivity. This, on the contrary, fairly enhanced the N uptake, leading to more extent N-limited areas in the SO. Thus, the faster growth stimulated N uptake and photosynthesis but inhibited Si uptake in some regions. This behaviour of diatoms has already been observed in laboratory and field experiments (e.g. Takeda, 1998). It has been shown that an increase in Si cell content due to Fe limitation produces thicker and stronger frustules, improving the protection from grazers (Wilken et al., 2011). This possibly leads to a decreases in zooplankton grazing, and concomitant changes in the sinking of organic matter. We could speculate that the opposite could occur in a future Fe fertilisation in the SO by increased iceberg calving.

7 *Pseudo-nitzschia subcurvata* flourished better under simulated glacial than interglacial ocean conditions

Abstract

The 'Iron Hypothesis' suggests a fertilisation of the Southern Ocean by increased dust deposition in glacial times. This promoted high primary productivity and contributed to lower atmospheric pCO_2. In this study, the diatom *Pseudo-nitzschia subcurvata*, known to form prominent blooms in the Southern Ocean, was grown under simulated glacial and interglacial climatic conditions to understand how iron (Fe) availability (no or Fe addition) in conjunction with different pCO_2 levels (190 and 290 μatm), affect growth, particulate organic carbon (POC) production and photophysiology. Even though the diatom was able to grow with similar rates in all treatments, glacial pCO_2 conditions (low pCO_2 and Fe input) favoured POC production by *P. subcurvata* rather than limiting it. Also, under Fe deficiency, the diatom reached similar high POC production rates, but they declined with increasing pCO_2, indicating a negative effect by high CO_2 and low Fe availability, as observed during interglacial conditions. Under the latter conditions, the diatom had, however, thicker silica shells, which may offer better protection against grazers. Overall, our results show that the combination of higher Fe availability with lower pCO_2, as during the glacial ocean was beneficial for *P. subcurvata*. Hence, the diatom may have contributed more to primary production during glacial compared to interglacial times. Thus, more carbon could have been taken up by *P. subcurvata* from the atmosphere and have been subsequently sequestered. In the interglacial ocean conditions, on the other hand, *P. subcurvata* could also have contributed to higher carbon export due to its higher degree of silicification.

7.1 Introduction

The Southern Ocean (SO) is the world's largest high-nutrient low-chlorophyll region (HNLC) and an area where physical forcing, atmospheric pCO_2, biological production and marine biogeochemical cycles are tightly linked. In this region, primary production is restricted by the bioavailability of the trace metal (TM) iron (Fe; Martin, 1990; de Baar et al., 1995; de Baar et al., 2005; Boyd and Ellwood, 2010). Fe is an essential trace element, which is needed by phytoplankton to transfer electrons in key cellular and metabolic processes including photosynthesis, respiration, chlorophyll production, carbon (C) and nitrogen (N) fixation (Raven and Falkowski, 1999). The availability of Fe strongly influences phytoplankton species composition and growth (Martin et al., 1994; Boyd et al., 2000; de Baar et al., 2005; Marchetti et al., 2006; Schuback et al., 2015), impacts the biological carbon pump and thus the global carbon cycle. Consequently, changes in Fe availability have caused feedback effects on climate over geological timescales. Furthermore, the SO is a region of high CO_2 exchange

between ocean and atmosphere (Takahashi et al., 2009; Hauck et al., 2018). The SO has been reported to be a major sink of atmospheric CO_2 during glacial periods, while it was on the other hand a source of CO_2 during glacial-interglacial transitions. At present day, the SO is the major sink of anthropogenic CO_2 (Raven and Falkowski, 1999; Gruber et al., 2009).

During the Last Glacial Maximum (LGM), the SO experienced changes in oceanic circulation and carbon storage. For instance, increased sea ice extent strengthened surface water stratification, thus limiting ocean ventilation and trapping more carbon in the deep ocean (Francois et al., 1997; Sigman and Boyle, 2000; Stephens and Keeling, 2000). Additionally, the northward displacement of the westerly winds prevented the upwelling of CO_2-rich deep water (Mayr et al., 2013). Besides physical mechanisms, the strength of the biological pump might explain 25 - 50% of the roughly 100 μatm pCO_2 discrepancy between glacial (180 μatm pCO_2) and interglacial (280 μatm pCO_2) times as argued in several studies (Kohfeld et al., 2005; Martínez-Garcia et al., 2014; Martínez-Garcia et al., 2009; Lambert et al., 2015). This supports John Martin's 'Iron Hypothesis', which suggests that an increase in dust deposition during glacial times would fertilise the ocean, stimulate marine productivity, and enhance C export (Martin, 1990; de Baar et al., 2005; Moore et al., 2006; Sunda, 2012; Trimborn et al., 2017). Indeed, analysis of sediment cores revealed a positive correlation between aeolian Fe supply and primary production during ice ages (Anderson et al., 2014; Martínez-Garcia et al., 2014). Proxy data as well as model simulations showed a doubling of the global dust deposition during the last glacial climate condition, when 826 Tg yr^{-1} dust were deposited in the global ocean, compared to the 440 Tg yr^{-1} dust in pre-industrial times (Kumar et al., 1995; Albani et al., 2016). The difference was mainly due to a dryer atmosphere and a reduced vegetation cover. Moore et al. (2006) used a biogeochemical model to estimate the impact of Fe deposition on the global ocean. Under current conditions, 33% of the world's oceans water masses have Fe concentrations, which limit the growth of phytoplankton. The model simulations revealed that the percentage of Fe-poor water masses decline to 25% and 13% with pre-industrial and LGM dust input, respectively. The SO showed, along with the North Pacific Ocean, the most significant difference in soluble Fe supply during glacial and interglacial times, accordingly presenting the largest impact on the marine biogeochemistry (Moore et al., 2006). The dust deposition in the SO during glacial times was roughly ten times higher (0.04 - 0.17 Tg yr^{-1}) than in pre-industrial times (0.005 - 0.018 Tg yr^{-1}) (Albani et al., 2016). However, the SO is geographically isolated from arid, dust-producing regions and is thus overall characterised by low aeolian Fe deposition (Wagener et al., 2008). Other sources of Fe include upwelling of deep nutrient-rich water, entrainment of sedimentary Fe from continental shelfs and resuspension, island-wake effects, seasonal sea ice extent and melt, as well as iceberg drift and melt (Boyd and Ellwood, 2010, and references therein).

The phytoplankton community in the current SO is dominated by different diatom species and the prymnesiophyte *Phaeocystis antarctica* (Arrigo et al., 1999). Diatoms account for 40% of the ocean's total primary production (Nelson et al., 1995; Tréguer et al., 1995; Smetacek, 1999; Smetacek, 2018) and dominate the export of particulate organic matter to the seafloor (Smetacek, 1985; Buesseler et al., 2001). In other words, diatoms are crucial for the ocean's ability to sequester C to the ocean's interior. Diatoms also have an extensive impact on the oceanic silica inventory, as they produce frustules containing silica. Some frustules are resistant to remineralisation and dissolution, are well preserved in the sediment, and thus provide precious information about past oceanic biogeochemistry. *Pseudo-nitzschia* species have been frequently observed in today's phytoplankton assemblages in Antarctic waters (Hasle, 1964). Mesoscale Fe fertilisation experiments in the SO triggered massive phytoplankton blooms dominated by large diatoms like the pennate *Pseudo-nitzschia* sp. (de Baar et al.,

2005; Smetacek et al., 2012). Large diatoms in the SO appear to have a higher Fe requirement compared to smaller phytoplankton because of physical constrains in the Fe uptake process (Strzepek et al., 2011). To compensate for this, they have evolved various strategies to acquire bioavailable Fe. They generally reduce their biogeochemical Fe requirement through metal or protein substitution (Allen et al., 2008) and reduce Fe-rich components of the photosystem apparatus (Schuback et al., 2015). Marchetti et al. (2006) suggested that *Pseudo-nitzschia* is able to accumulate intracellular Fe when ambient concentrations of this TM are high, while maintaining a low Fe demand. This luxury uptake and subsequent storage of Fe supports growth in subsequent low Fe environments and enables *Pseudo-nitzschia* to dominate phytoplankton assemblages across a wide range of oceanic Fe concentrations.

In SO diatoms, Fe limitation often results in slower growth and reduced C fixation. The photochemical quantum efficiency, which indicates how efficiently excitation energy is transferred to the reaction centres, is usually lowered (Greene, Geider, and Falkowski, 1991; Greene et al., 1992; Marchetti et al., 2006; Marchetti and Harrison, 2007). In an Fe-poor environment, cells usually increase the functional absorption cross sectional area of their reaction centres, enhancing thereby the target area, which absorbs incoming photons (Greene et al., 1992; Strzepek et al., 2011; Tortell et al., 2008). The absorbed photons can either drive photosynthesis, N reduction, C fixation, photorespiration or can be converted to heat (non-photochemical quenching). Fe deficiency induces changes in the photosystem II (PSII) reaction centres such as the reduction of the pigment content (van Leeuwe, Visser, and Stefels, 2014), causes less efficient electron transport (Greene, Geider, and Falkowski, 1991) and increases non-photochemical quenching to dissipate the excess light energy (Trimborn et al., 2019).

Besides Fe limitation, phytoplankton cells have experienced variations in CO_2 concentration in the past. Previous studies on the effect of high CO_2 concentrations on phytoplankton reported changes in their elemental composition (e.g. Reinfelder, 2012; Zhu et al., 2017), in cell size (e.g. Hoogstraten, Timmermans, and de Baar, 2012) and in the degree of silicification in diatoms (e.g. Sun et al., 2011). Furthermore, it was shown that low pCO_2 levels can influence the structure of Antarctic phytoplankton communities. For example, experiments with natural phytoplankton assemblages from different regions across the SO (Tortell et al., 2008; Hoppe et al., 2013; Trimborn et al., 2017) concluded that *Pseudo-nitzschia* flourished well at low pCO_2 levels, while it can hardly bear typical ocean acidification pCO_2 levels. Indeed, between ambient and future elevated pCO_2 levels, the growth of *P. subcurvata* in a laboratory experiment was not stimulated under ample Fe supply (Trimborn et al., 2013). Under similar Fe conditions, a phytoplankton community from the Ross Sea, Antarctica, responded to CO_2 increase from 100 to 800 ppm with a dramatical decrease in *P. subcurvata*, being replaced by *Chaetoceros* species (Tortell et al., 2008). Similarly, a community from the Weddell Sea, Antarctica, shifted from *Pseudo-nitzschia* to *Fragilariopsis* after Fe addition between 390 to 800 μatm pCO_2 (Hoppe et al., 2013), while no difference in species composition was found between the glacial (190 μatm) and the present-day (390 μatm) pCO_2 levels. This implies that reduced CO_2 concentrations during glacial periods potentially favoured pennate diatoms such as *Pseudo-nitzschia* while diatom species such as *Chaetoceros* and *Fragilariopsis* became most abundant under present-day and future pCO_2 levels (Tortell et al., 2008). A few studies investigated the SO phytoplankton assemblages and growth under low Fe supply in response to increasing pCO_2 (Feng et al., 2010; Hoppe et al., 2013; Trimborn et al., 2017). Hoppe et al. (2013) observed also a CO_2-dependent taxonomic shift in Fe deplete conditions with increasing pCO_2 with *Pseudo-nitzschia* being replaced by the pennate diatom *Synedropsis* between 390 and 800 μatm pCO_2 levels. Similarly, when pCO_2 increased from 390

to 900 μatm another SO plankton community changed from being dominated by *P. prolongatoides* to one, which was dominated by *P. antarctica* (Trimborn et al., 2017). Hence, irrespective of Fe availability the genus *Pseudo-nitzschia* was found to be susceptible to ocean acidification pCO_2 levels.

Studies that asses the effects of low pCO_2 on phytoplankton often compare their results with high pCO_2 levels to understand ocean acidification. However, little is known about the smaller variation from 180 (glacial) to 280 μatm (interglacial/pre-industrial) pCO_2 under different Fe availability. Indeed, the potential interactive effect of low-pCO_2 (180 and 280 μatm) together with different Fe availability (deplete and replete) on net primary production and export production is currently often not considered, when developing models or designing laboratory experiments simulating glacial and interglacial ocean conditions. Studies looking at N-isotopes and thorium-corrected sediment accumulation rates describe large fluxes of biogenic detritus out of surface waters in the glacial ocean due to a larger amount of lithogenic Fe transported by winds (Kumar et al., 1995). The latter study indicates that increased export production and thus enhanced C storage potentially contributed to the observed lower atmospheric CO_2 concentrations during glacial times (Muglia, Skinner, and Schmittner, 2018).

The above-mentioned studies offer first insights on how some phytoplankton species cope with glacial and interglacial climatic conditions. However, studies on the ecophysiology of Antarctic diatoms subject to glacial vs. interglacial ocean climate conditions under reduced Fe conditions, are yet lacking. In this study, the SO bloom-forming diatom *P. subcurvata* was grown under Fe and CO_2 conditions representative of glacial (lower CO_2 and higher Fe) and interglacial (higher CO_2 and lower Fe) times to untangle the influence of these two environmental factors on growth, elemental stoichiometry, photosynthetic carbon production and photophysiology. This allowed to assess its role in the paleo carbon cycle.

7.2 Material and methods

7.2.1 Experimental setup

Prior to the execution of the experiment, the oceanic diatom *P. subcurvata* (isolated by Philipp Assmy at 49°S, 2°E, R/V Polarstern cruise ANT-XXI/4, April 2004) was grown in Antarctic seawater with a low total dissolved Fe (dFe) concentration of 0.5 nmol L^{-1} for more than one year. Preacclimation and the main experiment was carried out in Fe-poor (0.4 nmol L^{-1}) Antarctic seawater collected at 60°32 S, 26°29 W (salinity of 33.8 $\pm$0.2), filtered through a sterilised, acid-cleaned 0.2 μm filter (Sartobran, Sartorius). This water was spiked with chelexed (Chelex® 100, Sigma Aldrich, Merck) macronutrients (100 μmol L^{-1} Si, 100 μmol L^{-1} NO_3^- and 6.25 μmol L^{-1} PO_4^{3-}) and vitamins (30 nmol L^{-1} B1, 23 nmol L^{-1} B7 and 0.228 nmol L^{-1} B12) according to the F/2R medium (Guillard and Ryther, 1962). In addition, a TM mix containing Zn (0.16 nmol L^{-1}), Cu (0.08 nmol L^{-1}), Co (0.09 nmol L^{-1} Co), Mn (1.9 nmol L^{-1}), Mo (0.05 nmol L^{-1}) in the ratio of the original F/2 recipe adjusted to 4 nmol L^{-1} Fe was added. As suggested by Gerringa, de Baar, and Timmermans (2000), in order to minimise the alteration of the natural seawater TM chemistry and ligands, no ethylenediaminetetraacetic acid (EDTA) was added. The Fe-deplete treatments (henceforth referred to as ***Control***) contained 0.4 nmol L^{-1} dFe while for the Fe-enriched treatments (henceforth referred to as ***+Fe***), 4 nmol L^{-1} $FeCl_3$ were added.

To avoid Fe contamination, TM clean techniques were used according to the GEOTRACES cookbook (Cutter et al., 2017). The sampling and handling of the incubations was conducted under a laminar flow hood (Class 100, Opta, Bensheim, Germany). All equipment

was soaked for one week in 1% Citranox, followed by two weeks in 1 N HCl for polycarbonate and 5 N HCl for polyethylene materials. In between and after the cleaning process, the equipment was rinsed seven times with Milli-Q (MQ, Millipore). Finally, everything was air dried under a clean bench (U.S. class 100, Opta, Bensheim, Germany) and packed in three polyethylene bags.

All *Control* and *+Fe* incubations were bubbled with humidified air containing pCO_2 levels of 190 and 290 μatm, henceforth referred to as ***190*** and ***290***, respectively. Using a gas flow controller (CGM 2000, MCZ Umwelttechnik, Bad Nauheim, Germany), both CO_2 gas mixtures were generated by combining CO_2 free air ($<$1 ppmv CO_2, Dominick Hunter, Kaarst, Germany) with pure CO_2 (Air Liquide Deutschland Ltd., Düsseldorf, Germany) in the respective ratios. They were regularly monitored with a Li-Cor (LI6252 Biosciences, Lincoln, NE) calibrated with CO_2 free air and purchased gas mixtures of 150 ± 10 and 1000 ± 20 ppmv CO_2 (Air Liquide Deutschland Ltd., Düsseldorf, Deutschland). Low pCO_2 and Fe input characterised the glacial ocean, which was here simulated in the *+Fe 190* treatment. Vice versa, the interglacial ocean was characterised by higher pCO_2 and no Fe input and mimicked by the *Control 290* treatment. In addition to the incubation bottles, Fe and carbonate chemistry were determined in the culture medium which was incubated in the same way as the respective incubation bottles (pCO_2 and Fe availability), to check if the different pCO_2 and Fe manipulations were successful.

All incubations were placed in front of LED (light-emitting diode) lamps at 100 μmol photons m^{-2} s^{-1} under a light : dark cycle of 16 : 8 h. The light intensity was adjusted with a LI-1400 datalogger (Li-Cor Biosciences, Lincoln, NE, USA) with a 4π-sensor (Walz, Effeltrich, Germany). For this experiment, the long-term low Fe acclimated *P. subcurvata* stock culture was inoculated to the different CO_2-Fe conditions and was acclimated to each experimental condition at 2 °C for at least two weeks. The main experiment was carried out in triplicate 4 L acid-cleaned polycarbonate bottles for each experimental treatment. The main experiment lasted between 8 and 9 days and cell densities reached between 67 000 and 107 000 cells mL^{-1} during final sampling.

7.2.2 Trace metal chemistry

At the end of the experiment, total dFe samples were taken from the culture medium by filtering 100 mL from each bottle through 0.2 μ μm HCl-cleaned polycarbonate filters (47 mm, Nuclepore, Whatman, GE Healthcare, Chicago, IL, USA) using a trace metal clean filtration system under a clean laminar flow hood (Class 100, Opta, Bensheim, Germany). The filtrate was then filled into a 125 ml HCl-cleaned PE bottle and stored triple-bagged at 2 °C until analysis. Between each filtration, the filtration manifold was cleaned in an acid bath consisting of 1 M HCl and rinsed seven times with Milli-Q. Prior to the dFe analysis, 0.2 μm pre-filtered seawater samples were acidified to pH 1.75 with double distilled HNO_3, minimising the formation of Fe and Mn hydroxides. Next, samples were UV (ultraviolet) oxidised for 1.5 h using a 450 W photochemical UV power supply (photochemical lamp 7825; Power Supply 7830, ACE GLASS Inc., Vineland N.J., USA). Total dFe concentration of the seawater samples and the processed blanks were measured with a seaFAST system (Elemental Scientific, Omaha, NE, USA Hathorne et al., 2012) coupled to a sector field inductively coupled plasma mass spectrometer (ICP-MS; Element 2, Thermo Fisher Scientific; resolution of R = 4000; oxide forming rates below 0.3%). To minimise matrix effects, the seawater dFe concentrations were analysed by standard addition. The accuracy of the dFe data was assessed by measuring NASS-6 (National Research Council of Canada) reference standards, with a recovery rate for Fe of 110%.

7.2.3 Carbonate chemistry

From the culture medium as well as from the incubation bottles at the end of the experiment, dissolved inorganic carbon (DIC) was filtered through 0.2 μm filters (Nalgene, Thermo Scientific) and was stored at 4 °C in 5 mL borosilicate glass bottles without headspace. The colorimetric analysis was performed with a QuAAtro autoanalyser (Seal Analytical Stoll et al., 2001). Again, from the culture medium as well as from the incubation bottles at the end of the experiment, samples for the total alkalinity (TA) were filtered through 0.6 μm GF/F filters (Whatman) and stored at 4 °C in 150 mL borosilicate glass bottles. TA was measured via potentiometric titration (Brewer, Bradshaw, and Williams, 1986) and the concentrations were calculated using a linear Gran Plot (Gran, 1952). The pCO_2 was calculated using the CO2Sys program (Heuven et al., 2011) with the equilibrium constants of Mehrbach et al. (1973) as refitted by Dickson and Millero (1987) using TA and DIC measurements, concentrations of phosphate and silicate, temperature and salinity.

7.2.4 Growth

Cell count samples of *P. subcurvata* were fixed with 10% acid lugol solution and stored at 2 °C in the dark until counting. Cell numbers of *P. subcurvata* were enumerated according to the method by Utermöhl (1958) using 3 ml sedimentation chambers (Hydrobios, Kiel, Germany) on an inverted microscope (Zeiss Axiovert 200) counting at least 400 cells. The growth rates μ (d^{-1}) were determined with

$$\mu = \frac{ln(N_t/N_0)}{\Delta t} \tag{7.1}$$

where N_0 and N_t denote the initial and the final cell concentrations of the experiments, respectively and Δt is the incubation time in days. Final harvest took place when the cells were in exponential growth and reached densities between 67 000 and 107 000 cells mL^{-1}.

The cell volume was computed using the volume formula of a prism on parallelogram base provided by Hillebrand et al. (1999). The apical and transapical axes were measured via microscopy, while the pervalvar axis was estimated to be half of the transapical axis with an average value of 1.2 μm.

7.2.5 Elemental composition

At the end of the experiment, particulate organic carbon (POC) and particulate organic nitrogen (PON) were measured after filtration onto pre-combusted (15 h, 500 °C) GF/F filters (pore size sin 0.6 μm, Whatman). Filters were stored at -20 °C and dried for $>$ 12 h at 60 °C. Analysis was performed using a Euro Elemental Analyzer 3000 CHNS-O (HEKAtech GmbH, Wegberg, Germany). At the end of the experiment, samples to determine biogenic silica (BSi) were filtered through a cellulose acetate filter (Sartorius, 0.6 μm) and stored at -20 °C. The dried filters were submerged in 0.2 N NaOH at 95 °C for 45 minutes, cooled in an ice bath for 15 minutes, neutralised with 1 M HCl according to Brzezinski and Nelson (1995) and analysed colorimetrically for silicate using standard spectrophotometric techniques (Koroleff, 1983). Contents of POC, PON and BSi were corrected for blank measurements and normalised to filtered volume and cell densities to obtain cellular quotas. Production rates of POC, PON and BSi were calculated by multiplying the cellular quotas with the respective growth rate.

7.2.6 Pigments

Pigment samples were collected onto GF/F filters, flash frozen in liquid nitrogen and stored at -80 °C until analysis. First, the pigments were homogenised and extracted for 24 h in 90% acetone at 4 °C in the dark. Second, they were centrifuged for five minutes (4 °C, 13000 rpm) and filtered through a 0.45 μm pore size nylon syringe filter (Nalgene, Nalge Nunc International, Rochester, NY, USA). The pigments were analysed by reversed phase High Performance Liquid Chromatography (HPLC) on a LaChromElite system equipped with a chilled autosampler L-2200 and a DAD detector L- 2450 (VWR-Hitachi International GmbH, Darmstadt, Germany). A SpherisorbODS-2 column (25 cm $\times$ 4.6 mm, 5 μm particle size; Waters, Milford, MA, USA) with a LiChropher100-RP-18 guard cartridge was used for the separation of pigments, applying a gradient according to Wright (1991). Peaks of light harvesting (LH) pigments chlorophyll a (Chl *a*) and c_2 (Chl c_2), fucoxanthin (Fuco), as well as of the light protective (LP) pigments diatoxanthin (Dt) and diadinoxanthin (Dd) were detected, identified and quantified by co-chromatography with the corresponding pigment standards (DHI Lab Products, Horsholm, Denmark) using the software EZChrom Elite ver. 3.1.3. (Agilent Technologies, Santa Clara, CA, USA). Pigment contents were normalised to filtered volume and cell densities to obtain cellular quotas.

7.2.7 Photophysiological parameters

The efficiency of photochemistry in the PSII of *P. subcurvata* was assessed regularly during and at the end of the experiment by means of a Fast Repetition Rate fluorometer (FRRf, FastOcean PTX) and a FastAct Laboratory system (both from Chelsea Technologies Group ltd., West Molesey, United Kingdom). Values were obtained using the FastPro8 software (Version 1.0.50 Oxborough et al., 2012). Measurements were performed at 2 °C after 10 minutes of dark-adaptation to ensure that all PSII reaction centres were fully oxidised and non-photochemical quenching (NPQ) was relaxed (Trimborn et al., 2014).

The fluorometer's LED (wavelength 450 nm) was automatically adjusted to a light intensity of $1.2{\cdot}10^{22}$ μmol photons m^{-2} s^{-1}. A single turnover flashlet was applied to cumulatively saturate PSII, thus to close all PSII reaction centres, and consisted of 100 flashlets on a 2 μs pitch, followed by a relaxation phase made of 40 flashlets on a 50 μs pitch to reopen the PSII reaction centres. The saturation phase of the single turnover acquisition, comprised 24 sequences and was fitted according to Kolber, Prasil, and Falkowski (1998). The minimum (F_0) and maximum (F_m) Chl *a* fluorescence were determined and the apparent maximum PSII quantum yield (F_v/F_m) was calculated according to the equation:

$$F_v / F_m = (F_m - F_0) / F_m \tag{7.2}$$

Further outputs of the FastPro8 software from the single turnover measurements of dark-adapted cells were the connectivity between PSII (P, dimensionless), thus the energy transfer between PSII units, the time constant for electron transport at the acceptor side of PSII (τ, μs), the functional absorption cross section of PSII photochemistry (σPSII, nm^{-2}) and the cellular concentration of functional PSII reaction centres (RCII, zmol cell^{-1}).

During the photosynthesis-irradiance-curve (PE-curve), cells were exposed to eight light levels ranging from 0 to 1868 μmol photons m^{-2} s^{-1} for five minutes each. At each light level the light-adapted minimum (F') and maximum (F_m') Chl *a* fluorescence were measured and the effective PSII quantum yield (F_q'/ F_m' = (F_m' - F')/ F_m') was calculated (Genty, Briantais, and Baker, 1989).

Cellular electron transport rates (cETR) were calculated following Suggett, MacIntyre, and Geider (2004) and Suggett et al. (2009) and normalised by RCII (Koch et al., 2018) using:

$$cETR = RCII \cdot \sigma_{PSII} \cdot E \cdot \frac{F'_q / F'_m}{F_v / F_m} \tag{7.3}$$

where E (photons m^{-2} s^{-1}) is the applied instantaneous irradiance, which was measured separately for each light level in seawater. The cETR versus E curve was fitted according to Ralph and Gademann (2005) allowing to derive the maximum cETR ($cETR_{max}$), the minimum saturating irradiance (I_K) determined by the interception of the light-limited region with the maximum photosynthetic rate, and the maximum light utilisation efficiency (α). NPQ of Chl *a* fluorescence was calculated using the Stern-Volmer equation at each light level:

$$NPQ = \frac{F_m}{F'_m} - 1 \tag{7.4}$$

7.2.8 Statistical assessment

To assess the effect of Fe concentration (*Control* and *+Fe*) and pCO_2 (*190* and *290*) on all experimental parameters among the different treatments of *P. subcurvata*, we used a two-way analysis of variance (2-way ANOVA) followed by a pairwise multiple comparison test (post hoc) using the Holm-Sidak method. All statistical analyses were performed using the program SigmaPlot (www.systatsoftware.com) (Version 13.0 from Systat Software, Inc., San Jose California USA). Statistical significance was defined when $p < 0.05$.

7.3 Results

7.3.1 Trace metal and carbonate chemistry

The total dFe concentrations of the different culture medium showed a significant difference between the *+Fe* and the *Control* treatments (2-way ANOVA: $p < 0.001$, Table 7.1), with the *+Fe* treatments having higher dFe concentrations than the *Control* treatments. The parameters of the carbonate system are given in Table 7.1. TA remained constant in all culture media and incubation bottles. As expected, increasing pCO_2 significantly enhanced the DIC concentration in all culture media and incubation bottles (2-way ANOVA: $p < 0.001$; post hoc *+Fe*: $p < 0.001$; post hoc *Control*: $p = 0.005$). While Fe availability did not alter DIC of the different culture media bottles, a significant Fe effect was found for the *P. subcurvata* incubations, but only for the *190* treatments (post hoc: $p < 0.04$). The interaction of CO_2 and Fe also led to significant effects in DIC of the *P. subcurvata* incubations (2-way ANOVA: $p < 0.02$). The pCO_2 calculated with TA and DIC was significantly different between the *190* and *290* treatments (2- way ANOVA: $p < 0.001$). Given comparable values of TA, DIC and pCO_2 between incubation bottles and abiotic culture media, carbonate chemistry was stable.

7.3.2 Growth and elemental composition

The growth rates of *P. subcurvata* were unaffected by Fe deficiency and changes in pCO_2 (Fig. 7.1A). Similarly, cell volumes remained constant across all treatments (Table 7.2).

Cellular POC quotas (Table 7.2) and POC production rates (Fig. 7.1B) in both pCO_2 treatments were not affected by Fe deficiency. On the other hand, the increase of CO_2 concentration resulted in a 20-30% decrease of cellular POC quotas (2-way ANOVA: $p < 0.001$;

TABLE 7.1: Carbonate chemistry determined at the end of the experiment and total dFe concentrations in the culture mediums (filtered seawater without cells) and of the *P. subcurvata* incubations of the four treatments (*+Fe 190*, *Control 190*, *+Fe 290* and *Control 290*). The pCO_2 was calculated from measured dissolved inorganic carbon (DIC) and total alkalinity (TA). The values for carbonate chemistry of the culture bottles and of the *P. subcurvata* incubations represent the means ± SD (n=2 and n=3, respectively). dFe values denote two measurements. Significant statistical differences between the individual treatments of the *P. subcurvata* incubations were determined with post hoc test and are denoted by different letters ($p < 0.05$), while the overall effects of Fe and CO_2 and their interaction were determined via 2-way ANOVA and in case they were significant indicated by X in the 'Significant effect' column.

Parameter	Culture medium						
	190		290				
	+Fe	Control	+Fe	Control			
TA (μmol kg^{-1})	2313 ± 5	2312 ± 7	2314 ± 10	2306 ± 4			
DIC (μmol kg^{-1})	2089 ± 12	2068 ± 9	2128 ± 3	2131 ± 1			
pCO_2 (μatm)	228 ± 21	204 ± 3	289 ± 20	302 ± 7			
dFe (nmol L^{-1})	3.01 ± 0.09	1.00 ± 0.06	1.38 ± 0.03	0.43 ± 0.06			
	P. subcurvata incubations						
	190		290		Significant effect		
	+Fe	Control	+Fe	Control	Fe	CO_2	Fe-CO_2
TA (μmol kg^{-1})	2317 ± 11^a	2324 ± 12^a	2327 ± 13^a	2320 ± 9^a			
DIC (μmol kg^{-1})	2046 ± 17^a	2071 ± 11^b	2138 ± 14^c	2118 ± 2^c		X	X
pCO_2 (μatm)	181 ± 15^a	202 ± 24^a	287 ± 31^b	283 ± 29^b		X	
dFe (nmol L^{-1})	-	-	-	-	-	-	-

Table 7.2) and POC production (2-way ANOVA: $p < 0.001$; Fig. 7.1B) in both *Control* and *+Fe* treatments.

TABLE 7.2: Volume and elemental composition determined at the end of the experiment in the four treatments of *P. subcurvata* (*+Fe 190*, *Control 190*, *+Fe 290* and *Control 290*). The values represent the means ± SD (n=3). Significant statistical differences between the individual treatments were determined with post hoc tests and are denoted by different letters ($p < 0.05$), while the overall effects of Fe and CO_2 were determined via 2-way ANOVA and in case they were significant indicated by X in the 'Significant effect' column.

Parameter	*P. subcurvata* incubations						
	190		290		Significant effect		
	+Fe	Control	+Fe	Control	Fe	CO_2	Fe-CO_2
Volume (μm^3)	31 ± 2^a	34 ± 4^a	34 ± 4^a	32 ± 3^a			
POC (pg C cell^{-1})	12.8 ± 0.9^a	11.7 ± 0.8^a	9.4 ± 0.9^b	8.2 ± 0.6^b		X	
PON (pg N cell^{-1})	2.1 ± 0.1^b	1.7 ± 0.1^a	1.5 ± 0.2^a	1.5 ± 0.2^a		X	
C:N (mol mol^{-1})	7.2 ± 0.6^a	8.1 ± 0.2^b	7.4 ± 0.4^a	6.9 ± 0.1^a			X
BSi (pg Si cell^{-1})	2.6 ± 0.2^a	2.8 ± 0.4^a	2.6 ± 0.2^a	3.1 ± 0.5^a			

At *190*, lowered Fe concentration led to a decrease of cellular PON concentrations by 19% (post hoc: $p < 0.03$), while no Fe effect was observed at *290*. In response to increasing pCO_2, the cellular PON concentration was strongly reduced (2-way ANOVA: $p = 0.005$; Table 7.2) in the *+Fe* (post hoc: $p < 0.004$), but not in the *Control* treatments (Table 7.2).

The PON production (Fig. 7.1C) followed the same pattern as cellular PON quotas, showing a significant decrease of 15% with reduced Fe availability in the *190* treatments (post hoc: $p < 0.03$), while remaining constant in the *290* treatments. With increasing pCO_2, a loss of 26% in PON production in the *+Fe* (post hoc: $p < 0.02$), but not in the *Control* treatments was observed, resulting from an interactive effect of Fe and CO_2 availability (2-way ANOVA: $p < 0.02$; Fig. 7.1C).

Molar C:N ratios ranged between 6.9 ± 0.1 and 8.1 ± 0.2 mol C : mol N. Fe deficiency led to a 13% increase in the C:N ratio in the *190* treatments (post hoc: $p < 0.04$), while no such Fe effect was observed in the *290* treatments. Furthermore, the increase of CO_2 concentration resulted in a decline of C:N by 15% in the *Control* (post hoc: $p < 0.02$), but not in the *+Fe* treatments. The interaction of Fe and CO_2 altered C:N ratios significantly (2-way ANOVA: $p < 0.03$; Table 7.2).

Neither low Fe concentrations nor increased pCO_2 changed the cellular BSi quota (Table 7.2). However, as a result of Fe deficiency the BSi production in *290* significantly increased by 35% (2-way ANOVA: $p = 0.007$; post hoc: $p = 0.006$; Fig. 7.1D), but not in *290*. A response to higher pCO_2 resulted in higher BSi production only in the *Control* treatments (post hoc: $p < 0.04$).

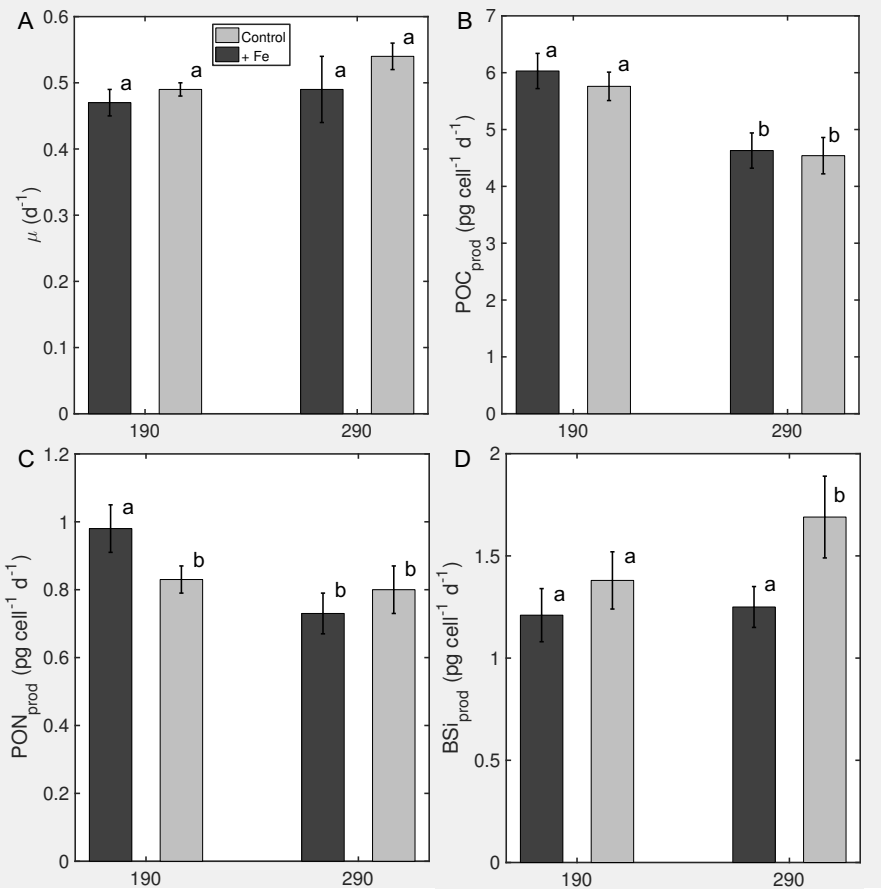

FIGURE 7.1: Effects of Fe reduction (*+Fe* vs *Control*) and pCO_2 increase (*190* vs *290*) on (A) growth rate (μ), (B) POC production, (C) PON production and (D) BSi production in the four treatments of *P. subcurvata* (*+Fe 190*, *Control 190*, *+Fe 290* and *Control 290*) at the end of the experiment. The values represent the means $\pm$ SD (n=3). Significant statistical differences between the individual treatments were determined with post hoc tests and are denoted by different letters ($p < 0.05$).

7.3.3 Pigment composition

All quantified pigments, except for Chl c_2, were significantly affected by Fe deficiency in either the *190* or the *290* treatments (2-way ANOVA: Chl *a* $p < 0.001$; Fuco $p < 0.02$; Dd $p < 0.02$; Dt $p < 0.02$; Fig. 7.2A and Table 7.3). At *190*, reduced Fe availability resulted in a decrease of Chl *a* by 37% (post hoc: $p = 0.002$), of Fuco by 34% (post hoc: $p < 0.02$) and of Dd by 29% (post hoc: $p = 0.03$), while Dt was not affected. At *290*, the reduction of Fe significantly reduced the Chl *a* concentration by 23% (post hoc: $p = 0.03$) and Dt by 60% (post hoc: $p = 0.007$), whereas Fuco and Dd remained constant. In response to elevated pCO_2, cellular Chl *a* quotas of *P. subcurvata* were significantly reduced in the *+Fe* (251 ± 17 to 192 ± 19 fg cell^{-1} for *190* and *290*, respectively; 2-way ANOVA: $p < 0.03$; post hoc: $p = 0.02$; Fig. 7.2A), while this trend was absent in the *Control*. No other pigments (Fuco, Chl c_2, Dd or Dt) responded to changes in the pCO_2.

The Chl *a*:C ratio in *P. subcurvata* was significantly affected by Fe deficiency (2-way ANOVA: $p = 0.005$; Table 7.3) leading to a decrease of 33% (post hoc: $p < 0.03$) and 27% (post hoc: $p < 0.04$) in the *190* and *290* treatments, respectively. Conversely, increased pCO_2 had no effect on the Chl *a*:C ratio.

TABLE 7.3: Pigment concentrations determined at the end of the experiment in the four treatments of *P. subcurvata* (*+Fe 190*, *Control 190*, *+Fe 290* and *Control 290*). The values represent the means ± SD (n=3). Significant statistical differences between the individual treatments were determined with post hoc test and are denoted by different letters ($p < 0.05$), while the overall effects of Fe and CO_2 were determined via 2-way ANOVA and in case they were significant indicated by X in the 'Significant effect' column.

Parameter	*P. subcurvata* incubations				Significant effect		
	190		290				
	+Fe	Control	+Fe	Control	Fe	CO_2	Fe-CO_2
Chlorophyll c_2 (fg cell^{-1})	28.9 ± 6.9^a	19.4 ± 5.7^a	22.3 ± 5.1^a	19.1 ± 5.0^a			
Fucoxanthin (fg cell^{-1})	140 ± 10^a	93 ± 24^b	110 ± 16^a	$86 \pm 24^{a,b}$	X		
Diadinoxanthin (fg cell^{-1})	28.3 ± 3.8^a	19.4 ± 4.5^b	24.1 ± 4.3^a	$17.7 \pm 3.9^{a,b}$	X		
Diatoxanthin (fg cell^{-1})	1.27 ± 0.24^a	$1.08 \pm 0.12^{a,b}$	1.47 ± 0.44^a	0.64 ± 0.21^b	X		
Chl *a*:C (mol mol^{-1})	0.21 ± 0.03^a	0.14 ± 0.02^b	0.22 ± 0.04^a	0.16 ± 0.03^b	X		

7.3.4 Maximum quantum yield and changes to PSII

The photosynthetic yield of *P. subcurvata* (F_v/F_m) showed a significant Fe effect (2-way ANOVA: $p < 0.001$; Fig. 7.2B). At *190*, F_v/F_m decreased significantly by 21% in response to Fe deficiency (from 0.52 ± 0.01 to 0.41 ± 0.02 in the *+Fe* and *Control*, respectively, post hoc: $p < 0.001$), while no Fe effect was observed in *290*. Interestingly, CO_2 enhancement differently affected the photosynthetic yield of the two Fe treatments. While increasing pCO_2 enhanced the F_v/F_m in the *Control* treatment by 15% (from 0.41 ± 0.02 to 0.47 ± 0.01, post hoc: $p = 0.005$), it reduced F_v/F_m in the *+Fe* treatments by 8% (from 0.52 ± 0.01 to 0.48 ± 0.01, post hoc: $p < 0.04$). Hence, there was a significant interactive effect of CO_2 and Fe availability on F_v/F_m (2-way ANOVA: $p = 0.002$; Fig. 7.2B).

The connectivity (P) was significantly affected by Fe deficiency (2-way ANOVA: $p = 0.002$; Table 7.4), with the *Control* treatment having an 11% smaller energy transfer between PSII units than the *+Fe* at *190* (post hoc: $p = 0.002$). In the *290* treatments, a similar, however, not significant, decreasing trend was seen. In contrast, no response of P to increased CO_2 was observed.

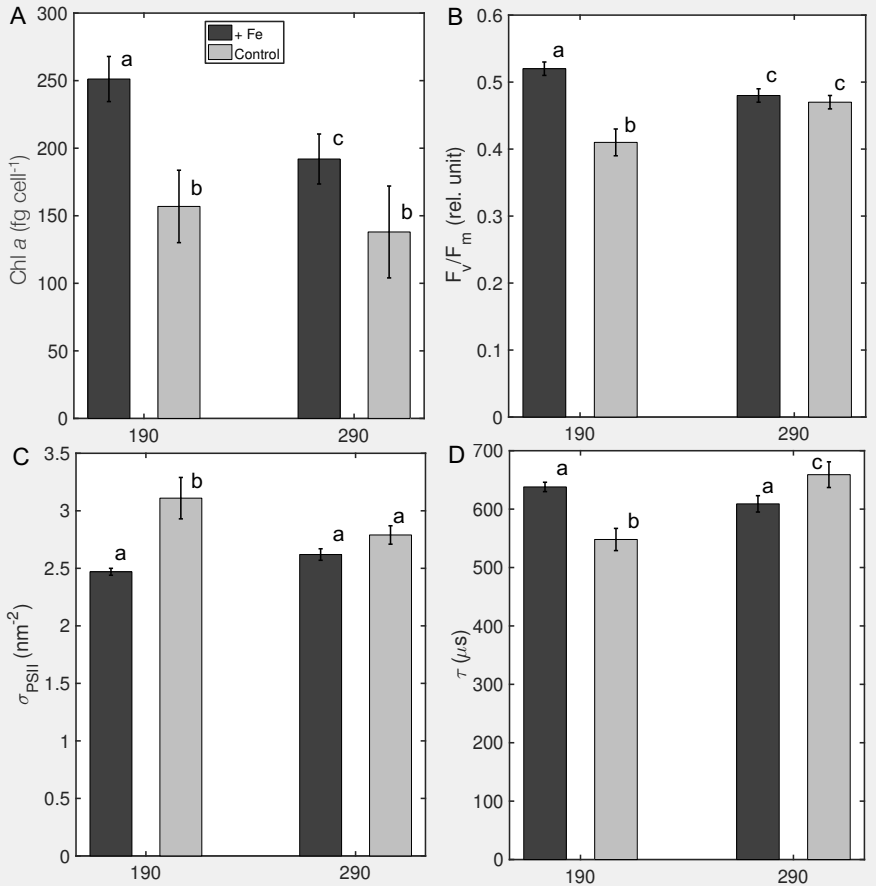

FIGURE 7.2: Effects of Fe deficiency and pCO_2 increase on (A) chlorophyll *a* (Chl *a*), (B) photosynthetic yields (F_v/F_m), (C) functional absorption cross sections (σ_{PSII}) and (D) time constants (τ) in the four treatments of *P. subcurvata* (*+Fe 190*, *Control 190*, *+Fe 290* and *Control 290*) at the end of the experiment. The values represent the means ± SD (n=3). Significant statistical differences between the individual treatments were determined with post hoc tests and are denoted by different letters ($p < 0.05$).

The functional absorption cross section of PSII (σ_{PSII}) showed a significant effect to Fe deficiency (2-way ANOVA: $p < 0.001$; Fig. 7.2C). While σ_{PSII} increased by 26% with reduced Fe availability in *190* (from 2.47 ± 0.03 to 3.11 ± 0.18 nm^{-2}, respectively, post hoc: $p < 0.001$), this Fe effect was not seen in the *290* treatments. Furthermore, only in the *Control* treatments σ_{PSII} was reduced by 10% from 3.11 ± 0.21 to 2.79 ± 0.09 nm^{-2} between *190* and *290*, respectively (post hoc: $p = 0.01$). Moreover, there was a synergistic effect between Fe and CO_2 on σ_{PSII} (2-way ANOVA: $p = 0.009$; Fig. 7.2C).

The cellular concentration of functional PSII reaction centres (RCII) was significantly altered by Fe deficiency (2-way ANOVA: $p < 0.04$; Table 7.4). This effect was only seen in *290*, where RCII increased by 29% (post hoc: $p < 0.02$). Increasing CO_2 significantly reduced the RCII concentration (2-way ANOVA: $p < 0.05$), but only in the *+Fe* treatments (post hoc: $p < 0.02$).

Fe deficiency differently influenced the time constant for electron transport at the acceptor of PSII (τ) in the two CO_2 treatments. While lower Fe concentration reduced τ when grown at *190* (post hoc: $p < 0.001$), it was enhanced at *290* (post hoc: $p = 0.006$; Fig. 7.2D). The effect of increased CO_2 on τ was significant (2-way ANOVA: $p < 0.004$). In the *Control* treatments, τ increased from 548 ± 21 to 659 ± 23 μs from 190 to 290 μatm pCO_2 (post

hoc: $p < 0.001$) while it remained constant in the *+Fe* treatments. Hence, there was a strong interactive effect of Fe and CO_2 on τ apparent (2-way ANOVA: $p < 0.001$).

TABLE 7.4: Connectivity (P), cellular concentration of functional PSII reaction centers (RCII), light utilisation efficiency at low irradiance (α), maximum cellular electron transport rate ($cETR_{max}$) and minimum saturating irradiance (I_k,) of *P. subcurvata* in the four treatments (*+Fe 190*, *Control 190*, *+Fe 290* and *Control 290*) at the end of the experiment. The values represent the means ± SD (n=3). Significant statistical differences between the individual treatments are determined with post hoc tests and are denoted by different letters ($p < 0.05$), while the overall effects of Fe and CO_2 were determined via 2-way ANOVA and in case they were significant indicated by X in the 'Significant effect' column.

Parameter	*P. subcurvata* incubations				Significant effect		
	190		290				
	+Fe	Control	+Fe	Control	Fe	CO_2	Fe-CO_2
P (rel. unit)	0.44 ± 0.01^a	0.39 ± 0.02^b	0.43 ± 0.01^a	$0.40 \pm 0.01^{a,b}$	X		
RCII (zmol cell^{-1})	515 ± 58^a	525 ± 42^a	370 ± 38^b	519 ± 47^a	X	X	
α (rel. unit)	0.75 ± 0.13^a	0.97 ± 0.14^b	0.58 ± 0.08^a	0.82 ± 0.07^b	X	X	
$cETR_{max}$ (amol e$^-$ cell^{-1} s^{-1})	119 ± 21^a	165 ± 26^b	85 ± 5^a	139 ± 19^b	X		
I_k (μmol photons m^{-2} s^{-1})	155 ± 9^a	$171 \pm 11^{a,b}$	143 ± 15^a	169 ± 9^b	X		

7.3.5 PE-curve

The cellular electron transport rates (cETR) of all treatments followed the shape of a typical PE-curve (Fig. 7.3A). The light utilisation efficiency of *P. subcurvata* at low irradiance (α) was significantly affected by Fe deficiency (2-way ANOVA: $p = 0.005$; Table 7.4), with α increasing by 29% at *190* (post hoc: $p < 0.04$) and by 41% at *290* (post hoc: $p < 0.02$). A CO_2 effect was also observed (2-way ANOVA: $p = 0.02$), where increased CO_2 reduced α,

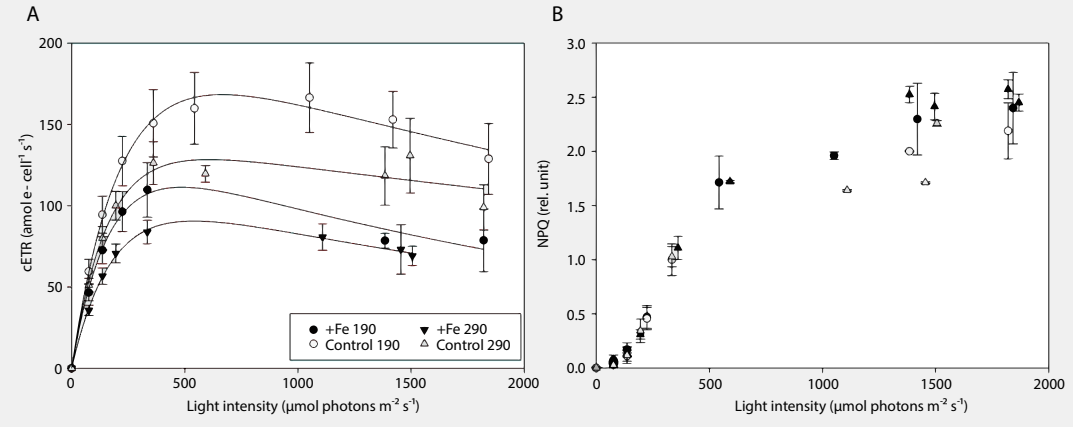

FIGURE 7.3: Effects of Fe deficiency and CO_2 increase on (A) cellular electron transport rates (cETR) and on (B) non-photochemical quenching (NPQ) in the four treatments with *P. subcurvata* (*+Fe 190*, *Control 190*, *+Fe 290* and *Control 290*) at the end of the experiment. The values represent the means ± SD (n=3).

but due to large uncertainties, the individual post hoc tests of the *+Fe* and *Control* treatments were not significant. In response to Fe deficiency, $cETR_{max}$ (Table 7.4 and Fig. 7.3A) was significantly enhanced (2-way ANOVA: $p < 0.006$) by 39% at *190* and by 64% at *290* (both post hoc: $p < 0.03$). The increase in CO_2, however, did not lead to significant changes in $cETR_{max}$. The minimum saturating irradiance (I_k) displayed a significant Fe effect (2-way ANOVA: $p < 0.02$; Table 7.4), where Ik increased by 10% in the *290* treatment (post hoc: $p < 0.04$). In the *190* treatments a similar trend was seen, but the large standard deviations prevented significant differences. I_k remained unchanged by increasing CO_2 irrespective of Fe availability.

The non-photochemical quenching of all treatments was similarly low at low irradiance (Fig. 7.3B). Exposed to irradiance higher than 350 μmol photons m^{-2} s^{-1}, the NPQ in *P. subcurvata* increased nearly linearly and then levelled off between ca. 1.5 and 2.5 for all treatments. No Fe or CO_2 effect on NPQ was observed in any treatment.

7.4 Discussion

The 'Iron Hypothesis' suggests that the fertilisation of the SO by increased dust deposition in glacial times promoted growth and productivity of phytoplankton. The biological pump in the SO was thus hypothesised to have reduced atmospheric pCO_2. In this study, we assessed the ecophysiological response of *P. subcurvata* simulating glacial and interglacial climate scenarios in terms of changes in Fe and CO_2 availability.

7.4.1 Increasing pCO_2 negatively affects POC production under Fe replete conditions

Between 190 and 290 μatm pCO_2, no change in growth rate was observed in the *+Fe* treatments of *P. subcurvata* (Fig. 7.1A). Previous laboratory studies with cultures of the same *P. subcurvata* strain also reported no changes in growth rate between 180 and 390 μatm pCO_2 (Trimborn et al., 2013). Similarly, the growth rates of the temperate *Pseudo-nitzschia pseudodelicatissima* were unaffected between 200 and 380 μatm pCO_2 (Sugie and Yoshimura, 2013), as well as the one of *T. pseudonana*, *T. rotula*, *T. oceanica* and *Proboscia alata* from 230 to 350 ppm (King et al., 2015) and from 135 to 200 μatm pCO_2 (Hoogstraten, Timmermans, and de Baar, 2012). Additionally, growth rates, pigment contents, photosynthesis and photoprotection of the Antarctic diatom *Chaetoceros brevis* did not change between 190 and 750 ppm (Boelen et al., 2011). Differently, however, is the study by (Zhu et al., 2017) which reported a stimulation of the growth rate of another *P. subcurvata* strain from 100 to 260 and 450 μatm pCO_2. Also, the growth of the temperate *Pseudo-nitzschia multiseries* was enhanced between 220 and 400 ppm pCO_2 (Sun et al., 2011). It appears therefore, that the growth of *Pseudo-nitzschia* in dependence of CO_2 presents strain-specific differences.

The similar growth rates at both pCO_2 levels and Fe availabilities maintained by *P. subcurvata* in our experiment, suggests very efficient carbon concentrating mechanisms (CCMs), which efficiently avoided CO_2 limitation. This can also be inferred from Hoppe et al. (2013) and Hoppe et al. (2013) where *Pseudo-nitzschia* was the most abundant species under both Fe-enriched and Fe-deplete conditions at 180 and 390 μatm. Previous studies showed that Antarctic phytoplankton species such as *P. subcurvata* operate very efficient CCMs which are constitutively expressed irrespective of the CO_2 availability (Tortell et al., 2008; Trimborn et al., 2008; Trimborn et al., 2013). An increase in pCO_2 decreased the Fe uptake affinity in *P. pseudodelicatissima*, which was accompanied by high uptake rates of C and nutrients, supporting the hypothesis that higher pCO_2 levels decrease the energy required for CCM operation (Sugie and Yoshimura, 2013, and references therein) and allow to maintain

high growth even under low CO_2 conditions.

In this experiment, increasing the CO_2 concentration led to a decrease of the F_v/F_m in *P. subcurvata* when Fe was added (Fig. 7.2B). Hence, F_v/F_m was highest in the *+Fe 190* treatment, indicating that *P. subcurvata* possessed highest photochemical fitness under high-Fe low-CO_2 conditions. Such a negative CO_2 effect in Fe-enriched conditions was also observed in the Chl *a* content and RCII (Table 7.3 and 7.4). Indeed, *P. subcurvata* cells grown under high-Fe high-CO_2 (*+Fe 290*) conditions had lower Chl *a* compared to the treatment at low pCO_2, thus absorbed less light for photosynthesis.

Moreover, while the BSi cell quotas and production remained constant with increasing pCO_2 in the *+Fe* treatments (Fig. 7.1D and Table 7.2), a decline in POC and PON quotas as well as in POC and PON production rates (Fig. 7.1B and Table 7.2) was induced. Such negative CO_2-effect on the POC and PON fixation again argues against CO_2 limitation of *P. subcurvata* at 190 μatm pCO_2. Reducing both POC and PON quotas, *P. subcurvata* was able to maintain constant C:N ratio with increasing pCO_2 under Fe-enriched conditions. Considering, however, that ETRs remained similar between *190* and *290* (Table 7.4), a reduction in POC and PON indicates that the contribution of linear electron transport was reduced while cycling of electron via alternative pathways was required to avoid excess light energy. These physiological characteristics resemble those observed in field incubation experiments under ocean acidification conditions, and indicate that *P. subcurvata* struggles at high pCO_2 (Tortell et al., 2008; Hoppe et al., 2013; Trimborn et al., 2017).

Overall, we can conclude that a pCO_2 of 190 μatm together with Fe enrichment was neither limiting growth nor POC production of *P. subcurvata*. On the contrary, these conditions were beneficial for biomass production and photochemical fitness of the diatom.

7.4.2 *P. subcurvata* adjusted its physiological machinery to cope with low Fe availability under glacial pCO_2 conditions

Contrary to other studies, we did not observe a decrease in cell volume in *P. subcurvata* grown with decreasing Fe availability (Marchetti and Harrison, 2007; Sugie and Kuma, 2008). This may have been masked by the fact that the *P. subcurvata* strain used in our experiment was acclimated to low Fe conditions for a long time. Indeed, it exhibited large and elongated cells compared to the much shorter cells of the stock culture grown in Fe-enriched conditions such as F2 medium containing 12 μM Fe (data not shown), thus increasing its surface area-to-volume ratio. Furthermore, this strain was isolated from open ocean waters in the Atlantic sector of the SO. It is well known that oceanic diatoms acclimate to Fe limitation by increasing their surface area-to-volume ratio in order to maximise the transporter sites and the nutrient uptake kinetics (Hudson and Morel, 1990; Sunda and Huntsman, 1995).

Many studies reported a decrease in growth rate with decreasing Fe availability (Greene, Geider, and Falkowski, 1991; Davey and Geider, 2001; Strzepek and Harrison, 2004; Marchetti et al., 2006; Marchetti et al., 2009; Marchetti and Harrison, 2007; Allen et al., 2008; Strzepek et al., 2012; Petrou et al., 2014; Schuback et al., 2015). Nonetheless, some of them also observed that particular oceanic diatoms grew at comparable rates under high and low Fe conditions (Strzepek and Harrison, 2004; Marchetti et al., 2006), as they have evolved acclimations strategies to reduce their Fe requirement. In our experiment, the growth rate of the oceanic *P. subcurvata* displayed also no difference between *+Fe* and *Control* conditions at the two pCO_2 levels tested. Marchetti and Harrison (2007) suggested that the response of physiological and biochemical parameters to Fe reduction precedes changes in growth rate. This may explain why we did not see a decrease in growth rate, despite observing typical

responses to Fe-limiting conditions as substantial reductions in photochemical quantum efficiency (Fig. 7.2B), connectivity (Table 7.4) and Chl *a* content (Fig. 7.2A) countered by an increase in functional absorption cross section (Fig. 7.2C Greene, Geider, and Falkowski, 1991; Greene et al., 1992; Davey and Geider, 2001; Strzepek et al., 2011; Strzepek et al., 2012; Petrou et al., 2014; Schuback et al., 2015; Trimborn et al., 2015).

Under Fe deficiency, lowered F_v/F_m values indicate that the excitation energy is less efficiently transferred in the antennae, due to damaged and altered parts of the photosynthetic apparatus of the phytoplankton (Greene et al., 1992). A decrease in F_v/F_m is commonly observed in cells grown in Fe-poor environments (Greene, Geider, and Falkowski, 1991; Greene et al., 1992; Strzepek et al., 2012; Petrou et al., 2014; Schuback et al., 2015; Trimborn et al., 2019), and, as expected, we observed this trend in Fe-deplete oceanic *P. subcurvata* grown at 190 μatm pCO_2. In line with the tested *P. subcurvata* here, oceanic *Pseudo-nitzschia* species usually decouple F_v/F_m and growth rate, reducing the former while maintaining the latter (Marchetti et al., 2006). This decoupling was suggested to be due to either a low energy requirement of the diatom, or a compensating mechanism that generates reducing power, and thus supports rapid growth (Marchetti et al., 2006).

The decrease in F_v/F_m and lower connectivity (P, Table 7.4) at low pCO_2 in the low Fe *P. subcurvata* cells indicate that the transfer of excitation energy to the reaction centres was compromised (Schuback et al., 2015). Fe deficiency affects the synthesis of Chl *a*, thereby significantly reducing its content, as seen in our data (Fig. 7.2A). As a consequence, light absorption was hampered in our diatom. While Davey and Geider (2001) held lowered pigment concentration during Fe starvation responsible for a decline in photosynthesis, we did not observe reduced POC production rates (Fig. 7.1B). Rather *P. subcurvata* compensated for a low Chl *a* content by increasing the absorption cross section of PSII (σ_{PSII}), which is a measure of the target area of the light harvesting antenna (Fig. 7.2C). In response to Fe deficiency this strategy can reduce the Fe demand and keep up the same capacity of the cell to absorb light (Ryan-Keogh et al., 2012). Our results agree with literature showing an increase in σ_{PSII} with Fe reduction (Greene, Geider, and Falkowski, 1991; Greene et al., 1992; Strzepek et al., 2011; Strzepek et al., 2012; Petrou et al., 2014; Schuback et al., 2015; Koch et al., 2018; Koch and Trimborn, 2019).

These photophysiological adjustments, however, did not prevent changes in light absorption completely, as shown by the strongly impacted light use capacities of Fe-limited *P. subcurvata*. Higher α values were found under Fe deficiency for both *190* and *290* treatments, indicating that photosynthesis became light-saturated at lower irradiance than for Fe-replete cells. Hence, less light was needed to cover the photosynthetic light requirement (Greene, Geider, and Falkowski, 1991). Surprisingly, this effect was counteracted by higher I_k values of *P. subcurvata*, even though this effect was not significant at *190*. In other studies, I_k either decreased (Greene, Geider, and Falkowski, 1991; McKay, Geider, and LaRoche, 1997) or remained unchanged (Davey and Geider, 2001; Trimborn et al., 2019) under Fe reduction.

Even though POC-fixation remained constant under Fe deficiency (Fig. 7.1B), $cETR_{max}$ and RCII concentration (only seen at 190 μatm pCO_2) were enhanced (Table 7.4), indicating similar linear electron transport, but also cycling of electrons into alternative pathways such as cyclic electron flow within PSII (Prasil et al., 1996) or Mehler reaction (Mehler, 1957). Considering, however, that the latter pathways are rather Fe-expensive, other pathways such as activity of a putative plastid plastoquinol terminal oxidase (PTOX) seem more plausible (Mackey et al., 2008). In support for this, Schuback et al. (2015) also observed constant C assimilation, but enhanced electron transport with Fe limitation in open ocean phytoplankton. Furthermore, a quicker turnover time at the acceptor side of PSII (τ) was found at 190 μatm pCO_2 in the Fe deficient *P. subcurvata* cells (Fig. 7.2D), supporting PTOX activity, as previously observed for the Fe-limited Antarctic diatom *Chaetoceros debilis* (Trimborn et al.,

2019). Interestingly, this was not reflected in higher NPQ activities.

At low pCO_2 the BSi quotas and production rates remained unaltered in response to Fe deficiency, as previously observed in *Chaetoceros debilis* (Trimborn et al., 2019), in *Corethron pennatum* (Timmermans, van der Wagt, and de Baar, 2004) or in *Chaetoceros dichaeta* (Hoffmann, Peeken, and Lochte, 2007). Considering the importance of Fe in C and N assimilation pathways, many studies reported a decrease in C and N under Fe deficiency (Greene, Geider, and Falkowski, 1991; Marchetti and Harrison, 2007). In Marchetti (2005) the C quota per cell volume raged between 0.02 and 0.03 pg μm^{-3} and was similar between Fe-replete and Fe-deficient treatments in the oceanic *Pseudo-nitzschia fraudulenta*, *P. heimii*, *P. inflatula* and *P. turgidula*, as well as in the coastal species *P. multiseries* and *P. pseudodelicatissima*. This matches with our results for the two tested pCO_2 levels (POC per cell volume at *190 +Fe*: 0.041 ± 0.002 pg μm^{-3}, *Control*: 0.035 ± 0.005 pg μm^{-3} and at *290 +Fe*: 0.029 ± 0.005 pg μm^{-3}, *Control*: 0.027 ± 0.003 pg μm^{-3}). The C:N ratio of diatoms was reported to increase (Sugie and Yoshimura, 2013), decrease (Bucciarelli, Pondaven, and Sarthou, 2010) or remain unchanged (Marchetti and Harrison, 2007; Trimborn et al., 2019) with reduced Fe availability. We observed an increase in the C:N ratio in response to Fe deficiency at 190 μatm pCO_2. In this case, POC quotas remained constant, whereas PON cell quotas decreased with Fe deficiency. Literature showed that Fe limitation can affect the supply of 'new nitrogen' to the cell as Fe is needed in some N-rich enzymes (Morel, Hudson, and Price, 1991; Milligan and Harrison, 2000). Koch et al. (2018) observed less abundant transcripts for nitrite reductase under Fe limiting conditions in *Phaeocystis antarctica*. Considering this, our reduced PON-fixation in *P. subcurvata* under low Fe conditions in conjunction with low pCO_2 could be coupled to a protein recycling process to avoid N-limitation (Allen et al., 2008; Nunn et al., 2013; Koch et al., 2018).

We can conclude that Fe deficiency results in a less efficient transfer of excitation energy in *P. subcurvata*, allowing it to reduce its Fe demand. In order to keep up the same POC production, *P. subcurvata* needed to rely on alternative electron pathways such as cyclic electron flow as well as PTOX activity to prevent over-excitation.

7.4.3 Increasing pCO_2 counteracted photophysiological adjustments to low Fe availability, but did not promote biomass build up

Previous experiments with *Pseudo-nitzschia* demonstrated on the one hand that the cell volume of of Fe-replete *P. pseudodelicatissima* decreased significantly as pCO_2 increased (Sugie and Yoshimura, 2013), while, on the other hand, cell volume was found to decrease with decreasing Fe availability (Marchetti and Harrison, 2007; Sugie and Kuma, 2008). In line with this, the cell volume of the here tested *P. subcurvata* did not decrease with reduced Fe availability and increased pCO_2, potentially due to a counteracting effect of both factors together (Table 7.2).

While F_v/F_m decreased in response to Fe reduction at *190* (Fig. 7.2B), such Fe-dependent decrease in F_v/F_m was not observed at *290*. This indicates that increasing pCO_2 had a positive effect on the maximum photochemical efficiency of low Fe *P. subcurvata* cells. A similar profitable modulation by high CO_2 concentration was also found for σ_{PSII} in Fe-deplete cells, being much smaller (Fig. 7.2C). Apparently, these positive CO_2 effects weakened the strong Fe reduction effects previously observed at *190*. Such positive response did, however, not translate into more efficient energy transfer from photochemistry to biomass production. In fact, re-oxidation of the primary electron acceptor Q_a of low Fe cells was strongly compromised at *290* (Fig. 7.2D). This was associated with reduced POC fixation and enhanced cETRs at *290*, and as a consequence, alternative electron acceptors were required.

Due to a synergetic effect of reduced Fe availability and increased pCO_2, in our experiment we observed the highest BSi production in low Fe and high pCO_2 conditions (Fig. 7.1D). This increase in BSi production with reduced Fe concentrations at *290* hints towards stronger silicification and the production of thicker shells in *P. subcurvata* (Hutchins and Bruland, 1998; Takeda, 1998; Boyle, 1998).

7.5 Conclusion: glacial vs. interglacial

In our study, *P. subcurvata* in an Fe-fertilised glacial ocean (*+Fe 190*) displayed similar growth rates as in interglacial ocean conditions (*Control 290*), despite lower Fe availability, hinting towards acclimation strategies to reduce the Fe requirement. Under glacial conditions, electrons were more efficiently transferred (higher P, lower τ), leading to higher cellular POC and PON concentrations and production rates. In comparison, the interglacial conditions with higher pCO_2 and reduced Fe availability, resulted in reduced POC buildup. Thus, we observed that the POC production of *P. subcurvata* was positively affected by both higher Fe availability and lower CO_2 concentration in the glacial ocean conditions. Indeed, lower pCO_2 favoured production, rather than being a limiting factor for *P. subcurvata*. Under the assumption that *P. subcurvata* dominated phytoplankton blooms in the SO in glacial and interglacial times, from our data we may conclude that *P. subcurvata* contributed more to primary production in glacial than interglacial ocean conditions. The higher POC production facilitated higher CO_2 uptake from the atmosphere and potentially higher C export in glacial conditions. This matches the 'Iron Hypothesis' of Martin (1990), which states that higher Fe input from dust in the LGM, fertilised the SO and led to higher primary production, reducing thereby the atmospheric CO_2 concentration. On the other hand, however, the thicker shells of *P. subcurvata* in the *290 Control* treatments hint towards reduced grazing and thus its higher contribution to C export in interglacial conditions (Hamm et al., 2003).

Biogeochemical cycles changed in the past and will change in response to future global climate change. Thus, understanding the dynamic interactions of the ocean's biogeochemistry and phytoplankton is important in order to better simulate past climatic scenarios and predict future environments.

Acknowledgements

This work was supported by German Federal Ministry of Education and Research (BMBF) as Research for Sustainability initiative (FONA); www.fona.de through Palmod project. We thank (in alphabetical order) T. Brenneis, C. Völkner and D. Wilhelms-Dick for laboratory assistance and for analysing the samples. Thanks also to K. Bischof and B. Meyer-Schlosser for the pigment analysis. ST, FK and FP were funded by the Helmholtz Association (HGF Young Investigators Group EcoTrace, VH-NG-901).

8 Conclusion and outlook

The oceanic Fe cycle is characterised by rather complex interactions of physical, biological and chemical processes. The unique property of Fe to behave both as a phytoplankton nutrient and as a scavenged element, makes Fe a very peculiar and interesting element. dFe is removed from the water column either by biological uptake or by physical scavenging on sinking particles. As a consequence of the dFe removal by scavenging, the residence time of dFe in the ocean is much shorter compared to other nutrients. This implies that the concentration of dFe and its distribution in the ocean are strongly dependent on its external and internal sources.

The performance of REcoM2 in reproducing dFe concentration in the world's oceans has been diagnosed. The modelled surface dFe values in the Atlantic Ocean resemble to a certain extent the observed meridional distribution. However, the concentrations downwind of the Sahara Desert are largely overestimated. In the Indian Ocean, the model reproduces high surface dFe concentrations in the Arabian Sea and low concentrations in the Bay of Bengal, while the concentrations in the open ocean are underestimated. The low surface dFe concentrations in the Southern Ocean and Pacific Ocean are roughly matched by the model, though the subtropical Pacific Ocean is too Fe-limited. At intermediate depth, observations show high dFe concentrations off Peru and Mexico due to upwelling and continental input. These features are partially reflected in the model output. Finally, the modelled deep ocean dFe concentrations are too homogeneous in comparison to the observations, which show diverse concentrations. This is most likely a consequence of a constant ligand distribution and the absence of a hydrothermal dFe source in the REcoM2 model.

In a sensitivity study on the scavenging rate (Chapter 4), we observed that different strengths of scavenging affect the world's oceans dFe concentration in a similar manner. In contrast, varying the sediment source not only influences the deep ocean dFe concentration in all basins, but also creates inter-basin differences. The surface Pacific Ocean for example, was much stronger affected by an enhanced sedimentary dFe input than other ocean basins. This study highlighted, how ocean basins react differently to changes in the dFe sediment source and that a simple tuning exercise on the scavenging rate and the sedimentary input of dFe only showed limited improvement in the simulation of the dFe concentration distribution in the oceans. A better simulation would probably require introducing new dFe sources and increasing the complexity of the description of the processes included in the model. Indeed, by missing important processes involved in the Fe cycle, the global biogeochemical model was shown not to be capable of reproducing the dFe distribution in wide regions of the oceans, as reflected in the weak correlation between in-situ data and colocated model values calculated in this study.

For the further progress of this thesis, we acknowledged this shortcoming on the side of the used global biogeochemical model - a shortcoming which is shared by most global biogeochemical models including an Fe cycle (Tagliabue et al., 2016). To improve the model's reproduction of regional patterns, we decided to pay particular attention to local processes and ocean basin differences. Therefore, two regions were investigated with respect to new dFe sources and sinks: the subtropical North Atlantic (Chapter 5) and the Southern Ocean

(Chapter 6).

The subtropical North Atlantic (Chapter 5) is characterised by high dust deposition and intensive Fe cycling. Based on observations from the GEOTRACES GA03 cruise, we reproduced the main dFe features and explained the key processes affecting the dFe concentrations along the section. This was achieved by introducing new dFe sources and sinks, as well as by changing some parameterisation. Introducing dFe scavenging on lithogenic particles reduced the overestimation in the surface water. Combined with scavenging on dead organic matter and the newly added scavenging on living phytoplankton, it intensified the subsurface dFe minimum. A new ligand parameterisation based on AOU was used to describe the high dFe concentrations in the OMZ off Cape Verde. Moreover, we increased the speed of sinking particles in order to deepen the too shallow remineralisation depth in the model, i.e. the depth at which recycling of dFe from organic matter occurs. Our model, as many other biogeochemical models, simulates a too homogeneous deep ocean dFe distribution. We learned that the observed East-West gradient at depth in the subtropical North Atlantic is generated by scavenging on dust. The model showed that more dFe is scavenged in the East, reducing the concentration at the surface as well as at depth. Furthermore, less dFe is recycled by sinking organic particles. The too homogeneous dFe concentrations modelled in the deep, could be rectified by introducing scavenging on dust, as well as by a deeper remineralisation and a new ligand concentration (not constant anymore). Additionally, we included a hydrothermal dFe source, which enabled the model to partly reproduce the plume of higher dFe concentrations expanding from the Mid-Atlantic-Ridge.

This study offered the possibility to understand which dFe sources and sinks are of key importance in the biogeochemistry of the subtropical North Atlantic Ocean. It provided important insight into the relative contribution of processes affecting the marine Fe cycle. It would be interesting to further investigate the impacts that these model changes have on the global distribution of marine primary production, as well as on the cycling of other elements, especially carbon. The new description of the Fe cycle improved the agreement between modelled and measured dFe distribution in the subtropical North Atlantic. However, no extensive study on its global effects was performed. This should be carried out in the future with the aim to set a new 'standard' description of the Fe cycle, which can be used by modellers of REcoM2 to further experiment on biogeochemical cycles. Yet, it is already clear that the ligand parameterisation used here, which is based on AOU as a measure of local remineralisation, cannot be applied globally, as too high dFe concentrations would be modelled in the deep Pacific Ocean. This reflects, that AOU accumulates over the course of the overturning circulation, which is probably not the case for Fe-binding ligands. Thus, for the next regional study reported in this thesis, the model experiments included all changes but the ligand parameterisation and the hydrothermal input.

Differently to the subtropical North Atlantic, the Southern Ocean (Chapter 6) is a large HNLC region, where aeolian deposition is low and dFe is a limiting micro-nutrient for phytoplankton. In this study, we analysed the importance of icebergs as a source of dFe to the surface waters. We learned, that when the dFe input is rather small, the dFe concentration mainly increases along the coast of Antarctica, while when the input is larger, the anomaly additionally expands farther north in a windmill-like pattern similar to the one described by the average trajectories of icebergs. The Fe fertilisation by icebergs in the model led to a clear increase in the net primary production of diatoms, while small phytoplankton showed more complex patterns. The regions of increased biomass of diatoms coincided with those of increased dFe concentration. On the contrary, the biomass of small phytoplankton mainly increased north of 55°S. Nevertheless, the combined increase in diatoms and small phytoplankton resulted in an enhanced C export from the water column in the Southern Ocean. We further

observed that Si:N export in the region was reduced by the additional dFe supply, caused by the reduced Si:N ratio in the diatoms' cells. It is important to consider the impact of dFe on the cellular Si:N/Si:C ratios in diatoms in order to study the Si and C export with changing dFe supplies. In future warmer climate scenarios more iceberg calving from the Antarctic continent is predicted. This could lead to an Fe fertilisation of the Southern Ocean affecting marine biota and having feedback effects on climate. The influence of icebergs to the dFe distribution in the Southern Ocean is a rather new field of research with a lot of potential for new studies. For example, a detailed analysis of the seasonality of icebergs' melting and thus the dFe supply to the seawater could be investigated, or a discussion on the depth of freshwater injection, its effects on the stratification of the upper ocean layers and thus on the surface dFe concentrations could be carried out.

Besides the local effects of icebergs and shelf regions in the Southern Ocean, widespread Fe fertilisation also occurred in the past during glacial periods due to larger dust deposition, as described in the "Iron Hypothesis" (Martin, 1990). In a laboratory experiment (Chapter 7) we grew the ecologically important Southern Ocean diatom *Pseudo-nitzschia subcurvata* under simulated glacial and interglacial climatic conditions. Here, the effect of two different dFe concentrations (growth-limiting and non-limiting) and pCO_2 levels (180 and 280 μatm) on the growth, carbon production and photophysiology of the diatom were analysed. In our experiment, *P. subcurvata* grew with similar rates in both conditions typical for a glacial and interglacial ocean. Under glacial conditions, the electrons generated at the photosystem PSII were efficiently transferred through the electron transport chain in the thylakoid membrane, and led to higher POC and PON production (Fig. 1.1). On the contrary, in interglacial conditions, though a similar amount of energy passed through the PSII, less biomass was produced due to higher pCO_2. The results showed that the combination of higher Fe availability with lower pCO_2, thus the glacial ocean, was beneficial for *P. subcurvata*. An increase in primary production of the bloom-forming *P. subcurvata* may have favoured the uptake of atmospheric CO_2 and potentially increased C export.

We further observed higher Si production in the interglacial conditions implying a higher degree of silicification. This corresponds to the result in the model experiment in the Southern Ocean in which, under Fe limited conditions (control run), the Si uptake by diatoms was maintained while N uptake was reduced. Similar results on the dependency of the Si:N ratio under Fe limitation have been found in other laboratory studies, and imply that diatoms under Fe-limitations have thicker shells. Possible consequences would be that Southern Ocean diatoms under Fe limitation undergo less grazing, and that also recycling by remineralisation is more difficult. Consequently, this has implications on the amount of C exported from the Southern Ocean surface into the deep ocean on the longer term.

It would be interesting to perform this experiment with a phytoplankton community as opposed to the single-species experiment reported here, to verify whether *P. subcurvata* actually dominates the bloom in both glacial and interglacial conditions. Furthermore, the results of the laboratory experiment could be incorporated in the physiological parameters of the biogeochemical model, considering *P. subcurvata* to be a typical Southern Ocean diatom.

The marine Fe cycle is modelled in biogeochemical models with different levels of complexity, also depending on the scientific question which is intended to be answered. This thesis contributes to the process-understanding of the Fe cycle by testing the impact of certain processes. We showed that including new sources helps to improve the understanding and the representation of the dFe distribution in the ocean. There is a lot of potential for further general improvements of the biogeochemical model REcoM2, which can be tested in the future. For example: 1) the constant Fe solubility of dust could be replaced with a field of varying solubilities; 2) the sediment source could be described more mechanistically; 3) the colloidal

size fraction, as well as the processes of colloidal pumping, could be included explicitly; 4) the ecosystem description could be made more comprehensive by accounting for more than the present two phytoplankton and one zooplankton groups.

But why do we care about the Fe cycle at all?

We model the Fe cycle because every living being on Earth necessitates Fe. Plants need it for photosynthesis and mammals for blood formation and oxygen transport. This holds true also for marine phyto- and zooplankton - and this can be modelled. However, Fe is a micro-nutrient and shows problematically low concentrations in the seawater - and this can be modelled. The more Fe is available in the ocean, the happier are algae and they feed, grow and reproduce greatly. This also means that they take up more CO_2 - and this can be modelled. The CO_2 that we humans so carelessly emit into the atmosphere, is stored and buried by oceanic algae in a much higher amount than tropical forests (and even more since forests are being felled irresponsibly) - and this can be modelled. Thus, Fe regulates how much CO_2 is in the atmosphere, influencing the climate of future scenarios as well as of past ice ages - and this can be modelled. The inconspicuous Fe in the ocean has impressive feedback effects in the Earth system - it is the pinch of salt in the cake.

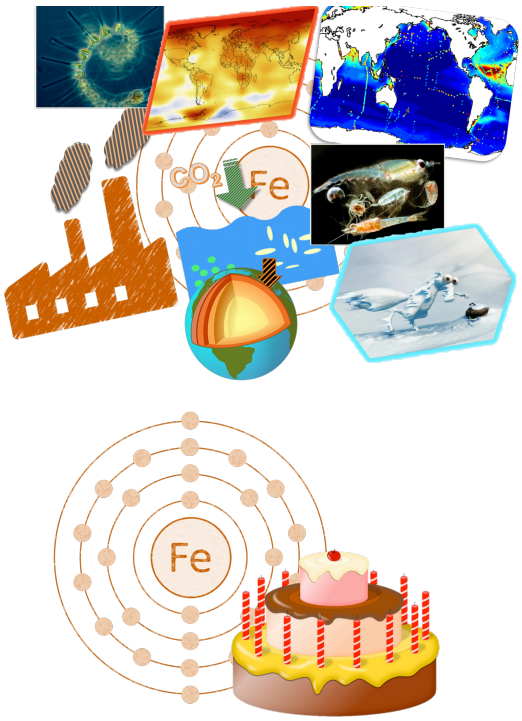

FIGURE 8.1: Slides of the Science Slam 2017/18

FIGURE 8.2: **Science and Art:** Iron and life in the water column. Exposed at the N^2 Science Communication Conference Art Contest, Berlin 2017

List of Figures

List of Tables

List of Acronyms

ACC **A**ntarctic **C**ircumpolar **C**urrent

AOU **A**pparent **O**xygen **U**tilisation

DCM **D**eep **C**hlorophyll **M**aximum

DIC **D**issolved **I**norganic **C**arbon

DIN **D**issolved **I**norganic **N**itrogen

FeMIP **Fe** **M**odel **I**nter-comparison **P**roject

FESOM **F**inite **E**lement **S**ea-**I**ce **O**cean **M**odel

HNLC **H**igh **N**utrient **L**ow **C**hlorophyll

IDP **I**ntermediate **D**ata **P**roduct

LGM **L**ast **G**lacial **M**aximum

MAR **M**id **A**tlantic **R**idge

MITgcm **M**assachusetts **I**nstitute of **T**echnology **g**eneral **c**irculation **m**odel

NPP **N**et **P**rimary **P**roduction

NPQ **N**on **P**hotochemical **Q**uenching

OM **O**rganic **M**atter

OMZ **O**xygen **M**inimum **Z**one

POC **P**articulate **O**organic **C**arbon

PON **P**articulate **O**organic **N**itrogen

ppm **p**arts **p**er **m**illion

PSI **P**hoto**S**ystem **I**

PSII **P**hoto**S**ystem **II**

REcoM2 **R**egulated **Eco**system **M**odel version **2**

SO **S**outhern **O**cean

TA **T**otal **A**lkalinity

TM **T**race **M**etal

WOA **W**orld **O**cean **A**tlas

Acknowledgements

I would like to thank Dr. Christoph Völker for the opportunity to carry out my PhD thesis in the realms of the section Marine Biogeoscience at the Alfred Wegener Institut. A special thanks goes to Dr. Christoph Völker and Dr. Ying Ye for their constant advice during the last three years. I am also thankful to Prof. Dr. Scarlett Trimborn, who gave me the opportunity to perform a laboratory experiment within the EcoTrace working group. In alphabetical order, I thank Tina Brenneis, Britta Meyer-Schlosser, Christian Völkner and Dr. Dorothee Wilhelms-Dick for the help given me during the experiment and for analysing the samples. I thank Prof. Dr. Gerrit Lohmann and Prof. Dr. Dieter Wolf-Gladrow for their support. Furthermore, I would like to thank Dr. Florian Koch for asking me to join the Polarstern expedition PS112. I am also grateful to Polmar for contributing in the expenses to participate at an international conference.

This work was supported by German Federal Ministry of Education and Research (BMBF) as Research for Sustainability initiative (FONA); www.fona.de through Palmod project.

I thank all the former and current members of the Marine Biogeoscience section for the time spent together. A very special thank goes to my PhD (or PhD to be) friends Eva, Franziska, Marianne, Sebastian and the members of the Dokteams 2017-2018 and 2018-2019 as well as many others for making this time memorable.

Most important, I am grateful to my parents, grandparents, Carlo, Stefania and Chilly for giving me financial and emotional support during my studies. Finally, I would like to thank Alex, my beloved boyfriend, for supporting me and encouraging me to finish this PhD.

Bibliography

Albani, S. et al. (2014). "Improved dust representation in the Community Atmosphere Model". In: *Journal of Advances in Modeling Earth Systems*. doi: 10.1002/2013MS000279.

Albani, S. et al. (2016). "Paleodust variability since the Last Glacial Maximum and implications for iron inputs to the ocean". In: *Geophysical Research Letters*. doi: 10.1002/2016GL067911.

Allen, A. E. et al. (2008). "Whole-cell response of the pennate diatom *Phaeodactylum tricornutum* to iron starvation". In: *Proceedings of the National Academy of Sciences*. doi: 10.1073/pnas.0711370105.

Anderson, R. F. et al. (2014). "Biological response to millennial variability of dust and nutrient supply in the Subantarctic South Atlantic Ocean". In: *Philosophical Transactions of the Royal Society A: Mathematical, Physical and Engineering Sciences*. doi: 10.1098/rsta.2013.0054.

Archer, D. E. and K. Johnson (2000). "A model of the iron cycle in the ocean". In: *Global Biogeochemical Cycles*. doi: 10.1029/1999GB900053.

Arrigo, K. R. et al. (1999). "Phytoplankton Community Structure and the Drawdown of Nutrients and CO_2 in the Southern Ocean". In: *Science*. doi: 10.1126/science.283.5400.365.

Assmy, P. et al. (2013). "Thick-shelled, grazer-protected diatoms decouple ocean carbon and silicon cycles in the iron-limited Antarctic Circumpolar Current". In: *Proceedings of the National Academy of Sciences*. doi: 10.1073/pnas.1309345110.

Aumont, O. and L. Bopp (2006). "Globalizing results from ocean in situ iron fertilization studies". In: *Global Biogeochemical Cycles*. doi: 10.1029/2005GB002591.

Aumont, O. et al. (2003). "An ecosystem model of the global ocean including Fe, Si, P colimitations". In: *Global Biogeochemical Cycles*. doi: 10.1029/2001GB001745.

Aumont, O. et al. (2015). "PISCES-v2: an ocean biogeochemical model for carbon and ecosystem studies". In: *Geosci. Model Dev. Discuss*. doi: 10.5194/gmdd-8-1375-2015.

Baker, A. R. and P. L. Croot (2010). "Atmospheric and marine controls on aerosol iron solubility in seawater". In: *Marine Chemistry*. doi: 10.1016/j.marchem.2008.09.003.

Balistrieri, L., P. G. Brewer, and J. W. Murray (1981). "Scavenging residence times of trace metals and surface chemistry of sinking particles in the deep ocean". In: *Deep Sea Research Part A. Oceanographic Research Papers*. doi: 10.1016/0198-0149(81)90085-6.

Barbeau, K. et al. (2001). "Photochemical cycling of iron in the surface ocean mediated by microbial iron(III)-binding ligands". In: *Nature*. doi: 10.1038/35096545.

Beaulieu, S. E., E. T. Baker, and C. R. German (2015). "Where are the undiscovered hydrothermal vents on oceanic spreading ridges?" In: *Deep Sea Research Part II: Topical Studies in Oceanography*. doi: 10.1016/j.dsr2.2015.05.001.

Beckler, J. S., M. E. Jones, and M. Taillefert (2015). "The origin, composition, and reactivity of dissolved iron(III) complexes in coastal organic- and iron-rich sediments". In: *Geochimica et Cosmochimica Acta*. doi: 10.1016/j.gca.2014.12.017.

Behrenfeld, M. J. and A. J. Milligan (2013). "Photophysiological Expressions of Iron Stress in Phytoplankton". In: *Annual Review of Marine Science*. doi: 10.1146/annurev-marine-121211-172356.

Behrenfeld, M. J. et al. (1996). "Confirmation of iron limitation of phytoplankton photosynthesis in the equatorial Pacific Ocean". In: *Nature*. doi: 10.1038/383508a0.

Bennett, S. et al. (2008). "The distribution and stabilisation of dissolved Fe in deep-sea hydrothermal plumes". In: *Earth and Planetary Science Letters*. doi: 10.1016/j.epsl.2008.01.048.

Berelson, W. et al. (2003). "A time series of benthic flux measurements from Monterey Bay, CA". In: *Continental Shelf Research*. doi: 10.1016/S0278-4343(03)00009-8.

Bergquist, B. A. and E. A. Boyle (2006). "Dissolved iron in the tropical and subtropical Atlantic Ocean". In: *Global Biogeochemical Cycles*. doi: 10.1029/2005GB002505.

Bergquist, B. A., J. Wu, and E. A. Boyle (2007). "Variability in oceanic dissolved iron is dominated by the colloidal fraction". In: *Geochimica et Cosmochimica Acta*. doi: 10.1016/j.gca.2007.03.013.

Blain, S., G. Sarthou, and P. Laan (2008). "Distribution of dissolved iron during the natural iron-fertilization experiment KEOPS (Kerguelen Plateau, Southern Ocean)". In: *Deep Sea Research Part II: Topical Studies in Oceanography*. doi: 10.1016/j.dsr2.2007.12.028.

Boelen, P. et al. (2011). "Neither elevated nor reduced CO_2 affects the photophysiological performance of the marine Antarctic diatom *Chaetoceros brevis*". In: *Journal of Experimental Marine Biology and Ecology*. doi: 10.1016/j.jembe.2011.06.012.

Boiteau, R. M. et al. (2018). "Siderophore profiling of co-habitating soil bacteria by ultrahigh resolution mass spectrometry". In: *Metallomics*. doi: 10.1039/C8MT00252E.

Bonnet, S. and C. Guieu (2004). "Dissolution of atmospheric iron in seawater". In: *Geophysical Research Letters*. doi: 10.1029/2003GL018423.

Borrione, I. et al. (2014). "Sedimentary and atmospheric sources of iron around South Georgia, Southern Ocean: a modelling perspective". In: *Biogeosciences*. doi: 10.5194/bg-11-1981-2014.

Bowie, A. R. et al. (2015). "Iron budgets for three distinct biogeochemical sites around the Kerguelen Archipelago (Southern Ocean) during the natural fertilisation study, KEOPS-2". In: *Biogeosciences*. doi: 10.5194/ bg-12-4421-2015.

Boyd, P. W. and M. J. Ellwood (2010). "The biogeochemical cycle of iron in the ocean". In: *Nature Geoscience*. doi: 10.1038/ngeo964.

Boyd, P. W. et al. (2000). "A mesoscale phytoplankton bloom in the polar Southern Ocean stimulated by iron fertilization". In: *Nature*. doi: 10.1038/35037500.

Boyle, E. (1998). "Pumping iron makes thinner diatoms". In: *Nature*. doi: 10.1038/31585.

Boyle, E. A. et al. (2015). "Introduction to the U.S. GEOTRACES North Atlantic Transect (GA-03): USGT10 and USGT11 cruises". In: *Deep Sea Research Part II: Topical Studies in Oceanography*. doi: 10.1016/j.dsr2.2015.02.031.

Brewer, P. G., A. L. Bradshaw, and R. T. Williams (1986). "Measurements of Total Carbon Dioxide and Alkalinity in the North Atlantic Ocean in 1981". In: *The Changing Carbon Cycle: A Global Analysis*. Ed. by J. R. Trabalka and D. E. Reichle. doi: 10.1007/ 978-1-4757-1915-4-18. Springer New York, pp. 348–370.

Bruland, K. W., K. J. Orians, and J. P. Cowen (1994). "Reactive trace metals in the stratified central North Pacific". In: *Geochimica et Cosmochimica Acta*. doi: 10.1016/0016-7037(94)90044-2.

Brzezinski, M. A. and D. M. Nelson (1995). "The annual silica cycle in the Sargasso Sea near Bermuda". In: *Deep Sea Research Part I: Oceanographic Research Papers*. doi: 10.1016/0967-0637(95)93592-3.

Bucciarelli, E., P. Pondaven, and G. Sarthou (2010). "Effects of an iron-light co-limitation on the elemental composition (Si, C, N) of the marine diatoms *Thalassiosira oceanica* and *Ditylum brightwellii*". In: *Biogeosciences*. doi: https://hal.univ-brest.fr/hal-00472043.

Buck, K. N. and K. W. Bruland (2007). "The physicochemical speciation of dissolved iron in the Bering Sea, Alaska". In: *Limnology and Oceanography*. doi: 10.4319/lo.2007.52.5.1800.

Buck, K. N., B. Sohst, and P. N. Sedwick (2015). "The organic complexation of dissolved iron along the U.S. GEOTRACES (GA03) North Atlantic Section". In: *Deep Sea Research Part II: Topical Studies in Oceanography*. doi: 10.1016/j.dsr2.2014.11.016.

Buesseler, K.O. et al. (2001). "Upper ocean export of particulate organic carbon and biogenic silica in the Southern Ocean along 170°W". In: *Deep Sea Research Part II: Topical Studies in Oceanography*. doi: 10.1016/S0967-0645(01)00089-3.

Buitenhuis, E. T. and R. J. Geider (2010). "A model of phytoplankton acclimation to iron light colimitation". In: *Limnology and Oceanography*. doi: 10.4319/lo.2010.55.2.0714.

Burd, A. B. (2013). "Modeling particle aggregation using size class and size spectrum approaches". In: *Journal of Geophysical Research: Oceans*. doi: 10.1002/jgrc.20255.

Burdige, D. J. (1993). "The biogeochemistry of manganese and iron reduction in marine sediments". In: *Earth-Science Reviews*. doi: 10.1016/0012-8252(93)90040-E.

Byrne, R. H., L. R. Kump, and K. J. Cantrell (1988). "The influence of temperature and pH on trace metal speciation in seawater". In: *Marine Chemistry*. doi: 10.1016/0304-4203(88)90062-X.

Cassar, N. et al. (2007). "The Southern Ocean Biological Response to Aeolian Iron Deposition". In: *Science*. doi: 10.1126/science.1144602.

Cefarelli, A. O., M. Vernet, and M. E. Ferrario (2011). "Phytoplankton composition and abundance in relation to free-floating Antarctic icebergs". In: *Deep Sea Research Part II: Topical Studies in Oceanography*. doi: 10.1016/j.dsr2.2010.11.023.

Charette, M. A. et al. (2016). "Coastal ocean and shelf-sea biogeochemical cycling of trace elements and isotopes: lessons learned from GEOTRACES". In: *Philosophical Transactions of the Royal Society A: Mathematical, Physical and Engineering Sciences*. doi: 10.1098/rsta.2016.0076.

Chiapello, I. et al. (1995). "An additional low layer transport of Sahelian and Saharan dust over the north-eastern Tropical Atlantic". In: *Geophysical Research Letters*. doi: 10.1029/95GL03313.

Christian, J. R. et al. (2001). "Biogeochemical modelling of the tropical Pacific Ocean. II: Iron biogeochemistry". In: *Deep Sea Research Part II: Topical Studies in Oceanography*. doi: 10.1016/S0967-0645(01)00111-4.

Chuang, P. Y. et al. (2005). "The origin of water soluble particulate iron in the Asian atmospheric outflow". In: *Geophysical Research Letters*. doi: 10.1029/2004GL021946.

Coale, K. H. et al. (1996). "A massive phytoplankton bloom induced by an ecosystem-scale iron fertilization experiment in the equatorial Pacific Ocean". In: *Nature*. doi: 10.1038/383495a0.

Coale, K. H. et al. (2004). "Southern Ocean Iron Enrichment Experiment: Carbon Cycling in High- and Low-Si Waters". In: *Science*. doi: 10.1126/science.1089778.

Conway, T. M. and S. G. John (2014). "Quantification of dissolved iron sources to the North Atlantic Ocean". In: *Nature*. doi: 10.1038/nature13482.

Cook, A. J. et al. (2016). "Ocean forcing of glacier retreat in the western Antarctic Peninsula". In: *Science*. doi: 10.1126/science.aae0017.

Cutter, G. et al. (2017). "Sampling and Sample-handling Protocols for GEOTRACES Cruises". In: Version 3, August 2017. Toulouse, France, GEOTRACES International Project Office doi: 10.25607/OBP-2.

Cutter, G. A. et al. (2018). "Multiple oxidation state trace elements in suboxic waters off Peru: In situ redox processes and advective/diffusive horizontal transport". In: *Marine Chemistry*. doi: 10.1016/j.marchem.2018.01.003.

Davey, M. and R. J. Geider (2001). "Impact of iron limitation on the photosynthetic apparatus of the diatom *Chaetoceros muelleri* (Bacillariophyceae)". In: *Journal of Phycology*. doi: 10.1046/j.1529-8817.2001.99169.x.

de Baar, H. J. W. and J. T. M. de Jong (2001). "Distributions, sources and sinks of iron in seawater". In: *Biogeochemistry of Iron in Seawater*. Ed. by D. Turner and K. A. Hunter. Wiley.

de Baar, H. J. W. et al. (1995). "Importance of iron for plankton blooms and carbon dioxide drawdown in the Southern Ocean". In: *Nature*. doi: 10.1038/373412a0.

de Baar, H. J. W. et al. (1999). "Low dissolved Fe and the absence of diatom blooms in remote Pacific waters of the Southern Ocean". In: *Marine Chemistry*. doi: 10.1016/S0304-4203(99)00022-5.

de Baar, H. J. W. et al. (2005). "Synthesis of iron fertilization experiments: From the Iron Age in the Age of Enlightenment". In: *Journal of Geophysical Research: Oceans*. doi: 10.1029/2004JC002601.

Death, R. et al. (2014). "Antarctic Ice Sheet Fertilises the Southern Ocean". In: *Biogeosciences*. doi: 10.5194/bg-11-2635-2014.

Depoorter, M. A. et al. (2013). "Calving fluxes and basal melt rates of Antarctic ice shelves". In: *Nature*. doi: 10.1038/nature12567.

Dickson, A. G. and F. J. Millero (1987). "A comparison of the equilibrium constants for the dissociation of carbonic acid in seawater media". In: *Deep Sea Research Part A. Oceanographic Research Papers*. doi: 10.1016/0198-0149(87)90021-5.

Duce, R. A. and N. W. Tindale (1991). "Atmospheric transport of iron and its deposition in the ocean". In: *Limnology and Oceanography*. doi: 10.4319/lo.1991.36.8.1715.

Duggen, S. et al. (2010). "The role of airborne volcanic ash for the surface ocean biogeochemical iron-cycle: a review". In: *Biogeosciences (BG)*. doi: 10.5194/bg-7-827-2010.

Dulaiova, H. et al. (2009). "Shelf-derived iron inputs drive biological productivity in the southern Drake Passage". In: *Global Biogeochemical Cycles*. doi:10.1029/2008GB003406.

Duprat, L. P. A. M., G. R. Bigg, and D. J. Wilton (2016). "Enhanced Southern Ocean marine productivity due to fertilization by giant icebergs". In: *Nature Geosciences*. doi: 10.1038/ngeo2633.

Elderfield, H. and A. Schultz (1996). "Mid-Ocean Ridge Hydrothermal Fluxes and the Chemical Composition of the Ocean". In: *Annual Review of Earth and Planetary Sciences*. doi: 10.1146/annurev.earth.24.1.191.

Elrod, V. et al. (2004). "The flux of iron from continental shelf sediments: A missing source for global budgets". In: *Geophysical Research Letters*. doi: 10.1029/ 2004GL020216.

Falkowski, P. G., R. T. Barber, and V. Smetacek (1998). "Biogeochemical Controls and Feedbacks on Ocean Primary Production". In: *Science*. doi: 10.1126/science.281.5374.200.

Feng, Y. et al. (2010). "Interactive effects of iron, irradiance and CO_2 on Ross Sea phytoplankton". In: *Deep Sea Research Part I: Oceanographic Research Papers*. doi: 10.1016/j.dsr.2009.10.013.

Field, C. B. et al. (1998). "Primary Production of the Biosphere: Integrating Terrestrial and Oceanic Components". In: *Science*. doi: 10.1126/science.281.5374.237.

Fitzsimmons, J. N., R. Zhang, and E. A. Boyle (2013). "Dissolved iron in the tropical North Atlantic Ocean". In: *Marine Chemistry*. doi: 10.1016/j.marchem.2013.05.009.

Fitzsimmons, J. N. et al. (2015a). "Partitioning of dissolved iron and iron isotopes into soluble and colloidal phases along the GA03 GEOTRACES North Atlantic Transect". In: *Deep Sea Research Part II: Topical Studies in Oceanography*. doi: 10.1016/j.dsr2.2014.11.014.

Fitzsimmons, J. N. et al. (2015b). "The composition of dissolved iron in the dusty surface ocean: An exploration using size-fractionated iron-binding ligands". In: *Marine Chemistry*. doi: 10.1016/j.marchem.2014.09.002.

Fitzsimmons, J. N. et al. (2017). "Iron persistence in a distal hydrothermal plume supported by dissolved- particulate exchange". In: *Nature Geoscience*. doi: 10.1038/ngeo 2900.

Francois, R. et al. (1997). "Contribution of Southern Ocean surface-water stratification to low atmospheric CO_2 concentrations during the last glacial period". In: *Nature*. doi: 10.1038/40073.

Frants, M. et al. (2016). "Constraints on the global marine iron cycle from a simple inverse model". In: *J.Geophys. Res. Biogeoscience*. doi: 10.1002/2015JG003111.

Garcia, H. E. et al. (2010a). "World Ocean Atlas 2009 Volume 3: Dissolved Oxygen, Apparent Oxygen Utilization, and Oxygen Saturation". In: *S. Levitus, Ed., NOAA Atlas NESDIS 70, U.S. Government Printing Office, Washington, D.C.* 344 pp.

Garcia, H. E. et al. (2010b). "World Ocean Atlas 2009, Volume 4: Nutrients (phosphate, nitrate, and silicate)". In: *S. Levitus, Ed., NOAA Atlas NESDIS 71, U.S. Government Printing Office, Washington, D.C.* 398 pp.

Gartman, A., A. J. Findlay, and G. W. Luther (2014). "Nanoparticulate pyrite and other nanoparticles are a widespread component of hydrothermal vent black smoker emissions". In: *Chemical Geology*. doi: 10.1016/j.chemgeo.2013.12.013.

Geider, R. J., H. L. Macintyre, and T. M. Kana (2003). "A dynamic regulatory model of phytoplanktonic acclimation to light, nutrients, and temperature". In: *Limnology and Oceanography*. doi: 10.4319/lo.1998.43.4.0679.

Genty, B., J.-M. Briantais, and N. R. Baker (1989). "The relationship between the quantum yield of photosynthetic electron transport and quenching of chlorophyll fluorescence". In: *Biochimica et Biophysica Acta (BBA) - General Subjects*. doi: 10.1016/S0304-4165(89)80016-9.

German, C. R. and K. L. Von Damm (2003). "Hydrothermal Processes". In: *The Oceans and Marine Geochemistry*. Ed. by Turekian K. K. Holland H. D. Vol. 6. Oxford: Elsevier, pp. 181–222.

German, C. R. et al. (2016). "Hydrothermal impacts on trace element and isotope ocean biogeochemistry". In: *Philosophical Transactions of the Royal Society A: Mathematical, Physical and Engineering Sciences*. doi: 10.1098/rsta.2016.0035.

Gerringa, L. J. A., H. J. W. de Baar, and K. R. Timmermans (2000). "A comparison of iron limitation of phytoplankton in natural oceanic waters and laboratory media conditioned with EDTA". In: *Marine Chemistry*. doi: 10.1016/S0304-4203(99)00092-4.

Gerringa, L. J. A. et al. (2012). "Iron from melting glaciers fuels the phytoplankton blooms in Amundsen Sea (Southern Ocean): Iron biogeochemistry". In: *Deep Sea Research Part II: Topical Studies in Oceanography*. doi: 10.1016/j.dsr2.2012.03.007.

Ginoux, P. et al. (2001). "Sources and distributions of dust aerosols simulated with the GOCART model". In: *Journal of Geophysical Research: Atmospheres*. doi: 10.1029/2000JD000053.

Gladstone, R. M., G. R. Bigg, and K. W. Nicholls (2001). "Iceberg trajectory modeling and meltwater injection in the Southern Ocean". In: *Journal of Geophysical Research: Oceans*. doi: 10.1029/2000JC000347.

Gledhill, M. and K. Buck (2012). "The Organic Complexation of Iron in the Marine Environment: A Review". In: *Frontiers in Microbiology*. doi: 10.3389/fmicb.2012.00069.

Gran, G. (1952). "Determination of the equivalence point in potentiometric titrations- part II". In: *Analyst*. doi: 10.1039/an9527700661.

Granger, J. and N. M. Price (1999). "The importance of siderophores in iron nutrition of heterotrophic marine bacteria". In: *Limnology and Oceanography*. doi: 10.4319/lo.1999.44.3.0541.

Greene, R. M., R. J. Geider, and P. G. Falkowski (1991). "Effect of iron limitation on photosynthesis in a marine diatom". In: *Limnology and Oceanography*. doi: 10.4319/lo.1991.36.8.1772.

Greene, R. M. et al. (1992). "Iron-Induced Changes in Light Harvesting and Photochemical Energy Conversion Processes in Eukaryotic Marine Algae". In: *Plant Physiology*. doi: 10.1104/pp.100.2.565.

Gruber, N. et al. (2009). "Oceanic sources, sinks, and transport of atmospheric CO_2". In: *Global Biogeochemical Cycles*. doi: 10.1029/2008GB003349.

Guieu, C. et al. (2005). "Biomass burning as a source of dissolved iron to the open ocean?" In: *Geophysical Research Letters*. doi: 10.1029/2005GL022962.

Guillard, R. R. L. and J. H. Ryther (1962). "Studies of marine planktonic diatoms: I. *Cyclotella nana* Hustedt, and *Detonula confervacea* Cleve Gran". In: *Canadian Journal of Microbiology*. doi: 10.1139/m62-029.

Hamm, C. E. et al. (2003). "Architecture and material properties of diatom shells provide effective mechanical protection". In: *Nature*. doi: 10.1038/nature01416.

Hamme, R. C. et al. (2010). "Volcanic ash fuels anomalous plankton bloom in subarctic northeast Pacific". In: *Geophysical Research Letters*. doi: 10.1029/2010GL044629.

Hasle, G. R. (1964). "*Nitzschia* and *Fragilariopsis* species studied in the light and electron microscopes: Some marine species of the groups *Nitzschia* and *Lanceolatae*". In: *Skrifter utgitt av Det Norske Videnskaps-Akademi i Oslo*.

Hathorne, E. C. et al. (2012). "Online preconcentration ICP-MS analysis of rare earth elements in seawater". In: *Geochemistry, Geophysics, Geosystems*. doi: 10.1029/2011GC003907.

Hatta, M. et al. (2015). "An overview of dissolved Fe and Mn distributions during the 2010 2011 U.S. GEOTRACES north Atlantic cruises: GEOTRACES GA03". In: *Deep Sea Research Part II: Topical Studies in Oceanography*. doi: 10.1016/j.dsr2.2014.07.005.

Hauck, J. et al. (2013). "Seasonally different carbon flux changes in the Southern Ocean in response to the southern annular mode". In: *Global Biogeochemical Cycles*. doi: 10.1002/2013GB004600.

Hauck, J. et al. (2018). "The Fate of Carbon and Nutrients Exported Out of the Southern Ocean". In: *Global Biogeochemical Cycles*. doi: 10.1029/2018GB005977.

Hawkes, J. A. et al. (2013). "The stabilisation and transportation of dissolved iron from high temperature hydrothermal vent systems". In: *Earth and Planetary Science Letters*. doi: 10.1016/j.epsl.2013.05.047.

Hayes, C. T. et al. (2015). "Thorium isotopes tracing the iron cycle at the Hawaii Ocean Time-series Station ALOHA". In: *Geochimica et Cosmochimica Acta*. doi: 10.1016/j.gca.2015.07.019.

Hayes, C. T. et al. (2018). "Replacement Times of a Spectrum of Elements in the North Atlantic Based on Thorium Supply". In: *Global Biogeochemical Cycles*. doi: 10.1029/2017GB005839.

Heuven, S. van et al. (2011). "MATLAB Program Developed for CO_2 System Calculations. ORNL/CDIAC-105b". In: Carbon Dioxide Information Analysis Center, Oak Ridge National Laboratory, U.S. Department of Energy, Oak Ridge, Tennessee. doi:10.3334/CDIAC/otg.CO2SYS-MATLAB-v1.1.

Hillebrand, H. et al. (1999). "Biovolume calculation for pelagic and benthic microalgae". In: *Journal of Phycology*. doi: 10.1046/j.1529-8817.1999.3520403.x.

Hoffmann, L., I. Peeken, and K. Lochte (2007). "Effects of iron on the elemental stoichiometry during EIFEX and in the diatoms *Fragilariopsis kerguelensis* and *Chaetoceros dichaeta*". In: *Biogeosciences (BG)*. doi: 10.5194/bg-4-569-2007.

Hohn, S. (2009). "Coupling and decoupling of biogeochemical cycles in marine ecosystems". In: PhD thesis, Universitat Bremen.

Homoky, W. B. et al. (2016). "Quantifying trace element and isotope fluxes at the ocean-sediment boundary: a review". In: *Philosophical Transactions of the Royal Society A: Mathematical, Physical and Engineering Sciences*. doi: 10.1098/rsta.2016.0246.

Honeyman, B. D., L. S. Balistrieri, and J. W. Murray (1988). "Oceanic trace metal scavenging: the importance of particle concentration". In: *Deep Sea Research Part A. Oceanographic Research Papers*. doi: 10.1016/0198-0149(88)90038-6.

Honeyman, B. D. and P. H. Santschi (1989). "A Brownian-pumping model for oceanic trace metal scavenging: Evidence from Th isotopes". In: *Journal of Marine Research*. doi: 10.1357/002224089785076091.

— (1991). "Coupling adsorption and particle aggregation: laboratory studies of "colloidal pumping" using iron-59-labeled hematite". In: *Environ. Sci. Technol.* doi: 10.1021/es00022a010.

Hoogstraten, A., K. R. Timmermans, and H. J. W. de Baar (2012). "Morphological and physiological effects in *Proboscia alata* (Bacillariophyceae) grown under different light and CO_2 conditions of the modern Southern Ocean". In: *Journal of Phycology*. doi: 10.1111/j.1529-8817.2012.01148.x.

Hoppe, C. J. M. et al. (2013). "Iron Limitation Modulates Ocean Acidification Effects on Southern Ocean Phytoplankton Communities". In: *PLOS ONE*. doi: 10.1371/journal.pone.0079890.

Hopwood, M. J. et al. (2017). "The heterogeneous nature of Fe delivery from melting icebergs". In: *Geochemical Perspectives Letters*. doi: 10.7185/geochemlet.1723.

Hudson, R. J. M. and F. M. M. Morel (1989). "Distinguishing between extra- and intracellular iron in marine phytoplankton." In: *Limnology and Oceanography*. doi: 10.4319/lo.1989.34.6.1113.

— (1990). "lron transport in marine phytoplankton: Kinetics of cellular and medium coordination reactions". In: *Limnology and Oceanography*. doi: 10.4319/lo.1990.35.5.1002.

Hunter, K. A. and P. W. Boyd (2007). "Iron-binding ligands and their role in the ocean biogeochemistry of iron". In: *Environmental Chemistry*. doi: 10.1071/EN07012.

Hunter, K. A. et al. (1997). "Aggregation of iron colloids in estuaries: a heterogeneous kinetics study using continuous mixing of river and sea waters". In: *Colloids and Surfaces A: Physicochemical and Engineering Aspects*. doi: 10.1016/S0927-7757(96)03719-3.

Hutchins, D. A. and K. W. Bruland (1998). "Iron-limited diatom growth and Si:N uptake ratios in a coastal upwelling regime". In: *Nature*. doi: 10.1038/31203.

Jenkins, W. J. et al. (2015). "Water mass analysis for the U.S. GEOTRACES (GA03) North Atlantic sections". In: *Deep Sea Research Part II: Topical Studies in Oceanography*. doi: 10.1016/j.dsr2.2014.11.018.

Jickells, T. D. and L. J. Spokes (2001). "Biogeochemistry of Iron in Seawaters". In: *Methods of Seawater Analysis. Series on Analytical and Physical Chemistry of Environmental Systems*. Ed. by D. Turner and K. A. Hunter. Vol. 7. Wiley, pp. 85–121.

Jickells, T. D. et al. (2005). "Global Iron Connections Between Desert Dust, Ocean Biogeochemistry, and Climate". In: *Science*. doi: 10.1126/science.1105959.

Johnson, K. S. (2001). "Iron supply and demand in the upper ocean: Is extraterrestrial dust a significant source of bioavailable iron?" In: *Global Biogeochemical Cycles*. doi: 10.1029/2000GB001295.

Johnson, K. S., F. P. Chavez, and G. E. Friederich (1999). "Continental shelf sediment as a primary source of iron for coastal phytoplankton". In: *Nature*. doi: 10.1038/19511.

Johnson, K. S., R. M. Gordon, and K. H. Coale (1997). "What controls dissolved iron concentrations in the world ocean?" In: *Marine Chemistry*. doi: 10.1016/S0304-4203(97)00043-1.

Jones, M. E., J. S. Beckler, and M. Taillefert (2011). "The flux of soluble organic-iron(III) complexes from sediments represents a source of stable iron(III) to estuarine waters and to the continental shelf". In: *Limnology and Oceanography*. doi: 10.4319/lo.2011.56.5.1811.

Kanna, N., T. Toyota, and J. Nishioka (2014). "Iron and macro-nutrient concentrations in sea ice and their impact on the nutritional status of surface waters in the southern Okhotsk Sea". In: *Progress in Oceanography*. doi: 10.1016/j.pocean.2014.04.012.

Kienast, S. S. et al. (2016). "Tracing dust input to the global ocean using thorium isotopes in marine sediments: ThoroMap". In: *Global Biogeochemical Cycles*. doi: 10.1002/2016GB005408.

King, A. L. et al. (2015). "Effects of CO_2 on growth rate, C:N:P, and fatty acid composition of seven marine phytoplankton species". In: *Mar. Ecol. Prog. Ser.* doi: 10.3354/meps11458.

Klunder, M. B. et al. (2012). "Dissolved iron in the Arctic Ocean: Important role of hydrothermal sources, shelf input and scavenging removal". In: *Journal of Geophysical Research: Oceans*. doi: 10.1029/2011JC007135.

Koch, F. and S. Trimborn (2019). "Limitation by Fe, Zn, Co and B12 results in similar physiological responses in two Antarctic phytoplankton species". In: *Front. Mar. Sci.* doi: 10.3389/fmars.2019.00514.

Koch, F. et al. (2018). "The impacts of iron limitation and ocean acidification on the cellular stoichiometry, photophysiology, and transcriptome of *Phaeocystis antarctica*". In: *Limnology and Oceanography*. doi: 10.1002/lno.11045.

Kohfeld, K. E. and S. P. Harrison (2001). "DIRTMAP: the geological record of dust". In: *Earth-Science Reviews*. doi: 10.1016/S0012-8252(01)00042-3.

Kohfeld, K. E. et al. (2005). "Role of Marine Biology in Glacial-Interglacial CO_2 Cycles". In: *Science*. doi: 10.1126/science.1105375.

Kok, J. F. et al. (2018). "Global and regional importance of the direct dust-climate feedback". In: *Nature Communications*. doi: 10.1038/s41467-017-02620-y.

Kolber, Z. S., O. Prasil, and P. G. Falkowski (1998). "Measurements of variable chlorophyll fluorescence using fast repetition rate techniques: defining methodology and experimental protocols". In: *Biochimica et Biophysica Acta (BBA) - Bioenergetics*. doi: 10.1016/S0005-2728(98)00135-2.

Korb, R. E. et al. (2008). "Magnitude and maintenance of the phytoplankton bloom at South Georgia: a naturally iron-replete environment". In: *Marine Ecology Progress Series*. doi: 10.3354/meps07525.

Koroleff, F. (1983). "Determination of silicon". In: *Methods of Seawater Analysis*. Ed. by K. Grasshoff and M. Kremling. Wiley-VCH, Weinheim, pp. 174–183.

Kriest, I. and A. Oschlies (2008). "On the treatment of particulate organic matter sinking in large-scale models of marine biogeochemical cycles". In: *Biogeosciences (BG)*. doi: 10.5194/bg-5-55-2008.

Kumar, N. et al. (1995). "Increased biological productivity and export production in the glacial Southern Ocean". In: *Nature*. doi: 10.1038/378675a0.

Lambert, F. et al. (2015). "Dust fluxes and iron fertilization in Holocene and Last Glacial Maximum climates". In: *Geophys. Res. Lett.* doi: 10.1002/2015GL064250.

Lancelot, C. et al. (2009). "Spatial distribution of the iron supply to phytoplankton in the Southern Ocean: a model study". In: *Biogeosciences*. doi: 10.5194/bg-6-2861-2009.

Landry, M. R. et al. (2000). "Biological response to iron fertilization in the eastern equatorial Pacific (IronEx II). III. Dynamics of phytoplankton growth and microzooplankton grazing". In: *Marine Ecology Progress Series*. doi: 10.3354/meps201057.

Lannuzel, D. et al. (2008). "Iron study during a time series in the western Weddell pack ice". In: *Marine Chemistry*. doi: 10.1016/j.marchem.2007.10.006.

Lannuzel, D. et al. (2010). "Distribution of dissolved iron in Antarctic sea ice: Spatial, seasonal, and inter-annual variability". In: *Journal of Geophysical Research: Biogeosciences*. doi: 10.1029/2009JG001031.

Lannuzel, D. et al. (2016). "Iron in sea ice: Review and new insights". In: *Elem Sci Anth*. doi: 10.12952/journal.elementa.000130.

Lefèvre, N. and A. J. Watson (1999). "Modeling the geochemical cycle of iron in the oceans and its impact on atmospheric CO_2 concentrations". In: *Global Biogeochemical Cycles*. doi: 10.1029/1999GB900034.

Li, W. et al. (2017). "Air pollution–aerosol interactions produce more bioavailable iron for ocean ecosystems". In: *Science Advances*. doi: 10.1126/sciadv.1601749.

Lin, H. et al. (2011). "Free-drifting icebergs as sources of iron to the Weddell Sea". In: *Deep Sea Research Part II: Topical Studies in Oceanography*. doi: 10.1016/j.dsr2.2010.11.020.

Liu, X. and F. J. Millero (2002). "The solubility of iron in seawater". In: *Marine Chemistry*. doi: 10.1016/S0304-4203(01)00074-3.

Löscher, B. M. et al. (1997). "The distribution of Fe in the Antarctic Circumpolar Current". In: *Deep Sea Research Part II: Topical Studies in Oceanography*. doi: 10.1016/S0967-0645(96)00101-4.

Luo, C. et al. (2008). "Combustion iron distribution and deposition". In: *Global Biogeochemical Cycles*. doi: 10.1029/2007GB002964.

Mackey, K. R. M. et al. (2008). "A photosynthetic strategy for coping in a high-light, low-nutrient environment". In: *Limnology and Oceanography*. doi: 10.4319/lo.2008.53.3.0900.

Mahowald, N. M. et al. (1999). "Dust sources and deposition during the last glacial maximum and current climate: A comparison of model results with paleodata from ice cores and marine sediments". In: *Journal of Geophysical Research: Atmospheres*. doi: 10.1029/1999JD900084.

Mahowald, N. M. et al. (2005). "Atmospheric global dust cycle and iron inputs to the ocean". In: *Global Biogeochemical Cycles*. doi: 10.1029/2004GB002402.

Mahowald, N. M. et al. (2009). "Atmospheric Iron Deposition: Global Distribution, Variability, and Human Perturbations". In: *Annual Review of Marine Science*. doi: 10.1146/annurev.marine.010908.163727.

Marchetti, A. (2005). "Ecophysiological aspects of iron nutrition and domoic acid production in oceanic and coastal diatoms of the genus *Pseudo-nitzschia*". In: PhD thesis, University of British Columbia.

Marchetti, A. and P. J. Harrison (2007). "Coupled changes in the cell morphology and elemental (C, N, and Si) composition of the pennate diatom *Pseudo-nitzschia* due to iron deficiency". In: *Limnology and Oceanography*. doi: 10.4319/lo.2007.52.5.2270.

Marchetti, A. et al. (2006). "Iron requirements of the pennate diatom *Pseudo-nitzschia*: Comparison of oceanic (high-nitrate, low-chlorophyll waters) and coastal species". In: *Limnology and Oceanography*. doi: 10.4319/lo.2006.51.5.2092.

Marchetti, A. et al. (2009). "Ferritin is used for iron storage in bloom-forming marine pennate diatoms". In: *Nature*. doi: 10.1038/nature07539.

Marshall, J. et al. (1997). "A finite-volume, incompressible Navier Stokes model for studies of the ocean on parallel computers". In: *Journal of Geophysical Research: Oceans*. doi: 10.1029/96JC02775.

Martin, J. H. (1990). "Glacial-interglacial CO_2 change: The Iron Hypothesis". In: *Paleoceanography*. doi: 10.1029/PA005i001p00001.

Martin, J. H. et al. (1994). "Testing the iron hypothesis in ecosystems of the equatorial Pacific Ocean". In: *Nature*. doi: 10.1038/371123a0.

Martínez-Garcia, A. et al. (2009). "Links between iron supply, marine productivity, sea surface temperature, and CO_2 over the last 1.1 Ma". In: *Paleoceanography*. doi: 10.1029/2008PA001657.

Martínez-Garcia, A. et al. (2014). "Iron Fertilization of the Subantarctic Ocean During the Last Ice Age". In: *Science*. doi: 10.1126/science.1246848.

Mawji, E. et al. (2008). "Hydroxamate Siderophores: Occurrence and Importance in the Atlantic Ocean". In: *Environmental Science Technology*. doi: 10.1021/es801884r.

Mayr, C. et al. (2013). "Intensified Southern Hemisphere Westerlies regulated atmospheric CO_2 during the last deglaciation". In: doi: 10.1130/G34335.1.

McKay, R. M. L., R. J. Geider, and J. LaRoche (1997). "Physiological and Biochemical Response of the Photosynthetic Apparatus of Two Marine Diatoms to Fe Stress". In: *Plant Physiology*. doi: 10.1104/pp.114.2.615.

Mehler, A. H. (1957). "Studies on reactions of illuminated chloroplasts: I. Mechanism of the reduction of oxygen and other Hill reagents". In: *Archives of Biochemistry and Biophysics*. doi: 10.1016/0003-9861(51)90082-3.

Mehrbach, C. et al. (1973). "Measurement of the apparent dissociation constants of carbonic acid in seawater at atmospheric pressure". In: *Limnology and Oceanography*. doi: 10.4319/lo.1973.18.6.0897.

Menemenlis, D. and C. Wunsch (1997). "Linearization of an Oceanic General Circulation Model for Data Assimilation and Climate Studies". In: *Journal of Atmospheric and Oceanic Technology*. doi: 10.1175/1520-0426(1997)014<1420:LOAOGC>2.0.CO;2.

Merino, N. et al. (2016). "Antarctic icebergs melt over the Southern Ocean: Climatology and impact on sea ice". In: *Ocean Modelling*. doi: 10.1016/j.ocemod.2016.05.001.

Milillo, P. et al. (2018). "Accelerated heterogeneous retreat of Thwaites glacier, West Antarctica, fueled by high subaqueous melting at the grounding line". In: *AGU Fall Meeting Abstracts*. https://ui.adsabs.harvard.edu/abs/2018AGUFM.C51F1133M.

Millero, F. J., W. Yao, and J. Aicher (1995). "The speciation of Fe(II) and Fe(III) in natural waters". In: *Marine Chemistry*. doi: 10.1016/0304-4203(95)00024-L.

Milligan, A. J. and P. J. Harrison (2000). "Effects of non-steady-state iron limitation on nitrogen assimilatory enzymes in the marine diatom *Thalassiosira weissflogii* (Bacillariophyceae)". In: *Journal of Phycology*. doi: 10.1046/j.1529-8817.2000.99013.x.

Mioni, C. E., L. Poorvin, and S. W. Wilhelm (2005). "Virus and siderophore-mediated transfer of available Fe between heterotrophic bacteria: characterization using an Fe-specific bioreporter". In: *Aquatic Microbial Ecology*. doi: 10.3354/ame041233.

Misumi, K. et al. (2013). "Humic substances may control dissolved iron distributions in the global ocean: Implications from numerical simulations". In: *Global Biogeochemical Cycles*. doi: 10.1002/gbc.20039.

Moore, C. M. et al. (2013). "Processes and patterns of oceanic nutrient limitation". In: *Nature Geoscience*. doi: 10.1038/ngeo1765.

Moore, J. K. and O. Braucher (2007). "Observations of dissolved iron concentrations in the World Ocean: implications and constraints for ocean biogeochemical models". In: *Biogeosciences Discussions*. https://hal.archives-ouvertes.fr/hal-00297886.

— (2008). "Sedimentary and mineral dust sources of dissolved iron to the world ocean". In: *Biogeosciences*. doi: https://hal.archives-ouvertes.fr/hal-00297688.

Moore, J. K., S. C. Doney, and K. Lindsay (2004). "Upper ocean ecosystem dynamics and iron cycling in a global three-dimensional model". In: *Global Biogeochemical Cycles*. doi: 10.1029/2004GB002220.

Moore, J. K. et al. (2001). "Iron cycling and nutrient-limitation patterns in surface waters of the World Ocean". In: *Deep Sea Research Part II: Topical Studies in Oceanography*. doi: 10.1016/S0967-0645(01)00109-6.

Moore, J. K. et al. (2006). "Nitrogen fixation amplifies the ocean biogeochemical response to decadal timescale variations in mineral dust deposition". In: *Tellus B: Chemical and Physical Meteorology*. doi: 10.1111/j.1600-0889.2006.00209.x.

Morel, F. M. M., R. J. Hudson, and N. M. Price (1991). "Limitation of productivity by trace metals in the sea". In: *Limnology and Oceanography*. doi: 10.4319/lo.1991.36.8.1742.

Morel, F. M. M., A. B. Kustka, and Y. Shaked (2008). "The role of unchelated Fe in the iron nutrition of phytoplankton". In: *Limnology and Oceanography*. doi: 10.4319/lo.2008.53.1.0400.

Morel, F. M. M. and N. M. Price (2003). "The Biogeochemical Cycles of Trace Metals in the Oceans". In: *Science*. doi: 10.1126/science.1083545.

Morris, P. J. and M. A. Charette (2013). "A synthesis of upper ocean carbon and dissolved iron budgets for Southern Ocean natural iron fertilisation studies". In: *Deep Sea Research Part II: Topical Studies in Oceanography*. doi: 10.1016/j.dsr2.2013.02.001.

Muglia, J., L. C. Skinner, and A. Schmittner (2018). "Weak overturning circulation and high Southern Ocean nutrient utilization maximized glacial ocean carbon". In: *Earth and Planetary Science Letters*. doi: 10.1016/j.epsl.2018.05.038.

Myriokefalitakis, S. et al. (2018). "Reviews and syntheses: the GESAMP atmospheric iron deposition model intercomparison study". In: *Biogeosciences*. doi: 10.5194/bg-15-6659-2018.

Nelson, D. M. et al. (1995). "Production and dissolution of biogenic silica in the ocean: Revised global estimates, comparison with regional data and relationship to biogenic sedimentation". In: *Global Biogeochemical Cycles*. doi: 10.1029/95GB01070.

Nielsdóttir, M. C. et al. (2009). "Iron limitation of the postbloom phytoplankton communities in the Iceland Basin". In: *Global Biogeochemical Cycles*. doi: 10.1029/2008GB003410.

Nishioka, J., H. Obata, and D. Tsumune (2013). "Evidence of an extensive spread of hydrothermal dissolved iron in the Indian Ocean". In: *Earth and Planetary Science Letters*. doi: 10.1016/j.epsl.2012.11.040.

Nunn, B. L. et al. (2013). "Diatom Proteomics Reveals Unique Acclimation Strategies to Mitigate Fe Limitation". In: *PLOS ONE*. doi: 10.1371/journal.pone.0075653.

Oelkers, E. H. et al. (2011). "The role of riverine particulate material on the global cycles of the elements". In: *Applied Geochemistry*. doi: 10.1016/j.apgeochem.2011.03.062.

Olgun, N. et al. (2011). "Surface ocean iron fertilization: The role of airborne volcanic ash from subduction zone and hot spot volcanoes and related iron fluxes into the Pacific Ocean". In: *Global Biogeochemical Cycles*. doi: 10.1029/2009GB003761.

Oxborough, K. et al. (2012). "Direct estimation of functional PSII reaction center concentration and PSII electron flux on a volume basis: a new approach to the analysis of Fast Repetition Rate fluorometry (FRRf) data". In: *Limnology and Oceanography: Methods*. doi: 10.4319/lom.2012.10.142.

Öztürk, M. et al. (2004). "Iron enrichment and photoreduction of iron under UV and PAR in the presence of hydroxycarboxylic acid: implications for phytoplankton growth in the Southern Ocean". In: *Deep Sea Research Part II: Topical Studies in Oceanography*. doi: 10.1016/j.dsr2.2000.10.001.

Pakhomova, S. V., A. G. Rozanov, and E. V. Yakushev (2009). "Dissolved and particulate forms of iron and manganese in the redox zone of the Black Sea". In: *Oceanology*. doi: 10.1134/S0001437009060046.

Parekh, P., M. J. Follows, and E. Boyle (2004). "Modeling the global ocean iron cycle". In: *Global Biogeochemical Cycles*. doi: 10.1029/2003GB002061.

Person, R. et al. (2019). "Sensitivity of ocean biogeochemistry to the iron supply from the Antarctic ice sheet explored with a biogeochemical model". In: *Biogeosciences Discussions*. doi: 10.5194/bg-2019-134, in review.

Petrou, K. et al. (2014). "The impact of iron limitation on the physiology of the Antarctic diatom *Chaetoceros simplex*". In: *Marine Biology*. doi: 10.1007/s00227-014-2392-z.

Pham, A. L. D. and T. Ito (2018). "Formation and Maintenance of the GEOTRACES Subsurface - Dissolved Iron Maxima in an Ocean Biogeochemistry Model". In: *Global Biogeochemical Cycles*. doi: 10.1029/2017GB005852.

Pollard, R. T. et al. (2009). "Southern Ocean deep-water carbon export enhanced by natural iron fertilization". In: *Nature*. doi: 10.1038/nature07716.

Prasil, O. et al. (1996). "Cyclic electron flow around Photosystem II in vivo". In: *Photosynthesis Research*. doi: 10.1007/BF00029472.

Prospero, J. M. et al. (2002). "Environmental characterization of global sources of atmospheric soil dust identified with the Nimbus 7 Total Ozone Mapping Spectrometer (TOMS) absorbing aerosol product". In: *Reviews of Geophysics*. doi: 10.1029/2000RG000095.

Rackow, T. et al. (2017). "A simulation of small to giant Antarctic iceberg evolution: Differential impact on climatology estimates". In: *Journal of Geophysical Research: Oceans*. doi: 10.1002/2016JC012513.

Raiswell, R. (2011). "Iceberg-hosted nanoparticulate Fe in the Southern Ocean: Mineralogy, origin, dissolution kinetics and source of bioavailable Fe". In: *Deep Sea Research Part II: Topical Studies in Oceanography*. doi: 10.1016/j.dsr2.2010.11.011.

Raiswell, R. et al. (2006). "Contributions from glacially derived sediment to the global iron (oxyhydr)oxide cycle: Implications for iron delivery to the oceans". In: *Geochimica et Cosmochimica Acta*. doi: 10.1016/j.gca.2005.12.027.

Raiswell, R. et al. (2008). "Bioavailable iron in the Southern Ocean: the significance of the iceberg conveyor belt". In: *Geochemical Transactions*. doi: 10.1186/1467-4866-9-7.

Raiswell, R. et al. (2016). "Potentially bioavailable iron delivery by iceberg-hosted sediments and atmospheric dust to the polar oceans". In: *Biogeosciences*. doi: 10.5194/bg-13-3887-2016.

Ralph, P. J. and R. Gademann (2005). "Rapid light curves: A powerful tool to assess photosynthetic activity". In: *Aquatic Botany*. doi: 10.1016/j.aquabot.2005.02.006.

Raven, J. A., M. C. W. Evans, and R. E. Korb (1999). "The role of trace metals in photosynthetic electron transport in O_2-evolving organisms". In: *Photosynthesis Research*. doi: 10.1023/A:1006282714942.

Raven, J. A. and P. G. Falkowski (1999). "Oceanic sinks for atmospheric CO_2". In: *Plant, Cell & Environment*. doi: 10.1046/j.1365-3040.1999.00419.x.

Reinfelder, J. R. (2012). "Carbon dioxide regulation of nitrogen and phosphorus in four species of marine phytoplankton". In: *Marine Ecology Progress Series*. doi: 10.3354/meps09905.

Resing, J. A. et al. (2015). "Basin-scale transport of hydrothermal dissolved metals across the South Pacific Ocean". In: *Nature*. doi: 10.1038/nature14577.

Rignot, E. et al. (2002). "Acceleration of Pine Island and Thwaites Glaciers, West Antarctica". In: *Annals of Glaciology*. doi: 10.3189/172756402781817950.

Rignot, E. et al. (2008). "Recent Antarctic ice mass loss from radarinterferometry and regional climatemodelling". In: *Nature Geoscience*. doi: 10.1038/ngeo102.

Rijkenberg, M. J. A. et al. (2012). "Fluxes and distribution of dissolved iron in the eastern (sub-) tropical North Atlantic Ocean". In: *Global Biogeochemical Cycles*. doi: 10.1029/2011GB004264.

Rijkenberg, M. J. A. et al. (2014). "The Distribution of Dissolved Iron in the West Atlantic Ocean". In: *PLOS ONE*. doi: 10.1371/journal.pone.0101323.

Rue, E. L. and K. W. Bruland (1995). "Complexation of iron(III) by natural organic ligands in the Central North Pacific as determined by a new competitive ligand equilibration/adsorptive cathodic stripping voltammetric method". In: *Marine Chemistry*. doi: 10.1016/0304-4203(95)00031-L.

Ryan-Keogh, T. J. et al. (2012). "The cyanobacterial chlorophyll-binding-protein IsiA acts to increase the in vivo effective absorption cross-section of PSI under iron limitation". In: *Journal of Phycology*. doi: 10.1111/j.1529-8817.2011.01092.x.

Saito, M. A., D. M. Sigman, and F. M. M. Morel (2003). "The bioinorganic chemistry of the ancient ocean: the co-evolution of cyanobacterial metal requirements and biogeochemical cycles at the Archean-Proterozoic boundary?" In: *Inorganica Chimica Acta*. doi: 10.1016/S0020-1693(03)00442-0.

Saito, M. A. et al. (2013). "Slow-spreading submarine ridges in the South Atlantic as a significant oceanic iron source". In: *Nature Geoscience*. doi: 10.1038/ngeo1893.

Sander, S. G. and A. Koschinsky (2011). "Metal flux from hydrothermal vents increased by organic complexation". In: *Nature Geoscience*. doi: 10.1038/ngeo1088.

Sarthou, G. et al. (2008). "The fate of biogenic iron during a phytoplankton bloom induced by natural fertilisation: Impact of copepod grazing". In: *Deep Sea Research Part II: Topical Studies in Oceanography*. doi: 10.1016/j.dsr2.2007.12.033.

Savoye, N. et al. (2006). "^{234}Th sorption and export models in the water column: A review". In: *Marine Chemistry*. doi: 10.1016/j.marchem.2005.10.014.

Schlitzer, R. et al. (2018). "The GEOTRACES Intermediate Data Product 2017". In: *Chemical Geology*. doi: 10.1016/j.chemgeo.2018.05.040.

Schodlok, M. P. et al. (2006). "Weddell Sea iceberg drift: Five years of observations". In: *Journal of Geophysical Research: Oceans*. doi: 10.1029/2004JC002661.

Schuback, N. et al. (2015). "Interacting Effects of Light and Iron Availability on the Coupling of Photosynthetic Electron Transport and CO_2-Assimilation in Marine Phytoplankton". In: *PLOS ONE*. doi: 10.1371/journal.pone.0133235.

Sedwick, P. N. and G. R. DiTullio (1997). "Regulation of algal blooms in Antarctic Shelf Waters by the release of iron from melting sea ice". In: *Geophysical Research Letters*. doi: 10.1029/97GL02596.

Sedwick, P. N. et al. (2005). "Iron in the Sargasso Sea (Bermuda Atlantic Time-series Study region) during summer: Eolian imprint, spatiotemporal variability, and ecological implications". In: *Global Biogeochemical Cycles*. doi: 10.1029/2004GB002445.

Sedwick, P. N. et al. (2015). "A zonal picture of the water column distribution of dissolved iron(II) during the U.S. GEOTRACES North Atlantic transect cruise (GEOTRACES GA03)". In: *Deep Sea Research Part II: Topical Studies in Oceanography*. doi: 10.1016/j.dsr2.2014.11.004.

Shaw, T. J. et al. (2011). "^{234}Th-Based Carbon Export around Free-Drifting Icebergs in the Southern Ocean". In: *Deep Sea Research Part II: Topical Studies in Oceanography*. doi: 10.1016/j.dsr2.2010.11.019.

Sherlock, R. E. et al. (2011). "Near-field zooplankton, ice-face biota and proximal hydrography of free-drifting Antarctic icebergs". In: *Deep Sea Research Part II: Topical Studies in Oceanography*. doi: 10.1016/j.dsr2.2010.11.025.

Sigman, D. M. and E. A. Boyle (2000). "Glacial/interglacial variations in atmospheric carbon dioxide". In: *Nature*. doi: 10.1038/35038000.

SigmaPlot (www.systatsoftware.com). In: Version 13.0 from Systat Software, Inc., San Jose California USA.

Smetacek, V. (1999). "Diatoms and the Ocean Carbon Cycle". In: *Protist*. doi: 10.1016/S1434-4610(99)70006-4.

— (2018). "Seeing is Believing: Diatoms and the Ocean Carbon Cycle Revisited". In: *Protist*. doi: 10.1016/j.protis.2018.08.004.

Smetacek, V. S. (1985). "Role of sinking in diatom life-history cycles: ecological, evolutionary and geological significance". In: *Marine Biology*. doi: 10.1007/BF00392493.

Smetacek, V. S. et al. (2012). "Deep carbon export from a Southern Ocean iron-fertilized diatom bloom". In: *Nature*. doi: 10.1038/nature11229.

Smith, K. L. (2011). "Free-drifting icebergs in the Southern Ocean: An overview". In: *Deep Sea Research Part II: Topical Studies in Oceanography*. doi: 10.1016/j.dsr2.2010.11.003.

Smith, K. L. et al. (2007). "Free-Drifting Icebergs: Hot Spots of Chemical and Biological Enrichment in the Weddell Sea". In: *Science*. doi: 10.1126/science.1142834.

Statham, P. J., M. Skidmore, and M. Tranter (2008). "Inputs of glacially derived dissolved and colloidal iron to the coastal ocean and implications for primary productivity". In: *Global Biogeochemical Cycles*. doi: 10.1029/2007GB003106.

Stephens, B. B. and R. F. Keeling (2000). "The influence of Antarctic sea ice on glacial - interglacial CO_2 variations". In: *Nature*. doi: 10.1038/35004556.

Stern, A. A., A. Adcroft, and O. Sergienko (2016). "The effects of Antarctic iceberg calving-size distribution in a global climate model". In: *Journal of Geophysical Research: Oceans*. doi: 10.1002/2016JC011835.

Stoll, M. H. C. et al. (2001). "Continuous-Flow Analysis of Dissolved Inorganic Carbon Content in Seawater". In: *Analytical Chemistry*. doi: 10.1021/ac010303r.

Strzepek, R. F. and P. J. Harrison (2004). "Photosynthetic architecture differs in coastal and oceanic diatoms". In: *Nature*. doi: 10.1038/nature02954.

Strzepek, R. F. et al. (2005). "Spinning the "Ferrous Wheel": The importance of the microbial community in an iron budget during the Fe Cycle experiment". In: *Global Biogeochemical Cycles*. doi: 10.1029/2005GB002490.

Strzepek, R. F. et al. (2011). "Adaptive strategies by Southern Ocean phytoplankton to lessen iron limitation: Uptake of organically complexed iron and reduced cellular iron requirements". In: *Limnology and Oceanography*. doi: 10.4319/lo.2011.56.6.1983.

Strzepek, R. F. et al. (2012). "Iron-light interactions differ in Southern Ocean phytoplankton". In: *Limnology and Oceanography*. doi: 10.4319/lo.2012.57.4.1182.

Suggett, D. J., H. L. MacIntyre, and R. J. Geider (2004). "Evaluation of biophysical and optical determinations of light absorption by photosystem II in phytoplankton". In: *Limnology and Oceanography: Methods*. doi: 10.4319/lom.2004.2.316.

Suggett, D. J. et al. (2009). "Interpretation of fast repetition rate (FRR) fluorescence: signatures of phytoplankton community structure versus physiological state". In: *Marine Ecology Progress Series*. doi: 10.3354/meps07830.

Sugie, K. and K. Kuma (2008). "Resting spore formation in the marine diatom *Thalassiosira nordenskioeldii* under iron- and nitrogen-limited conditions". In: *Journal of Plankton Research*. doi: 10.1093/plankt/fbn080.

Sugie, K. and T. Yoshimura (2013). "Effects of pCO_2 and iron on the elemental composition and cell geometry of the marine diatom *Pseudo-nitzschia pseudodelicatissima* (Bacillariophyceae)[1]". In: *Journal of Phycology*. doi: 10.1111/jpy.12054.

Sun, J. et al. (2011). "Effects of changing pCO_2 and phosphate availability on domoic acid production and physiology of the marine harmful bloom diatom *Pseudo-nitzschia multiseries*". In: *Limnology and Oceanography*. doi: 10.4319/lo.2011.56.3.0829.

Sunda, W. G. (2012). "Feedback Interactions between Trace Metal Nutrients and Phytoplankton in the Ocean". In: *Frontiers in Microbiology*. doi: 10.3389/fmicb.2012.00204.

Sunda, W. G. and S. A. Huntsman (1995). "Iron uptake and growth limitation in oceanic and coastal phytoplankton". In: *Marine Chemistry*. doi: 10.1016/0304-4203(95)00035-P.

Sunda, W. G., D. G. Swift, and S. A. Huntsman (1991). "Low iron requirement for growth in oceanic phytoplankton". In: *Nature*. doi: 10.1038/351055a0.

Tagliabue, A., L. Bopp, and O. Aumont (2009). "Evaluating the importance of atmospheric and sedimentary iron sources to Southern Ocean biogeochemistry". In: *Geophysical Research Letters*. doi: 10.1029/2009GL038914.

Tagliabue, A. and C. Völker (2011). "Towards accounting for dissolved iron speciation in global ocean models". In: *Biogeosciences*. doi: 10.5194/bg-8-3025-2011.

Tagliabue, A. et al. (2010). "Hydrothermal contribution to the oceanic dissolved iron inventory ". In: *Nature Geoscience*. doi: 10.1038/ngeo818.

Tagliabue, A. et al. (2012). "A global compilation of dissolved iron measurements: focus on distributions and processes in the Southern Ocean". In: *Biogeosciences*. doi: 10.5194/bg-9-2333-2012.

Tagliabue, A. et al. (2014). "A ventilation-based framework to explain the regeneration-scavenging balance of iron in the ocean". In: *Geophysical Research Letters*. doi: 10.1002/2014GL061066.

Tagliabue, A. et al. (2016). "How well do global ocean biogeochemistry models simulate dissolved iron distributions?" In: *Global Biogeochemical Cycles*. doi: 10.1002/2015GB005289.

Tagliabue, A. et al. (2017). "The integral role of iron in ocean biogeochemistry". In: *Nature*. doi: 10.1038/nature21058.

Takahashi, T. et al. (2009). "Climatological mean and decadal change in surface ocean pCO_2, and net sea-air CO_2 flux over the global oceans". In: *Deep Sea Research Part II: Topical Studies in Oceanography*. doi: 10.1016/j.dsr2.2008.12.009.

Takeda, S. (1998). "Influence of iron availability on nutrient consumption ratio of diatoms in oceanic waters". In: *Nature*. doi: 10.1038/31674.

Tchernia, P. (1980). "Descriptive Regional Oceanography". In: *Elsevier, New York*.

Tegen, I. and I. Fung (1994). "Modeling of mineral dust in the atmosphere: Sources, transport, and optical thickness". In: *Journal of Geophysical Research: Atmospheres*. doi: 10.1029/94JD01928.

Timmermans, K. R., B. van der Wagt, and H. J. W. de Baar (2004). "Growth rates, half-saturation constants, and silicate, nitrate, and phosphate depletion in relation to iron availability of four large, open-ocean diatoms from the Southern Ocean". In: *Limnology and Oceanography*. doi: 10.4319/lo.2004.49.6.2141.

Toggweiler, J. R., J. L. Russell, and S. R. Carson (2006). "Midlatitude westerlies, atmospheric CO_2, and climate change during the ice ages". In: *Paleoceanography*. doi: 10.1029/2005PA001154.

Tortell, P. D., M. T. Maldonado, and N. M. Price (1996). "The role of heterotrophic bacteria in iron-limited ocean ecosystems". In: *Nature*.

Tortell, P. D. et al. (2008). "CO_2 sensitivity of Southern Ocean phytoplankton". In: *Geophysical Research Letters*. doi: 10.1029/2007GL032583.

Tréguer, P. et al. (1995). "The Silica Balance in the World Ocean: A Reestimate". In: *Science*. doi: 10.1126/science.268.5209.375.

Trimborn, S. et al. (2008). "Inorganic carbon acquisition in potentially toxic and non-toxic diatoms: the effect of pH-induced changes in seawater carbonate chemistry". In: *Physiologia Plantarum*. doi: 10.1111/j.1399-3054.2007.01038.x.

Trimborn, S. et al. (2013). "Sensitivity of Antarctic phytoplankton species to ocean acidification: Growth, carbon acquisition, and species interaction". In: *Limnology and Oceanography*. doi: 10.4319/lo.2013.58.3.0997.

Trimborn, S. et al. (2014). "Photophysiological responses of Southern Ocean phytoplankton to changes in CO_2 concentrations: Short-term versus acclimation effects". In: *Journal of Experimental Marine Biology and Ecology*. doi: 10.1016/j.jembe.2013.11.001.

Trimborn, S. et al. (2015). "Physiological characteristics of open ocean and coastal phytoplankton communities of Western Antarctic Peninsula and Drake Passage waters". In: *Deep Sea Research Part I: Oceanographic Research Papers*. doi: 10.1016/j.dsr.2014.12.010.

Trimborn, S. et al. (2017). "Iron sources alter the response of Southern Ocean phytoplankton to ocean acidification". In: *Marine Ecology Progress Series*. doi: 10.3354/meps12250.

Trimborn, S. et al. (2019). "Susceptibility of Two Southern Ocean Phytoplankton Key Species to Iron Limitation and High Light". In: *Frontiers in Marine Science*. doi: 10.3389/fmars.2019.00167.

Turekian, K. K. (1977). "The fate of metals in the oceans". In: *Geochimica et Cosmochimica Acta*. doi: 10.1016/0016-7037(77)90109-0.

Utermöhl, H. (1958). "Methods of collecting plankton for various purposes are discussed." In: *SIL Communications, 1953-1996*. doi: 10.1080/05384680.1958.11904091.

van Leeuwe, M. A., R. J. W. Visser, and J. Stefels (2014). "The pigment composition of *Phaeocystis antarctica* (Haptophyceae) under various conditions of light, temperature, salinity, and iron". In: *Journal of Phycology*. doi: 10.1111/jpy.12238.

Vancoppenolle, M. et al. (2013). "Role of sea ice in global biogeochemical cycles: emerging views and challenges". In: *Quaternary Science Reviews*. doi: 10.1016/j.quascirev.2013.04.011.

Vernet, M. et al. (2011). "Impacts on phytoplankton dynamics by free-drifting icebergs in the NW Weddell Sea". In: *Deep Sea Research Part II: Topical Studies in Oceanography*. doi: 10.1016/j.dsr2.2010.11.022.

Voelker, B. M. and D. L. Sedlak (1995). "Iron reduction by photoproduced superoxide in seawater". In: *Marine Chemistry*. doi: 10.1016/0304-4203(95)00029-Q.

Völker, C. and A. Tagliabue (2015). "Modeling organic iron-binding ligands in a three-dimensional biogeochemical ocean model". In: *Marine Chemistry*. doi: 10.1016/j.marchem.2014.11.008.

Vraspir, J. M. and A. Butler (2009). "Chemistry of Marine Ligands and Siderophores". In: *Annual Review of Marine Science*. doi: 10.1146/annurev.marine.010908.163712.

Wadley, M. R., T. D. Jickells, and K. J. Heywood (2014). "The role of iron sources and transport for Southern Ocean productivity". In: *Deep Sea Research Part I: Oceanographic Research Papers*. doi: https://doi.org/10.1016/j.dsr.2014.02.003.

Wagener, T., C. Guieu, and N. Leblond (2010). "Effects of dust deposition on iron cycle in the surface Mediterranean Sea: results from a mesocosm seeding experiment". In: *Biogeosciences*. doi: 10.5194/bg-7-3769-2010.

Wagener, T. et al. (2008). "Revisiting atmospheric dust export to the Southern Hemisphere ocean: Biogeochemical implications". In: *Global Biogeochem*. doi: 10.1029/2007GB002984.

Watson, A. J. and A. C. Naveira Garabato (2006). "The role of Southern Ocean mixing and upwelling in glacial-interglacial atmospheric CO_2 change". In: *Tellus B: Chemical and Physical Meteorology*. doi: 10.1111/j.1600-0889.2005.00167.x.

Wedepohl, K. H. (1995). "The composition of the continental crust". In: *Geochimica et Cosmochimica Acta*. doi: 10.1016/0016-7037(95)00038-2.

Werner, M. et al. (2002). "Seasonal and interannual variability of the mineral dust cycle under present and glacial climate conditions". In: *Journal of Geophysical Research: Atmospheres*. doi: 10.1029/2002JD002365.

Wesche, C. and W. Dierking (2015). "Near-coastal circum-Antarctic iceberg size distributions determined from Synthetic Aperture Radar images". In: *Remote Sensing of Environment*. doi: https://doi.org/10.1016/j.rse.2014.10.025.

Wilken, S. et al. (2011). "Diatom frustules show increased mechanical strength and altered valve morphology under iron limitation". In: *Limnology and Oceanography*. doi: 10.4319/lo.2011.56.4.1399.

Williams, R. J. P. and R. E. M. Rickaby (2012). "Evolution's destiny: Co-evolving chemistry of the environment and life". In: Royal Society of Chemistry Publishing, Cambridge, United Kingdom.

Wright, S. W (1991). "Improved HPLC method for the analysis of chlorophylls and carotenoids from marine phytoplankton". In: *Mar. Ecol. Prog. Ser.* doi: 10.3354/meps07718.

Wu, J., M. J. Wells, and R. Rember (2011). "Dissolved iron anomaly in the deep tropical-subtropical Pacific: Evidence for long-range transport of hydrothermal iron". In: *Geochimica et Cosmochimica Acta*. doi: 10.1016/j.gca.2010.10.024.

Ye, Y. and C. Völker (2017). "On the Role of Dust-Deposited Lithogenic Particles for Iron Cycling in the Tropical and Subtropical Atlantic". In: *Global Biogeochemical Cycles*. doi: 10.1002/2017GB005663.

Ye, Y., C. Völker, and D. A. Wolf-Gladrow (2009). "A model of Fe speciation and biogeochemistry at the Tropical Eastern North Atlantic Time-Series Observatory site". In: *Biogeosciences (BG)*. doi: doi:10.5194/bg-6-2041-2009.

Yücel, M. et al. (2011). "Hydrothermal vents as a kinetically stable source of iron-sulphide-bearing nanoparticles to the ocean". In: *Nature Geoscience*. doi: 10.1038/ngeo1148.

Zhang, Y. et al. (2015). "Modeling the global emission, transport and deposition of trace elements associated with mineral dust". In: *Biogeosciences*. doi: 10.5194/bg-12-5771-2015.

Zhu, Z. et al. (2017). "Individual and interactive effects of warming and CO_2 on *Pseudo-nitzschia subcurvata* and *Phaeocystis antarctica*, two dominant phytoplankton from the Ross Sea, Antarctica". In: *Biogeosciences*. doi: 10.5194/bg-14-5281-2017.